Preparation and characterization of lead free $(K_{0.5}Na_{0.5})NbO_3$ ferroelectric bulk and thin films

A Thesis Submitted to
Indian Institute of Technology Guwahati
for the Degree of

Doctor of Philosophy

By

P. Mahesh

Department of Physics
Indian Institute of Technology Guwahati
Assam, India

December 2016

INDIAN INSTITUTE OF TECHNOLOGY GUWAHATI
Department of Physics
Guwahati – 781039

STATEMENT

The present thesis entitled, **"Preparation and characterization of lead free $(K_{0.5}Na_{0.5})NbO_3$ ferroelectric bulk and thin films"** has been carried out by me under the supervision of Dr. D. Pamu, Department of Physics, Indian Institute of Technology Guwahati. This work has not been submitted elsewhere for the award of any degree.

December, 2016

(**P. Mahesh**)
Department of Physics,
Indian Institute of Technology Guwahati,
Guwahati – 781 039

INDIAN INSTITUTE OF TECHNOLOGY GUWAHATI
Department of Physics
Guwahati – 781039

CERTIFICATE

It is certified that the work described in this thesis, entitled "**Preparation and characterization of lead free $(K_{0.5}Na_{0.5})NbO_3$ ferroelectric bulk and thin films**", done by Mr. P. Mahesh, a Ph.D. student of Department of Physics, Indian Institute of Technology Guwahati, for the award of degree of *Doctor of Philosophy* has been carried out under my supervision. This work has not been submitted elsewhere for the award of any degree.

December, 2016.

Dr. D. Pamu
Associate Professor,
Department of Physics,
Indian Institute of Technology Guwahati,
Guwahati – 781 039.

Dedicated to my family

ACKNOWLEDGEMENTS

Almost five years of hard work and the countless help and support from the people around me made it today possible to complete the thesis work.

It is honour for me to thank my research supervisor, Dr. D. Pamu, Department of Physics, for his constant support, guidance, encouragement, advices, and valuable discussions, which helped me to improve an understanding of the subject along with skills and successful culmination of my thesis work. I must acknowledge him for providing the unconditional freedom to work, think and express on whatever I have done in my research work by keeping the faith on my capabilities.

I am highly thankful to my doctoral committee members, Prof. S. Ravi (Chairman), Prof. A. Perumal and Dr. S. Kanagaraj for their continuous academic guidance and checking my work progress and seminars during my Ph.D. Their valuable discussions and suggestions were truly encouraging for me.

I express my sincere thanks to Prof. S. Ravi for providing lab space and facilities and treated me as one of his students. I am also thankful to Prof. A. Perumal, Prof. A. Srinivasan, Dr. Dilip Pal and Prof. A. Khare for extending lab facilities.

I would like to express my sincere gratitude to Prof. Poulose Poulose, head of the Department of the Physics, and former head of the departments, Prof. Saurabh Basu, and Prof. S. Ravi, for giving me the opportunity to work in the department and to use departmental facilities. I am also grateful to all the faculty members of the Physics department. I would also like to thank Dr. Sidananda Sarma for his technical assistance and friendly discussions. My special thanks to all scientific officers and staff members in our department and central instruments facility.

My sincere thanks to Dr. A. R. James (DMRL, Hyderabad) for providing ferroelectric measurements and Prof. K. C. James Raju (University of Hyderabad) for providing thin film microwave dielectric measurements. My special thanks to Mrs. S. Josephine for helping me in doing microwave dielectric measurements. I acknowledge Prof. P. K. Iyer for providing the electrical measurements of thin films. I specially want to thank Dr. Subhash Thota for his generous help and friendly discussions.

The financial support for this thesis is provided by Indian Institute of Technology Guwahati and Ministry of Human Resource and Development. Also, I would like to express my heartfelt thanks to Department of Science and Technology (DST), New Delhi; Board of Research in Nuclear Sciences, Mumbai; Defense Research and Development Organization, New Delhi; and Board of Research in Fusion Science & Technology, Gandhinagar, Gujarat through research projects for various experimental facilities. The XRD facility provided by DST, New Delhi, through FIST program [SR/FST/PSII-020/2009] is also acknowledged.

I am also grateful to my seniors Dr. T. Santhosh Kumar, Dr. Ranjan Kumar Bhuyan, Dr. Tribedi Bora, Dr. P. Rajender, Dr. P. Muninder, Dr. Akhilesh Singh, and Dr. Bhargab Deka for sharing their knowledge and useful discussions. I would like to thank my research team members and colleagues Anil, Pallabi, Srinivas, Susmita, Bipul, Junmoni, Gyan, Bibhuti, Pratap, Sanjeev, Deep, Ram, Aakanksha and Jagan for their help, suggestions and enjoyable company. I am grateful to Dr. G. Murali, Dr. N. Subbarao, Dr. P. Suresh, and Ajeet for their help in electrical measurements.

I would like to thank my best friends at IIT Guwahati, especially, Ramakrishna, Venkanna, Ranganatha, Hari, Rajender, Ravi, Suresh, Bheem, Pradeep, Ajay, Sharma, and Sushant for creating a friendly and homely atmosphere. I would also like to thank my village friends Praveen, Naresh, Ashok, Ram, and laxman for their support in every step of my life.

Finally, I would like to express my deepest gratitude to my family, especially, my parents (Laxmi and Komuraiah), sisters (Manjula and Samatha), brother (Shiva), brother-in-law (Ailesh), Nephews (Sweekrith and Riyaarth) and all other family members, who gave blessings, moral support and continuous encouragement.

P. Mahesh

Abstract

Piezoelectric materials have the ability to generate the electric potential by the applied mechanical stress (direct effect) or the change in the shape by the application of external electric field (indirect effect). The ability of the piezoelectric materials to produce the strain, are useful applications in actuators such as sonars, buzzers, and medical ultrasonic transducers. These materials can exhibit the direct piezoelectric effect; have been used in sensors applications, etc. Furthermore, the piezoelectric materials have many useful applications in our daily life, such as quartz clocks, gas igniters, piezoelectric transformers, and automotive applications. The ferroelectric materials possess the spontaneous polarization, and that can be reoriented with the application of external electric field. Further, ferroelectric materials are widely used as high permittivity capacitors, microwave tunable, electro-optic devices, and memory applications, such as non-volatile ferroelectric random access memories (FERAM).

In addition, thin films with high ε_r, low *tanδ,* and improved ferroelectric and piezoelectric properties are required for the sensor, microelectromechanical systems (MEMS), and memory applications. In order to enhance the charge storage and to decrease the device dimensions, the material with high ε_r, low *tanδ* are required. The higher ε_r, low *tanδ* are the key factors for the high performance piezoelectric applications. Ferroelectric thin films also exhibit good linear and nonlinear optical properties which are promising in optical switches, anti-reflection coatings, and nonlinear photonic applications. Therefore, a suitable composition in bulk form will be identified to fabricate the thin films and characterize toward the applications.

Based on the unit cell structure, ferroelectric materials are divided into four types: (a) the tungsten-bronze, (b) the oxygen octahedral (ABO_3), (c) the pyrochlore, and (d) the bismuth layer structure. Among these groups, ABO_3 perovskite type ferroelectrics are considered as the most important due to their outstanding properties and economic. The materials such as, barium titanate ($BaTiO_3$) and lead zirconate titanate ($Pb(Zr_xTi_{1-x})O_3$) based compositions have dominated throughout the history due to their promising ferroelectric and piezoelectric properties. However, due to the lower Curie temperature of $BaTiO_3$ ceramics, they have limitations for use in high temperature ferroelectric applications. In spite of their

excellent piezoelectric, ferroelectric properties and high Curie temperature of lead zirconate titanate based ceramics are confined as per European Union (EU) regulation on Restriction of Hazardous Substances (RoHS) due to the toxicity of lead in the composition. Therefore, the research on the lead-free piezoelectric materials has focused and increased rapidly in the last few years.

The lead-free piezoelectric materials, such as, sodium potassium niobate ($K_{0.5}Na_{0.5}NbO_3$ (KNN)), sodium bismuth titanate ($Na_{0.5}Bi_{0.5}TiO_3$ (NBT)), and potassium bismuth titanate ($K_{0.5}Bi_{0.5}TiO_3$ (KBT)) are well known due to their promising ferro and piezoelectric properties, and these values are comparable to PZT.

Among the lead free piezoelectric ceramics, KNN based compositions exhibit higher ferroelectric and piezoelectric properties. The enhanced properties were obtained at the morphotrophic phase boundary (MPB) composition 50:50 ratios of solid solution of $KNbO_3$ and $NaNbO_3$. The $KNbO_3$ is ferroelectric in orthorhombic phase and $NaNbO_3$ is the antiferroelectric orthorhombic phase at room temperature. The crystal structure of the KNN material at the MPB 50:50 compositions is orthorhombic. The KNN ceramics undergo the structural phase transitions from paraelectric cubic phase to ferroelectric tetragonal phase around 400 ^oC, ferroelectric tetragonal to ferroelectric orthorhombic phase at 200 ^oC, and low temperature orthorhombic to rhombohedral phase at -80 ^oC. The dielectric properties (ε_r = 290, $tan\delta$ = 0.04), Curie temperature (T_C = 420 ^oC) piezoelectric coefficient (d_{33} = 80 pC/N), and electromechanical coupling factor (k_p = 0.29) of the dense KNN prepared by using conventional solid state reaction method. The enhanced piezoelectric properties of KNN ceramics were achieved by using spark plasma sintering (d_{33} =148 pC/N) and the hot pressing techniques (d_{33} =160 pC/N). Saito *et al*. reported the enhanced properties (ε_r = 1570, T_C = 253 ^oC, d_{33} = 461 pC/N, k_p = 0.61) for the composition $(K_{0.44}Na_{0.52}Li_{0.04})(Nb_{0.84}Ta_{0.10}Sb_{0.06})O_3$ prepared by using reactive-templated grain growth method, which are almost comparable to lead based ceramics. Thereafter, a world wide effort is underway to substitute the lead based materials by replacing with KNN based ceramics. Most of the of improved properties were observed in the KNN system are by replacing the alkaline, and niobium ions with Li^+, Sb^{5+}, and Ta^{5+} ions. The doping of Li^+ ion in the A-site, and Sb^{5+}, Ta^{5+} ions in the B-site of the KNN ceramics prepared by using conventional solid state reaction method, greatly enhance the dielectric (ε_r = 1024, $tan\delta$ = 0.06) and piezoelectric (d_{33}

= 390 pC/N, k_p = 0.49) properties at the MPB. The shift in the orthorhombic-tetragonal phase transition towards the lower temperature side can greatly enhance the dielectric and piezoelectric properties. On the other hand, few reports were available on the rare-earth doped KNN ceramics. Wei *et al.* reported the enhancement in the ferroelectric, piezoelectric, and photo luminescent properties of Pr^{3+} doped KNN ceramics. Wang *et al.* reported the coexistence of orthorhombic and tetragonal phases at room temperature with the doping of rare-earth oxides such as Pr_2O_3 and Yb_2O_3 to the $(K_{0.4}Na_{0.6})_{0.95}Li_{0.05}$ $(Nb_{0.95}Sb_{0.05})O_3$. Gao *et al.* reported the improved dielectric permittivity and higher densification in CeO_2-doped $K_{0.5}Na_{0.5}NbO_3$ ceramics. However, there are no reports are available on rare-earth oxides Gd_2O_3 and Dy_2O_3 doped KNN ceramics.

Further, KNN based thin films are considered as most promising materials to be used in sensors, MEMS, energy harvesters, ultrasound imaging devices, and electro-optic waveguide modulators. KNN thin films prepared by using different techniques such as radio frequency (RF) magnetron sputtering, pulsed laser deposition (PLD), and sol-gel method were found to exhibit the enhanced ferroelectric and piezoelectric properties. Larger values of refractive index and electro-optic coefficient, high optical transparency with a wide-band gap of the KNN thin films make it suitable for the optical wave guide, and nonlinear optical applications. However, to the best of the author's knowledge, there were no reports available on the nonlinear optical properties and microwave dielectric properties of the KNN thin films. Therefore, an attempt has been made to deposit the KNN thin films by an economical process and study their linear and nonlinear optical properties, and dielectric properties.

Our continuous effort on the lead-free piezoelectric materials, we have chosen the KNN material and study their properties in the bulk form prepared by using solid state reaction method. Thin films of KNN were deposited by using RF magnetron sputtering method. We have studied the effect of rare-earth oxides on dielectric properties of KNN ceramics and optimized the composition with high relative permittivity and low dielectric loss. Further, the optimized composition was chosen as sputtering target to deposit the thin films. RF magnetron sputtering technique is an effective method compared to other techniques, due to the high rate of deposition, good adhesion, and economical. We have optimized the deposition parameters to get high quality thin films.

The objective of the present study is to get the better understanding of structural, microstructural, dielectric, ferroelectric, and piezoelectric properties of the pure and rare-earth oxide contained KNN ceramics and to deposit the pure and rare-earth doped KNN thin films and to study their optical, dielectric and electrical properties. Further to investigate the nonlinear optical properties and microwave dielectric properties of the thin films, which are useful in nonlinear photonic applications, and high power microwave devices. The present thesis has been divided into six chapters.

Chapter 1 provides the brief introduction to piezoelectric, ferroelectric, and dielectric materials, and their applications. The historical background of the perovskite piezoelectric materials is presented. The basic requirements for high performance piezoelectric applications and a brief overview on leading piezoelectric materials are discussed. Further, the outstanding performance of the lead based ceramics and thin films in piezoelectric and optical applications and their drawbacks are also being described. The evolvement of lead-free piezoelectric materials and different approaches to improve the piezoelectric properties are discussed. Among the lead-free piezoelectric ceramics, the motivation behind choosing the $K_{0.5}Na_{0.5}NbO_3$ (KNN) and brief overview on its structural, dielectric, ferroelectric and piezoelectric properties are presented.

Chapter 2 deals with the preparation methods and characterization techniques being used for both KNN ceramics and thin films. All the pure and rare-earth doped KNN ceramics were prepared by using solid state reaction method. Ball milling parameters, calcination and sintering conditions were optimized to achieve the maximum relative density. The densities of all the ceramics were measured by using Archimedes's method. RF magnetron sputtering technique was used for the deposition of the thin films. Structural and microstructural properties of all the ceramics and thin films were examined using X-ray diffraction (XRD) and microscope techniques. The ultraviolet-visible-near infrared (UV-Vis-NIR) spectroscopy technique was used for optical characterization. Frequency and temperature dependent dielectric properties were measured by using LCR meter and impedance analyzer. Microwave dielectric properties of the thin films estimated using a split post dielectric resonator (SPDR) technique. The modified single beam z-scan technique was used to study the nonlinear optical properties of the films.

In chapter 3, the preparation of KNN ceramics by using solid state reaction method and optimization of calcination and sintering temperatures were discussed. The processing parameters such as milling time, milling speed, ball to powder ratio, calcination, sintering temperatures, and sintering duration were optimized. The structural, microstructural, densification, dielectric, and ferroelectric properties of KNN ceramics are presented. The improved ferroelectric properties ($2P_r$ = 19.09 μC/cm^2 and $2E_c$ = 21.95 kV/cm) and dielectric properties (ε_r = 578 and $tan\delta$ = 0.048) were enhanced with the sintering temperature upto 1050 ^oC. The optimized conditions were used to make the ceramic target of $K_{0.5}Na_{0.5}NbO_3$ composition to deposit the thin films by using RF magnetron sputtering. The deposition parameters such as a target to substrate distance, substrate temperature, working pressure, and RF power were optimized to achieve the stoichiometry in the deposited films.

The effect of substrate temperatures and oxygen mixing percentage (OMP) on crystallinity, microstructure, optical, mechanical and dielectric properties of $(K_{0.5}Na_{0.5})NbO_3$ thin films deposited onto different substrates quartz and $Pt/TiO_2/SiO_2/Si$ using RF reactive magnetron sputtering were studied. The films deposited at 400 °C show significant crystallinity with $K_2Nb_6O_{16}$ as a secondary phase, while the films deposited at room temperature and 200 ^oC showed the amorphous nature. The larger values of refractive indices in the range of 2.0 - 2.16 at 600 nm, hardness (1.0 - 9.4 GPa), and elastic modulus (26.7-100.2 GPa) are observed for the film deposited 400 ^oC under higher oxygen partial pressures. The Metal-Insulator-Metal (MIM) capacitors were fabricated for KNN ($Ag/KNN/Pt/TiO_2/SiO_2/Si$) thin films and measured the dielectric properties in the frequency range of 1 kHz to 1MHz. The measured dielectric properties were in the range of ε_r = 234.4 - 229 and $tan\delta$ = 0.024 - 0.009.

By using the optimized conditions, the KNN thin films were deposited at 400 ^oC under various OMP and annealed at 700 ^oC in oxygen atmosphere. The effects of OMP on the crystallographic orientation, surface morphology, optical and electrical properties of the KNN thin films were discussed. The annealed film deposited under pure oxygen atmosphere shown the phase pure perovskite structure without any secondary phases. The optical properties of as-deposited and annealed KNN thin films were calculated from transmittance spectra. The optical bandgap (E_g) is calculated by using the Tauc relation, and found to be in the range 4.34 – 4.40 eV and 4.29 – 4.37 eV for the as-deposited and annealed films,

respectively. The refractive index (n_{700}) of the films found to be in the range of 1.98 – 2.01 and 1.99 – 2.07 for as-deposited and annealed films, correspondingly. The refractive index dispersion is analyzed by using Wemple–DiDomenico (W–D) single-oscillator model. The effects of annealing and OMP on the refractive index, packing density and W–D parameters have been investigated. The microwave dielectric properties of the films measured in the frequency range of 10 - 20 GHz using the split post dielectric resonator (SPDR) method. The microwave dielectric properties of the annealed films are in the range of ε_r = 238 - 287 (215 - 250) and $tan\delta$ = 0.047 - 0.010 (0.049 - 0.013) measured at frequency 10 GHz (20 GHz). The Curie temperature of the films found to be in the range of 369 ^{o}C - 373 ^{o}C. Jonscher double power law was used to analyze the ac-conductivity of the KNN thin films. The leakage current characteristics of KNN thin films revealed that ohmic conduction and a relative low leakage current density (3.14×10^{-5} A/cm^2 at 50 kV/cm) were observed for the film deposited in pure oxygen plasma.

Chapter 4 describes the optimization and processing conditions of $(K_{0.5}Na_{0.5})NbO_3$ + x wt.% Dy_2O_3 (x = 0 -1.5) (KNND) ceramics prepared by solid state reaction method. The effect of Dy_2O_3 and sintering temperature on the structural, microstructural, densification and broadband dielectric properties were presented. With the addition of Dy_2O_3, the crystal structure of the KNN ceramics is changed from orthorhombic to psuedocubic symmetry, which is explained from the XRD and Raman's spectroscopy results. Improvement in the densification and reduction in the grain size was observed with the addition of Dy_2O_3. The KNN ceramic added with 0.5 wt.% of Dy_2O_3 shown a maximum density (93%) and improved dielectric properties [high ε_r = 677 and low $tan\delta$ = 0.012 (1MHz)]. For the higher concentrations of Dy_2O_3, the Curie temperature of the KNN ceramics found to be decreased from 388 ^{o}C to 97 ^{o}C with enhanced permittivity from 577 to 1121 (1MHz). For $x \geq 1.0$ samples, the frequency dependent relative permittivity maxima temperature was observed and satisfied the Vogel–Fulcher law. The diffuseness exponent γ found to be increased from 1.27 to 1.95 with the amount of Dy_2O_3 indicates that the degree of relaxor behaviour enhanced. High frequency (10^6 Hz to 10^8 Hz) dielectric properties of KNND ceramics investigated in a broad temperature (from -140 ^{o}C to 400 ^{o}C) range. AC-conductivity of the KNND ceramics was analyzed using Mott's Variable range hopping (VRH) model in the temperature regimes -140 ^{o}C - 33 ^{o}C and 37 ^{o}C - 197 ^{o}C. The VRH parameters such as,

average hopping length (R_H), hopping energy (E_H), and density of states ($N(E_F)$) were estimated in different temperature regimes. The tunability was found to be higher for the sample with x = 0.5. The obtained observations and detailed discussion are presented in this chapter.

Furthermore, the sputtering target was prepared using the composition with improved dielectric properties by solid state reaction method. $(K_{0.5}Na_{0.5})NbO_3$ + 0.5wt.% Dy_2O_3 (KNN05D) thin films were prepared using optimization conditions by RF magnetron sputtering method. KNN05D thin films are deposited at a substrate temperature of 400 ^oC onto quartz and Pt/Ti/SiO_2/Si substrates under various OMP. The KNN5D thin films were crystallized after annealing at 700 ^oC for 1h. The effect of OMP on crystallographic orientation, surface morphology, dielectric, electrical, linear and nonlinear optical properties has been studied systematically. The optical constants (n_{700} = 2.08 - 2.21, E_g = 4.28 -4.30 eV) are extracted from transmission spectra and dispersion in the refractive index was analyzed using W-D single oscillator model. The enhanced microwave dielectric properties (ε_r = 281-332, $tan\delta$ = 0.012 - 0.019) were obtained for the film deposited at 100% OMP film, measured in the frequency range 5 GHz - 15 GHz by split a split dielectric resonator technique. The nonlinear optical properties of the KNN05D films have been measured by using single beam z-scan technique and the larger values of nonlinear refractive index $n_2 = 7.04\times10^{-6}$ cm^2/W, nonlinear absorption coefficient β_{eff} =1.70 cm/W and third order nonlinear susceptibility $|\chi^{(3)}| = 1.40 \times10^{-3}$ esu was obtained for the film deposited under pure oxygen atmosphere.

Chapter 5 describes the Gd_2O_3 (0.5 - 1.5 wt.%) effect on the structural, microstructural, densification, electrical, and dielectric properties of the KNN ceramics (KNN + x wt.% Gd_2O_3 (x = 0 - 1.5)) and thin films. As the concentration of Gd_2O_3 increased, a phase transformation from orthorhombic to pseudo-cubic crystal structure was observed and is supported by XRD and Raman spectroscopy studies. The refinement was carried out by considering *Amm2* space group and lattice parameters, and unit cell volumes are extracted. The average grain size of the ceramics decreased from 2.26 μm to 0.35μm with the addition of Gd_2O_3. However, the density of the samples found to be enhanced. The positions of the both phase transitions were shifted towards room temperature with enhanced permittivity. The relaxor behaviour was induced in Gd_2O_3 ($x \geq 0.5$) contained KNN ceramics, and it is explained by using modified Curie-weiss law and Vogel–Fulcher law. The low

frequency dielectric measurements revealed that KNN + 1 wt.% Gd_2O_3 (KNN1G) composition displayed the improved room temperature dielectric properties such as high ε_r = 1112 and low $tan\delta$ = 0.032 (1MHz). However, maximum ε_r = 4147 and relatively low $tan\delta$ = 0.008 were observed at Curie temperature for x = 0.5 sample. The temperature dependent (27 ^oC – 327 ^oC) ac-conductivity of the KNN + x wt.% Gd_2O_3 (x = 0 & 0.5) ceramics were analyzed using Mott's VRH model. The broadband (1 MHz – 1 GHz) dielectric properties of the ceramics measured in the wide temperature range of -140 ^oC - 400 ^oC. The grain size dependent dielectric relaxation was explained by using Havriliak – Negami (H-N) function. The voltage dependent real and imaginary parts of permittivity indicate that all the samples show the ferroelectric response and higher tunability (7.59%) for x = 0.5 sample. The composition with higher density, and improved dielectric properties have been chosen for deposition of thin film by using RF magnetron sputtering.

KNN1G thin films were deposited onto quartz and Pt/Ti/SiO_2/Si substrates by RF magnetron sputtering. The effect of OMP on crystallographic orientation, surface morphology, dielectric, electrical, linear and nonlinear optical properties have been studied systematically. The films grown in pure oxygen atmosphere exhibited higher tetragonality ratio (1.0023) and improved grain morphology with an average grain size of 66.12 nm. The evolution of crystallographic orientation (001) with OMP was explained in terms of Lotgering orientation factor (F) and change in the position and FWHM of the internal vibration modes of NbO_6 octahedra. The optical bandgap of the films was calculated by using Tauc relation, and were in the range of 4.30 - 4.20 eV. The larger value of refractive index was obtained for 100% OMP, and were in the range of 2.07 – 2.19. The dispersion in the refractive index was analyzed using W-D single-oscillator model. The temperature dependent dielectric properties revealed that the Curie temperature of the films is found to be around 269^{o}C. The effect of OMP on microwave dielectric properties and leakage current characteristics were discussed. The nonlinear optical properties of the KNN1G thin films measured by using single beam z-scan technique. The films deposited under pure oxygen plasma shown the larger third order nonlinearity with nonlinear refractive index n_2 = 2.46 $\times 10^{-5}$ cm^2/W, nonlinear absorption coefficient β_{eff} = 5.02 cm/W, real and imaginary parts of nonlinear susceptibility are $\chi_R^{(3)} = 3.07\times 10^{-3}$ esu, and $\chi_I^{(3)} = 3.16\times 10^{-3}$ esu, respectively. The improvement in the dielectric, linear, and nonlinear optical properties of KNN1G thin film

with OMP was briefly discussed. These results indicate that they are suitable for in nonlinear photonic and high frequency microwave device applications.

Chapter 6 describes the summary and highlights of the thesis work and their potential applications in devices. Furthermore, the future scope of the work is discussed.

ABBREVIATIONS

Units of measurement

m	Meter
cm	Centimeter
μm	Micrometer
nm	Nanometer
Å	Angstrom
^{o}C	Centigrade (degree)
kHz	Kilo hertz
MHz	Mega hertz
GHz	Giga hertz
h	Hour
SCCM	Standard cubic centimeter per minute
F	Farad
pC	Pico Coulomb
μC	Micro Coulomb
N	Newton
V	Volt
eV	Electron-volt
GPa	Giga Pascal
g	Gram
W	Watt
esu	Electrostatic unit
A	Ampere

Electrical measurements

ε_r	Relative permittivity
tan δ	Loss tangent
A	Area of the electrodes

ε'	Real part of permittivity
ε''	Imaginary part of permittivity
ε_0	Permittivity of vacuum
σ_{ac}	AC-conductivity
χ_e	Electric susceptibility
J	Leakage current density
k_{33}	Electromechanical coupling coefficient
d_{33}	Piezoelectric constant
E	Electric field
C	Capacitance
d	Thickness
D	Electric polarization
T	Stress
s	Strain
S	Electric compliance
g_{ij}	Piezoelectric voltage coefficient
P	Polarization
p	Dipole moment
V	Unit cell volume
Z	Impedance
Z'	Resistance
Z''	Reactance
f_r	Resonant frequency
f_a	Anti-resonance frequency
Q	Quality factor
P_s	Saturation polarization
P_r	Remnant polarization
E_c	Coercive field
τ	Relaxation time
$\Delta\varepsilon$	Dielectric relaxation strength

α and β	Symmetric and asymmetric distribution parameters
DC	Direct current
AC	Alternative current
γ	Degree of diffuseness
f_0	Debye frequency
E_A	Activation energy
ω	Angular frequency
k_B	Boltzmann constant
T_f	Freezing temperature
T_{CW}	Curie-Weiss temperature
T_{R-O}	Rhombohedral to orthorhombic transition temperature
T_{O-T}	Orthorhombic to tetragonal transition temperature
T_{T-C}	Tetragonal to cubic transition temperature
T_C	Curie temperature
ρ_{ac}	AC-resistivity
ξ	Decay length
$N(E_F)$	Density of states
R_H	Hopping length
W_H	Hopping energy

Optical measurements

α	Absorption coefficient
n	Refractive index
n_{700}	Refractive index at 700 nm
n_b	Bulk refractive index
P	Packing density
E_g	Optical bandgap
E_o	Average oscillator energy gap
E_d	Dispersion energy
E_u	Urbach energy

h	Planck's constant
ω_0	Beam waist
z_0	Rayleigh length
n_2	Nonlinear refractive index
β_{eff}	Nonlinear absorption coefficient
$\chi^{(2)}$	Second order nonlinear susceptibility
$\chi^{(3)}$	Third order nonlinear susceptibility
$\chi_R^{(3)}$	Real part of third order nonlinear susceptibility
$\chi_I^{(3)}$	Imaginary part of third order nonlinear susceptibility
L_{eff}	Effective thickness of the thin film
λ	Wavelength
c	Velocity of light
$h\nu$	Photon energy

Other parameters

θ	Angle
D	Crystallite size
FWHM	Full width at half maximum
a, b, c	Lattice parameters
χ^2	Chi-square
R_{Bragg}	Bragg factor
R_f	Profile factor
F	Orientation factor
$F_{(001)}$	Orientation factor for the (001) plane
E_r	Elastic modulus
H	Hardness
ρ	Density
wt.	Weight
rms	Root mean square
TD	Theoretical density

EU	European union
WEEE	Waste of electrical and electronic equipment
RoHS	Restriction of hazardous substances
CSSR	Conventional solid state reaction
RT	Room temperature
RF	Radio frequency
REO	Rare earth oxide
PL	Photoluminescence
FE	Ferroelectric
RFE	Relaxor ferroelectric
PNR	Polar nanoregions
OMP	Oxygen mixing percentage
VRH	Variable range hopping
CCD	Charge coupled device
SPDR	Split post dielectric resonator
MIM	Metal-insulator-metal
DSC	Differential scanning calorimetry
TGA	Thermal gravimetric analysis
XRD	X-Ray diffraction
AFM	Atomic force microscopy
SEM	Scanning electron microscopy
FESEM	Field emission scanning electron microscopy
EDS	Energy dispersive X-ray spectrometer
KNN	$K_{0.5}Na_{0.5}NbO_3$
KNN05D	$K_{0.5}Na_{0.5}NbO_3$ + 0.5wt.% Dy_2O_3
KNN1G	$K_{0.5}Na_{0.5}NbO_3$ + 1.0wt.% Gd_2O_3
BT	$BaTiO_3$
NBT	$Na_{0.5}Bi_{0.5}TiO_3$
KBT	$K_{0.5}Bi_{0.5}TiO_3$
LN	$LiNbO_3$

LT	$LiTaO_3$
LS	$LiSbO_3$

CONTENTS

LIST OF FIGURES

LIST OF TABLES

Chapter 1

Introduction to piezoelectric and ferroelectric bulk and thin films

1.1 Background and motivation

The usage of smart and functional materials such as piezoelectric materials is increasing rapidly every year. The global market for these materials in 2014 was $26.0 billion, and it is expected to reach around $42.2 billion in 2019 with a compound annual growth rate of 10.2% during the period of 2014-2019 [1]. The physical and chemical properties of smart and functional materials are very sensitive to the changes in the surrounding atmosphere, such as pressure, temperature, electric and magnetic fields. Among the smart materials, piezoelectric materials are most promising in many applications such as sensors, actuators, transducers and accounts more than 50% of the global market [1].

Most of the piezoelectric devices and applications in the market are based on the lead zirconate titanate (PZT), which is the solid solution of $PbZrO_3$ and $PbTiO_3$ [2]. Due to its outstanding dielectric, ferroelectric and piezoelectric performance of PZT and PZT based materials such as $Pb(Mg_{1/3}Nb_{2/3})O_3$-$PbTiO_3$ and $Pb(Zn_{1/3}Nb_{2/3})O_3$-$PbTiO_3$ materials were used as sensors, actuators and many other applications [3]. However, PZT based ceramics contain more than 60 weight percentage of lead, which is hazardous to the human health and environment. Therefore, the European Union (EU) stated that the waste of electrical and electronic equipment (WEEE) and restriction of hazardous substances (RoHS) to avoid the usage of toxic materials [4]. Therefore, the search has begun for the lead-free piezoelectric ceramics; nevertheless, the performance of existing lead-free materials was not comparable to lead based ceramics.

Most of the lead-free piezoelectric ceramics belongs to the perovskite, bismuth layer and the tungsten-bronze structures. The perovskite type ferroelectrics exhibited the improved electromechanical properties as compared to the other type of lead-free piezoelectric ceramics. Among the ABO_3 perovskite type of lead-free piezoelectric ceramics, barium titanate ($BaTiO_3$ (BT)), sodium potassium niobate ($K_{0.5}Na_{0.5}NbO_3$ (KNN)), sodium bismuth titanate ($Na_{0.5}Bi_{0.5}TiO_3$ (NBT)), and potassium bismuth titanate

($K_{0.5}Bi_{0.5}TiO_3$ (KBT)) are well known due to their promising ferroelectric and piezoelectric properties, and these values are comparable to PZT [5]. BT is the first lead-free ferroelectric/piezoelectric material and potential lead-free alternative to PZT [6]. BT exhibits a high relative permittivity (ε_r = 1700), low loss ($tan\delta$ = 0.005), high piezoelectric constant (d_{33} = 190 pC/N) and electromechanical coupling factor (k_{33} = 0.50), makes it suitable for capacitors and other energy storage applications [7-8]. However, BT has a disadvantage of low Curie temperature (T_C ~ 120 ^oC) that can be known from the ferroelectric tetragonal to paraelectric cubic phase transition and low electromechanical coupling factor as compared to PZT [9-10]. These characteristics limit the usage of BT in high temperature ferroelectric applications. Therefore, high T_C ferroelectrics such as NBT, BKT and KNN are considered as promising candidates for high performance piezoelectric applications even at high temperatures [11-13]. BNT ceramics prepared by using hot pressing sintering method showed the high piezoelectric constant (d_{33} = 98 pC/N) and larger electromechanical coupling coefficient (k_{33} = 0.48) [14]. At the same time, BKT ceramics exhibited the d_{33} = 69 pC/N, which is lower than that of BNT ceramics [12]. Most of the BNT based ceramics exhibited the enhanced piezoelectric and ferroelectric properties near the morphotrophic phase boundary (MPB) compositions and ternary systems with BT, BKT, KNN, and other compositions [15-18]. However, BNT based ceramics require high sintering temperature (>1150 ^oC), ineffective poling due to its high conductivity and depolarization temperature of 200 ^oC makes this material difficult to be used in most of the applications. Shirane *et al.* [19] reported the dielectric properties of KNN ceramics. KNN ceramics prepared by conventional sintering method possesses the high density (95% of theoretical density), large piezoelectric constant (d_{33} = 98 pC/N), and electromechanical coupling constant (k_t = 0.45) [20], which are higher than other ferroelectric materials. The high relative density (99%) with enhanced ε_r = 420, d_{33}=160 pC/N, k_{33} = 0.53 and high T_C = 420 ^oC were achieved by the hot pressing method [21-22]. Similarly, the improved properties (ε_r = 606, $tan\delta$ = 0.036, d_{33} =148 pC/N, and k_p= 0.39) were obtained for the KNN ceramics, prepared using spark plasma sintering method [23-25]. Accordingly, based on the premise that the properties of the KNN ceramics are to be enhanced and as possible to replace the lead based ceramics. The compositions with interesting properties were directed toward optimizing and characterizing the ferroelectric and piezoelectric properties for the suitable applications. Once the optimized composition was identified, then the efforts can be made to fabricate

the thin films and study their properties toward the applications in non-volatile memories, microwave tunable devices and nonlinear optical devices.

1.2 Theory and fundamentals

1.2.1 Dielectrics

Dielectrics are the materials that virtually do not contain free charge carriers; however, they are bound to the atoms. Therefore, dielectric materials exhibit the insulating properties. These dielectric materials can be polarised when they were placed under the electric potential. An electric field can cause the relative displacement between centres of negatively charged electrons and positively charged nucleus, which can form the electric dipole moments in the specimens. However, there is no transfer of charge carriers, but instead the charge separation occurs. These type materials have the ability to store the electric charge and acts as capacitors. By definition, the electric polarization (P) is the net dipole moment (p) per unit volume (V) and denoted as,

$$\vec{P} = \sum_k \frac{\vec{p_k}}{V} \tag{1.1}$$

Basically, four types of polarization mechanisms occur in the dielectric materials. They are (a) space charge polarization, (b) orientational, (c) ionic, and (d) electronic polarizations [26]. The space charge polarization is arises due to the accumulated charge carriers at the grain boundaries and interface between electrodes and material surface. The orientational polarization is related to the alignment of permanent dipoles. The relative displacement of cation and anions with an applied electric field will give the ionic polarization. A small separation of negatively charged electron cloud with the positively charged core is called as electronic polarization. The relation between induced polarization and applied electric field is given by following expression,

$$\vec{P} = \chi_e \varepsilon_0 \vec{E} \tag{1.2}$$

Where, χ_e is the electric susceptibility, which is dependent on all polarization mechanisms and as well as frequency of applied electric field and ε_0 is the permittivity of the free space. For linear dielectrics, the relation between susceptibility χ_e and relative permittivity ε_r can be written as,

$$\chi_e = \varepsilon_r - 1 \tag{1.3}$$

The relative permittivity (ε_r) can be defined as the ratio between the permittivity of the dielectric material (ε) and permittivity of the free space (ε_0). It is the measure of the storage of energy in the dielectric material under the application of electric field. It can enhance the capacitance of the capacitor by a factor of ε_r when the dielectric material sandwiched between the plates of the capacitor. The ε_r can be calculated using the following equation,

$$\varepsilon_r = \frac{\varepsilon}{\varepsilon_0} = \frac{Cd}{\varepsilon_0 A} \tag{1.4}$$

where, C is the measured capacitance, d is the thickness of the specimen, and A is the area of the electrodes. The loss tangent ($tan\delta$) characterizes the dissipation of applied electric energy in the dielectric material. As the electric field is applied, the dissipation appears in the form of heat and distributed throughout the material. The loss tangent is the ratio of the imaginary (ε'') part of the permittivity to real (ε') of the permittivity.

$$\tan\delta = \frac{\varepsilon''}{\varepsilon'} \tag{1.5}$$

1.2.2 Piezoelectricity

The piezoelectricity was discovered in some crystals such as Rochelle's salt ($KNaC_4H_4O_6.4H_2O$), quartz (SiO_2), tourmaline and other materials by Jacques and Pierre Curie in 1880 [27]. They observed the generation of electrical charges on the surface of the crystals, when the sufficient load was applied. The Piezoelectricity is divided into two types (1) direct piezoelectric effect and (2) converse piezoelectric effect. The ability to generate the electric potential by the applied mechanical stress is called as direct piezoelectric effect and the change in the shape by the application of external electric field is called as a converse piezoelectric effect. The materials can exhibit the direct piezoelectric effect is being used in sensors applications. Furthermore, the piezoelectric materials have many useful applications in our daily life, such as quartz clocks, gas igniters, piezoelectric transformers, and automotive applications. The ability of the piezoelectric materials is to produce the strain, which find applications in actuators such as sonars, buzzers, and medical ultrasonic transducers. Later, the piezoelectric effect was explained using the crystallographic principles. Depends upon the centre of symmetry, rotation about axes and mirror planes within the crystals, they were classified into 32 crystallographic point groups [8, 26-27] and are displayed in Figure 1.1. Among these point groups, only 21 are exhibits the non-centrosymmetric structure. Out of these 21

non-centrosymmetric structures, all point groups (20) exhibits the piezoelectric nature, except 432 point group. Among the 20 point groups, 10 possess the spontaneous polarization, which means the existence of permanent dipole moment even in the absence of electric field. The materials that exhibit the spontaneous polarization are called as ferroelectric materials.

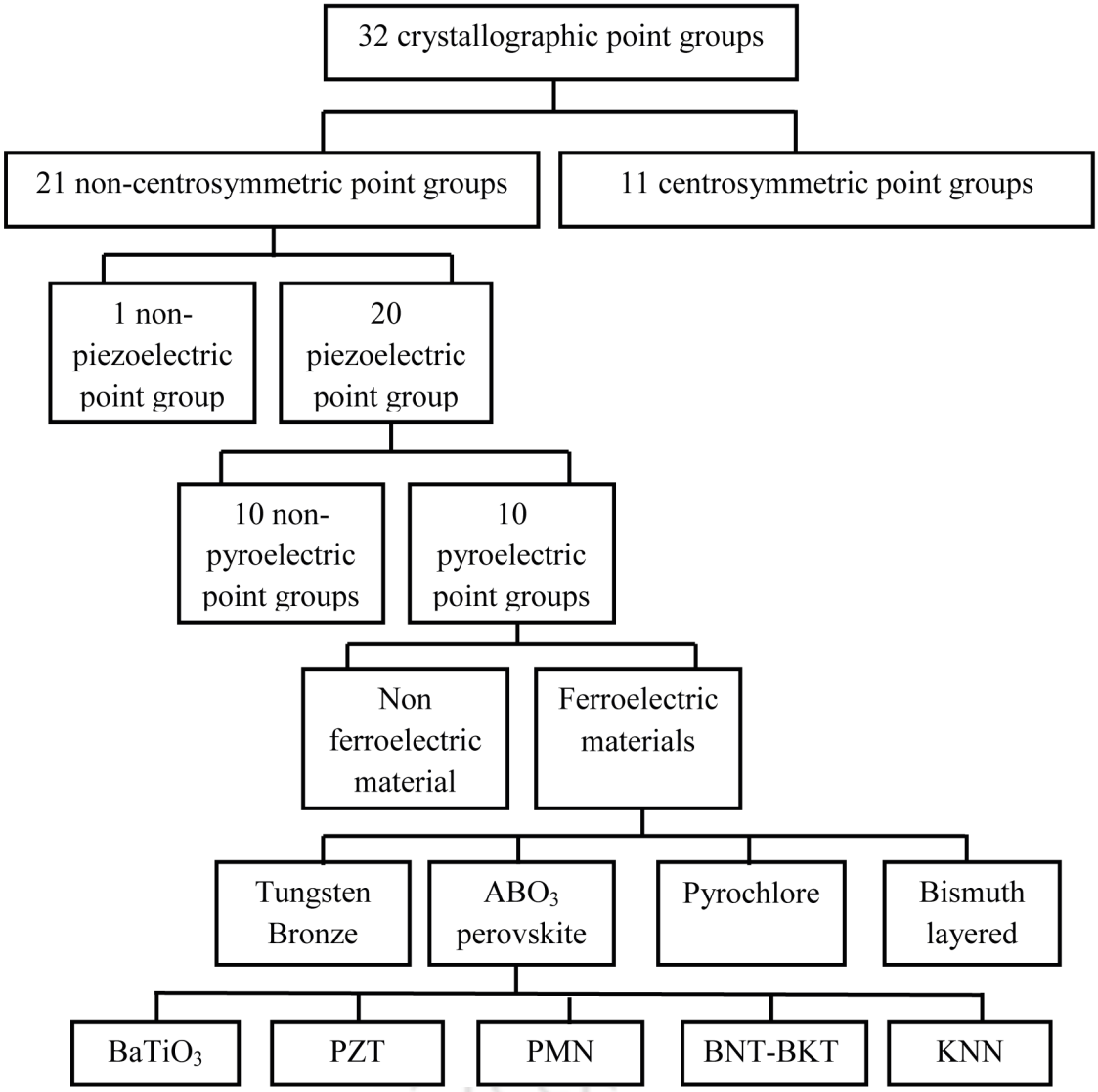

Figure 1.1: *The classification of point groups of crystals based on their symmetry* [8].

The non-centre of symmetry is important for the appearance of piezoelectricity, and one cannot produce the net polarization in centrosymmetric structure. If the material exhibits the non-centrosymmetric structure, then the formation of electric dipoles by a relative displacement of positive and negative ions under the application of stress. The magnitude and sign of the induced polarization is dependent on the type of stress such as

compressive or tensile. The direct piezoelectric effect can be described by the following equation,

$$D = dT + \varepsilon E \tag{1.6}$$

where, D is the electric polarization (C/m^2), d is the piezoelectric coefficient (C/N), T is the stress (N/m^2), ε is the permittivity (F/m) and E is the electric field (V/m). In the absence of an external electric field, the above equation can be written as,

$$D_i = d_{ijk} T_{jk} \tag{1.7}$$

here, D_i is the first rank vector; d_{ijk} is the third rank tensor, and T_{jk} is the second rank tensor.

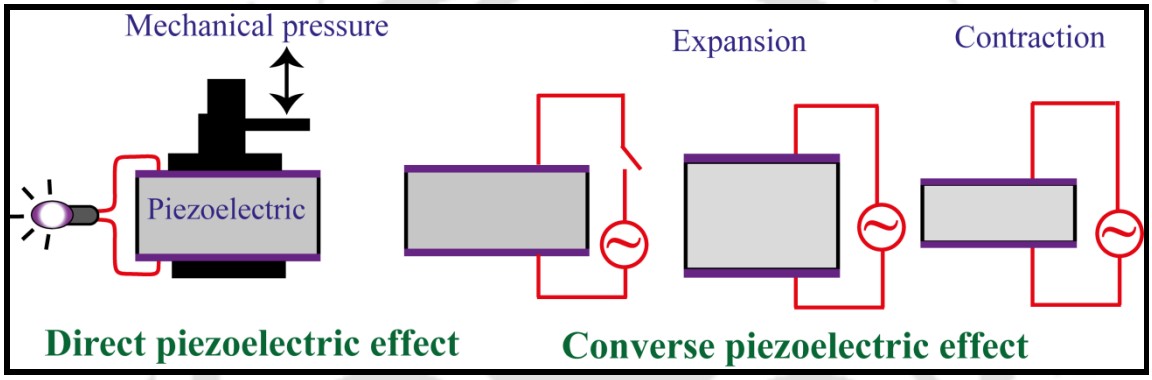

***Figure 1.2**: Direct and converse piezoelectric effect in piezoelectric ceramics.*

In the converse piezoelectric effect, the strain be can be induced by the application of electric field by the following equation,

$$s = ST + dE \tag{1.8}$$

where, s is strain component, S is the electric compliance; T is stress (N/m^2), d is the piezoelectric coefficient (m/V), and E is the electric field (V/m). In the absence of additional mechanical stress, the strain is related to the applied electric field by,

$$s_{jk} = d_{ijk} E_i \tag{1.9}$$

Both the electric displacement and strain are directional dependent, and, hence, usually denoted with subscripts to identify the determined conditions.

The piezoelectric voltage coefficient (g_{ij}) is also used to study the ability of generation of electric field to the applied mechanical stress or the induced strain to the applied charge density. It can be obtained from the following relation,

$$g_{ij} = \frac{d_{ij}}{\varepsilon_r \varepsilon_0} \tag{1.10}$$

where, ε_r is the relative permittivity, ε_0 is vacuum permittivity, and d_{ij} is the piezoelectric charge coefficient.

The mechanical quality factor (Q_m) is defined as the ratio of the stored electrical energy to the dissipated energy per cycle, and the reciprocal of the Q_m gives the mechanical loss. The ceramics with higher Q_m should be employed for high efficient actuators and transducers. The mechanical quality factor can be estimated using the following equation,

$$Q_m = \frac{1}{2\pi f_r z C}\left(\frac{f_a^2}{f_a^2 - f_r^2}\right) \tag{1.11}$$

where, z is the impedance at resonant frequency f_r, and f_a is the anti-resonance frequency, and C is the capacitance measured at low frequencies.

The electromechanical coupling factor (k) is the efficiency of the conversion of electrical energy into mechanical energy and vice versa. The k values found to be always less than unity, due to the incomplete conversion of mechanical to electrical energy or vice versa. It can be considered as the figure of merit for the piezoelectric materials.

$$k^2 = \frac{stored\ electrical\ (mechanical)\ energy}{applied\ mechanical\ (electrical)\ energy} \tag{1.12}$$

The planar (k_p) and thickness extensional (k_{33}) coupling coefficients are measured using the f_r and f_a values by following expressions.

$$k_p = \frac{f_a^2 - f_r^2}{f_r^2} \tag{1.13}$$

$$k_{33}^2 = \frac{\frac{\pi}{2}}{1 + \frac{f_a - f_r}{f_r}} \tan\left(\frac{\frac{\pi(f_a - f_r)}{2f_r}}{1 + \frac{(f_a - f_r)}{f_r}}\right) \tag{1.14}$$

1.2.3 Pyroelectricity

Out of the 20 point groups of the piezoelectric materials, a subgroup of 10 point groups exhibits unique polar axis and polarization changes with the temperature [28].

These types of materials are called as pyroelectric materials. Unlike the normal piezoelectric ceramics, the spontaneous polarization in pyroelectric materials developed by change in the temperature and forms the dipoles without any stress or external electric field. The change in spontaneous polarization (dP_s) with temperature (dT) can be written as,

$$dP_s = -p\,dT \tag{1.15}$$

where, p is the pyroelectric coefficient, and negative sign indicates decreasing of polarization with a rise in temperature.

1.2.4 Ferroelectricity

Among the pyroelectric materials, some materials exhibit the spontaneous polarization and the direction of polarization can be reversed by the application of appropriate electric field. This property is called as ferroelectricity. The ferroelectricity in the material was explained by three different theories are (a) first principle theory, (b) soft mode theory, and (3) phenomenological theory [29]. The phenomenological theory was explained by Muller, Ginzburg, and Devonshire. According to this theory, the free energy (F) of the system was expanded as a function of polarization and strain. If the applied stress is hydrostatic, then the free energy of the system in ferroelectric phase can be written as,

$$F(P,T) = \frac{1}{2}\alpha P^2 + \frac{1}{4}\beta P^4 + \frac{1}{6}\gamma P^6 + ... \tag{1.16}$$

Where, α, β, and γ are temperature dependent parameters and describe the nature of the phase transitions and dielectric behaviour in the vicinity of Curie temperature (T_C). In ferroelectric phase, both α and γ are positive.

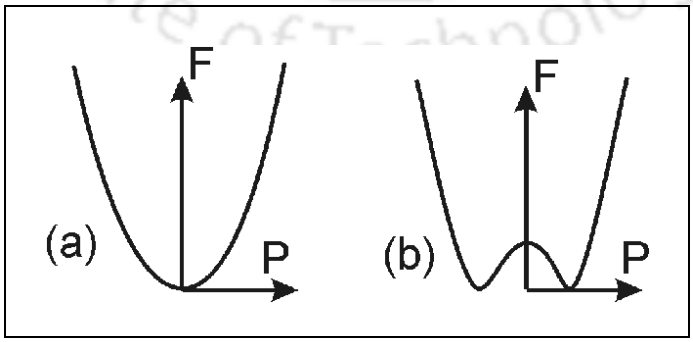

***Figure 1.3**:Free energy as a function of polarization for (a) $T>T_C$, and for (b) $T<T_C$* [30].

Figure 1.3 shows the polarization dependent free energy in paraelectric ($T>T_C$) and ferroelectric ($T<T_C$) regions. The sign of the β determines the transformation of free energy between these phases and the nature of the ferroelectric to paraelectric transition such as, continuous or discontinuous. For the first order phase transition, β is negative, whereas it is positive for the second order phase transition.

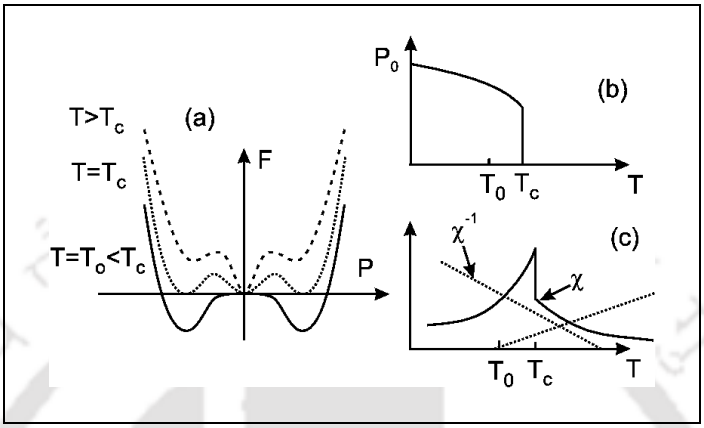

***Figure 1.4**: (a) Polarization dependence of free energy and temperature dependence of (b) spontaneous polarization, and (c) susceptibility in first order phase transition* [30].

In first order phase transitions ($\beta < 0$), the free energy has the minimum value even when the temperature is above T_0. The temperature T_0 defined as; where α change its sign and it is close but not equal to T_C. As the temperature decreases, the free energy is further reduced and thermodynamically favoured. This will happen at T_C, and it will exceed T_0. In this phase transition, the order parameter is polarization and the linear susceptibility jump discontinuously at T_C (Figure 1.4). Both the ferroelectric and paraelectric phases coexist at T_C and associate with the latent heat. In the second order phase transition ($\beta > 0$), the transition occurs at $T = T_0$ and there is no discontinuous change in the polarization was observed. As the temperature decreases below T_0, the spontaneous polarization and free energy continuously increase (Figure 1.5). The dielectric susceptibility was found to be diverging at $T = T_0$, and the dielectric stiffness will be vanished. There is no coexistence of the both phases, and the atomic displacements are relatively small as compared to the first order phase transition. In the second order phase transition, heat capacity shows the discontinuity without latent heat.

However, the main limitations of this theory are (a) it did not explain the macroscopic atomic interpretation (b) limited explanation on hysteresis phenomena, and (c) intrinsic, quasi static and single domain properties were explained without considering the extrinsic

contribution. In contrast, most of the ferroelectrics are polycrystalline materials and the frequency response of the polycrystalline materials was not analyzed.

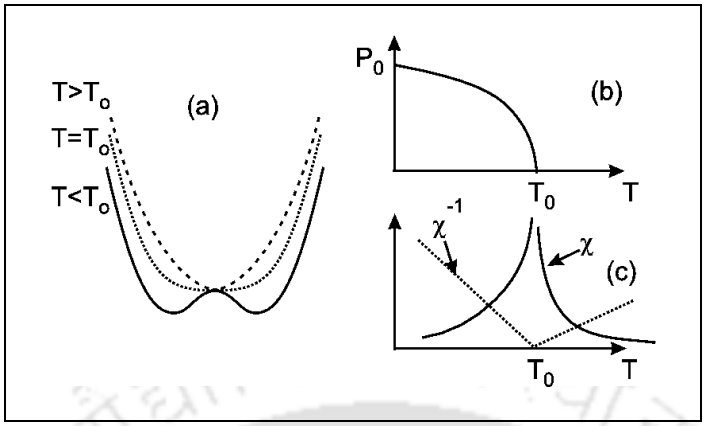

Figure 1.5*: (a) Polarization dependence of free energy and temperature dependence of (b) spontaneous polarization, and (c) susceptibility in second order phase transition* [30].

In 1960, Cochran explained the ferroelectricity using the soft mode theory [31]. According to this theory, the ferroelectric transition takes place due to the instability of crystal lattice by the softening of optical phonon mode. The important condition for the lattice stability is that the frequencies of all normal modes of vibrations are real and finite. As the frequency of particular mode decreases to zero, then the stability of the crystal no longer exists. Once the frequency of the mode is softened, then the atoms are displaced from their equilibrium positions, in particular, vibrations and there are no restoring forces to bring back to their original positions. At this temperature, the atoms find their equilibrium positions to depend on the symmetry of the mode, and the structural phase transition occurs. This decrease in the frequency of soft mode near the transition is due to the cancellation of short range and long range coulomb forces and also it depends upon the temperature, composition and applied fields. The soft mode theory was successfully explained the microscopic phenomena of structural and ferroelectric transitions in ABO_3 perovskites.

Further, the origin of ferroelectricity was explained clearly using first principle theory in 1990 [32-33]. The soft mode distortion in the in BT ceramics was estimated using linearized augmented plane wave energy calculations method and exchange as well as correlations among the electrons using local density approximation and is shown in Figure 1.6. It is observed that the ferroelectric instability arises from the hybridization between oxygen (O_{2p}) and titanium (Ti_{3d}) states. It is observed that the energy wells are found to be deeper for rhombohedral displacements [111] compared to the tetragonal

[001] displacements, which indicates that BT is more stable along the [111] direction. Therefore, BT underdoes three series of structural phase transitions from cubic to tetragonal, tetragonal to orthorhombic, and orthorhombic to rhombohedral phase with decreasing the temperature. Similar phase transitions were also observed in $KNbO_3$ (KN) related materials.

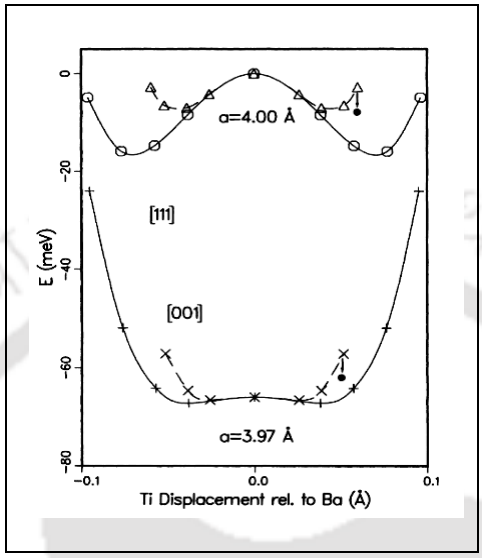

***Figure 1.6**: The ferroelectric behaviour in BT ceramics analyzed using first principle theory* [33].

According to the first principle calculations, the long range coulomb forces can favour the off centering of atoms, which causes the larger electrostatic energy for the atoms in the ideal positions of the perovskite structure. Short range forces can acts as repulsive forces to keep the atoms as far as possible. However, the repulsion between the atoms can be reduced by the hybridization between the B-site cations (*d* orbital) and oxygen anions (*p* orbital) and favours the atoms to move off center. The lone electrons in the A-site (*s* orbital) also have the contribution to the off centering of A-site ions. As a result, the ferroelectric behaviour appears below the Curie temperature.

The ferroelectric transitions are mainly two types; they are (1) displacive and (2) order-disorder phase transitions. In displacive phase transitions, as the phase transition temperature approaches, then the frequency of the soft mode decreases and causes the off-center of atoms and gives the non-zero polarization. Further, with rise in (or decreasing) the temperature, the frequency of the soft mode increases. In case of order-disorder phase transitions, the off centered displacements remain above Curie temperature. The nature of transition depends on the coupling strength between the displacements in neighbouring unit cells and energy well depths relative to temperature.

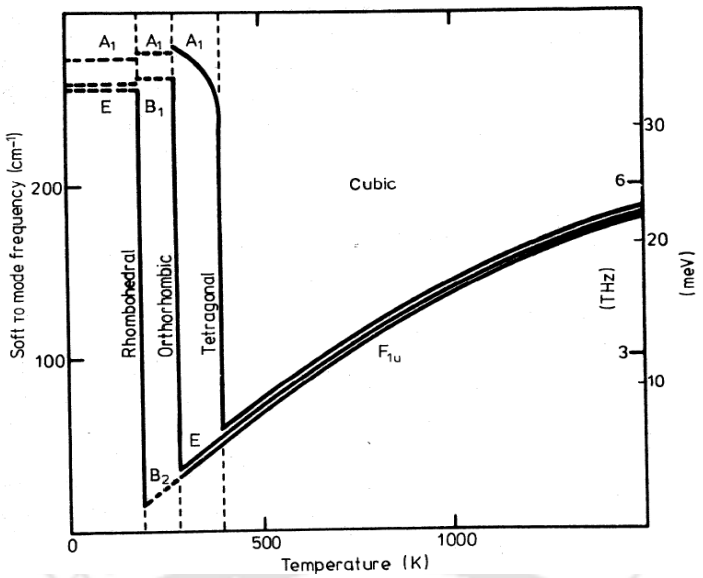

***Figure 1.7**: The soft mode frequency behaviour in BT as a function temperature* [34].

In some materials like BT and KN, the soft mode in the cubic phase is triply degenerate. At the transition from tetragonal to cubic one mode hardens, whereas the other two modes remain softens. As the temperature decreases, one by one mode become hardens across the phase transitions. All the modes are hardened only below the orthorhombic to rhombohedral phase transition (Figure 1.7).

Ferroelectric materials are subdivision of pyroelectric and piezoelectric materials and possess the spontaneous polarization, which can be switchable under the application of an electric field. The non-ferroelectric materials do not show the switchable polarization, when an electric field is applied. It is due to the existence of only one equilibrium state for the spontaneous polarization. In ferroelectric materials, there must be more equilibrium states, so that the polarization vector can switches between the states with an applied electric field. The spontaneous polarization in the ferroelectric materials arises due to the displacement of atoms from their centro-symmetric positions and disappears above its Curie temperature (T_C). These ferroelectric materials are widely used in high permittivity capacitors, microwave tunable devices, electro-optic devices, and memory applications, such as non-volatile ferroelectric random access memories (FERAM). Generally, ferroelectric ceramics exhibit the polycrystalline nature, and each unit cell possesses the net dipole moment. However, this net dipole moment could not contribute to macroscopic polarization due to the randomly orientated domains in the polycrystalline sample. The domains are the small areas where the adjacent unit cells possess the same polarization direction. The origin of the domains is due to the minimization of the

electrostatic energy. Therefore, in order to obtain the net dipole moment in the ferroelectric, a strong electric field is required to switch the dipoles in the particular polar axis. This process is called as poling and carried out at elevated temperatures below its Curie temperature [35]. The poled ferroelectric ceramic acts like single crystal and exhibit the net polarization.

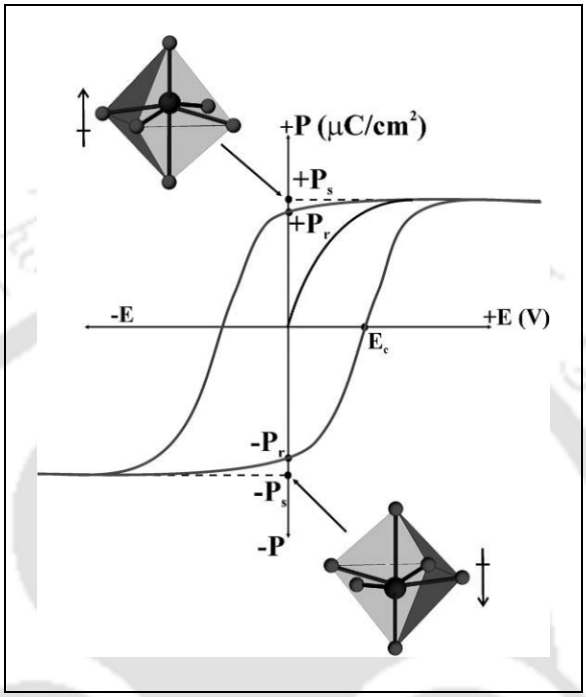

Figure 1.8*: The typical polarization-electric field (P-E) loop of ferroelectric ceramics* [36].

Ferroelectric properties of the materials are mainly concluded based on the polarization response to the applied electric field. Ferroelectric materials can exhibit the nonlinear polarization (hysteresis loop) as a function of the electric field. Ferroelectric materials do not show polarization without applying electric field due to the random orientation of dipoles. When an electric field is applied, the dipoles try to align in the direction of the field. The polarization becomes saturated, and no further increase in polarization is observed with a rise in the electric filed, this state is called as the saturation polarization (P_s). In addition, with decreasing the field, the polarization also reduces and shows a finite value of polarization even when the field is reduced to zero. This polarization called as the remnant polarization (P_r) and it is which lower as compared to P_s. A field is required to reduce the polarization to zero, which is called as the coercive field (E_c). The polarization-electric field (P-E) hysteresis curve is shown in Figure 1.8. If the field is increased in negative direction, then it also reaches saturation polarization in negative direction.

1.2.5 Perovskite ferroelectrics

Among the four types of ferroelectric ceramics, perovskite type ferroelectric ceramics are well known and widely used in piezoelectric and ferroelectric applications. The perovskite structure has a general formula of ABO_3, where the large 'A' cations coordinated occupies at the corners, smaller 'B' cations occupies at the center, and oxygen (O) sits at the face centers of the unit cell. The schematic diagram of the undistorted ABO_3 perovskite structure is shown in Figure 1.9. The A-site cations are 12-fold coordinated; B-site cations are 6-fold coordinated and oxygen anions are 6-fold coordinated in the perovskite structure. In order to obtain the piezoelectric properties, non-centrosymmetric modifications such as change in right angles or unit cell axis are required. In the ABO_3 structure, the valence of the A-site can be occupied by A^{1+} , A^{2+}, or A^{3+} and the B-site cations can be either B^{3+}, B^{4+}, or B^{5+}, respectively. The closed packed perovskite structure contains the BO_6 octahedra in the centre with corner sharing dodecahedrally coordinated A-site cations.

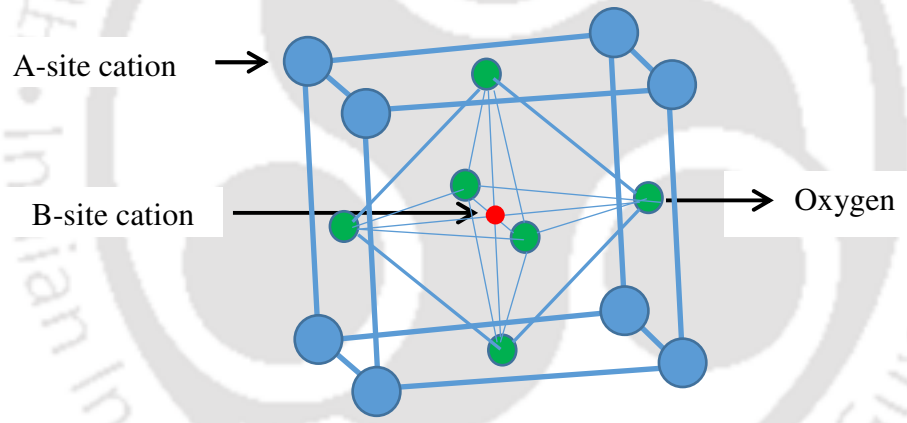

***Figure 1.9**: Typical unit cell structure of the ABO_3 perovskite structure.*

The Goldschmidt tolerance factor (t) help us to predict the formation of better geometrical packing in perovskite structures [37]. This can be estimated based on the ionic radii by using the following expression,

$$t = \frac{r_A + r_O}{\sqrt{2}(r_B + r_O)} \tag{1.17}$$

where, r_A, r_B, and r_O are the ionic radii of the A-site, B-site cations and oxygen anions, respectively. For the ideal cubic perovskite structures t value is equal to unity, in which the lattice is treated as closed packed atoms. In general, the most perovskite structures are orthorhombic, rhombohedral, and tetragonal structures, and these distorted structures are

having the tolerance factor values deviating from unity. For the cubic perovskite structures, the *t* value is in the range of 0.9-1.0, whereas the orthorhombic structures having the *t* value in the range of 0.75-0.90 [38]. The decrease in the A-cation radius and increase in the B-cation radius causes the reduction in the *t* value.

1.2.6 Relaxor ferroelectrics

In the normal ferroelectrics, the ferroelectric (FE) to paraelectric transition is identified from the temperature maximum of ε_r, whereas some other kind of ferroelectrics called as relaxor ferroelectrics (RFE) and they exhibits the broad peak in the temperature dependence of relative permittivity [39-42]. Because of the larger width of ε_r values in the vicinity of transition temperature, the RFEs can be used in the capacitor applications. The main differences between the FE and RFE are (a) FE shows the sharp phase transitions at T_C, whereas RFE shows the diffuse phase transitions at Curie maxima T_{max}, (b) FE shows the weakly frequency dependent at T_C, whereas RFE shows the strong frequency dependence at T_{max}, (c) FE follows the Curie-Weiss law above the T_C, whereas RFE follows the modified Curie-Weiss law, (d) FE exhibits the larger P_r values and RFE exhibits the smaller values of P_r, and (e) FE shows the strong anisotropy response to light, whereas RFE shows the weak anisotropic response to the light. Smolenskii *et al.* [43] explained the origin of RFE behaviour is due to the compositional heterogeneity in the A or B sites of ABO_3 perovskite structure, which can disturb the long range polar ordering. The dielectric behaviour of RFE also explained based on the formations and dynamics of polar nanoregions (PNR) [41-42]. In RFE, the soft mode phonons cannot be distributed in the crystal lattice due to the presence of disorder. Therefore, the fluctuations in dipoles cannot freeze at a particular temperature like FE, but the frequency of the soft mode phonon continuously decreases with temperature [44]. Burns *et al.* [45] reported the RFE behaviour was due to the existence of glass polar phase. However, most of the reports on dielectric dispersion concluded that the distribution of relaxation times [41-42].

The following properties were essential for these materials to be used in high performance piezoelectric applications,

(a) high piezoelectric coefficient (d_{ij})

(b) high relative permittivity (ε_r)

(c) low dielectric loss ($tan\delta$)

(d) high remnant polarization (P_r)

(e) high electrostriction coefficient (Q_{ij})

High relative permittivity is desirable for miniaturization and to match the electrical impedance, whereas the low *tanδ* is desirable for high energy conversion and low power losses. All these parameters are interrelated by following expression,

$$d_{ij} = 2Q_{ij}\varepsilon_r\varepsilon_0 P_r \tag{1.18}$$

where, the subscripts *i* and *j* denotes induced and applied directions, respectively.

1.2.7 Defects in ferroelectrics

The processing and fabrication of ferroelectric materials would be held at high temperatures. Therefore, there may be a possibility to develop the imperfections such as vacancies, dislocations, and some other defects. The intrinsic defects are charge carriers such as electrons, holes, and interstitials [46], whereas the extrinsic defects arise from the doping elements. In perovskite materials, A-site vacancies and oxygen vacancies shows the most significant effect on the material properties. Most of the perovskite oxides contain the transition elements, which are partially filled *d* (or *f*) orbital. These cations can alter their valance state depending on the surrounding oxygen atmosphere and temperature. The ratio between the cations reveals the defect type, either excessive or deficient. These defects arise from either intrinsic disorder or substitutional impurities. In order to maintain the charge neutral in the crystal lattice, the host ion will be replaced by either acceptor or donor impurities. These impurities (acceptor/donor) replace the host ions depend on their matching of valance and ionic radii. In case of alkaline based perovskite materials, the volatile nature of alkali elements causes the A-site deficiency and oxygen vacancies formed during the high temperature processing. Therefore, in order to compensate these vacancies and to improve the electrical properties, it is necessary to add the donor type impurities. The substitution of donor type cations can compensate the positively charged oxygen vacancies and enhance the electrical resistivity of the ferroelectric material.

1.3 Well known piezoelectric materials

1.3.1 Lead based piezoelectric materials

Among the piezoelectric ceramics, lead zirconate titanate ($Pb(Zr_{1-x},Ti_x)O_3$) PZT, is the most prominent material, which is being used in various applications due to its high dielectric, best ferroelectric and piezoelectric properties. PZT is a solid solution of antiferroelectric lead zirconate ($PbZrO_3$) and ferroelectric lead titanate ($PbTiO_3$) [2].

$PbZrO_3$ (PZ) exhibits the rhombohedral phase with *R3m* symmetry at room temperature, whereas the $PbTiO_3$ (PT) exhibits the tetragonal phase with *P4mm* symmetry. The PZT composition with x = 0.47 - 0.55 exhibited the improved properties near the morphotrophic phase boundary (MPB) due to the co-existence of rhombohedral and tetragonal phases at room temperature [2, 47-49]. The coexistence of these phases can provide the 14 polarization directions (6 from tetragonal phase and 8 from rhombohedral phase). Therefore, the maximum number of polarization directions across the unit cell can facilitate the polarization reorientation from grain to grain during the poling process, which enhances the piezoelectric properties in the vicinity of MPB regime [48-49]. The pure PZT ceramics possess the optimum dielectric properties (ε_r = 730, $tan\delta$ = 0.004) with a high Curie temperature (386 ^oC) and larger values of piezoelectric coefficients (d_{33} = 220 pC/N and k_{33} = 67%) [47]. Further, the improvements in the piezoelectric properties were obtained by compositional modifications. The donor type dopants such as La^{3+} in Pb^{2+} site and Nb^{5+} in Zr^{4+} sites were used to compensate the p-type conductivity caused by A-site vacancy and to enhance the electrical resistivity of the PZT [8,50-51]. This type of dopants can increase the ε_r, $tan\delta$, P_r, and electromechanical coupling factors, whereas the coercive filed decreases (soft PZT ceramics). The acceptor type dopants such as K^+, Na^+ in A-site and Mg^{2+}, Fe^{3+} in B-site are used to compensate the oxygen vacancies caused during the sintering process [52-54]. Nevertheless, this type of dopants decreases the dielectric, ferroelectric and piezoelectric properties except aging rates (hard PZT ceramics). The isovalent dopants such as Ba^{2+}/Sr^{2+} in A-site and Sn^{4+} in B-site, enhanced the dielectric properties and aging rate, whereas they reduce the Curie temperature [55-56]. The other lead based piezoelectric ceramics such as $Pb(Zn_{1/3}Nb_{2/3})O_3$-$PbTiO_3$ and $Pb(Mg_{1/3}Nb_{2/3})O_3$-$PbTiO_3$ displayed the enhanced the dielectric (ε_r = 5000, $tan\delta$ = 0.01 at 1kHz), ferroelectric (P_r = 43 μC/cm^2, E_c = 3 kV/cm) and piezoelectric properties (d_{33} > 2500 pC/N, k_{33} = 0.94 and strain level > 0.6%) [3]. However, lead oxide is the toxic in nature and its harmful concerns on human health as well as environment, European Union has stated the directives in 2006 such as WEEE and RoHS for the exclusion of hazardous substances. Lead has the maximum permissible concentration around 0.1wt.%, conversely, in the case of PZT, it contains above 60 wt.%. The poisoning of lead oxide can lead to kidney damage, pains in muscles, reduction in intelligence quotient (IQ), and abdominal discomfort, etc. Even though, PZT based materials are still using in piezoelectric applications due to the absence of the lead-free counterparts. Therefore, the search has begun for the development of lead-free piezoelectric materials.

1.3.2 Lead-free piezoelectric ceramics

Among the lead-free piezoelectric perovskite type ceramics, BT is the first man made ferroelectric material and is being used in varieties of applications due to its larger coupling factors, piezoelectric constants, and dielectric properties. However, low Curie temperature (120 ^{o}C) of BT restricted its usage at high temperature piezoelectric applications. Within the perovskite structure, presently most of the scientific studies focused on bismuth alkali titanate and alkali niobate based materials.

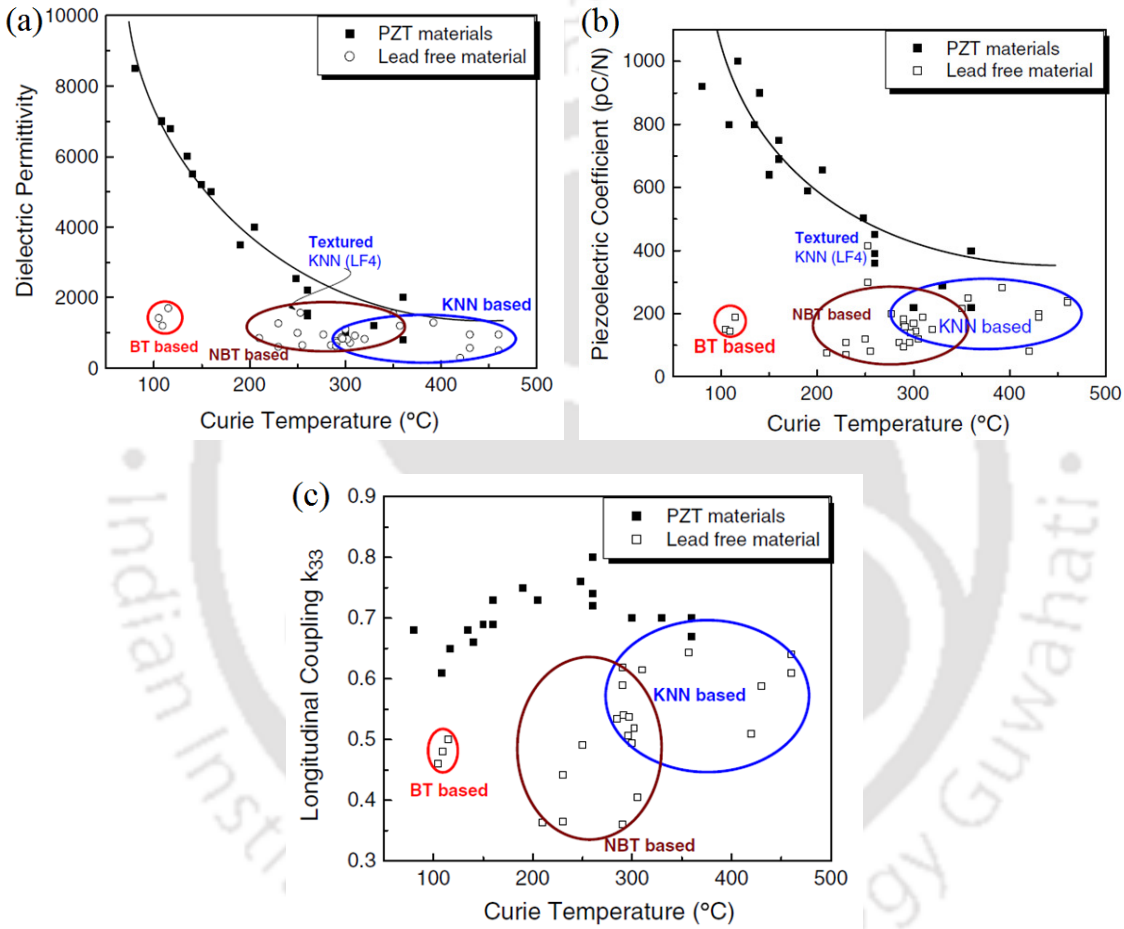

***Figure 1.10**: (a) ε_r (b) d_{33}, and (c) k_{33} as a function of Curie temperature of different piezoelectric ceramics measured at room temperature [5].*

In case of BNT, bismuth (Bi) and sodium (Na) atoms will sit in the A-site position, whereas titanium atoms will be filled in B-site of the perovskite structure. The BNT ceramics exhibited the higher remnant polarization around 38μC/cm^2 and also giant coercive field (73 kV/cm) [11]. The Curie temperature of BNT ceramics was found to be 320 ^{o}C and another transition called as depolarization temperature around 200 ^{o}C, which is the ferroelectric to anti-ferroelectric transition temperature. BNT ceramics exhibit the rhombohedral structure at room temperature. However, due to its large coercive field and

high conductivity makes BNT ceramics hard to pole and decreases the piezoelectric properties. On the other hand, these ceramics need relatively high sintering temperature (above 1200 ^{o}C) to get the dense body, which results in loss of A-site cations. Another ferroelectric material KBT possesses the tetragonal structure at room temperature with the Curie temperature around 437 ^{o}C, which is higher than the BNT ceramics [57]. Even though, the ferroelectric properties (P_r = 22.2 μC/cm^2 and E_c = 52.5 kV/cm) and piezoelectric properties (d_{33} = 70 pC/N and k_{33} = 0.28) were lower as compared to BNT ceramics. The KNN ceramics are one of the successful lead-free piezoelectric and ferroelectric ceramics having the high Curie temperature (~ 420 ^{o}C) as well as good piezoelectric properties (d_{33} = 160 pC/N, and k_{33} = 0.53) [21-22]. Figure 1.10 shows the comparison of the ε_r, d_{33} and k_{33} of the piezoelectric materials. It is observed that the most of the properties of KNN based ceramics were comparable to PZT based ceramics.

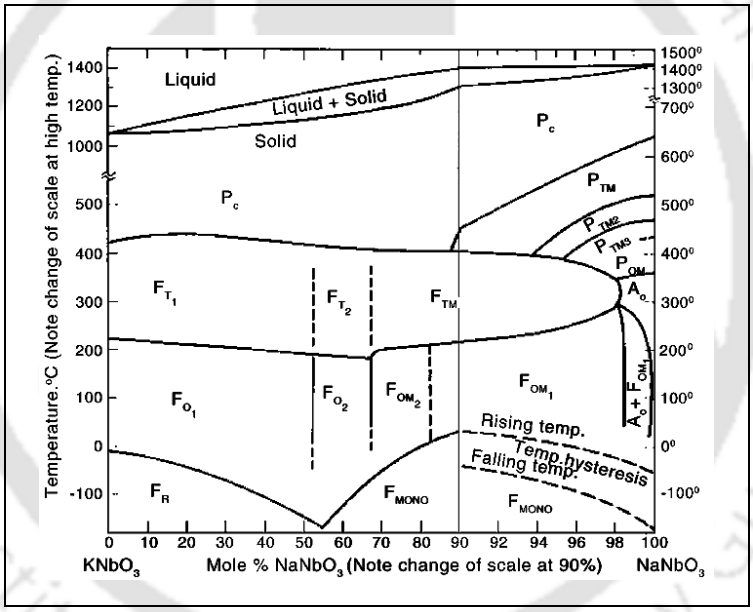

***Figure 1.11**: The phase diagram of KNN system* [58-59].

KNN is a solid solution of ferroelectric potassium niobate ($KNbO_3$) and anti-ferroelectric sodium niobate ($NaNbO_3$). From the phase diagram (Figure 1.11), four number of phase boundaries were observed around 52.5%, 67.5%, 82.5%, and 98% of $NaNbO_3$ of $KNbO_3$-$NaNbO_3$ system. The composition with 50/50 ratio was identified as MPB due to the separation of two orthorhombic phases. KNN ceramics possess the orthorhombic symmetry at room temperature. KNN ceramics undergo three compositions independent phase transitions from paraelectric cubic (C) to ferroelectric tetragonal phase (T) around ~ 400 ^{o}C, and other ferroelectric phase transitions at ~200 ^{o}C and at -80 ^{o}C are

tetragonal to orthorhombic phase (O) and orthorhombic to rhombohedral phase (R), respectively.

Due to the existence of the MPB, higher Curie temperature, larger values of electromechanical coupling factor and piezoelectric constants and most important environment friendly nature of KNN made it promising for various applications. However, the main drawback of this system is very difficult to produce the well sintered samples due to the hygroscopic nature of alkaline oxides and their volatilization at high temperatures, which can deteriorate the piezoelectric performance of KNN ceramics [60]. The KNN ceramics were prepared in normal air-firing have exhibited the d_{33} in the range of 70-110 pC/N and the relative density (ρ) of 93-95% of theoretical density 4.51 g/cm^3 [58]. Maximum density of KNN ceramics was achieved by the hot pressing method (ρ = 99.78% and d_{33} = 160 pC/N) [21] and spark plasma sintering method (ρ = 99.33% and d_{33} = 148 pC/N) [24-25]. Different approaches have been adopted to enhance the properties such as addition of an excessive amount of alkaline oxides and sintering in oxygen environment [61-62]. Sol-gel [63], hydrothermal method [64], and Pechini [65] methods were used to decrease the initial particle size to enhance the density as well as piezoelectric properties. In order to enhance the density of KNN ceramics, CuO, Bi_2O_3, ZnO, GeO_2, Borax, MnO_2, $K_4CuNb_8O_{23}$, and $K_{5.4}CuTa_{10}O_{29}$ were also used as sintering aids [66-69]. The addition of these sintering aids causes the liquid phase during the sintering, which can enhance the density and reduce the sintering temperature. There have been also used the dopants in A-site and B-site of the ABO_3 perovskite structure of KNN system [70-72]. Regardless of all these efforts on KNN ceramics were failed to replace the PZT based ceramics. However, in 2006, Saito *et al.* [73] reported the enhanced piezoelectric properties (d_{33} = 416 pC/N) prepared using reactive-templated grain growth method, which is almost nearly equals to the PZT ceramics. Then after, a worldwide effort is started to replace the lead based components with the KNN based ceramics. Most of the improved dielectric, ferroelectric and piezoelectric properties of KNN ceramics were observed by doping with Li^+ in A-site and Ta^{5+} and Sb^{5+} in B-site. The improvement in the piezoelectric property is correlated to the shift in the orthorhombic to tetragonal (T_{O-T}) polymorphic phase transition towards room temperature (RT). Ahn *et al.* [74] reported the relation between room temperature d_{33} and T_{O-T} as d_{33} = (306.21-1.02T_{O-T}) pC/N. This shows that the coexistence of orthorhombic and tetragonal phases near RT which would significantly enhance the piezoelectric constant.

Table 1.1: *Dielectric, ferroelectric and piezoelectric properties of Li, Ta, and Sb doped KNN ceramics.*

Composition	ε_r (1kHz)	$tan\delta$ (1kHz)	T_C (^oC)	T_{O-T} (^oC)	d_{33} (pC/N)	k_{33}/ k_p	P_r ($\mu C/cm^2$)	E_c (kV/cm)	Ref
KNN	290	0.04	420	195	80	0.35			[13]
0.058LN-0.942KNN	> 650	0.01-0.07	490		314	0.41	13.7	2.69	[75]
0.05LT-0.95KNN	570	~ 0.05	~ 420		200	0.36	9	12.5	[76]
0.05LT-0.95KNN	440	0.04			250	0.37			[77]
0.052LS-0.0948KNN	1372	0.019	385		286	0.51			[78]
0.05LS-0.95KNN	1412	0.028	364	35	270	0.47	25.7	11.1	[79]
$(K_{0.44}Na_{0.52}Li_{0.04})(Nb_{0.86}Sb_{0.04}Ta_{0.10})O_3$	1570		253		416	0.61			[73]
$(K_{0.44}Na_{0.52}Li_{0.04})(Nb_{0.84}Ta_{0.1}Sb_{0.06})O_3$	1175		264	25	345				[80]
$(K_{0.44}Na_{0.52}Li_{0.04})(Nb_{0.76}Ta_{0.2}Sb_{0.04})O_3$	1503	0.025			252	0.42			[81]
$(Na_{0.52}K_{0.435}Li_{0.045})Nb_{0.905}Sb_{0.045}Ta_{0.05}O_3$	1009	0.019	339		308	0.51	26	16	[82]
$(Na_{0.515}K_{0.44}Li_{0.045})Nb_{0.905}Sb_{0.045}Ta_{0.05}O_3$	1024	0.068	320	25	390	0.49			[83]

The solid solution of $LiNbO_3$ (LN), $LiTaO_3$ (LT) and $LiSbO_3$ (LS) with KNN exhibited a morphotrophic phase boundary between tetragonal and orthorhombic (O-T) phases with improved piezoelectric properties, which are listed in Table 1.1. Further, many authors have studied the effect of different ions in KNN-LN, KNN-LS, and KNN-LT-LS ceramics. Hagh *et al.* [84] studied the effect of Cu^{2+} (0.5-2 mol.%) on the KNN-LT-LS system using different processing methods and observed the change in the grain growth as well as electrical properties. It is also observed that the sample prepared using the mixed-oxide route exhibited the improved dielectric (ε_r = 1230 and $tan\delta$ = 0.008), ferroelectric (P_r = 13.5 $\mu C/cm^2$ and E_c = 6.9 kV/cm) and piezoelectric (d_{33} = 260 pC/N and k_{33}=0.63) properties. Wu *et al.* [85] investigated the effect of Ag on the structural and piezoelectric properties of KNN-LT-LS system and observed the enhanced electrical (ε_r = 1478, $tan\delta$ = 0.02, and d_{33} = 263 pC/N) with good aging response.

Table 1.2: *Ternary systems of KNN based ceramics.*

Composition	Phase boundary	ε_r (1kHz)	$tan\delta$ (1kHz)	d_{33} (pC/N)	k_{33}/ k_p	T_C (^oC)	Ref
$(0.97\text{-}x)K_{0.48}Na_{0.52}NbO_3$-$0.03Bi_{0.5}(Na_{0.7}K_{0.2}Li_{0.1})_{0.5}ZrO_3$ - $xB_{0.5}Na_{0.5}TiO_3$ (x = 0.5 - 1.5%)	R-T	1235	0.031	285	0.40	347	[94]
(xNBT-yBT-(1-x-y)KNN) (x = 0.035, y = 0.01)	O-T	531 (100 kHz)	0.038 (100 kHz)	210	0.32	329	[95]
(1-x)(0.99KNN–0.01NBT)–xLS (x = 0.01 - 0.04)	O-T	640	0.031	250	0.29	339	[96]
(1-x)KNN–x(0.15BNT–$0.85Bi_{0.5}Na_{0.5}ZrO_3$) ($x$ = 0.06)	R-T	1604	0.206	318	0.43	326	[97]
(1-x)KNN–x(0.80LS–0.20CT) (x = 0.03 - 0.07)	O-T	~1500	~0.03	172-253	0.49-0.55	348-373	[72]
$(NaK)(NbSb)O_3$–LT–$xBaZrO_3$ (x = 0.025)	R-T			365	0.45	170	[98]

The solid solution of different ferroelectric ceramics with KNN exhibited the improved electrical properties near the MPB. Ahn *et al.* [86] reported that the 0.95KNN-0.05BT system displayed the good piezoelectric properties (d_{33} = 225 pC/N and k_p = 0.36), and further; the addition of CuO and MnO_2 to this system greatly enhanced the piezoelectric properties (d_{33} = 248 pC/N and k_p = 0.41) due to the improved densification [87]. With the incorporation of BT into $[(K_{0.5}Na_{0.5})_{0.95}Li_{0.05}](Nb_{0.95}Sb_{0.05})O_3$ system caused the relaxor behaviour with enhanced electrical properties (ε_r = 1371, $tan\delta$ = 0.03, k_p = 0.50 and d_{33} = 269 pC/N) and good temperature stability [88]. Another metal titanate, $CaTiO_3$ (CT) also formed the solid solution with KNN and exhibited the MPB at 3-7 mol.% of $CaTiO_3$ between the O and T phases, and changed to T phase above 7mol.% [89]. KNN-CT ceramics exhibited the relaxor behaviour with high piezoelectric properties of ε_r = 1316, k_p = 0.41 and d_{33} = 241 pC/N. Similarly, relaxor behaviour was also observed in bismuth based perovskite $BiScO_3$ contained KNN ceramics [90] with the considerable enhancement in dielectric and piezoelectric properties (ε_r = 1591, T_C = 328 ^oC, k_p = 0.46 and d_{33} = 288 pC/N) [72]. The solid solution of KNN with NBT ceramics exhibited the MPB at 2-3% of NBT due to the ferroelectric O-T phase boundary [91]. The higher values of d_{33} = 195 pC/N, k_p = 0.43 and T_C = 375 ^oC were observed at MPB. Similarly, KNN-KBT solid solution also exhibited the MPB at 2-3% of KBT with the d_{33} = 192 pC/N, k_p = 0.45 and T_C = 370 -380 ^oC [92]. A giant piezoelectricity (d_{33} = 440 - 450 pC/N and 742 - 834 pm/V) was observed in (K, Na)(Nb,Sb)O_3 - $Bi_{0.5}Na_{0.5}AO_3$ (A = Hf

and Zr) due to the existence of MPB (3.5 - 4.5%) of rhombohedral and tetragonal phases (R-T), whereas relatively low values of piezoelectric constants ($d_{33} \leq 200$ pC/N and 600 pm/V) obtained for A = Ti and Sn due to the O-T and O phase boundaries, respectively [93]. Different ternary systems of KNN ceramics were also fabricated to improve the dielectric, ferroelectric, and piezoelectric properties and are listed in Table 1.2. The enhanced electrical properties of a ternary system of KNN ceramics observed at MPB of R-T phase boundary as compared to O-T phase boundary.

1.3.2.1 Rare-earth doped KNN ceramics

The doping of rare-earth (RE) elements to ferroelectric ceramics is very helpful for stabilizing and lowering the dielectric loss and also used as activator ions to achieve the good luminescent property. Lanthanum (La) modified KNN ceramics exhibited the enhanced densification with larger dielectric and piezoelectric properties [99-100]. The incorporation of La, inhibits the grain growth of KNN ceramics and induces the diffuse phase transition across the T_C. The relaxor behaviour increases and both the transition temperatures found to decrease with La concentration. Gao *et al.* [101] reported the effect of CeO_2 on the density and electrical properties of KNN ceramics. The authors reported that the doping of CeO_2 is an effective way to decrease the grain growth and to enhance the density of the KNN ceramics. Normally, the diffusion coefficient decreases with donor dopants, and mass transportation weakens; therefore, the grain growth was found to be inhibited. Sun *et al.* [102] reported that the doping of praseodymium (Pr) to KNN ceramics can greatly enhance the photoluminescence (PL) intensity of green and red emission peaks and are suitable for the applications in solid state lighting. Along with the PL properties, the enhancement in the ferroelectric (1.2 times) and piezoelectric properties (1.25 times) was observed in Pr^{3+} doped KNN ceramics [103]. Wang *et al.* [104] studied the effects of rare-earth oxides (REO) Pr_2O_3 and Yb_2O_3 on LS modified KNN ceramics and revealed that the improvement in the ferroelectric properties due to the co-existence of O-T phase boundary at room temperature. The co-doping effect of Yb and Er on the LN modified KNN ceramics studied by Wang *et al.* [105]. They also reported that the relaxor like behaviour induced, and the polarization found to be enhanced due to the suppression of alkali elements with the incorporation of Yb. The Er doped KNN ceramics showed the better up-conversion, and luminescent properties as well as electric properties [105-107]. The elimination of loss behaviour with enhanced piezoelectric properties and the red-orange emission properties were obtained in Sm_2O_3

modified KNN-LS ceramics [108-109]. In addition, Sm_2O_3 modified KNN-LS ceramics showed the good fatigue resistance and temperature stability. However, there have been no reports available on Dy_2O_3 and Gd_2O_3 doped KNN ceramics. Furthermore, there are no reports available on the complete picture of dielectric and conductivity studies of KNN ceramics in wide frequency range (500 Hz - 1 GHz) and temperature range (-140 ^oC – 450 ^oC). Therefore, in this thesis, the effects of REOs Dy_2O_3 and Gd_2O_3 on KNN ceramics were studied systematically. The trivalent RE ions (Dy^{3+} and Gd^{3+}) substitution in the univalent $(K, Na)^+$ causes the vacancies in the A-site to maintain the charge neutrality. It can help to decrease the vacancies created by the evaporation of alkali elements during sintering and also formation of defect dipoles. Normally, the electrical properties of the ferroelectric ceramics will depend upon the domain structure, non-180^o domain wall movement, and interaction among defects and domain walls [110]. These defect dipoles would migrate through the domain walls during the poling process and help to easy re-orientation of domain walls, which yields to improvement in the piezoelectric properties [103].

1.3.3 KNN-based thin films

The perovskite KNN thin films have received much attention in various applications such as sensors, non-volatile memories, actuators, varactors, optical coatings, electro-optic devices, and high frequency tunable devices due to their outstanding dielectric, ferroelectric and piezoelectric performance [111-118]. However, obtaining the stoichiometric KNN thin films is difficult due to the volatile nature of alkali elements. The non-stoichiometry in the films causes the non-perovskite phases, which weakens the electrical properties. This degree of volatilization of alkali elements depends on the fabrication process. Therefore, different methods have been used to prepare the KNN thin films such as sol-gel [119-127], pulsed laser deposition (PLD) [128-133], and radio frequency (RF) magnetron sputtering methods [134-143]. The suppression of secondary phases ($K_4Nb_6O_{17}$) and improvement in the structural and electrical properties of the KNN thin films were observed with the addition of an excess amount of alkaline elements due to the compensation of loss during heating process [120,144-146]. However, excess amounts of alkaline elements were alone not effective to enhance the electrical properties of KNN thin films. Therefore, various elements were chosen as dopants to tailor the properties of KNN thin films. Similar to the bulk KNN ceramics, Li, Ta, and Sb modified KNN thin films were also being fabricated using different methods have shown the

improved electrical properties [121,124,131-132,147-149]. Other dopants such as Mn, Co, V, Y, Ba, Ti, La and etc. were used to enhance the electrical properties of KNN thin films [123,125-126,132,150-154]. Wang *et al.* [125] reported that the Mn doped KNN thin films significantly decreased the leakage current (10^4 times) with the enhanced dielectric and ferroelectric properties, which was explained as the reduction in the concentration of free carrier-holes and oxygen vacancies. Li *et al.* [152] studied the effect of V doping on the dielectric and ferroelectric properties of KNN thin films and best properties observed with doping due to the high tetragonal phase. Co and Ti dopants also played the significant role in decreasing the leakage current in KNN thin films, whereas the resistivity of the films increased with the Ba-doping [132]. However, there have been only few reports are available on the rare-earth doped KNN thin films. The La-doped KNN thin films prepared using chemical solution deposition method exhibited the low leakage current density and increased relative permittivity, whereas the dielectric loss was found to be decreased in Y-doped KNN thin films [153-154].

RF magnetron sputtering is a very attractive technique due to its good adhesion, low cost and used in various applications since the deposition of the films can be employed over larger substrates. Large number of groups has studied the properties of KNN thin films fabricated by using RF magnetron sputtering. Blomqvist *et al.* [134] fabricated the epitaxial KNN thin films on $LaAlO_3$ substrates with good dielectric response (ε_r = 470, $tan\delta$ = 0.010, and tunability = 16.5% at 200 kV/cm), ferroelectric (23.5μC/cm^2 at 600 kV/cm), and low leakage current (30 nA/cm^2 at 400 kV/cm). Kugler *et al.* [136-137] deposited the KNN thin films on SiO_2/Si(001) and $Pt_{80}Ir_{20}$ substrates at different substrate temperatures from 300 ^oC to 450 ^oC and studied the microstructure and electrical performance of the films as a function of substrate temperature. These films showed the crystalline phase at substrate temperatures 450 ^oC and 300 ^oC for SiO_2/Si(001) and $Pt_{80}Ir_{20}$ substrates, respectively. Kim *et al.* [155] studied the effect of annealing atmospheres K_2O, Na_2O, and KNN on the structural and electrical properties of KNN thin films and observed that the films annealed under KNN atmosphere exhibited the good electrical properties. Li *et al*. [139,156] prepared the (001) oriented KNN thin films on different substrates $LaNiO_3$ and $SrRuO_3$ buffered $SrTiO_3$ (001) single crystal substrates at a substrate temperature of 550 ^oC in Ar:O_2 (9:1) pressure and annealed at 750 ^oC in oxygen atmosphere. The Curie temperature of the KNN film deposited on Pt/Ti/SiO_2/Si substrate is around 360 ^oC [140], whereas the $SrRuO_3$-buffered $SrTiO_3$

substrates shown the phase transitions around $T_{O\text{-}T}$ = 120 ^{o}C and T_C = 310 ^{o}C [142]. As compared to the other fabrication techniques, the better electrical properties were observed in the KNN films deposited using RF magnetron sputtering method even without any doping. Although, most of the studied on KNN thin films prepared by different techniques were mainly focused on dielectric, ferroelectric and piezoelectric properties. But, only few reports were available on optical characterization of the KNN thin films [118, 157-160]. Blomqvist *et al.* [118, 157-159] studied the optical and waveguiding properties of KNN thin films on different substrates, measured using prism-coupling technique and transverse method. The larger effective linear electro-optic coefficient (r_{eff} = 28 pm/V) was obtained for the film deposited on Al_2O_3 substrate, whereas the larger values of ordinary refractive index (n_o=2.261 ± 0.002), extraordinary refractive index (n_e = 2.216 ± 0.002), and optical birefringence (Δn = -0.054 ± 0.003) obtained for the KNN/$LaAlO_3$ film due to the good crystallinity.

Most of the researchers were fabricated the KNN thin films in high argon mixing pressure and have not deposited the films in pure oxygen atmosphere. The oxygen deficiency would play a crucial role in the electrical properties of the films. Therefore, it is necessitated depositing the KNN thin films in oxygen atmosphere. It is very important that the KNN thin films exhibit the good linear optical properties and large electro-optic coefficient, which makes them suitable for nonlinear photonic applications. However, there has been no systematic work done on the linear optical properties such as refractive index and optical bandgap of the films and no reports available on the nonlinear optical study of KNN based thin films. Since the KNN thin films were used in high frequency tunable devices, but the dielectric properties of KNN thin films are reported only at low frequencies and no reports available at microwave frequencies. Mainly, most of the groups studied the properties of KNN system either in the bulk form or thin film form, but there is no combined and comparative study of both bulk and thin film forms of KNN system. Therefore, in the present thesis, we have optimized the composition of rare-earth oxides (Dy_2O_3 and Gd_2O_3) doped KNN ceramics in bulk form. Further, the optimized composition was chosen as the target to deposit the thin films. The effect of oxygen mixing percentage on the linear, nonlinear and microwave dielectric properties of the pure and rare-earth oxides doped KNN thin films have been discussed.

1.4 Objective of the present work

The following objects are presented in this thesis work,

(a) Preparation of KNN ceramics by conventional solid state reaction (CSSR) method and optimization of calcination and sintering temperatures based on the better dielectric and ferroelectric properties.

(b) The optimized KNN composition will be is chosen to make the sputtering target to deposit the thin films using RF magnetron reactive sputtering method in different oxygen mixing atmospheres.

(c) Achieving the low temperature crystallization of KNN thin films.

(d) Study the effect of oxygen mixing percentage (OMP) on optical, low frequency and microwave frequency dielectric properties of KNN films.

(e) Optimization of REOs such as Dy_2O_3 and Gd_2O_3 content in KNN ceramics (CSSR method) near MPB to obtain better dielectric and ferroelectric properties.

(f) Conductivity analysis of REO doped KNN ceramics

(g) Depositions of REO doped KNN thin films by RF magnetron reactive sputtering using optimized compositions, and study their suitability in various applications.

1.5 References

[1] Smart Materials and Their Applications: Technologies and Global Markets, (January 2015).

[2] B. Jaffe, *J. Appl. Phys.* **25** [6] (1954) 809.

[3] S.-E. Park and T. R. Shrout, *J. Appl. Phys.* **82** [4] (1997) 1804.

[4] Directive 2002/95/EC, *Off. J. Eur. Union* **46** [L37] (2003) 19.

[5] T. R. Shrout and S. J. Zhang, *J. Electroceram.* **19** [1] (2007) 113.

[6] A. V. Hippel, *Rev. Mod. Phys.* **22** [3] (1950) 221.

[7] M. M. Vijatovic, J. D. Bobic and B. D. Stojanovic, *Sci. Sinter.* **40** [3] (2008) 235.

[8] G. H. Haertling, *J. Am. Ceram. Soc.* **82** [4] (1999) 797.

[9] W. J. Merz, *Phys. Rev.* **76** [8] (1949) 1221.

[10] M. Kim, J. Kim and W. Cao, *J. Appl. Phys.* **99** [7] (2006) 074102.

[11] G. A. Smolenskii, V. A. Isupov, A. I. Agranovskaya, and N. N. Krainik, *Sov. Phys. Solid State* **2** (1961) 2651.

[12] Y. Hiruma, K. Marumo, R. Aoyagi, H. Nagata and T. Takenaka, *J. Electroceram.* **21** [1-4] (2007) 296.

[13] L. Egerton and D. M. Dillon, *J. Am. Ceram. Soc.* **42** [9] (1959) 438.

[14] H. Nagata, T. Shinya, Y. Hiruma, and T. Takenaka, *Ceram. Transact.* **167** (2004) 213.

[15] W. Jo, J. E. Daniels, J. L. Jones, X. Tan, P. A. Thomas, D. Damjanovic and J. r. Rödel, *J. Appl. Phys.* **109** [1] (2011) 014110.

[16] Y.-R. Zhang, J.-F. Li, B.-P. Zhang and C.-E. Peng, *J. Appl. Phys.* **103** [7] (2008) 074109.

[17] J. Hao, B. Shen, J. Zhai, C. Liu, X. Li and X. Gao, *J. Appl. Phys.* **113** [11] (2013) 114106.

[18] Y. Hiruma, H. Nagata and T. Takenaka, *Jpn. J. Appl. Phys.* **48** [9] (2009) 09KC08.

[19] G. Shirane, R. Newnham and R. Pepinsky, *Phys. Rev.* **96** [3] (1954) 581.

[20] H. Birol, D. Damjanovic and N. Setter, *J. Eur. Ceram. Soc.* **26** [6] (2006) 861.

[21] R. E. Jaeger and L. Egerton, *J. Am. Ceram. Soc.* **45** [5] (1962) 209.

[22] G. H. Haertling, *J. Am. Ceram. Soc.* **50** [6] (1967) 329.

[23] J.-F. Li, K. Wang, B.-P. Zhang and L.-M. Zhang, *J. Am. Ceram. Soc.* **89** [2] (2006) 706.

[24] B.-P. Zhang, J.-F. Li, K. Wang and H. Zhang, *J. Am. Ceram. Soc.* **89** [5] (2006) 1605.

[25] K. Wang, B.-P. Zhang, J.-F. Li and L.-M. Zhang, *J. Electroceram.* **21** [1-4] (2007) 251.

[26] A. J. Moulson and J. M. Herbert, Electroceramics: Materials, Properties, Applications, *Wiley* (2003).

[27] B. Jaffe, W. R. Cook and H. L. Jaffe, Piezoelectric ceramics, *Academic Press* (1971).

[28] C. B. Carter and M. G. Norton, Ceramic Materials: Science and Engineering, *Springer,* New York (2007).

[29] H. Ehrenreich and F. Spaepen, Solid state physics advances in research and applications, *Academic Press,* San Diego (2001).

[30] P. Chandra. P. B. Littlewood, *arXiv:cond-mat/0609347* (2008).

[31] W. Cochran, *Phys. Rev. Lett.* **3** [9] (1959) 412.

[32] L. L. Boyer, R. E. Cohen, H. Krakauer and W. A. Smith, *Ferroelectr.* **111** [1] (1990) 1.

[33] R. E. Cohen and H. Krakauer, *Phys. Rev. B* **42** [10] (1990) 6416.

[34] Y. Luspin, J. L. Servoin and F. Gervais, *J. Phys. C: Solid State Phys.* **13** [19] (1980) 3761.

[35] J. Y. Li, R. C. Rogan, E. Ustundag and K. Bhattacharya, *Nat. Mater.* **4** [10] (2005) 776.

[36] K. M. Ok, E. O. Chi and P. S. Halasyamani, *Chem. Soc. Rev.* **35** [8] (2006) 710.

[37] S. A. Bhalla, R. Guo and R. Roy, *Mater. Res. Innov.* **4** [1] (2000) 3.

[38] M. R. Levy, Crystal Structure and Defect Properties in Ceramic Materials, *PhD thesis, Imperial College of London* (2005).

[39] T. R. Shrout and J. Fielding, *Ultrason. Symp., 1990, Proc., IEEE, 1990*, **2** 711 (1990).

[40] R. A. Cowley, S. N. Gvasaliya, S. G. Lushnikov, B. Roessli and G. M. Rotaru, *Adv. Phys*. **60** [2] (2011) 229.

[41] L. E. Cross, *Ferroelectr.* **151** [1] (1994) 305.

[42] A. A. Bokov and Z. G. Ye, *J. Mater. Sci.* **41** [1] (2006) 31.

[43] G. Smolensky, *Ferroelectr.* **53** [1] (1984) 129.

[44] T. Takaaki, S. Kouji, K. Toshio and D. Masaki, *Jpn. J. Appl. Phys.* **33** [4R] (1994) 1959.

[45] G. Burns and F. H. Dacol, *Ferroelectr.* **104** [1] (1990) 25.

[46] D. M. Smyth, The Defect Chemistry of Metal Oxides, *Oxford University Press* (2000).

[47] C. A. Randall, N. Kim, J.-P. Kucera, W. Cao and T. R. Shrout, *J. Am. Ceram. Soc.* **81** [3] (1998) 677.

[48] R. Guo, L. E. Cross, S. E. Park, B. Noheda, D. E. Cox and G. Shirane, *Phys. Rev. Lett.* **84** [23] (2000) 5423.

[49] D. Damjanovic, *Appl. Phys. Lett.* **97** [6] (2010) 062906.

[50] S.-Y. Chu, T.-Y. Chen, I. T. Tsai and W. Water, *Sens. Actuators A: Phys.* **113** [2] (2004) 198.

[51] A. Garg and D. C. Agrawal, *Mater. Sci. Eng.: B* **86** [2] (2001) 134.

[52] J. F. Fernández, C. Moure, M. Villegas, P. Durán, M. Kosec and G. Drazic, *J. Eur. Ceram. Soc.* **18** [12] (1998) 1695.

[53] K. Toshio, S. Toshimasa, T. Takaaki and D. Masaki, *Jpn. J. Appl. Phys.* **31** [9S] (1992) 3058.

[54] M. I. Morozov and D. Damjanovic, *J. Appl. Phys.* **104** [3] (2008) 034107.

[55] K. Ramam, M. Lopez and K. Chandramouli, *Philos. Mag. Lett.* **88** [6] (2008) 429.

[56] P. K. Panda and B. Sahoo, *Ferroelectr.* **474** [1] (2015) 128.

[57] Y. Hiruma, R. Aoyagi, H. Nagata and T. Takenaka, *Jpn. J. Appl. Phys.* **44** [7A] (2005) 5040.

[58] B. Jaffe, H. L. C. Jaffé and W. R. Cook, Piezoelectric Ceramics, by Bernard Jaffe and William R. Cook Jr. and Hans Jaffe (1971).

[59] E. Ringgaard and T. Wurlitzer, *J. Eur. Ceram. Soc.* **25** [12] (2005) 2701.

[60] M. D. Maeder, D. Damjanovic and N. Setter, *J. Electroceram.* **13** [1] (2004) 385.

[61] P. C. Goh, K. Yao and Z. Chen, *J. Am. Ceram. Soc.* **92** [6] (2009) 1322.

[62] N. Marandian Hagh, B. Jadidian and A. Safari, *J. Electroceram.* **18** [3-4] (2007) 339.

[63] A. Chowdhury, J. Bould, Y. Zhang, C. James and S. J. Milne, *J. Nanopart. Res.* **12** [1] (2009) 209.

[64] C. Sun, X. Xing, J. Chen, J. Deng, L. Li, R. Yu, L. Qiao and G. Liu, *Eur. J. Inorg. Chem.* **2007** [13] (2007) 1884.

[65] A. Chowdhury, S. O'Callaghan, T. A. Skidmore, C. James and S. J. Milne, *J. Am. Ceram. Soc.* **92** [3] (2009) 758.

[66] D. Lin, M. S. Guo, K. H. Lam, K. W. Kwok and H. L. W. Chan, *Smart Mater. Struct.* **17** [3] (2008) 035002.

[67] J. Hao, Z. Xu, R. Chu, Y. Zhang, G. Li and Q. Yin, *Mater. Res. Bull.* **44** [10] (2009) 1963.

[68] K. Chen, J. Zhou, F. Zhang, X. Zhang, C. Li, L. An and J. R. G. Evans, *J. Am. Ceram. Soc.* **98** [6] (2015) 1698.

[69] M. Matsubara, K. Kikuta and S. Hirano, *J. Appl. Phys.* **97** [11] (2005) 114105.

[70] H. Du, F. Luo, S. Qu, Z. Pei, D. Zhu and W. Zhou, *J. Appl. Phys.* **102** [5] (2007) 054102.

[71] B. Malic, J. Bernard, J. Holc, D. Jenko and M. Kosec, *J. Eur. Ceram. Soc.* **25** [12] (2005) 2707.

[72] Q. Zheng, D. Lin, X. Wu, C. Xu, C. Yang and K. W. Kwok, *J. Mater. Sci.: Mater. Electron.* **21** [6] (2009) 625.

[73] Y. Saito, H. Takao, T. Tani, T. Nonoyama, K. Takatori, T. Homma, T. Nagaya and M. Nakamura, *Nat.* **432** [7013] (2004) 84.

[74] C.-W. Ahn, C.-S. Park, D. Viehland, S. Nahm, D.-H. Kang, K.-S. Bae and S. Priya, *Jpn. J. Appl. Phys.* **47** [12] (2008) 8880.

[75] P. Zhao, B.-P. Zhang and J.-F. Li, *Appl. Phys. Lett.* **90** [24] (2007) 242909.

[76] Y. Guo, K.-i. Kakimoto and H. Ohsato, *Mater. Lett.* **59** [2-3] (2005) 241.

[77] M.-S. Kim, S.-J. Jeong and J.-S. Song, *J. Am. Ceram. Soc.* **90** [10] (2007) 3338.

[78] G.-Z. Zang, J.-F. Wang, H.-C. Chen, W.-B. Su, C.-M. Wang, P. Qi, B.-Q. Ming, J. Du, L.-M. Zheng, S. Zhang and T. R. Shrout, *Appl. Phys. Lett.* **88** [21] (2006) 212908.

[79] J. Wu, D. Xiao, Y. Wang, J. Zhu, P. Yu and Y. Jiang, *J. Appl. Phys.* **102** [11] (2007) 114113.

[80] E. K. Akdoğan, K. Kerman, M. Abazari and A. Safari, *Appl. Phys. Lett.* **92** [11] (2008) 112908.

[81] Z. Yang, Y. Chang and L. Wei, *Appl. Phys. Lett.* **90** [4] (2007) 042911.

[82] B.-Q. Ming, J.-F. Wang, P. Qi and G.-Z. Zang, *J. Appl. Phys.* **101** [5] (2007) 054103.

[83] L. Zhengfa, L. Yongxiang and Z. Jiwei, *Curr. Appl. Phys.* **11** [3] (2011) S2.

[84] N. Marandian Hagh, K. Kerman, B. Jadidian and A. Safari, *J. Eur. Ceram. Soc.* **29** [11] (2009) 2325.

[85] J. Wu, Y. Wang, D. Xiao, J. Zhu and Z. Pu, *Appl. Phys. Lett.* **91** [13] (2007) 132914.

[86] C.-W. Ahn, H.-Y. Park, S. Nahm, K. Uchino, H.-G. Lee and H.-J. Lee, *Sens. Actuators A: Phys.* **136** [1] (2007) 255.

[87] C.-W. Ahn, S. Nahm, M. Karmarkar, D. Viehland, D.-H. Kang, K.-S. Bae and S. Priya, *Mater. Lett.* **62** [20] (2008) 3594.

[88] W. Wu, D. Xiao, J. Wu, J. Li, J. Zhu and B. Zhang, *Ceram. Int.* **38** [3] (2012) 2277.

[89] H.-Y. Park, K.-H. Cho, D.-S. Paik, S. Nahm, H.-G. Lee and D.-H. Kim, *J. Appl. Phys.* **102** [12] (2007) 124101.

[90] H. Du, W. Zhou, F. Luo, D. Zhu, S. Qu, Y. Li and Z. Pei, *J. Appl. Phys.* **104** [4] (2008) 044104.

[91] R. Zuo, X. Fang and C. Ye, *Appl. Phys. Lett.* **90** [9] (2007) 092904.

[92] R. Zuo, X. Fang, C. Ye and L. Li, *J. Am. Ceram. Soc.* **90** [8] (2007) 2424.

[93] T. Zheng, J. Wu, D. Xiao, J. Zhu, X. Wang and X. Lou, *ACS Appl. Mater. Interfaces* **7** [36] (2015) 20332.

[94] X. Cheng, J. Wu, X. Wang, B. Zhang, J. Zhu, D. Xiao, X. Wang, X. Lou and W. Liang, *J. Appl. Phys.* **114** [12] (2013) 124107.

[95] S. Gupta and S. Priya, *Appl. Phys. Lett.* **102** [1] (2013) 012906.

[96] Y. Liu, Y. Huang, H. Du, H. Li and G. Zhang, *J. Alloy. Compd.* **506** [1] (2010) 407.

[97] Q. Gou, D.-Q. Xiao, B. Wu, M. Xiao, S.-S. Feng, D.-D. Ma Zhao, J.-G. Wu and J.-G. Zhu, *RSC Adv.* **5** [39] (2015) 30660.

[98] R. Zuo and J. Fu, *J. Am. Ceram. Soc.* **94** [5] (2011) 1467.

[99] J. Yoo and B. Seo, *Ferroelectr.* **425** [1] (2011) 106.

[100] D. Gao, K. W. Kwok, D. Lin and H. L. W. Chan, *J. Phys. D: Appl. Phys.* **42** [3] (2009) 035411.

[101] D. Gao, K. W. Kwok, D. Lin and H. L. W. Chan, *J. Mater. Sci.* **44** [10] (2009) 2466.

[102] H. Sun, D. Peng, X. Wang, M. Tang, Q. Zhang and X. Yao, *J. Appl. Phys.* **111** [4] (2012) 046102.

[103] Y. Wei, Z. Wu, Y. Jia, J. Wu, Y. Shen and H. Luo, *Appl. Phys. Lett.* **105** [4] (2014) 042902.

[104] Z. Wang, Y. Zhuo, D. Xiao, W. Wu, C. Zhang, X. Huang and J. Zhu, *Curr. Appl. Phys.* **11** [3] (2011) S143.

[105] J. Wang, L. Luo, Y. Huang, W. Li and J. A. Varela, *J. Am. Ceram. Soc.* **99** [5] (2016) 1625.

[106] X. Wu, K. W. Kwok and J. A. Varela, *J. Am. Ceram. Soc.* **97** [5] (2014) 1504.

[107] X. Wu, K. W. Kwok and F. Li, *J. Alloy. Compd.* **580** (2013) 88.

[108] J. Hao, Z. Xu, R. Chu, W. Li and J. Du, *J. Appl. Phys.* **117** [19] (2015) 194104.

[109] J. Hao, Z. Xu, R. Chu, W. Li and P. Fu, *Mater. Res. Bull.* **65** (2015) 94.

[110] G. Arlt and N. A. Pertsev, *J. Appl. Phys.* **70** [4] (1991) 2283.

[111] C.-R. Cho, S.-H. Park, B.-M. Moon, J. Sundqvist, A. Hårsta and A. Grishin, *Integr. Ferroelectr.* **49** [1] (2002) 21.

[112] S. Abadei, *Microwave Conference, 2002, 32nd European* (2002) 1.

[113] Y. Zhen, M. Wang, S. Wang and Q. Xue, *Ceram. Int.* **40** [7] (2014) 10263.

[114] I. Kanno, T. Ichida, K. Adachi, H. Kotera, K. Shibata and T. Mishima, *Sens. Actuators A: Phys.* **179** (2012) 132.

[115] C.-R. Cho, A. Grishin, J. Andrèasson, T. Lindbäck, S. Abadei and S. Gevorgian, *MRS Proc.* **656** (2000) DD3.2.

[116] B. Zhu, Z. Zhang, T. Ma, X. Yang, Y. Li, K. K. Shung and Q. Zhou, *Appl. Phys. Lett.* **106** [17] (2015) 173504.

[117] C.-R. Cho, J.-H. Koh, A. Grishin, S. Abadei and S. Gevorgian, *Appl. Phys. Lett.* **76 [**13] (2000) 1761.

[118] M. Blomqvist, S. Khartsev, A. Grishin and A. Petraru, *Integr. Ferroelectr.* **54** [1] (2003) 631.

[119] F. Söderlind, P.-O. Käll and U. Helmersson, *J. Cryst. Growth* **281** [2-4] (2005) 468.

[120] C. W. Ahn, S. Y. Lee, H. J. Lee, A. Ullah, J. S. Bae, E. D. Jeong, J. S. Choi, B. H. Park and I. W. Kim, *J. Phys. D: Appl. Phys.* **42** [21] (2009) 215304.

[121] P. Chin Goh, K. Yao and Z. Chen, *Appl. Phys. Lett.* **99** [9] (2011) 092902.

[122] P. C. Goh, K. Yao and Z. Chen, *Appl. Phys. Lett.* **97** [10] (2010) 102901.

[123] S. S. Won, J. Lee, V. Venugopal, D.-J. Kim, J. Lee, I. W. Kim, A. I. Kingon and S.-H. Kim, *Appl. Phys. Lett.* **108** [23] (2016) 232908.

[124] C. Won Ahn, H. Jin Seog, A. Ullah, S. Young Lee, J. Won Kim, S. Su Kim, M. Park, K. No and I. Won Kim, *J. Appl. Phys.* **111** [2] (2012) 024110.

[125] L. Wang, W. Ren, P. Shi, X. Chen, X. Wu and X. Yao, *Appl. Phys. Lett.* **97** [7] (2010) 072902.

[126] M. Abazari and A. Safari, *Appl. Phys. Lett.* **97** [26] (2010) 262902.

[127] L. Wang, W. Ren, P. Shi and X. Wu, *J. Appl. Phys.* **115** [3] (2014) 034103.

[128] T. Saito, T. Wada, H. Adachi and I. Kanno, *Jpn. J. Appl. Phys.* **43** [9B] (2004) 6627.

[129] J. S. Park, D. Do, M. H. Lee, D. J. Kim, M. H. Kim, J. S. Kim, R. Kambale, S. W. Kim, W. J. Kim, S. S. Kim, K. W. Jang, I. R. Hwang, B. H. Park and T. K. Song, *Ferroelectr.* **465** [1] (2014) 60.

[130] A. Tian, W. Ren, L. Wang, P. Shi, X. Chen, X. Wu and X. Yao, *Appl. Surf. Sci.* **258** [7] (2012) 2674.

[131] M. Abazari, E. K. Akdoğan and A. Safari, *J. Appl. Phys.* **103** [10] (2008) 104106.

[132] M. Abazari and A. Safari, *J. Appl. Phys.* **105** [9] (2009) 094101.

[133] J. Miao, X. G. Xu, Y. Jiang, L. X. Cao and B. R. Zhao, *Appl. Phys. Lett.* **95** [13] (2009) 132905.

[134] M. Blomqvist, J.-H. Koh, S. Khartsev, A. Grishin and J. Andréasson, *Appl. Phys. Lett.* **81** [2] (2002) 337.

[135] I. Kanno, T. Mino, S. Kuwajima, T. Suzuki, H. Kotera and K. Wasa, *IEEE trans. Ultrason. Ferroelectr. Freq. control* **54** [12] (2007) 2562.

[136] V. M. Kugler, F. Söderlind, D. Music, U. Helmersson, J. Andreasson and T. Lindbäck, *J. Cryst. Growth* **254** [3-4] (2003) 400.

[137] V. M. Kugler, F. Söderlind, D. Music, U. Helmersson, J. Andreasson and T. Lindbäck, *J. Cryst. Growth* **262** [1-4] (2004) 322.

[138] H. J. Lee, I. W. Kim, J. S. Kim, C. W. Ahn and B. H. Park, *Appl. Phys. Lett.* **94** [9] (2009) 092902.

[139] T. Li, G. Wang, D. Remiens and X. Dong, *Ceram. Int.* **39** [2] (2013) 1359.

[140] K. Shibata, K. Suenaga, A. Nomoto and T. Mishima, *Jpn. J. Appl. Phys.* **48** [12] (2009) 121408.

[141] Y. Tsujiura, E. Suwa, F. Kurokawa, H. Hida, K. Suenaga, K. Shibata and I. Kanno, *Jpn. J. Appl. Phys.* **52** [9S1] (2013) 09KD13.

[142] J. Wu and J. Wang, *J. Appl. Phys.* **106** [6] (2009) 066101.

[143] J. S. Kim, H. J. Lee, S. Y. Lee, I. W. Kim and S. D. Lee, *Thin Solid Films* **518** [22] (2010) 6390.

[144] G. Li, X. Wu, W. Ren and P. Shi, *Thin Solid Films* **548** (2013) 556.

[145] G. Li, X.-Q. Wu, W. Ren, P. Shi, X.-F. Chen and X. Yao, *Ceram. Int.* **38** (2012) S279.

[146] K. Tanaka, H. Hayashi, K.-i. Kakimoto, H. Ohsato and T. Iijima, *Jpn. J. Appl. Phys.* **46** [10B] (2007) 6964.

[147] S. Y. Lee, C. W. Ahn, J. S. Kim, A. Ullah, H. J. Lee, H.-I. Hwang, J. S. Choi, B. H. Park and I. W. Kim, *J. Alloy. Compd.* **509** [20] (2011) L194.

[148] L. Wang, R. Zuo, L. Liu, H. Su, M. Shi, X. Chu, X. Wang and L. Li, *Mater. Chem. Phys.* **130** [1-2] (2011) 165.

[149] S. Y. Lee, J. S. Kim, C. W. Ahn, A. Ullah, H. J. Lee and I. W. Kim, *Curr. Appl. Phys.* **11** [3] (2011) S157.

[150] S. Y. Lee, C. W. Ahn, A. Ullah, H. J. Seog, J. S. Kim, S. H. Bae and I. W. Kim, *Curr. Appl. Phys.* **11** [3] (2011) S266.

[151] L. Wang, W. Ren, P. Shi and X. Wu, *J. Alloy. Compd.* 608, 202-206 (2014).

[152] N. Li, W. L. Li, L. D. Wang, S. Q. Zhang, J. W. Ye and W. D. Fei, *J. Alloy. Compd.* **509** [31] (2011) 8028.

[153] M. H. M. Akmal, A. R. M. Warikh, U. A. A. Azlan, M. A. Azam and S. Ismail, *Mater. Lett.* **170** (2016) 10.

[154] X.Vendrell, O. Raymond, D. A. Ochoa, J. E. García and L. Mestres, *Thin Solid Films* **577** (2015) 35.

[155] B.-Y. Kim, T.-G. Seong, I.-T. Seo, M.-S. Jang, S. Nahm, J.-Y. Kang and S.-J. Yoon, *Acta Mater.* **60** [6-7] (2012) 3107.

[156] T. Li, G. Wang, K. Li, G. Du, Y. Chen, Z. Zhou, D. Rémiens and X. Dong, *Ceram. Int.* **40** [1] (2014) 1195.

[157] M. Blomqvist, S. Khartsev and A. Grishin, *IEEE Photonics Technol. Lett.* **17** [8] (2005) 1638.

[158] M. Blomqvist, S. Khartsev and A. Grishin, *Integr. Ferroelectr.* **80** [1] (2006) 97.

[159] M. Blomqvist, S. Khartsev, A. Grishin, A. Petraru and C. Buchal, *Appl. Phys. Lett.* **82** [3] (2003) 439.

[160] Y. B. Yao, H. T. Chan, C. L. Mak and K. H. Wong, *Thin Solid Films* **537** (2013) 156.

Chapter 2

Preparation and characterization techniques

The present chapter describes the preparation methods and measurement techniques that are being used to characterize both the bulk and thin films of $K_{0.5}Na_{0.5}NbO_3$ (KNN) ceramics.

Initially, the preparation method was used to prepare the KNN ceramics, sintering mechanisms and the techniques were used to measure the structural, microstructural, dielectric and ferroelectric properties were illustrated. Later, we have also discussed about the deposition of KNN thin films by RF magnetron sputtering and characterization tools that are used for measuring various properties such as structural, microstructural, optical and electrical properties of the films were presented.

2.1 Preparation of bulk KNN ceramics

In general, ceramics are polycrystalline materials with small crystalline grains and significant amount of imperfections like impurities, pores, and grain boundaries, etc. Due to their brittle nature, shaping and densifying without any cracks is a challenge. Nowadays, there have been varieties of methods developed for the preparation of KNN ceramics with good homogeneity, purity and finer particle size. Since, the KNN ceramics have to be characterized for its dielectric, ferroelectric and piezoelectric properties, therefore, they have to be prepared with higher densification and uniform geometry. The available methods are (a) conventional solid state reaction (CSSR) method, (b) wet chemical method (c) precursor method. However, in the present study, we have prepared the KNN ceramics using solid state reaction method.

2.1.1 Conventional solid state reaction method

The CSSR method is widely used for the preparation of polycrystalline ceramics [1]. This method can provide the selection of wide range of starting materials such as metal oxides, carbonates, etc. Two important steps are involved in this method are the uniform mixing of starting materials for better homogenization and heat treatment at high temperatures for phase formation. The solids cannot react with each other at room temperature (RT) and they required higher temperatures for the phase formation and densification. The advantage of this CSSR method is its environment friendly nature,

cost-effective; reaction takes place without any solvents, and the structurally pure final products. The main disadvantage of this method is that it requires high processing temperature. Different steps were involved in CSSR method are explained in the following sections.

2.1.2 Weighing of starting materials

Initially, the raw materials were heated in an oven at 150 ^{o}C for 1h to remove the moisture presented in the initial reagents. To control over the impurities and for reproducible KNN ceramics, high purity chemicals (> 99.99%) were used. These materials are weighed according to the stoichiometric ratio using the following equation.

$$K_2CO_3 + Na_2CO_3 + 2Nb_2O_5 \rightarrow 4(K_{0.5}Na_{0.5}NbO_3) + 2CO_2 \qquad (2.1)$$

The samples were measured by using an electronic balance (M/s Mettler Toldo, AG135), which has the accuracy ~0.01 milligram (mg).

2.1.3 Uniform mixing of raw materials

The weighed powders were uniformly mixed to increases the contacts between the reagents, which will act as product layer formation centers. A planetary ball mill (M/s Fritsch, Pelverisette 6) was used for the uniform mixing of the powders in a zirconia jar with a different diameter (5 and 10 mm) of zirconia balls and distilled water as milling media. The powders were mixed at a speed of 120 rotations per minute for 5h and the photography of the planetary ball mill being used in this study is depicted in Figure 2.1.

Figure 2.1: *Photograph of the planetary ball mill.*

2.1.4 Calcination

In order to obtain the desired phase formation, the samples need to be heated to a suitable temperature, which is called as calcination temperature [2]. Calcination is the process of heat treatment at lower temperatures prior to the sintering. In the calcination stage, the chemical decomposition reactions take place in which the unwanted gases such as carbonates, nitrides, sulphates, and other metal oxide components were removed and form a new solid phase. The parameters such as calcination temperature, duration and atmospheres will play an important role on the crystal structure of the ceramics. Generally, the phase formation temperature is decided from differential scanning calorimetry and thermo gravimetric analysis. Further, the phase formation temperature and presence of secondary phases could be identified with the help of X-ray diffraction pattern of the calcined powders.

2.1.5 Particle size reduction

It is the well-known fact that the smaller size particles having a higher surface to a volume ratio as compared to larger particles, which can have the high chemical reactivity. Therefore, initial smaller particle size reduces the sintering temperature and increases the density of the ceramics. For this purpose, the planetary ball mill is used for decreasing the initial particle size. During the milling process, the particles experience the mechanical stress due to the compression and shear with milling medium and other particles. It can lead to be elastic as well as inelastic deformation. If the mechanical stress is beyond the strength of the particle, the crack will happen. In this study, we have used the ball mill twice; first time is for the uniform mixing of initial reagents and second time to reduce the particle size after calcination.

2.1.6 Pelletization

After the ball milling, the slurry was dried at 120 ^{o}C to obtain the fine powders. These powders were added with an appropriate amount of binder (Polyvinyl alcohol, PVA) and pressed into cylindrical shaped pellets of 10 mm in diameter and 1 mm in thickness using KBr hydraulic press. The role of PVA is to enhance the green strength of powders and to reduce the friction between the powder and walls of die. In order to make the green pallets, the rust free dies should be used. For the smooth inner surface of the dies, an internal lubricant such as stearic acid was used. The pressure should be applied slowly to

facilitate the leak of the trapped air. The applied pressure on the upper part of the die as a function of the distance is given by the following equation,

$$P_x = P_a \exp^{\frac{-4\mu KL}{D}} \quad (2.2)$$

where, P_x is the pressure gradient; P_a is the applied pressure, μ is the friction coefficient; K is the constant, L and D are the length and diameters of the die, respectively [3]. The pressurization can be done in two different methods (a) uniaxial pressing and (b) isostatic pressing. In case of uniaxial pressing, the pressure will be applied in only one direction, whereas the pressure will be applied from all directions in isostatic pressing method. In the present study, we have used the uniaxial pressing method to prepare the green pellets.

2.1.7 Sintering

The main purpose of sintering is to densify the ceramics and reduce the porosity. The density and porosity are very important parameters and which can directly affect the electrical properties of the ceramics. The particle size, shape and distribution, pore size distribution, pressure, time, temperature, green density, uniformity of green microstructure, impurities and gas atmosphere factors show the dominant effect on sintering [4-5]. An increase in temperature will greatly enhance the sintering kinetics and bulk diffusion mechanisms, which lead to densification. The ceramic with higher green density possesses the higher final density. The green density is directly related to the uniform green microstructure and the absence of agglomerates. The atmospheres also play a critical role on densification, and sometimes they can increase the diffusivity as well as the coarsening. The small concentration of impurities (sintering aids) can enhance the sintering kinetics and form the low temperature eutectics. The main driving force for the densification is the decrease in the surface area. Therefore, larger the surface area, higher the driving force. However, with an increase in the surface to a volume ratio of the particles, the electrostatic and some other surface related forces developed, which leads to agglomeration. These agglomerates sinter together into larger particle at higher temperatures. However, fine particles create the bigger pores, which are difficult to eliminate. The development of microstructure and densification during sintering is a direct consequence of mass transportation, which is activated by temperature. The sintering phenomena are of two types: (a) solid state sintering and (b) liquid phase sintering. In a solid state sintering process, the densification occurs by change in particle

shape without any rearrangement, whereas some kind of liquid will present in the liquid phase sintering.

Sintering of the ceramics can be completed in three different stages as shown in Figure.2.2. In the first stage, there is surface smoothening of grains (or particles), neck growth and rounding of interconnected pores. The density of the green pellets is around 60% of the theoretical density (TD) and at the end of the first stage, the density will be around 70%. After reaching the reaching the sintering temperature, the 10% of densification occurs quickly due to the larger surface area and high driving force [6].

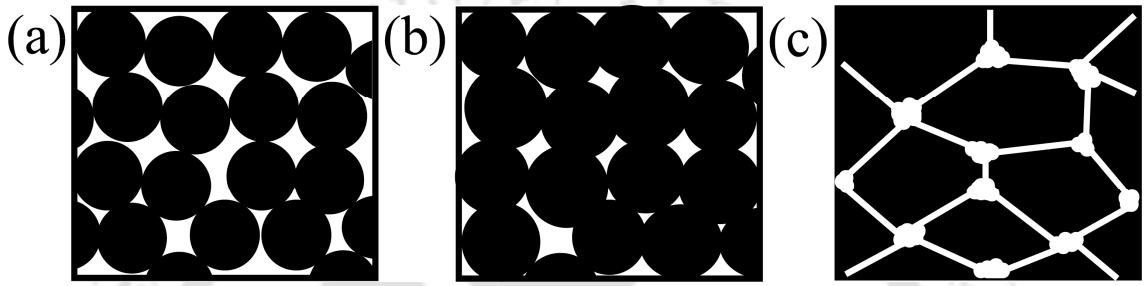

Figure 2.2: *(a) First (b) intermediate and (c) final stages of sintering of particles.*

During the intermediate stage, the formation of neck growth as densification further proceeds. A number of competing paths were transported to the neck area, and few of them lead to the densification by the approaching the centers of particles each other. Some of these paths could help to coarsening and reduction in the surface area by the neck growth between the particles. An important transport mechanism is the surface diffusion, which can involve in particle joining, surface smoothing and pore rounding. The lattice diffusion and grain boundary diffusion also causes the neck growth and volume shrinkage. At the end of the intermediate stage, the density of the ceramics is around 90% of TD. The final stage of sintering begins around 93 - 95 % of TD. During the final stage of sintering, the mass transportation from a grain boundary to pore can lead to eliminate the isolated pores and development of uniform grain growth takes place. The grain boundary and lattice diffusions play the key role in eliminating the pores on grain boundary and pores inside the grains, respectively. The maximum elimination of porosity is happens when all the void spaces are connected to fast and short diffusion paths along the grain boundaries. However, the lattice diffusivity has a slower effect on the annihilation of pores as compared to grain boundary diffusion. The elimination of pores, which are attached at the grain boundary, is very important to obtain the high density. At higher sintering temperatures, both grain boundary and lattice diffusions will dominate

and promote densification. Low temperature sintering may cause the coarsening and porous material. Therefore, it requires the dopants to enhance the densification at lower temperatures without affecting the electrical properties of the ceramics. These additives (or dopants) can help to reduce the rate of coarsening in the earlier stages of sintering and enhance the rate of densification.

2.1.8 Recrystallization and grain growth

In general, crystallization can be divided into two types, primary and secondary recrystallization processes. During the primary recrystallization process, nucleation and growth of a new generation of strain- free grains occur in a matrix which has been plastically deformed [6]. In a secondary recrystallization process, few large grains are nucleated and enlarge at the expanse of other small grained, which causes the abnormal or discontinuous grain growth.

Primary recrystallization process has its driving force in the increased energy of a matrix, which has been plastically deformed. The constant rate of grain growth for the new strain free grains occurs when the isothermal change in the grain size of strain released crystals even after an initial induction period. The grain size (d) can be expressed as [6],

$$d = U(t - t_o) \tag{2.3}$$

where, U is the grain growth rate (cm/sec), t is the time and t_o is the induction period. Here t_o relate to the time required for unstable embryos present to grow to the size of a stable nucleus. For a steady nucleus, its size must be larger than the critical diameter at which the free energy of the new grains equals to the surface free energy. The rate of nucleation increases with a rise in the number of sites after an initial induction period and also increases with temperature.

Grain growth is the process that the average grain size of the strain free crystals increases continuously during the sintering without a change in the grain size distribution. Even without primary recrystallization, an aggregation of small grained crystals increases when heated at higher temperatures. The average grain size increases with shrinkage and disappearance of some grains. Grain growth is the rate of disappearance of smaller grains, and it remains constant until the grains begin to impinge on one other. For this process, the driving force is the energy difference between small and large sized grains. The larger

grain size can be formed to minimize the surface free energy by decreasing the grain boundary area.

2.2 Preparation of KNN thin films

By definition, thin films are three dimensional solids; however, the thickness of the films is several orders lower as compared to the other two dimensions. The thickness of the film may vary from a fraction of nanometers to few micrometers. They are very attractive not only due to the smaller dimension but also for their outstanding properties, which are different from the bulk ceramics. These properties are dependent on the deposition conditions. Therefore, it is better to understand the nature of the films to get the high quality thin films. Ideally, the deposition of the films takes place atom by atom in a proper time interval between the successive depositions. The deposited atoms or molecules occupy the lower potential energy configuration with respect to the substrate and earlier deposited layers to get the thermo dynamical equilibrium. The incoming atoms can sit in the positions and orientations in such a way that energetically compatible with previously deposited atoms or layers. Further increase in the atomic layers, the effect of substrate as well as initial layers will slowly decrease, but the effect of freshly formed layers remains present. The deposition conditions were carried in normal environments will deviate from the ideal deposition conditions, which means atomic layers do not have the proper time for achieving the thermodynamic equilibrium condition or incomplete layer formation. These deviations cause the formation of meta-stable films. The atoms deposit favorably on particular sites during the early stage leading to accumulations of atoms called as nuclei (clusters). Further, these nuclei could increase to form monolayers and also thickness after fresh impingement of more atoms.

Mostly, thin films were prepared using chemical vapor deposition (CVD) and physical vapor deposition (PVD) methods.

2.2.1 Chemical vapor deposition method

The CVD method is a process, where the volatile precursors are flowing into a reaction chamber via vapor phase, where they deposited on a heated substrate. This method can be associated with the production of chemical byproducts that are exhausted out of the chamber along with the other unreacted precursor gases. This method can be suitable when a volatile material to be deposited.

2.2.2 Physical vapor deposition method

The PVD method is used to deposit the thin films by the condensation of vaporized material onto the substrate. This method deals with a purely physical process such as thermal evaporation and sputtering rather than involving a chemical reaction in the case of CVD technique. In evaporation technique, the atoms are removed from the source material by heating, whereas in case of sputtering the atoms are dislodged from the target material by the bombardment of ionized gas.

In thermal evaporation technique, the thermally released atoms move onto the substrate in straight trajectories without any collisions under high vacuum. Different methods were used to heat the source material such as direct and indirect resistive heating, inductive heating, electron evaporator, arc discharges, laser ablation, and flash evaporation.

2.2.3 Sputtering

As we have discussed earlier, sputtering is the process that the ejection of surface atoms from the target material, when bombarded with high energy particles, mostly positive ions. This sputtering phenomenon was first discovered by Grove in 1852. The measure of ejection rate of atoms called as the sputter yield (Y), which is the ratio between the ejected atoms to the incident projectiles. The sputter yield can be expressed as [7],

$$Y = \frac{3}{4\pi^2}\alpha\frac{4m_1m_2}{(m_1+m_2)^2}\frac{E}{U_s} \tag{2.4}$$

where, m_1 and m_2 (amu) are the masses of the projectile and target atoms, α is the dimensionless parameter, which depends on the ion energy and mass ratio, E is the projectile energy, and U_s is the binding energy of the surface atoms. In order to eject an atom from the target, the momentum transfer from the ion-induced collision should overcome the binding energy of the surface atoms. Therefore, sputtering yield is inversely proportional to the binding energy. At lower energies, an incoming ion transfers the maximum momentum to target atoms when the both masses are equal ($m_1 = m_2$).

The source of sputtering for ions is provided by the glow discharge due to an applied voltage between the anode and cathode at low pressures [8]. When a particular value of voltage between the electrodes is reached, then the gas breaks down to conduct

electricity. This glow discharge is depend on the applied voltage and ionization current and it is called as the normal glow when it is maintained at constant voltage, and termed as an abnormal glow, where voltage and current increase together. A luminous layer, which covers the cathode partially in the normal glow and completely in the abnormal glow, is known as a cathode glow. Next to the cathode glow, a region with relatively low luminosity is known as a cathode dark space. It is the most important region, because most of the applied voltage will drop across it. Further in the sequence, a bright negative glow region, Faraday dark space and positive column region appear. Figure 2.3 illustrates the different regions of glow discharge.

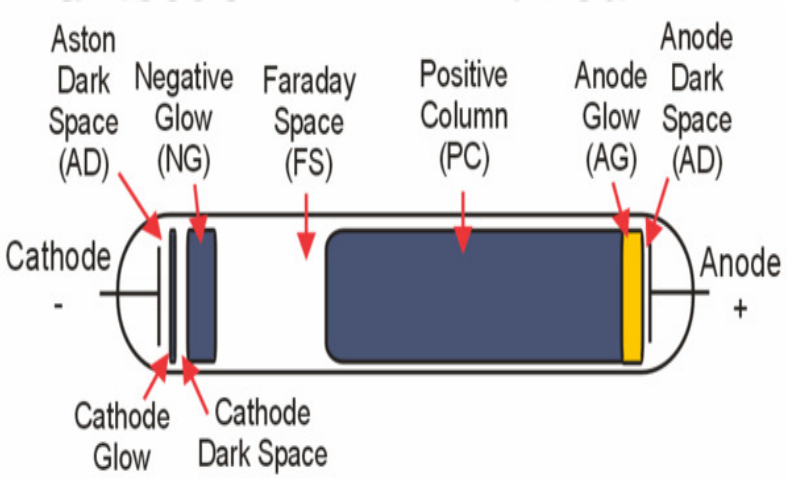

Figure 2.3: *Different regions in a typical glow discharge* [8].

Between the two electrodes, the sputtered gas converts into ions and electrons and accelerates across this region. These energetic electrons participate in more collisions with gas atoms in the vicinity of glow and cause the ionization. The energetic ions impinge on the target to produce the sputtered flux and secondary electrons, which are helpful to sustain the glow. The effective sputtering is possible only when both the number of ions and their energy are large and controllable.

There have been different types of sputtering techniques were used for the deposition of thin films such as (a) direct current (DC) sputtering, (b) radio frequency (RF) sputtering, (c) magnetron sputtering, and (d) reactive magnetron sputtering.

(a) DC sputtering

This is the simplest among all the sputtering methods. In this method, the target material is connected to the negative terminal of a DC power supply, whereas the substrate is placed on an anode, which may be biased. The sputtering chamber will be

filled with an inert gas, typically argon (Ar), which serves as a medium in which the glow discharge is initiated under the application of DC voltage. The Ar atoms will be ionized (Ar^+) in the applied potential and accelerated towards the cathode and eject the atoms from the target material. These sputtered atoms transfer through the glow discharge and deposit onto the substrate. However, the main disadvantages are low deposition rates, high discharge voltages, high gas and low plasma densities and used only for conducting targets.

(b) RF sputtering

In DC sputtering, when the energetic Ar ions hit the target; their electric charge is neutralized, and they become to Ar atoms. For the insulating target, a positive charge layer will form on the target surface instead of the neutralization process. It can cause the repulsion of bombarding ions and eventually the sputtering process stops. To overcome this problem, the polarity should be changed to eliminate the surface charges on the target. It can be done by applying the RF signal to the cathode. This type of sputtering is called as RF sputtering. In this technique, a frequency of 13.56 MHz is applied to the cathode via impedance matching network.

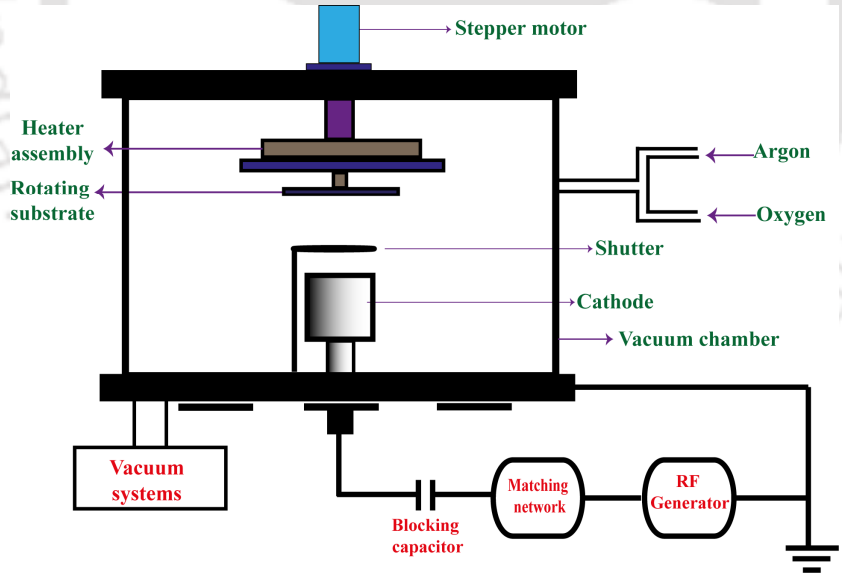

Figure 2.4: *Block diagram of simple RF sputtering system.*

A blocking capacitor will also connected in between RF power supply and cathode to avoid shorting the target to be ground, which is shown in Figure 2.4. The target and the substrate holder acts as electrodes. As the RF power is applied, then electrons follow the RF signal and oscillate between the electrodes and acquire sufficient energy for ionizing

collisions and sustain the plasma. In the positive half cycle, the target act as anode and acquire electrons and during the negative half cycle it will acquire enough ions and resulting in the sputtering as well as deposition of target material.

(c) Magnetron sputtering

In normal DC or RF sputtering techniques, many electrons are removed from the target and reach the anode through fewer collisions with gas (Ar) atoms because the ionization cross section reduces with increasing electron energy. The probability of ionization of gas atoms is less when far from the cathode. Therefore, the ionization efficiency as well as deposition rate decreases.

These limitations can be overcome in the magnetron sputtering systems by trapping of electrons near the cathode surface. In this configuration, magnetic field (B) is parallel to the cathode surface, whereas the electric field (E) acts normal to the surface. The magnets are arranged in such a way that one of the poles is positioned at the centre of the target, and the other pole is placed near the edge of target, which can form the magnetic field lines (Figure 2.5) [9].

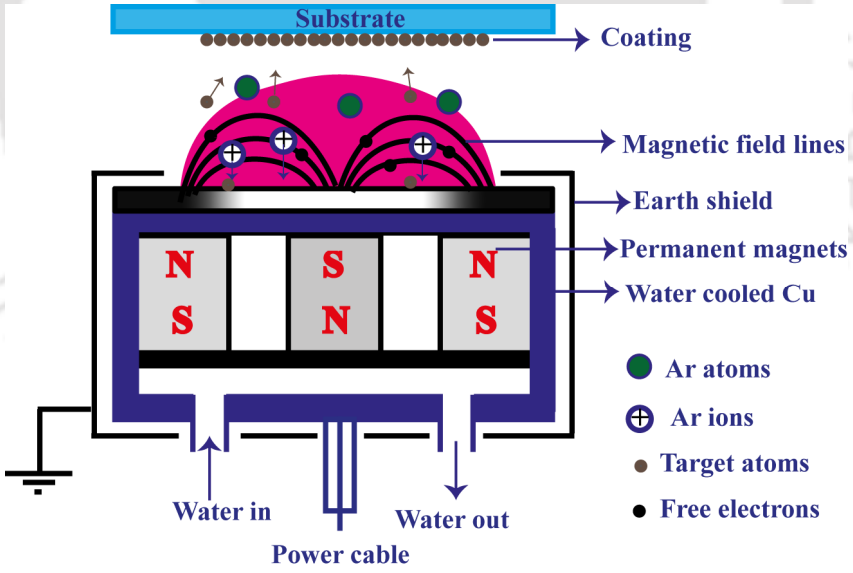

Figure 2.5: *Block diagram of magnetron sputtering system.*

The electrons emitted from the cathode and moves with velocity component perpendicular to the magnetic field will spiral around the magnetic field lines and trapped by the field. The trapping of electrons can significantly enhance the probability of ionization efficiency, which results in high rate of deposition onto the substrate even at lower working pressures. This technique can be used in both DC and RF sputtering.

(d) Reactive magnetron sputtering

In general, the inert gas (argon) is being used as sputtering gas to avoid the chemical reactions between the target and sputtered gas. However, some cases such as the deposition of nitrides and oxides, reactive gases are intentionally added with argon to react with sputtered material. This type of sputtering process is called as a reactive magnetron sputtering [10]. The addition of reactive gases to the sputtering chamber can significantly affect the deposition rate and stoichiometry of the compound.

In the present thesis, RF reactive magnetron sputtering system (M/s Advanced Process Technologies, Pvt. Ltd., India) has been used for the deposition of pure and rare earth doped KNN thin films. The photographic image of the RF reactive magnetron system is shown in Figure 2.6.

Figure 2.6: *RF reactive magnetron sputtering system.*

The sputtering system consists of a vacuum chamber equipped with pumping systems, sputtering source, heating assembly, and rotating substrate holder. A two inch target is power-driven by an RF generator (M/s RF VII, Inc. RF-3-XIII) through an impedance matching network. The high vacuum (~10^{-6} mbar) in the system is achieved by a turbo molecular pump (M/s Leybold vacuum, TD20). In this system, both reactive (Ar and O_2) and non-reactive (Ar) type of sputtering have been employed.

2.3 Characterization techniques

2.3.1 Thermal analysis

The differential scanning calorimetry (DSC) and thermal gravimetric analysis (TGA) methods are used to study the heat flow and temperature related material transitions as a function of time and temperature [11]. The DSC analysis can be used to investigate the heat flow, which can be absorbed or radiated by the material on the base of temperature change between the test sample and reference (Alumina). In this measurement, two pans, one pan is for test sample and other pan is for reference sample is placed on thermoelectric disk enclosed by a furnace. The furnace is heated with constant heating rate in argon atmosphere. The heat transfers to the both test sample pan and reference pan via the thermoelectric disk. Depends on the heat capacity of the sample, there would be the temperature difference between the both pans and corresponding heat flow is measured. Depending on the phase transitions of the sample, it can exhibit either exothermic (heat release) or endothermic (heat absorption) reactions relative to the reference. The system shown in Figure 2.7 is used to measure the DSC and TGA curves of the KNN sample.

Figure 2.7: *Photographic image of the DSC-TGA system.*

The TGA technique is used to measure the change in the mass of the sample as a function of temperature and time using a controlled temperature program. The TGA instrument contains a sample pan that is connected with a precision balance. The change in mass of the sample is monitored throughout the experiment. The mass (weight) change of the sample may be due to the evaporation of moisture or volatile components, decomposition of material and other solvent residues. Therefore, this technique is used to estimate the temperature at which chemical reactions start and finish.

In the present thesis, thermal analysis of the KNN ceramic powders were analyzed using high temperature differential scanning calorimetry/ thermo gravimetric system (M/s Netzsch, STA449F3A00). The DSC/TGA measurements were performed at the rate of 10 ^{o}C /minute in the temperature range of 30 ^{o}C - 1000 ^{o}C.

2.3.2 X-Ray diffraction

X-ray diffraction (XRD) technique is a powerful tool for the identification of crystalline phase, and refinement of crystal structure. The wavelength of X-rays is in the range of few Å to 0.1 Å, which is equivalent to size of the atoms. Therefore, X-rays are suitable to investigate the structural arrangement of atoms in different materials. A monochromatic X-ray beam having the wavelength (λ) incident onto a sample at an angle (θ), then the interaction between the X-rays and electrons of atoms leads the diffraction. Depending on the atomic arrangement of material, the scattered X-rays exhibit the constructive or destructive interference pattern.

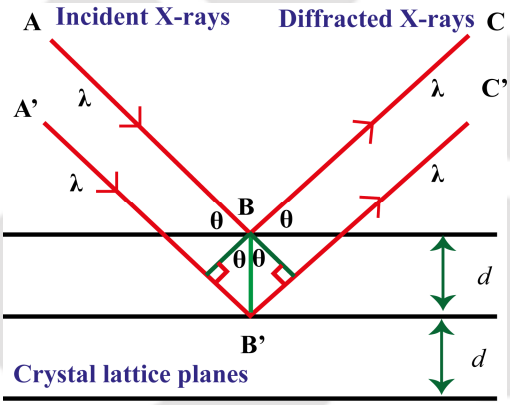

Figure 2.8: *Bragg's law for X-ray diffraction.*

According to the constructive interference, the path difference between two diffracted rays is equal to the integral multiple of the incident wavelength, which is explained using Bragg's law [12],

$$n\lambda = 2d\sin\theta \qquad (2.5)$$

where, d is the inter planar spacing and n is an integer. From the Figure 2.8, the diffracted X-rays exhibit constructive interference when the difference between ABC and A'B'C' paths ($2d\sin\theta$) is equals to the integer number of λ.

In the present thesis, Rigaku X-ray diffractometer (M/s Rigaku, TTRAX-III 18 kW) with CuK_{α} (λ = 1.5406 Å) radiation was used to characterize the KNN based ceramics and thin films. Figure 2.9 shows the photographic view of the X-ray

diffractometer used in the present thesis. All the samples have been measured using the conditions such as scanning step size 0.03° and scanning rate 3°/minute between the 2θ range of 20-60°. The 2θ calibration was be done using standard Si sample to account for the instrumental line broadening, which is approximately equal to the 0.15°. The XRD patterns of the KNN based ceramics and thin films were analyzed using Rietveld refinement method using Fullprof software [13].

Figure 2.9: *Photograph of the X-ray diffractometer.*

2.3.3 Density measurement

The relative density of the sintered KNN based ceramics was measured by using Archimedes's method. According to this method, when an object is floated or partially immersed or fully immersed in a fluid, there is an upward force (buoyance force) produced by the fluid on the object. The force is acts upward and has the magnitude equal to weight of the fluid displaced by it. The apparent weight of the object is equal to the difference between the object's actual weight and magnitude of the buoyance force. The apparent density (ρ_a) of the object is calculated using the following formula,

$$\rho_a = \left(\frac{w_1}{w_2 - w_3} \right) \times \rho_w \ \ gm/cm^3 \qquad (2.6)$$

where, w_1 is the weight of the object measured in air, w_2 is the weight of the object immersed in the fluid, and w_3 is the weight of the object after removed from the fluid, and

ρ_w is the density of the fluid used. In the present study, the distilled water (ρ_w = 1 gm/cm^3) used as the fluid. Further, the relative density of the sample was calculated using following expression.

$$relative\ density = \frac{\rho_a}{theoritical\ density} \tag{2.7}$$

2.3.4 Scanning electron microscopy

In the present study, the microstructural images and chemical composition of the KNN based ceramics and thin films have been by using the scanning electron microscopy (SEM) (M/s LEO, 1430vp) equipped with energy dispersive X-ray spectrometer (EDS or EDAX) and filed emission scanning electron microscopy (FESEM) (M/s Zeiss, Sigma).

SEM is an electronic microscope that images a surface of the sample by scanning with high energy electrons in a raster scan pattern. It can also be used to characterize the morphology, chemical composition and crystallographic information. In SEM, the electrons are thermionically emitted from a tungsten filament and accelerated towards an anode with the significant amount of kinetic energy. In FESEM, electrons can be emitted from field emission. The energy of electrons is dissipated as different signals depend on the interactions between the electrons and samples.

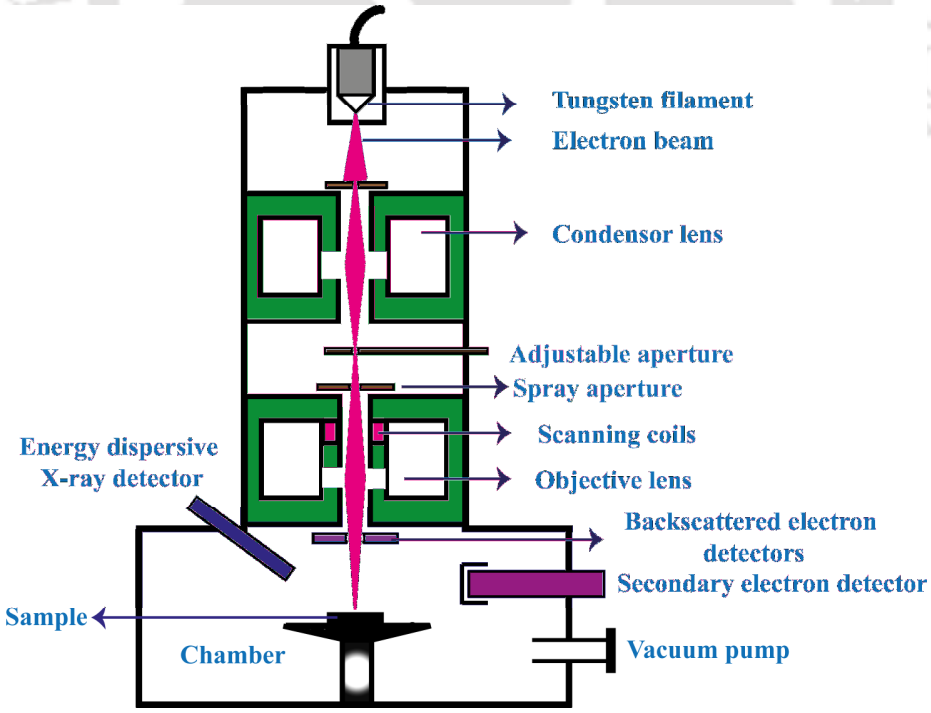

Figure 2.10: *Block diagram of scanning electron microscope.*

Among these signals, secondary electrons and backscattered electrons are used to obtain the surface morphology and photons are used for elemental analysis, and others are cathode luminescence and heat. Secondary electrons can produce the classic topographic images, whereas the backscattered electrons provide the information about the variations in the composition. The schematic diagram of SEM is shown in Figure 2.10. The energy of an electron beam is in the range of a few hundred *eV* to 50 *keV*. The thermally emitted electron beam is accelerated through a high voltage and pass through an aperture and electromagnetic objective lenses to produce the thin electron beam. Then after the electron beam scans the surface of the sample by means of scan coils. Since, electrons interact with the material, the sample must be conducting. These electrons bombard on the surface of the sample and dislodge electrons from the sample. The dislodged electrons called as secondary electrons, which are collected by a positively biased detector and converts into signals. Further, the signals are amplified, analyzed and converted into topography images being examined.

EDS is an analytical technique used for the chemical characterization of a sample. Its characterization capabilities originate from the fact that each element has a unique atomic structure, which produce a unique characteristic X-ray. When a high energy electron beam strikes an atom and ejects the electron from the inner shell of the atom, it results in an electron vacancy in the shell. To return the atom to its ground state, the vacancy can be filled by an electron from a high-energy shell by releasing of some energy in the form of X-rays. The atoms of every element in the sample release X-rays with unique amount of energy during this process. These X-rays are detected in SEM equipped with an energy dispersive X-ray detector. An EDS spectrum show the peaks correspond to the energy levels for which the X-rays had been received. Each peak of the spectrum is unique to an atom (element) and the intensity of the peak defines the concentration of elements presented in the sample.

2.3.5 Raman spectroscopy

Raman spectroscopy is a spectroscopy which is observed as inelastically scattered light, allows for the identification of molecular and crystal vibrations. Raman spectroscopy is sensitive to the crystal structure, bonding, and chemical composition of the material and does not require any sample preparation. These characteristics make it very important method for identifying the material in any physical form; solids, liquids, and gases.

Raman scattering phenomenon was first discovered by Sir Chandrasekhara Venkata Raman in 1928 [14]. When the light interacts with the matter, a small fraction of light may be scattered either elastically or inelastically. Therefore, the energy of the scattered light is either higher or lower as compared to that of incoming light, which is known as Raman Effect. The anti-Stokes lines exhibit the higher energy, whereas the Stokes lines having lower energy. The difference in the energies between the incident and scattered lights of anti-Stokes and Stokes lines will cause the destruction and creation of phonons, respectively. The scattering without change in the energy of the photons is known as Rayleigh scattering (elastic scattering).

The Raman effect occurs when an incident light (laser beam) of frequency ν_0 is scattered from the vibrating molecules of the sample. The change in displacement (Δx) of the normal coordinates of the molecules about their equilibrium position due to a particular vibrational mode can be expressed as [15],

$$\Delta x = x_0 \cos(2\pi \nu_m t) \tag{2.8}$$

where, ν_m is the vibrational mode frequency and x_0 is the vibrational amplitude. The molecule vibrates with a frequency, which is dependent on the bond strength and reduced mass. The electric field of the incident laser beam which oscillates with time (t) is expressed as,

$$E = E_0 \cos(2\pi \nu_0 t) \tag{2.9}$$

where, E_0 is the amplitude of oscillating electric field. The induced polarization (P) in the molecule by the application of electric field can be written as,

$$P = \alpha E \tag{2.10}$$

where, α is the molecular polarizability that depends on the crystal structure and bond nature. Further, α can be expanded as

$$\alpha = \alpha_0 + \left[\frac{\partial \alpha}{\partial x}\right]\Delta x + \ldots \tag{2.11}$$

where, α_0 is the molecular polarizability at equilibrium position. The equation 2.10 can be re-written as,

$$P = \alpha_0 E_0 \cos(2\pi \nu_0 t) + \frac{1}{2}\left(\frac{\partial \alpha}{\partial x}\right) x_0 E_0 [\cos(2\pi\{\nu_0 + \nu_m\}t) + \cos(2\pi\{\nu_0 - \nu_m\}t)] \tag{2.12}$$

Above equation represents the electric oscillating dipole, which emits the photons with three different frequencies. The first frequency ν_0 belong to the Rayleigh scattering, second frequency term $\nu_0 + \nu_m$ corresponds to the Anti-Stokes lines and third term frequency term $\nu_0 - \nu_m$ corresponds to the Stokes lines. (Figure 2.11) It is observed that the Raman effect occurs only if the polarizability must change with the displacement $[(\partial\alpha/\partial x) \neq 0]$ to get Raman active mode. The Raman intensity is directly related to the square of the ratio of change in polarizability with respect to the change in displacement $[(\partial\alpha/\partial x)^2]$. The Raman intensity is also depended on the molecular composition, excitation wavelength, and vibrational modes of the molecules. The difference in frequency of incident and emitted radiation is called as Raman's shift ($\Delta\nu$), which is typically measured in the units of cm^{-1}. The magnitude of the Raman shift is determined by the different vibrational modes of the molecules present in the sample.

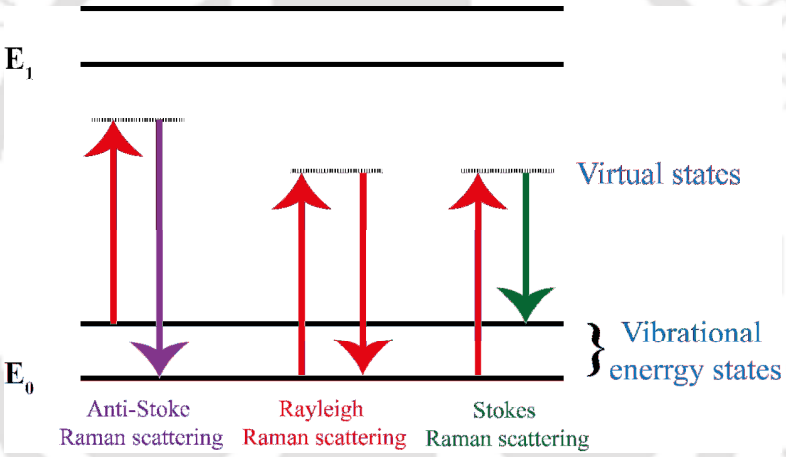

Figure 2.11: *Energy level diagram for Rayleigh and Raman Scattering.*

In the present thesis, Raman spectra of KNN based bulk and thin films were recorded using LABRAM HR800 Raman spectrometric analyzer developed by Horiba Jobin Yvon with an excitation wavelength of 488 nm of an Ar-ion laser. The microscope coupled confocally to an 800 nm focal length spectrograph equipped with two switchable gratings. The beam splitter is used to reflect the laser beam and split into two equal parts. The beam is allowed to hit the sample, where it undergoes the Rayleigh scattering as well as Raman scattering. The notch filter is used to allow only the Raman scattered signal and to block the incident signal. Further, this Raman signal was allowed to pass through grating to resolve the weak Raman signal. Finally, the beam was allowed into a charge-coupled device (CCD) to detect the change in polarizability with respect to change in the displacement, and later it converts into the Raman intensity.

2.3.6 Dielectric measurements

The dielectric properties such as the relative permittivity (ε_r) and loss tangent ($tan\delta$) are very important parameters to understand the different polarization mechanisms and also provide the information about the applicability of the piezoelectric materials in intended applications.

Figure 2.12: Photographs of the (a) LCR meter and (b) RF impedance/material analyzer equipped with temperature control systems used to measure the dielectric properties.

For the dielectric measurements, the samples were painted with silver paste on both sides to make metal-insulator-metal (MIM) capacitors. In the present study, the low frequency (20 Hz -1 MHz) dielectric properties measured in the temperature range 25 ^{o}C - 500 ^{o}C using a LCR meter (M/s Wayne Kerr Electronics Pvt. Ltd., 1J43100) connected to computer via RS232 connection (Figure 2.12(a)). The sample was kept inside the oven and a PID controller (M/s Eurotherm, 3216) is used to control the temperature of the oven. A K-type thermocouple placed inside the oven near to the sample to measure the temperature with an accuracy of ± 1.5 ^{o}C. The high frequency (1 MHz -1 GHz) dielectric properties of the KNN based ceramics were measured using the RF material analyzer (M/s Agilent Technologies, E4991A) in the wide temperature range of -160 ^{o}C – 400 ^{o}C with stability of 0.01 ^{o}C due to the 4 channel Quatro controller containing PID control

algorithms (M/s Novocontrol, Concept 70). The photograph of the RF material analyzer being used in this study is displayed in Figure 2.12(b). The liquid nitrogen was used as cooling/heating medium. A controlled heating element was placed inside the Dewar to build up a specified pressure to create the constant nitrogen stream. Dewar pressure and temperatures are measured by two channels of the Quatro controller. The nitrogen stream, heated to an appropriate temperature to reach the desired sample temperature and flows directly through the sample cell mounted in the cryostat. The gas and sample temperatures are measured by the other two channels of the Quatro controller.

Theory

Impedance spectroscopy (IS) is a powerful technique to characterize the electrical properties of the materials and their interfaces [16]. When an AC voltage is applied to a sample, then the impedance of the system measured according to Ohm's law as the ratio of applied voltage to be measured current in the time domain.

$$V(t) = V_0 \exp(j\omega t) \tag{2.13}$$

$$I(t) = I_0 \exp(j\omega t + \varphi) \tag{2.14}$$

Where, j = √-1, ω is an angular frequency and φ is the phase angle. The complex impedance can be expressed in terms of both magnitude (|Z|) and phase angle (φ) as,

$$Z^*(\omega) = |Z| \exp(-j\varphi) \tag{2.15}$$

$$Z^*(\omega) = |Z| \cos(\varphi) - j|Z| \sin(\varphi) \tag{2.16}$$

$$Z^*(\omega) = Z'(\omega) - jZ''(\omega) \tag{2.17}$$

where, $Z'(\omega)$ and $Z''(\omega)$ are the real and imaginary parts of complex impedance, and $|Z| = \sqrt{[\ Z'(\omega)^2 + Z''(\omega)^2]}$. These impedance data can be used to calculate the complex admittance (Y*), complex permittivity (ε*), and complex modulus (M*).

$$Y^*(\omega) = Y'(\omega) + jY''(\omega) = 1/Z^* \tag{2.18}$$

$$\varepsilon^*(\omega) = \varepsilon'(\omega) - j\varepsilon''(\omega) = 1/j\omega C_0 Z^* \tag{2.19}$$

$$M^*(\omega) = M'(\omega) + jM''(\omega) = j\omega C_o Z^* \tag{2.20}$$

The complex functions Y* and ε* are parallel functions (at low frequencies), whereas the Z* and M* are series functions at high frequencies.

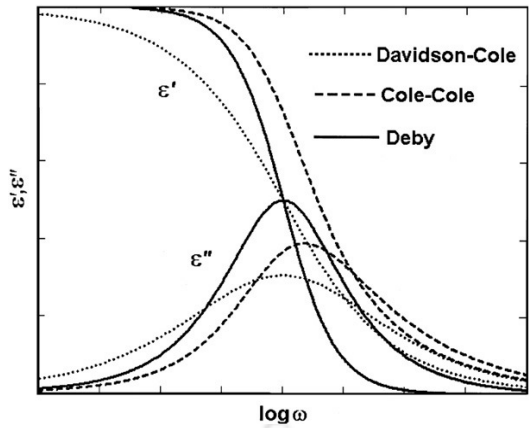

Figure 2.13: *The real and imaginary parts of complex permittivity as a function of frequency for different relaxation models* [17].

In the present thesis, the frequency (1MHz - 1GHz) dependent complex permittivity of KNN based ceramics is analyzed using Havriliak–Negami (HN) function [18],

$$\varepsilon^* = \varepsilon_\infty + \frac{\Delta\varepsilon_j}{(1+(j\omega\tau_j)^\alpha)^\beta} + \frac{\sigma_0}{j\varepsilon_0\omega^s} \qquad (2.21)$$

where, ε_∞ is the high frequency dielectric permittivity, σ_0 is the dc conductivity, ε_0 is the permittivity of vacuum, s is an exponent, $\Delta\varepsilon_j$ is the measure of dielectric relaxation strength, ω is the relaxation frequency, τ_j is the relaxation time of the j^{th} process, and α, β are the symmetric and asymmetric distribution parameters of relaxation time, respectively. The parameters α and β should satisfy the relation $0 < \alpha\beta \leq 1$. In the case of $\alpha = \beta = 1$, the relaxation is Debye type relaxation. If $0 < \alpha < 1$, $\beta = 1$, this relaxation process corresponds to Cole - Cole relaxation, and if $\alpha = 1$, $0 < \beta < 1$ then it corresponds to Davidson-Cole relaxation. The graphical representations of real and imaginary parts of complex permittivity as a function of frequency for different relaxation natures are shown in Figure 2.13. The frequency dependent real and imaginary parts of complex permittivity of KNN ceramics have been analyzed through H–N function using WinFit software program [19].

2.3.7 Ferroelectric measurements

The important property of the ferroelectric materials is the polarization reversal (domain-wall switching) by an application of external electric field, which can lead to development of the hysteresis loop in polarization versus electric field (*P-E*) measurement. The *P-E* loops of the samples were determined using an advanced

ferroelectric test system (M/s aixACCT systems GmbH, TF analyzer 2000) is shown in Figure 2.14. The virtual ground feedback method is used to collect the data, which is realized by a current to voltage converter and enables the highest precision for ferroelectric measurements. The TF Analyzer 2000 consists of a basic unit and measurement modules, which are placed very close to the device under test (DUT), to improve the signal to noise ratio (SNR). The ferroelectric (FE) module consists of three amplifiers with optimum SNR. The measurement frequency is limited by the drive limits of the amplifier. The current amplifier is used to select the current range, and this current range should be close to the current response of the sample during the measurement for the best results. The current response from the material mainly depends on the input parameters such as frequency, amplitude, and sample geometry.

Figure 2.14: *Photographic view of the ferroelectric polarization-electric field tester.*

In order to avoid the electric breakdown in air, the samples were immersed in silicon oil, and the measurements were performed at room temperature using the parameters such as frequency (20 Hz - 25 Hz), hysteresis amplitude (upto 5 kV) and triangular waveform.

2.3.8 Atomic force microscope

Atomic force microscope (AFM) can provide a 3D surface profile of the samples on a nanoscale, by measuring different types of forces between a tip and surface of sample [20-21]. An AFM consists of a tip (short probe) attached to the flexible cantilever,

scanner, controller and signal processing unit. AFM tip scans the sample's surface in raster scanning fashion and it feels the peaks and valleys of surface topography depend on the interactions between the tip atoms and surface atoms.

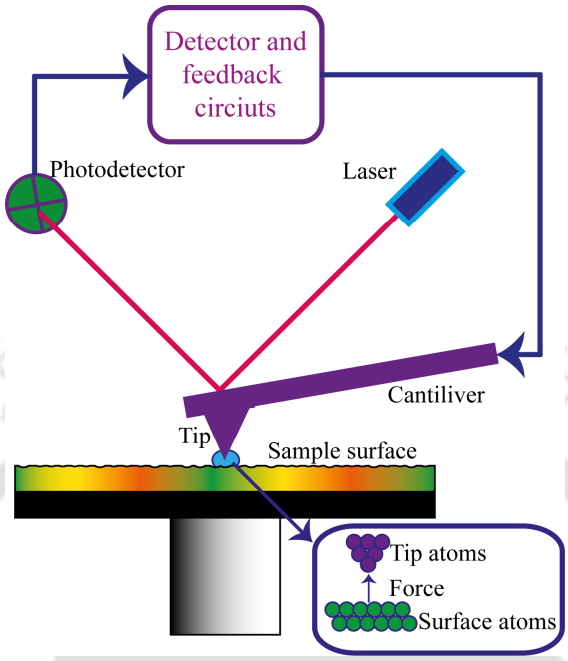

Figure 2.15: *Block diagram of atomic force microscope.*

When the tip is brought in the vicinity of a sample's surface, the Van der Waals forces between the tip atoms, and surface atoms leads to a deflection of the cantilever. This deflection is measured using a laser reflected back from the cantilever to a photo detector (Figure 2.15). The photo detector connected to a feedback electronic circuit, which keep the tip at constant force from the surface. Further, these feedback signals are sent to signal processing unit to generate the 3D topography image along with phase and amplitude.

The static (DC) mode and dynamic (AC) modes are the two different operating modes of AFM [21]. In the DC mode, the cantilever does not vibrate during scanning, whereas in AC mode, the cantilever vibrates at its resonant frequency. Both the DC and AC modes can be operated in contact mode; however, DC mode is often operated as a contact mode. In the contact mode, the interaction between the tip and surface is repulsive, and the force kept constant during scanning by maintains a constant deflection through the feedback circuit. In non-contact mode, the tip hovers above the sample surface, and the tip scans the surface with an attractive Van der Waals force. The AC mode can be either amplitude modulated AFM or frequency modulated AFM. The

resonant frequency, oscillation amplitude, and phases are modified by the forces between the tip and surface, which can provide the typical sample characteristics. In the present thesis, The AFM images of the KNN thin films were obtained using atomic force microscope (M/s Agilent, 5500 series) and image processing was done using WSXM software [22].

2.3.9 Surface profilometer

The rate of deposition and thickness of the films on different substrates was estimated using a stylus profilometers (M/s Veeco Dektak, 6M) and (M/s Veeco Dektak, 150). The photograph of the stylus profilometer being used in the present thesis is shown in Figure 2.16. The stylus profilometer measures the thickness of thin films electromechanically by moving the thin films below a diamond-tipped stylus. A high precision X-Y stage moves the thin films under the stylus according to the given program (Scan length, speed and force), where the stylus is mechanically coupled with the linear variable differential transformer (LVDT). As the films moves beneath the stylus, surface variations of films cause the vertical displacements in the stylus. These vertical displacements are converted into electrical signals by LVDT and further the signals are converted to digital format through an analog-to-digital converter, where it can be displayed on the computer screen. The analysis time and resolution can be tuned by the parameters such as scan length and speed, whereas stylus force can be varied to be compatible with different surfaces.

Figure 2.16: *Photographic view of the stylus profilometer.*

2.3.10 Optical characterization

2.3.10.1 Linear optical properties

The linear optical properties of the thin films were calculated using envelope technique [23]. The fundamental optical constants such as linear refractive index (n), absorption coefficient (α), and optical bandgap (E_g) of the thin films were determined from transmission spectra. The spectral transmission characteristics of the films deposited onto transparent substrates measured in the wavelength range of 200 -1500 nm using a UV-VIS-NIR spectrophotometer (M/s SHIMADZU, UV 3101PC).

As shown in the Figure 2.17, a film of refractive index n with the thickness d, deposited onto a transparent substrate having the refractive index n_s and thickness d_s. When the light is incident on the film, then some fraction of an incident is reflected and some fraction is transmitted at the interfaces of air-film, film-substrate, and substrate-air. The reflected and transmitted light may exhibit the interference pattern because the beams originated from a single coherent source.

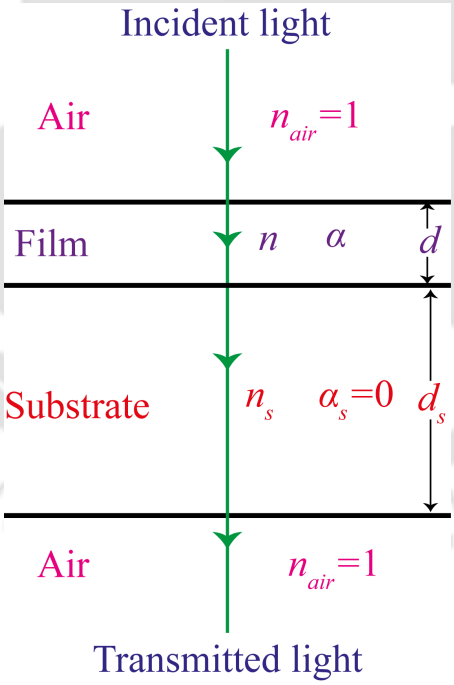

Figure 2.17: *Thin film on a transparent substrate.*

The condition for the constructive interference is,

$$2nd = m\lambda \tag{2.22}$$

where, m is the order of interference, it is an integer for maxima and half integer for minima.

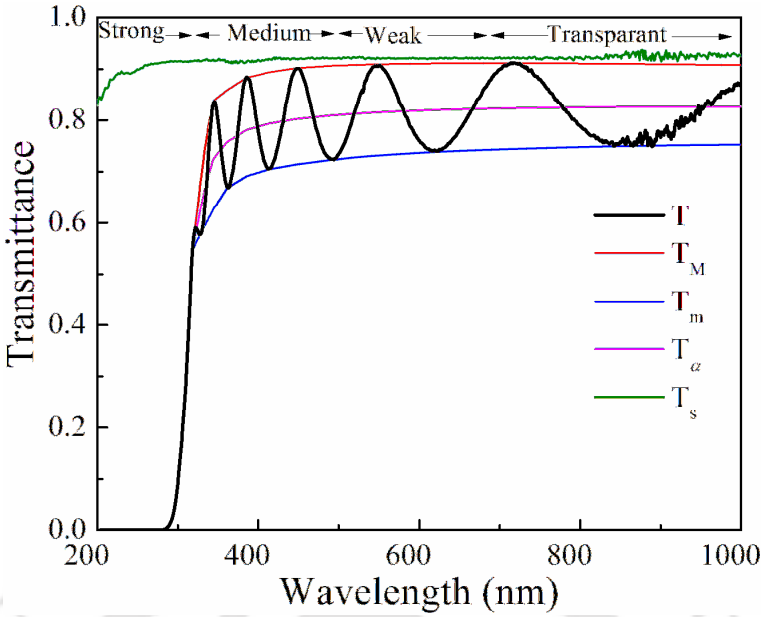

Figure 2.18: *Typical transmittance spectrum of a thin film.*

The typical transmittance spectrum of the film deposited onto a transparent substrate is shown in Figure 2.18. It is assumed that the transmission is a continuously varying function of wavelength; therefore, an envelope can be drawn across the spectrum by connecting the all maxima and all minima.

The expression for the transmittance (T) for normal incidence is given as [23],

$$T(\lambda, n_s, n, d, \alpha) = \frac{Ax}{B - Cx\cos\phi + Dx^2} \tag{2.23}$$

where, $A = 16n^2 n_s$,

$B = (n + 1)^3 (n + n_s)^2$

$C = 2(n^2\text{-}1)(n^2\text{-}n_s^2)$

$D = (n - 1)^3 (n - n_s^2)$

$\phi = 4\pi nd/\lambda$

$x = \exp(-\alpha d)$.

The extreme values of transmission at the constructive and destructive interference fringes are obtained by using the interference condition $\cos\phi = +1$ for maxima (T_M) and $\cos\phi = -1$ for minima (T_m) in equation 2.23.

The refractive index of the films calculated using the following expression,

$$n = \sqrt{N + \sqrt{N^2 - n_s^2}} \tag{2.24}$$

where,
$$N = 2n_s \frac{T_M - T_m}{T_M T_m} + \frac{n_s^2 + 1}{2} \tag{2.25}$$

$$n_s = \frac{1}{T_s} + \sqrt{\frac{1}{T_s^2} - 1} \tag{2.26}$$

If n_1 and n_2 are the refractive indices at two successive maxima (or minima) at wavelengths λ_1 and λ_2, then according to the constructive interference equation,

$$2n_1 d = m_1 \lambda_1 \tag{2.27}$$

and
$$2n_2 d = m_2 \lambda_2 \tag{2.28}$$

by solving the both equations using the rule $|m_1 - m_2| = 1$, then we get thickness of the film using the following expression.

$$d = \frac{\lambda_1 \lambda_2}{2(n_1 \lambda_2 - n_2 \lambda_1)} \tag{2.29}$$

From the Beer-Lambert's law [24],

$$I = I_0 \exp(-\alpha d) \tag{2.30}$$

where, I_0 is the incident light intensity, I is the intensity of the light at wavelength λ, d is the thickness of the film, and α is the absorption coefficient, which can be related to the transmittance as,

$$\alpha = \frac{-\ln T_\alpha}{d} \tag{2.31}$$

where, $T_\alpha = (T_M T_m)^{0.5}$.

Further, knowing the values of α, the optical bandgap (E_g) of the films can be calculated using the Tauc relation [25],

$$(\alpha h\nu)^m = B(h\nu - E_g) \tag{2.32}$$

The E_g of the films would be obtained from the extrapolated linear portion of $(\alpha h\nu)^m$ versus $(h\nu)$ curve, where $h\nu$ is the incident photon energy, B is a measure of crystalline order, and m determines the type of electronic transition between the valence band and conduction band. In the present thesis, the E_g has been calculated by assuming an allowed direct electronic transition (m=2). The error associated with the measurement of n and d is ±0.02 and ±10 nm, respectively. Further, to know the clear information about the optical bandgap, defects and the quality of the deposited films were characterized using photoluminescence (PL) spectroscopy. The PL spectra of the films were obtained through

thermo-spectronic double monochromator coupled with a GaAs photomultiplier with a conventional photon counting system (M/s AMINOCO-Bowman, series 2).

2.3.10.2 Nonlinear optical properties

The interaction of electromagnetic field such as light with the matter can change either the direction of propagation, spatial profile or transmission of an applied field in the material. According to the light-matter interaction theory, the electric polarization (P) induced by the applied electromagnetic field in the material can be written as [26],

$$P = \varepsilon_0 \chi^{(1)} E + \varepsilon_0 \chi^{(2)} E^2 + \varepsilon_0 \chi^{(3)} E^3 + ... \quad (2.33)$$

where, ε_0 is the vacuum permittivity, E is the electric filed, $\chi^{(1)}$ is the linear susceptibility, $\chi^{(2)}$ and $\chi^{(3)}$ are the second- and third-order nonlinear susceptibilities of the sample, respectively. The second order nonlinear susceptibility ($\chi^{(2)}$) is related to the electro-optic effect, second-harmonic generation, and other sum as well as difference frequency generation. The third-order nonlinear susceptibility ($\chi^{(3)}$) is related to the intensity dependent third order nonlinear effect and third harmonic generation. The intensity dependent nonlinear refraction and absorption are expressed by the following equations [27],

$$\alpha(I) = \alpha + \beta_{eff} I \quad (2.34)$$

$$n(I) = n_0 + n_2 I \quad (2.35)$$

where, α is the linear absorption coefficient, n_0 is the linear refractive index, n_2 is the nonlinear refractive index, β_{eff} is the nonlinear absorption coefficient and I is the intensity of the light (laser) beam.

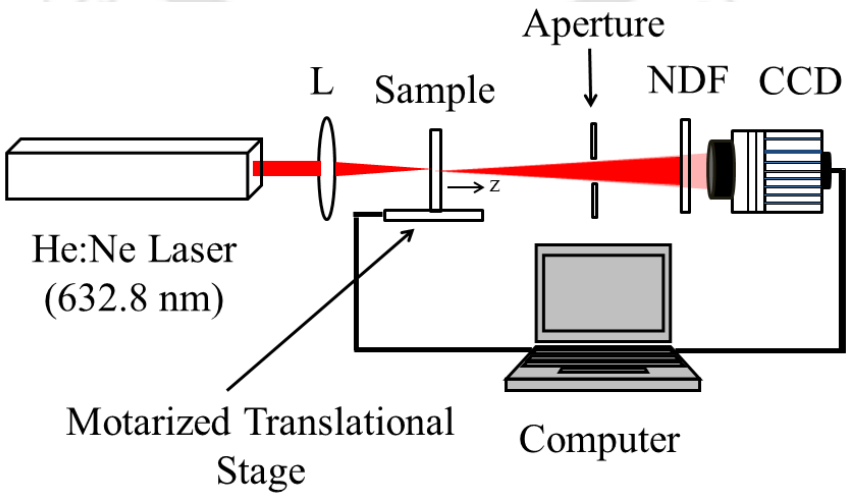

Figure 2.19: *Block diagram of z-scan technique.*

In the present thesis, the nonlinear optical properties of the thin films were measured using modified single beam z-scan technique [28]. This technique relies on the spatial beam broadening and narrowing of the focused Gaussian beam in the far field region as a result of the optical nonlinearity present in the sample. In this technique, sample transmittance is measured as a function of sample position with respect to the focal plane, in the longitudinal direction. As shown in the Figure 2.19, a continuous wave (cw) He:Ne laser (λ = 632.8 nm) beam is focused by a 5 cm focal length lens on to the sample mounted on the motorized translational stage. The sample is translated along the beam propagation direction, and the corresponding transmitted image is recorded using a charged couple device (CCD) camera. A neutral density filter (NDF) of 3.0 optical density (OD) is placed in front of CCD to avoid its saturation. An iris diaphragm of ~6 mm diameter is placed after the sample to avoid the multiple reflected and scattered light entering in the detector. The Rayleigh length (z_0) should have to be much greater than the sample thickness in order to satisfy the thin sample approximation for z-scan. The signals corresponding to the open aperture (OA) and closed aperture (CA) z-scan are simultaneously deduced from the single scanned images obtained from CCD camera. The open aperture z-scan curve obtained from the integrated intensity over the entire image as a function of sample position with respect to focal plane, gives the nonlinear absorption coefficient (β_{eff}). The closed aperture z-scan curve is obtained from the integrated intensity of the partially masked images of open z-scan, by placing a suitable synthetic aperture in the central region through a MATLAB programme. In order to extract the signal corresponding to the purely refractive nonlinearity, the closed aperture signal is divided by the open aperture signal.

The nonlinear absorption coefficient (β_{eff}) and nonlinear refractive index (n_2) are estimated from the following equations [27],

$$T_{open}(z) = 1 - \frac{\beta_{eff} I_0 L_{eff}}{2^{3/2}[1 + (z/z_0)^2]} \tag{2.36}$$

$$T_{Closed}(z) = 1 - \frac{4 n_2 I_0 L_{eff} (z/z_0) k}{[1 + (z/z_0)^2][9 + (z/z_0)^2]} \tag{2.37}$$

where, $T_{Open}(z)$ and $T_{Closed}(z)$ are the normalized open and closed aperture transmittances, respectively. L_{eff} = [1- $exp(-\alpha L)$]/α is the effective thickness of the film, α is the linear absorption coefficient, L is the film thickness, k is the magnitude of the wave vector.

The real as well as imaginary part of the third order nonlinear susceptibilities, $\chi_R^{(3)}$ and $\chi_I^{(3)}$, were evaluated from the following relations [29],

$$\chi_R^{(3)}(esu) = 10^{-4} \frac{\varepsilon_0 {n_0}^2 c^2}{\pi} n_2 (cm^2/W) \tag{2.38}$$

$$\chi_I^{(3)}(esu) = 10^{-2} \frac{\varepsilon_0 {n_0}^2 c^2 \lambda}{4\pi^2} \beta_{eff} (cm/W) \tag{2.39}$$

where, ε_0, c, and λ are the vacuum permittivity, speed of light in vacuum, and wavelength of the laser used, respectively.

2.3.11 Microwave dielectric properties

The split post dielectric resonator (SPDR) technique is a well- established and non - destructive technique for the measurement of complex permittivity of low loss dielectric substrates and thin films at spot frequencies in the microwave region [30 -31]. In the present thesis, the microwave dielectric properties of the films were measured in the frequency range of 5 - 20 GHz using a vector network analyzer (M/s Agilent Technologies, 8722 ES) and (M/s Rohde & Schwarz, ZVA24) by employing SPDR technique. SPDRs are typically operated with $TE_{01\delta}$ mode that has only an azimuthal electric field component, so that the electric field remains continuous across the dielectric interfaces, which makes the measurement insensitive to the presence of air gaps perpendicular to the z-axis of the fixture [31]. In order to compute the resonant frequencies, unloaded Q-factors, and other parameters, the Rayleigh-Ritz method was used. The cross section of a SPDR is shown in Figure 2.20.

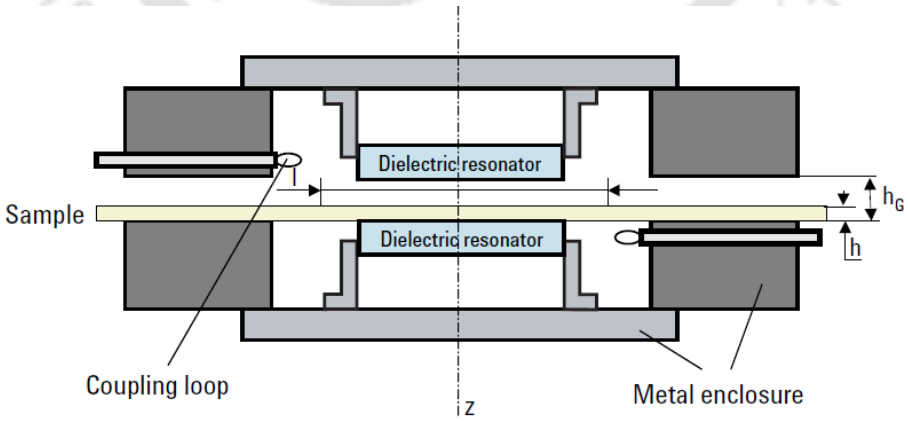

Figure 2.20: *Typical cross sectional view of SPDR fixture* [30-31].

The relative permittivity (ε_r) and loss tangents ($tan\delta$) of the films and substrates are mainly dependent on the resonant frequency and quality factor. In order to extract the

microwave dielectric properties of films alone, the frequency shift and quality factor of the films have to be separated from the overall frequency shift of the film substrate. Therefore, it is necessitated to measure the resonant frequency and quality factor (f_{01}, Q_{01}) of the empty resonator and do the same (f_0, Q_0) with the substrate. After the film deposition, the resonant frequency and quality factor of the (f_s, Q_s) substrate coated with the films have to be measured again. The relative permittivity and loss tangent of the films were calculated based on the thickness and resonant frequencies in iterative method by using following equations,

$$\varepsilon_r = 1 + \frac{(f_0 - f_s)}{h f_0 K_s(\varepsilon_r, h)} \tag{2.40}$$

where, h is the thickness of the film, f_0 and f_s are the resonance frequencies of the bare substrate and film coated substrate of the SPDR. K_s is a slowly varying function of the sample's ε_r and h.

$$\tan\delta = \frac{Q^{-1} - Q_{Dr}^{-1} - Q_c^{-1}}{P_{es}} \tag{2.41}$$

where, Q is related to the unloaded quality factor of SPDR containing dielectric thin film, Q_{Dr} is related to the dielectric losses in the empty resonators, and Q_c belongs to the metal losses for the resonant cavity containing the thin film. The uncertainty in ε_r and $tan\delta$ is estimated as,

$$\frac{\Delta\varepsilon_r}{\varepsilon_r} \le 0.15\% + T\frac{\Delta h}{h} \tag{2.42}$$

where, 1<T<2, and $\Delta tan\delta = \pm 2.0\times10^{-5}$.

2.3.12 Mechanical properties

The mechanical properties such as elastic modulus (E_r) and hardness (H) of the KNN thin films measured using Nanoindenter (M/s CETR, UMT-2). The Oliver – Pharr method was used to calculate the E_r and H of the films from load-displacement (P-h) plot, which is depicted in Figure 2.21.

These E_r and H were estimated using the following equations [32],

$$E_r = \frac{\sqrt{\pi}S}{2\beta\sqrt{A}} \tag{2.43}$$

$$H = \frac{P_{max}}{A} \tag{2.44}$$

where, P_{max} is the maximum indentation load, A is the projected area of contact under load, β is a dimensionless constant that depends on the geometry of the indenter tip, S is the contact stiffness (dP/dh) measured from the slope of the unloaded curve.

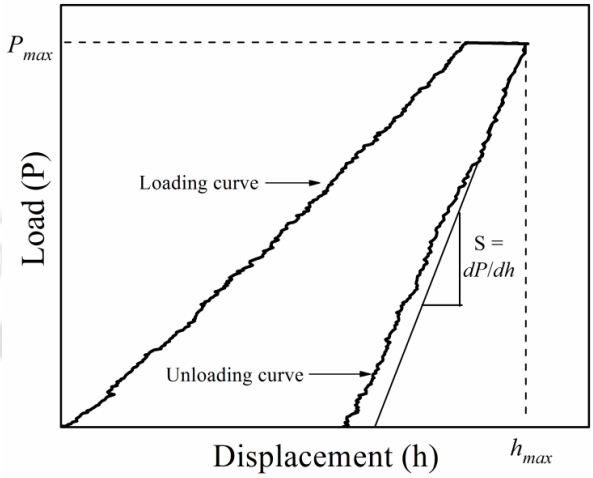

Figure 2.21: *Schematic diagram of indentation load-displacement curve.*

2.3.13 I-V characteristics

Most of the applications of the ferroelectric thin films are based on the application of an external voltage, which can lead to the occurrence of leakage current. The large leakage currents in the films can hide the influence of polarization variation, which cannot be acceptable for the applications in non-volatile ferroelectric memories [33].

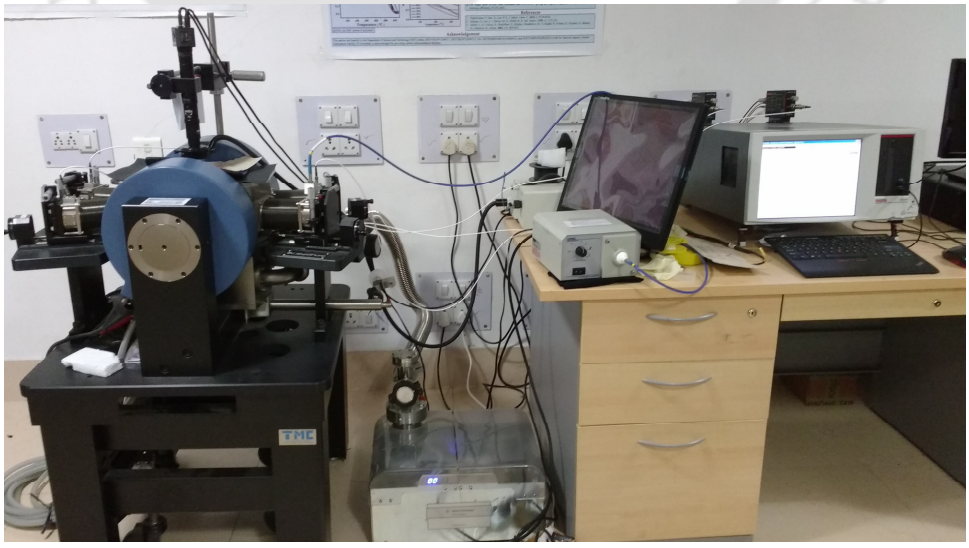

Figure 2.22: *Photographic view of the Keithley 4200 semiconductor systems along with probe station.*

The solutions to decrease the leakage current in the films can be found only if the origin of the conduction is fully understood. Therefore, it is very important to study the charge transport in thin films to identify the conduction mechanisms responsible for the leakage current, when they are subjected to external voltage. In the present thesis, the leakage current characteristics (*I-V*) of the thin films were measured using a parameter analyzer (M/s Keithely, 4200 SCS) connected with a probe station (J Microtechnology LMS 2709 DC), which is shown in Figure 2.22.

2.4 References

[1] M. N. Rahaman, Ceramic Processing and Sintering, *Taylor & Francis* (2003).

[2] A. J. Moulson and J. M. Herbert, Electroceramics: Materials, Properties, Applications, *Wiley* (2003).

[3] S.-J. L. Kang, Sintering: Densification, Grain Growth and Microstructure, *Elsevier Science* (2004).

[4] A. L. Sutuijts, Proc 1st International Conference on Ferrites, *University of Tokyo press*, Tokyo (1971).

[5] M. Barsoum and M. W. Barsoum, Fundamentals of Ceramics, *Taylor & Francis* (2002).

[6] W. D. Kingery, H. K. Bowen and D. R. Uhlmann, Introduction to ceramics, *Wiley* (1976).

[7] P. Sigmund, *Phys. Rev.* **184** [2] (1969) 383.

[8] K. Wasa, M. Kitabatake and H. Adachi, Thin Film Materials Technology: Sputtering of Compound Materials, *Elsevier Science* (2004).

[9] P. J. Kelly and R. D. Arnell, *Vac.* **56** [3] (2000) 159.

[10] W. D. Sproul, D. J. Christie and D. C. Carter, *Thin Solid Films* **491** [1-2] (2005) 1.

[11] M. E. Brown, Handbook of Thermal Analysis and Calorimetry: Principles and Practice, *Elsevier Science* (1998).

[12] B. D. Cullity, Elements of X-ray Diffraction, *Addison-Wesley Publishing Company* (1978).

[13] R. A. Young and R. A. Young, The Rietveld Method, *Oxford University Press* (1995).

[14] C. V. Raman, K. S. Krishnan, *Nat.* **121** (1928) 501.

[15] J. R. Ferraro, Introductory Raman Spectroscopy, *Elsevier Science* (2003).

[16] E. Barsoukov and J. R. Macdonald, Impedance Spectroscopy: Theory, Experiment, and Applications, *Wiley* (2005).

[17] A. A. Lukichev, *J. Non-Cryst. Solids* **358** [3] (2012) 447.

[18] S. Havriliak and S. Negami, *Polym.* **8** (1967) 161.

[19] http://www.novocontrol.de/html/winfit.htm.

[20] G. Binnig, C. F. Quate and C. Gerber, *Phys. Rev. Lett.* **56** [9] (1986) 930.

[21] V. Gupta, Crystal Lattice Imaging Using Atomic Force Microscopy, *INTECH Open Access Publisher* (2012).

[22] I. Horcas, R. Fernandez, J. M. Gomez-Rodriguez, J. Colchero, J. Gomez-Herrero and A. M. Baro, *Rev. Sci. Instrum.* **78** [1] (2007) 013705.

[23] R. Swanepoel, *J. Phys. E: Sci. Instrum.* **16** [12] (1983) 1214.

[24] D. F. Swinehart, *J. Chem. Educ.* **39** [7] (1962) 333.

[25] J. C. Tauc, Optical Properties of Solids, F. Abeles ed. *North-Holland Publishing*, Amsterdam (1972).

[26] R. W. Boyd, Nonlinear Optics, *Elsevier Science* (2008).

[27] M. Sheik-Bahae, A. A. Said, T. H. Wei, D. J. Hagan and E. W. V. Stryland, *IEEE J. Quantum electron.* **26** [4] (1990) 760.

[28] I. Kumar and A. Khare, *Optic. Laser Technol.* **77** (2016) 51.

[29] K. K. Nagaraja, S. Pramodini, A. Santhosh Kumar, H. S. Nagaraja, P. Poornesh and D. Kekuda, *Opt. Mater.* **35** [3] (2013) 431.

[30] J. Krupka, *J. Eur. Ceram. Soc.* **23** [14] (2003) 2607.

[31] J. Krupka, A. P. Gregory, O. C. Rochard, R. N. Clarke, B. Riddle and J. Baker-Jarvis, *J. Eur. Ceram. Soc.* **21** [15] (2001) 2673.

[32] W. C. Oliver and G. M. Pharr, *J. Mater. Res.* **19** [1] (2004) 3.

[33] J. F. Scott, Ferroelectric Memories, *Springer* (2000).

Chapter 3

Synthesis and characterization of pure $(K_{0.5}Na_{0.5})NbO_3$ ceramics and thin films

3.1 Introduction

$(K_xNa_{1-x})NbO_3$ (KNN) based lead-free ferroelectric ceramics and thin films have drawn great attention due to their promising dielectric, ferroelectric, piezoelectric properties and broad temperature range of operation. KNN is a solid solution of ferroelectric $KNbO_3$ and antiferroelectric $NaNbO_3$ having the morphotrophic phase boundaries at x = 0.17, 0.35 and 0.50. The optimum dielectric and ferroelectric properties were obtained for the composition with K = Na = 0.5 [1-2]. The KNN ceramics exhibit the orthorhombic crystal structure at room temperature. The KNN ceramics undergo the structural phase transitions from paraelectric cubic phase to ferroelectric tetragonal phase around 400 ^oC, ferroelectric tetragonal to ferroelectric orthorhombic phase at 200 ^oC, and low temperature orthorhombic to rhombohedral phase at -80 ^oC [3]. The dense KNN ceramics exhibits the dielectric properties of (ε_r = 290, $tan\delta$ = 0.04), Curie temperature (T_C) = 420 ^oC, piezoelectric coefficient (d_{33}) = 80 pC/N, and electromechanical coupling factor (k_p) = 0.29 for the samples prepared by using conventional solid state reaction method [3]. The main disadvantage of the KNN ceramics is the volatilization and hygroscopic nature of the alkali elements, which causes the high leakage current and deteriorates the ferroelectric and piezoelectric properties. In order to compensate the above difficulties, many researchers added excess amount of alkali elements and doped with suitable elements in the A or B site of ABO_3 perovskite structure. The enhanced piezoelectric properties were achieved for the KNN ceramics prepared by using spark plasma sintering was d_{33} =148 pC/N and for the hot pressing techniques d_{33} = 160 pC/N [4-5]. However, these methods are cost-ineffective and are not suitable for the production of a large amount of samples. Hence, the present work demonstrates the preparation and optimization of calcination, sintering temperatures to achieve maximum relative density, best dielectric and ferroelectric properties of KNN ceramics using conventional solid state reaction method. To compensate the volatilization, the surplus amount of Na_2CO_3 was

added. The sample with best dielectric and ferroelectric properties was chosen for the thin film deposition. The processing parameters were optimized to get the single phase KNN thin films deposited by RF reactive magnetron sputtering. The effects of substrate temperature and oxygen mixing percentage (OMP) on crystallinity, microstructure, optical, mechanical and dielectric properties of $(K_xNa_{1-x})NbO_3$ thin films are investigated. The effect of annealing temperature on structural, microstructural, optical, and dielectric properties of the films are also being discussed.

3.2 Experimental procedure

KNN ceramics were prepared by conventional solid-state reaction method from individual high purity powders (>99.99%, M/s Sigma Aldrich, USA) of K_2CO_3, Na_2CO_3, and Nb_2O_5 (99.8%, M/s Nuclear Fuel Complex, India). The starting materials were mixed in accordance with a desired stoichiometry of the KNN ceramics. A planetary ball mill (M/s Fritsch, Pelverisette 6) was used to mix these powders. The powders were mixed with propanol/distilled water, and the mixed powders were dried and calcined at different temperatures (600 ^oC, 700 ^oC, 800 ^oC and 900 ^oC) for five hours. The calcined powders again grounded for 5 hours and are uniaxially pressed into pellets under the pressure of 3000 Kg/cm^2. These pellets were sintered at different temperatures from 950 ^oC to 1050 ^oC for 5h. The sintered pellets were painted with silver paste on both sides to make metal-insulator-metal (MIM) capacitors for the dielectric and ferroelectric measurements.

A homemade KNN ceramic sputtering target was prepared from the optimized conditions using the KBr die, having diameter and thickness of 62 mm and 4 mm, respectively. The KNN thin films were deposited by using RF reactive magnetron sputtering technique onto quartz and $Pt/TiO_2/SiO_2/Si$ substrates. The deposition of the films was carried out at room temperature (RT), 200 ^oC, and 400 ^oC. Prior to the deposition, the chamber was evacuated up to a base pressure of 1.0×10^{-6} mbar and then after the sputtering gas such as mixture of argon and oxygen inserted into the chamber in terms of 0 - 20 standard cubic centimetre per minute (SCCM) or 0 - 100 oxygen mixing percentage (OMP) to get the working pressure of 2×10^{-2} mbar. Initially, KNN thin films were deposited under distinctive OMPs with the RF power of 50 W and estimated the rate of deposition. In order to get the same thickness, the films were deposited at different durations under various OMPs. Further, KNN thin films deposited at 400 ^oC with the RF power 70 W under the working pressure of 1×10^{-2} mbar. These films were annealed at 700 ^oC in oxygen atmosphere.

3.3 Preparation and optimization of processing parameters for KNN ceramics

3.3.1 Thermal analysis of KNN powder

In order to optimize the crystallization temperature of KNN powder prepared by solid state reaction method, the thermal treatment is used. Figure 3.1 shows the change in mass (weight) percentage of KNN powder with the temperature. The overall weight loss of the KNN powder from 30 ^{o}C to 1000 ^{o}C is around 45%. The ~ 6% of weight loss was observed from room temperature to 120 ^{o}C and the corresponding exothermic peak at 120^{o}C is due to the evaporation of water molecules. Further, the weight loss in between 280^{o}C and 570 ^{o}C is about 12%, which causes the exothermic peak at 282 ^{o}C is due to the decomposition and release of CO_2 molecules. It is observed that the maximum weight loss found to be around 27% in the temperature range 570 ^{o}C - 710 ^{o}C and the last exothermic peak observed at 672 ^{o}C is due to the elimination of secondary phases and crystallization of KNN powder. In addition, with increasing the temperature up to 1000^{o}C, no significant mass loss was observed. This indicates that crystallization of the KNN powder was around 700 ^{o}C.

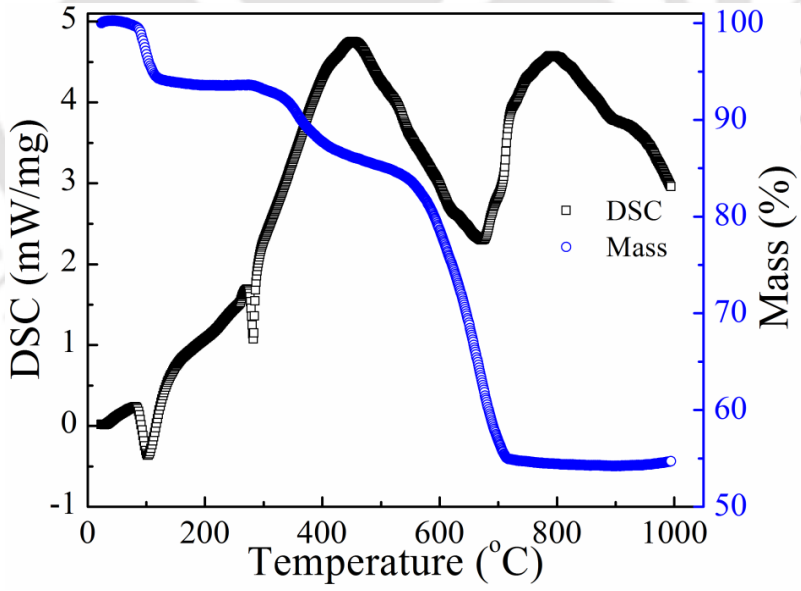

Figure 3.1: *DSC and TGA curves of the KNN powder as a function of temperature.*

3.3.2 Structural analysis

The XRD patterns of the KNN ceramics, calcined at different temperatures for 5 h is shown in Figure 3.2(a). It is observed that all the samples exhibited a single phase

except for the sample calcined at 600 °C. It is also observed that as the calcination temperature increases, the full width at half maximum (FWHM) of all peaks are decreased, and peak position shifted towards lower angle.

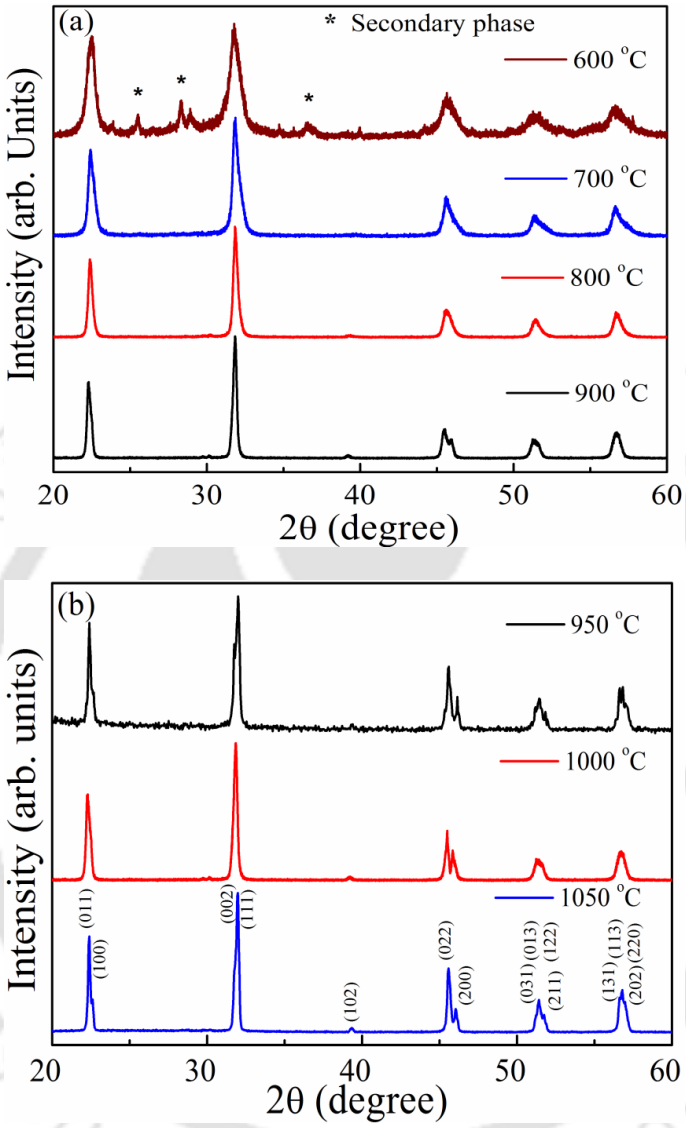

Figure 3.2: *XRD patterns of KNN ceramics (a) calcined at different temperatures and (b) sintered at different temperatures in between 950 °C -1050 °C for 5 h.*

The average crystallite size (D) of the calcined powders was calculated by using Scherrer's equation [6].

$$crystallite\ size\ (D) = \frac{K\lambda}{\beta \cos\theta} \tag{3.1}$$

where, K is the Scherrer's constant (0.89 - 0.94), λ is the wavelength of X-ray used (1.5406 Å), and β is the full width at half maxima (in radians), and θ is the Bragg angle. The average crystallite size found to be increased from 13 nm to 36 nm with the

calcination temperature. Chang *et al.* [7] reported the single phase for the KNN ceramics at 850°C. This shows the importance of mixing initial reagents by high energy milling in reducing the initial particle size and uniform mixing for the low temperature synthesis of KNN ceramics. The smaller particle sizes would accelerate the chemical reaction between the initial reagents and also reduces the reaction temperature and time. Hence, the sample calcined at temperature 700 °C and above, exhibited complete phase formation of KNN. Therefore, the calcination temperature 700 °C was chosen for the further analysis of KNN ceramics. Figure 3.2(b) shows the XRD patterns of the KNN ceramics calcined at 700 °C and sintered at different temperatures for a constant duration of 5 h. All the samples exhibited the orthorhombic phase without any secondary phases, and the peaks were indexed according to the *Amm2* space group. The crystallite size of the sintered pallets was enhanced from 39 nm to 60 nm with increasing the sintering temperature.

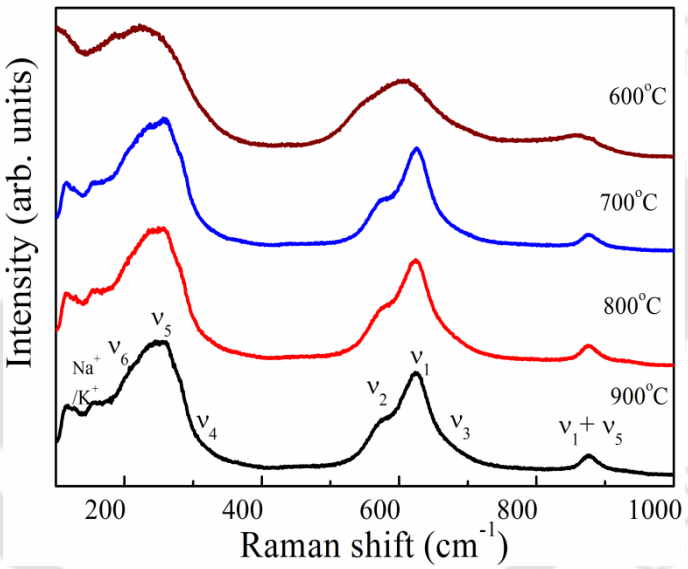

Figure 3.3: *Raman spectra of KNN ceramics calcined at different temperatures for 5 h.*

The Raman spectroscopy is very sensitive to structural deformations caused by impurities or deficiencies of A-site cations and phase transitions. Figure 3.3 shows the Raman spectra of KNN powders recorded at room temperature. The powders calcined above 700 °C, exhibited the orthorhombic phase with a space group *Amm2* and coherent with earlier reports [8-11]. According to the group theory calculations, *Amm2* phase consists of $4A_1+4B_1+3B_2+A_2$ Raman active optical modes. The vibrational modes of NbO_6 octahedron consist of $1A_{1g}(\nu_1)+1E_g(\nu_2)+2F_{1u}(\nu_3,\nu_4)+1F_{2g}(\nu_5)+1F_{2u}(\nu_6)$. Among these vibrations, $A_{1g}(\nu_1)$, $E_g(\nu_2)$, and $F_{1u}(\nu_3)$ are stretching modes and remaining vibrations are bending modes. The region below 200 cm^{-1} correspond to the translational modes of alkaline (K^+ and Na^+/K^+) cations and rotations of the NbO_6 octahedra. It is observed that

all the vibrational modes are present and v_1 and v_5 modes are identified as relatively strong bands due to the near-perfect equilateral octahedral symmetry.

3.3.3 Microstructure and relative density of KNN ceramics

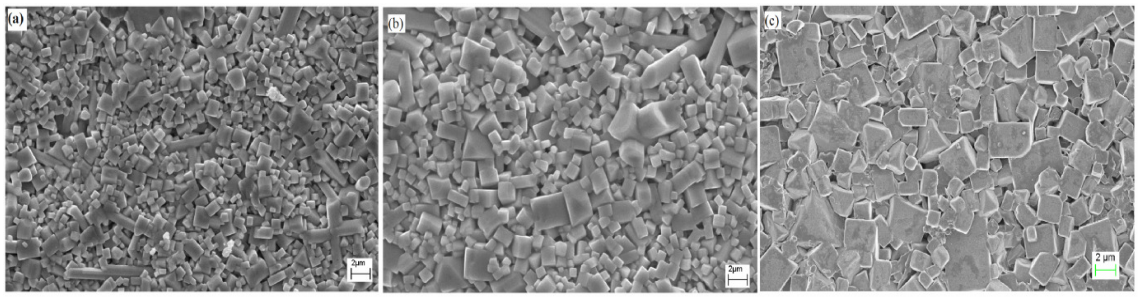

Figure 3.4: *Surface micrographs of KNN ceramics calcined at 700 °C and sintered at different temperatures (a) 950 °C (b) 1000 °C, and (c) 1050 °C for 5 h.*

The microstructures of the KNN ceramics calcined at 700 °C and sintered at different temperatures are shown in Figure 3.4. The sample sintered at 950 °C exhibited the dense microstructure, but a non-uniform structure with an average grain size of 1.55 ± 0.61 µm. The average grain sizes are found to be increased with the sintering temperature and are 1.98 ± 0.59 µm, 2.40 ± 0.80 µm for 1000 °C and 1050 °C, respectively. The relative density of the KNN ceramics measured using Archimedes method and was in the range of 90.4 - 92.2% of the theoretical density (4.51 g/cm^3). The maximum relative density of 92.2% (4.16 g/cm^3) was obtained for the sample sintered at 1050 °C due to the uniform and larger grain size.

3.3.4 Dielectric properties

Figure 3.5 shows the temperature dependent relative permittivity (ε_r) and loss tangent ($tan\delta$) of KNN ceramics calcined at different temperatures, sintered at 1000 °C for 5 h. It is observed that two sharp phase transitions are observed in temperature dependent ε_r curve corresponding to the phase transitions from orthorhombic phase to tetragonal phase around 184 °C and tetragonal to cubic phase at 385 °C, respectively. The phase transition around 184 °C is the ferroelectric phase transition temperature whereas the transition around 385 °C is the ferroelectric to paraelectric transition temperature, which is also called as the Curie temperature (T_C).

It is observed that the KNN sample calcined at 600°C exhibited lowest Curie temperature, low dielectric constant and high dielectric loss attributed to the presence of secondary phases; on the other hand KNN sample calcined at 700 °C exhibited the higher

ε_r and low *tanδ*. Further, with increasing the calcination temperature dielectric properties as well as Curie temperature decreases; this may due to the volatilization of alkali elements. The maximum of relative permittivity at the Curie temperature can be explained by the fact that the softening of the frequency of transverse optical phonon mode [12].

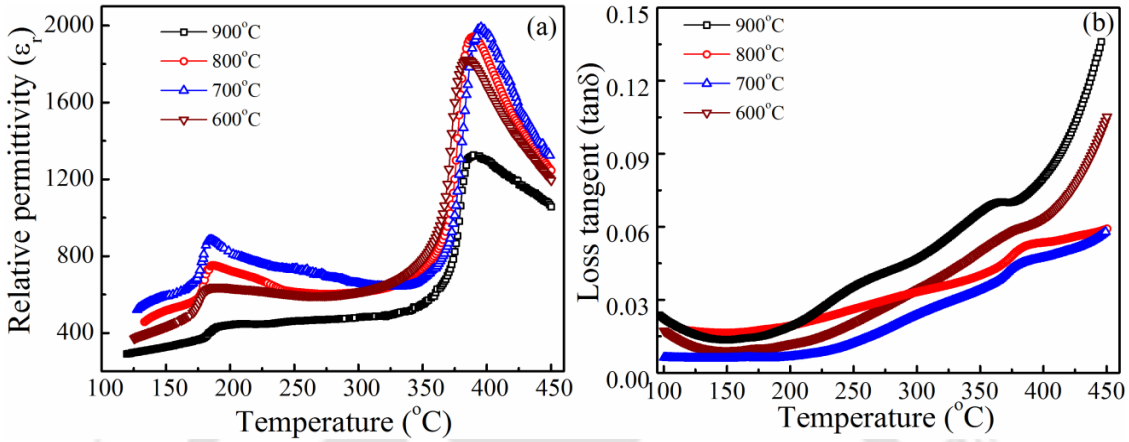

***Figure 3.5**: Temperature dependence of (a) ε_r and (b) tanδ of KNN ceramics calcined at different temperatures, sintered at 1000 °C.*

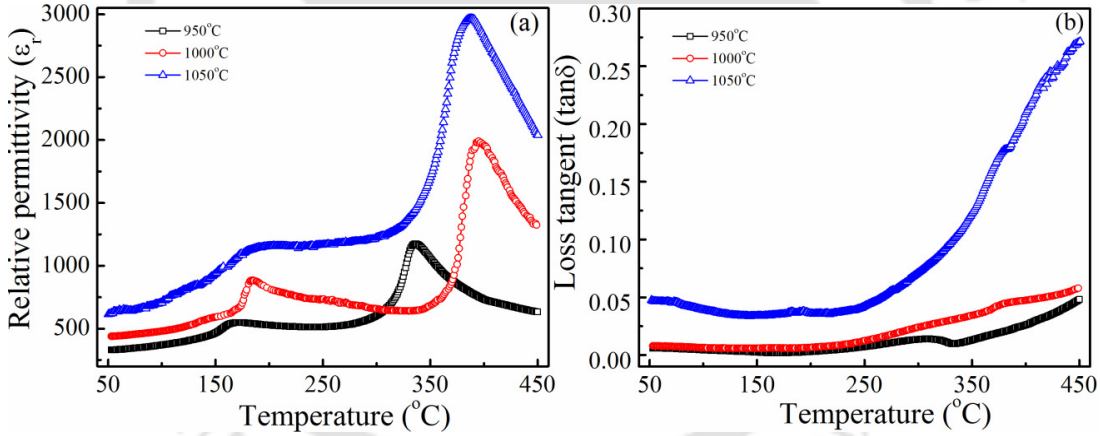

***Figure 3.6**: Temperature variation of (a) ε_r and (b) tanδ of KNN ceramics sintered at different temperatures, measured at 1MHz.*

The temperature variation of ε_r and *tanδ* of KNN ceramics calcined at 700 °C and sintered at different temperatures, measured at 1MHz is shown in Figure 3.6. All the samples have shown the two phase transitions as discussed in earlier section. The Curie temperature of the ceramics increases from 335 °C to 387 °C with the increasing the sintering temperature from 950 °C to 1050 °C. The ferroelectric orthorhombic to ferroelectric tetragonal phase transition temperature also found to be shifted towards high temperature with the sintering temperature. The room temperature ε_r of the ceramics found to be enhanced from 340 to 614 with increasing the sintering temperature. It can be

attributed the higher relative density (92.2%) and larger grain size for the sample sintered at 1050 °C. Lower ε_r and *tanδ* were obtained for the sample sintered at 950 °C and the dielectric loss found to be increased with the sintering temperature. The ε_r, and *tanδ* of the ceramics sintered at 1050 °C are 614 and 0.046, respectively. These obtained dielectric properties of pure KNN ceramics are found to be higher compared to the available reports prepared by solid state reaction method [3].

3.3.5 Ferroelectric properties

Polarization-Electric field hysteresis loops of KNN ceramics were shown in Figure 3.7. The KNN ceramics sintered at 1000 °C and 1050 °C were exhibited the well saturated hysteresis loops as compared to 950 °C sintered sample. The values of remnant polarization (P_r) and coercive field (E_c) of the ceramics sintered at 950 °C were 8.78 μC/cm^2 and 11.01 kV/cm, respectively. The E_c decreases and P_r increases with the increasing of sintering temperature. The P_r and E_c of the ceramics sintered at 1050 °C of KNN ceramics are 9.03 μC/cm^2 and 10.83 kV/cm, respectively. The improvement in the ferroelectric properties of the KNN ceramics sintered at 1050 °C might be due to the higher ε_r, relative density, and improved surface morphology.

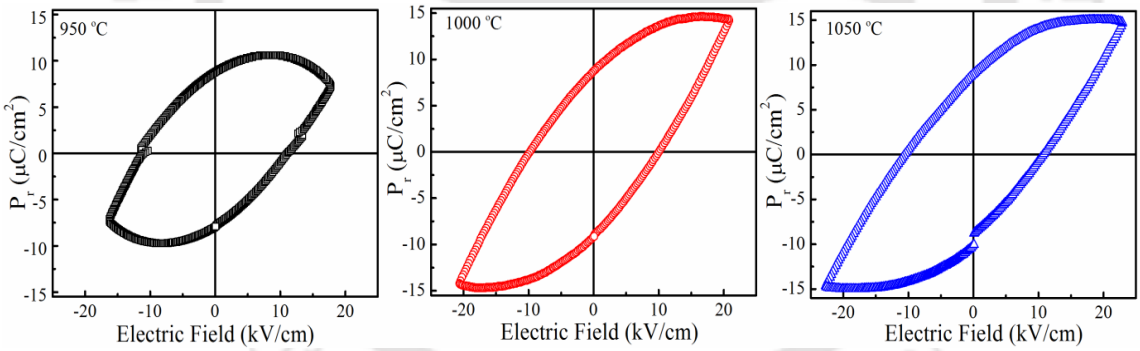

***Figure 3.7**: Hysteresis (P-E) loops of KNN ceramics calcined at 700 °C and sintered at different temperatures, measured at 25Hz.*

3.4 Deposition and characterization of pure KNN thin films

3.4.1 KNN thin films deposited at different substrate temperatures

3.4.1.1 Crystallinity of the films

A series of KNN thin films were deposited at different substrate temperatures (RT, 200 °C, and 400 °C) under different oxygen mixing percentages to know the effect of substrate temperature and oxygen percentage during the deposition. The films deposited at temperatures RT and 200 °C do not show any crystalline nature, whereas the films deposited at 400 °C shown a significant crystallinity. Oxide thin films naturally

grow in the amorphous state, unless the activation energy is given either in the form of temperature or ion bombardment to initiate the crystal growth. To study the effect of OMP on crystallinity, the KNN films were deposited at temperature 400 °C under different oxygen atmospheres.

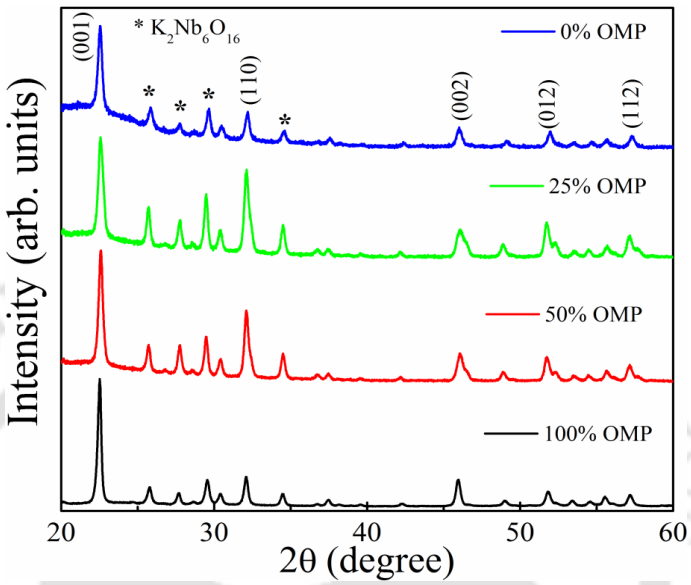

***Figure 3.8**: Room temperature XRD pattern of the KNN films deposited at 400 °C under different OMPs.*

Figure 3.8 depicts the XRD patterns of the KNN films deposited at 400 °C under different OMPs. It is clearly observed that all the films crystallized in perovskite phase with pseudocubic structure along with a considerable amount of secondary phase of $K_2Nb_6O_{16}$ [JCPDS file # 28-0788]. Normally, the subordinate phases $K_2Nb_6O_{16}$ and $K_4Nb_6O_{17}$ forms at lower temperatures as compared to KNN phase and the higher volatilization of Na than that of K could be the another reason [10]. With increasing the OMP in the sputtering gas, the integrated intensity of the (001) peaks of the perovskite enhances and (110) peak decreased. This is due to the lower surface energy of (001) plane as compared to the (110) plane of KNN [13]. In addition, the peak intensities of the $K_2Nb_6O_{16}$ phase found to decrease with increasing the OMP due to the variations in the sputtering yields of K and Na. It is also observed that the FWHM of the (001) peak decreases with an increase in OMP. The estimated average crystallite size was found to be in the range of 21 - 40 nm. A comparative study of the literature suggests that the films fabricated in the present study exhibit better crystallinity even at lower substrate temperature of 400 °C [14-16]. This can be understood as follows: It is generally known that the nucleation of the crystalline phase is determined by the energetic particles

impinging on growing film and large adatom mobility in the films at high substrate temperature, which results in the formation of crystalline or amorphous phase. The presently observed crystallinity at low substrate temperature deposited films indicates the possible combined effect of intrinsic energies of the sputtering process and substrate temperature. Furthermore, the crystallinity of KNN films is found to rise with increasing OMP. This can be correlated to the fact that when oxygen is introduced into the chamber, the sputtered atoms react with oxygen molecules to cause the heat generation and energy redistribution on the surface of the substrate. This process simultaneously promotes migration and crystallization of the sputtered species.

Tian *et al.* [17] deposited the KNN films at different substrate temperatures (680 - 760 °C) by pulsed laser deposition. They observed the presence of $K_2Nb_8O_{21}$ and $K_4Nb_6O_{17}$ as secondary phases along with the KNN phase. Pure KNN phase was observed for the films deposited above 720 °C. Brunckova *et al.* [18] prepared the $(K_{0.5}Na_{0.5})NbO_3$ thin films by sol-gel method on to Pt/Al_2O_3 and $Pt/SiO_2/si$ substrates, and the films were annealed at 650 °C. They observed that the films deposited on Pt/Al_2O_3 are Na rich and exhibit $Na_2Nb_8O_{21}$ as a secondary phase. The composition of the film after annealing has been changed to $(K_{0.65}Na_{0.35})NbO_3$. In addition, it is known to form the $(Na, K)Nb_8O_{21}$ as secondary phases in the KNN based ceramics due to the volatization of K and Na. Further, it is also observed that K rich films form the $K_2Nb_6O_{16}$ whereas Na rich films form the $Na_2Nb_6O_{16}$ as a secondary phase [19]. In this study, the presence of $K_2Nb_6O_{16}$ may be attributed to the excess K. It is important to note that the crystallinity of the secondary phase was very low, and it is practically impossible to do the correct quantitative analysis of the phase composition in the film. Furthermore, the formation of secondary phases depends upon the deposition technique, surface free energy of the substrate and the deposition and annealing temperatures. Moreover, to quantify the weight percentage of the secondary phase is calculated using the following expression [20],

$$W_A = \left\{ \frac{1}{\left[1 + 1.265\left(I_B / I_A\right)\right]} \right\} \times 100 \qquad (3.2)$$

where, I_A and I_B denote the intensities of the strongest reflections of $K_2Nb_6O_{16}$ and KNN phases, respectively. The obtained weight percentage of the secondary phase is listed in

Table 3.1. It was observed that the weight fraction of the secondary phase increase up to 25% OMP and above that it started decreasing.

Table 3.1: *Atomic percentage of the $K_2Nb_6O_{16}$ phase*

OMP (%)	Percentage of the secondary phase
0	4.2
25	5.3
50	3.5
100	2.1

In addition, to see the effect of secondary phase, the lattice parameters and unit cell volume of the sputtering target and the deposited films are calculated and summarized in Table 3.2. It is observed that the lattice constant, and the volumes of the unit cell are found to decrease as compared to bulk KNN ceramics, and the obtained values are in good agreement with the earlier reports [21-22]. These differences in the lattice constants and volume could be due to the compressive stress from the substrate due to thermal expansion during the deposition, slight variations in the composition of the films.

Table 3.2: *Lattice parameters and unit cell volumes of bulk KNN and thin films.*

OMP (%)	*a* (Å)	*b* (Å)	*c* (Å)	*V* (Å)
Bulk	3.9837	3.9674	3.9788	62.8846
0	3.9421	3.9333	3.9402	61.0946
25	3.9361	3.9378	3.9470	61.1790
50	3.9482	3.9286	3.9476	61.2339
100	3.9482	3.9370	3.9391	61.2332

3.4.1.2 Microstructure of the KNN thin films

Figure 3.9 depicts the surface micrographs of the KNN thin films deposited at various substrate temperatures under different OMPs. It is observed that the microstructure of the films significantly changed with the substrate temperature, i.e, the as-deposited films at room temperature and 200 °C under pure oxygen atmosphere shows fine particles morphology with distinct grains of average size less than 50 nm; the morphology of 400 °C substrate temperature deposited films was highly densified along with a homogeneous distribution of particles with average grain size of more than 400 nm.

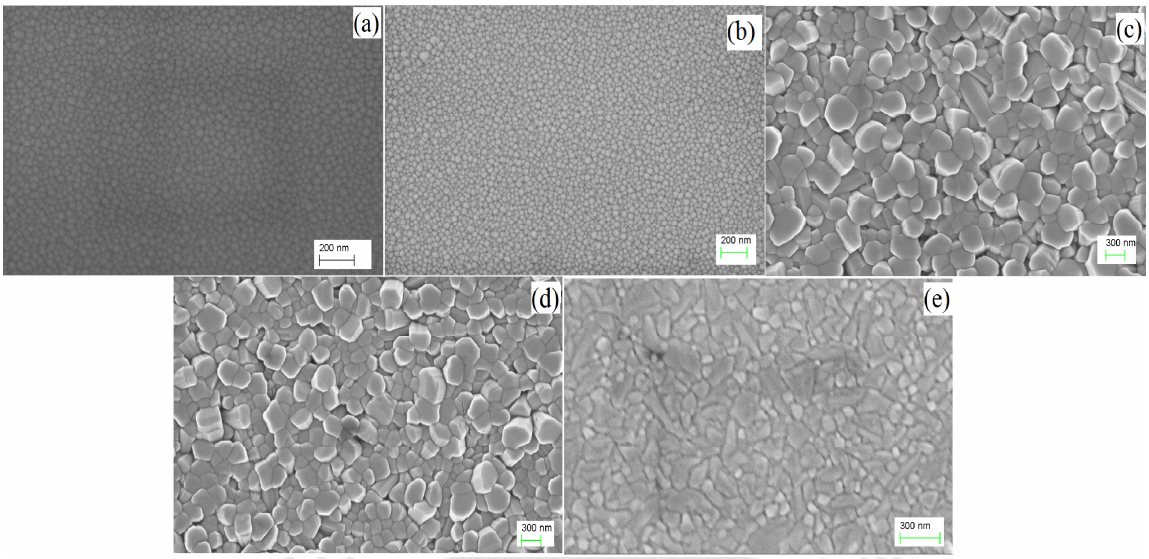

***Figure 3.9**: Surface micrographs of the KNN films deposited under 100%* OMP *at different substrate temperatures (a) room temperature, (b) 200 °C, (c) 400 °C, and (d) deposited at 400 °C under 50% OMP, and (e) deposited at 400 °C under 0% OMP.*

To study the effect of different OMPs on the surface morphology; the micrographs were obtained for the KNN films deposited at 400 °C under different OMPs are depicted in Figure 3.9(c-e). Although the microstructures and the densification of the films deposited at 400 °C under 100% and 50% OMPs are similar, the average particle size is found to decrease to around 300 nm with lowering the OMP from 100% to 50%. Further reducing the OMP to zero, the microstructure of the film is found to be non-uniform with different nature of the particle shape. The average size of the particles reduces down below 150 nm. The improvement in the microstructure and average grain size of the films is attributed to the nucleation, grain growth and crystallinity which are facilitated by the substrate temperature. The results confirm that the deposition temperature and the presence of OMP play a major role on controlling the growth morphology of the KNN films. The films deposited at 400 °C exhibited cuboidal grain shape, which is in agreement with the earlier reports. Tian *et al.* [17] observed the enhancement in the average particle size with increasing the deposition temperature. Li *et al.* [23] observed dense columnar microstructure with quadrangular grains for the RF sputtered KNN films. In order to confirm stoichiometry of KNN films and compositional analysis was performed using EDS spectroscopy. The observed films compositions and the details of the elemental percentages of films grown under different conditions are tabulated in Table 3.3. These results reveal that the compositions of the film are found to be closer to that of

the target, but with a slight richness in K and deficiency in Na. This can be due to the different sputtering yields between Na and K.

Table 3.3: *Elemental composition of the KNN thin films deposited at 400 °C.*

Element	Atomic percentages			
	0% OMP	25% OMP	50% OMP	100% OMP
Na	5.2	5.6	5.4	6.3
K	7.0	7.4	7.7	8.0
Nb	27.0	24.6	26.0	24.3
O	60.8	62.4	60.9	61.4
Composition	$(K_{0.35}Na_{0.26})Nb_{1.35}O_{3.04}$	$(K_{0.37}Na_{0.28})Nb_{1.23}O_{3.11}$	$(K_{0.38}Na_{0.27})Nb_{1.29}O_{3.04}$	$(K_{0.40}Na_{0.31})Nb_{1.21}O_{3.07}$

3.4.1.3 Optical properties of KNN thin films

Figure 3.10(a) displays the transmittance curves of the KNN films deposited at different substrate temperatures. It is observed that the films deposited at RT and 200 °C exhibited higher transmittances as compared to the film deposited at 400 °C. Furthermore, the transmittance of the KNN films deposited at 400 °C decreases with increasing OMP (Figure 3.10 (b)).

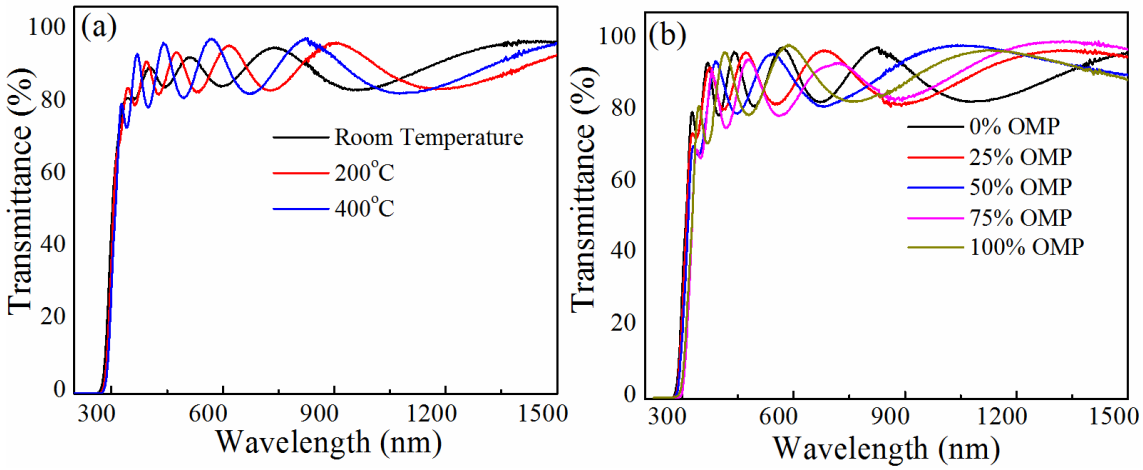

Figure 3.10*: Transmittance spectra of KNN thin films (a) deposited at different temperatures under Pure Ar atmosphere and (b) deposited at 400 °C under different OMPs.*

The reduction in transmittance with increasing OMP and deposition temperatures can be due to higher scattering of light by the large sized particles as observed in SEM micrographs. It has also been observed that the transmittance spectra of the films are

almost coincides with the transmittance spectrum of the substrate, which indicates that the deposited KNN thin films are promising for optical applications. The transmittance curves of the films displayed the interference fringes, which originates due to the interference at the air and substrate-film interfaces. The decrease in transmission and disappearance of fringes at lower wavelength is due to fundamental absorption of the films.

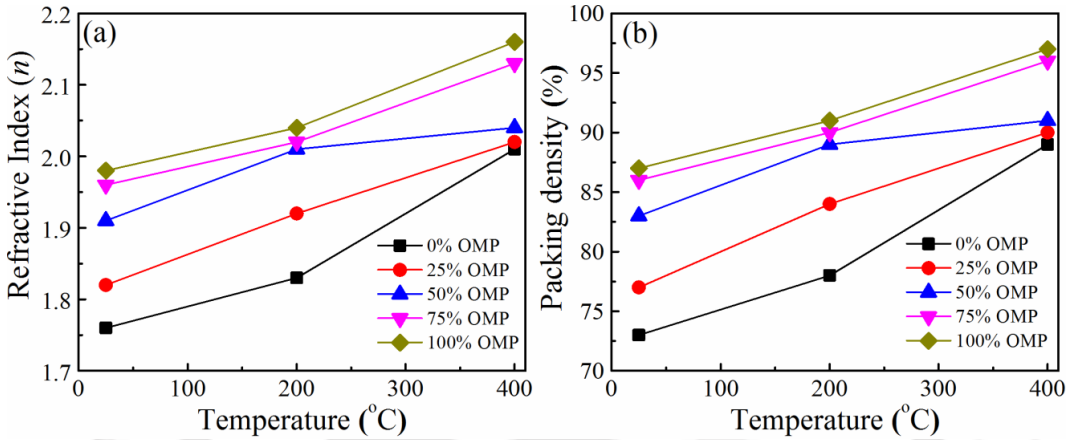

***Figure 3.11**: Variation in the (a) refractive index and (b) packing density of the KNN thin films deposited at different substrate temperatures under various OMPs.*

The optical constants were calculated by using Swanepoel's envelope method [24]. The refractive index (n) of the films was calculated using the equation 2.24. After knowing the refractive index values, the packing density of the films was calculated by using following equation [25],

$$P = \left(\frac{n_f^2 - 1}{n_f^2 + 2}\right)\left(\frac{n_b^2 + 2}{n_b^2 - 1}\right) \tag{3.3}$$

where, n_b is the bulk refractive index (2.2) of KNN [26] and n_f is the observed film refractive index. The n_f values were calculated in the dispersion-free region (600 nm-700 nm). The thicknesses (d) of the films were found to be in the range of 464 - 498 nm. From the figure 3.11, it has been observed that the refractive index rises linearly with increasing substrate temperature and OMP. A similar behaviour has been observed for packing density of the films as well. The observed values of refractive index for the films deposited at RT and 200 °C were in the range of 1.76 – 1.98 and 1.83 – 2.05, respectively whereas the packing densities of these films were in between 0.73 – 0.87 and 0.78 – 0.91, correspondingly. On the other hand, the refractive index and packing density of the films deposited at 400°C were in the range of 2.02 – 2.17 and 0.89 – 0.97, respectively. The

inferior values of *n* at lower substrate temperatures (RT and 200 °C) can be correlated to the amorphous nature and low adatom mobility of the films. At higher substrate temperature 400 °C, the nucleation and improved grain growth was observed due to the higher adatom mobility. In addition, the enhancement in the densification and crystallinity of the films leads to an increase in the refractive index. Extinction coefficient indicating a fraction of light lost in scattering and absorption per unit distance in a participating medium was estimated and found to be on the order of 10^{-3} to 10^{-4}. These values indicate that the presently investigated films exhibit low optical loss.

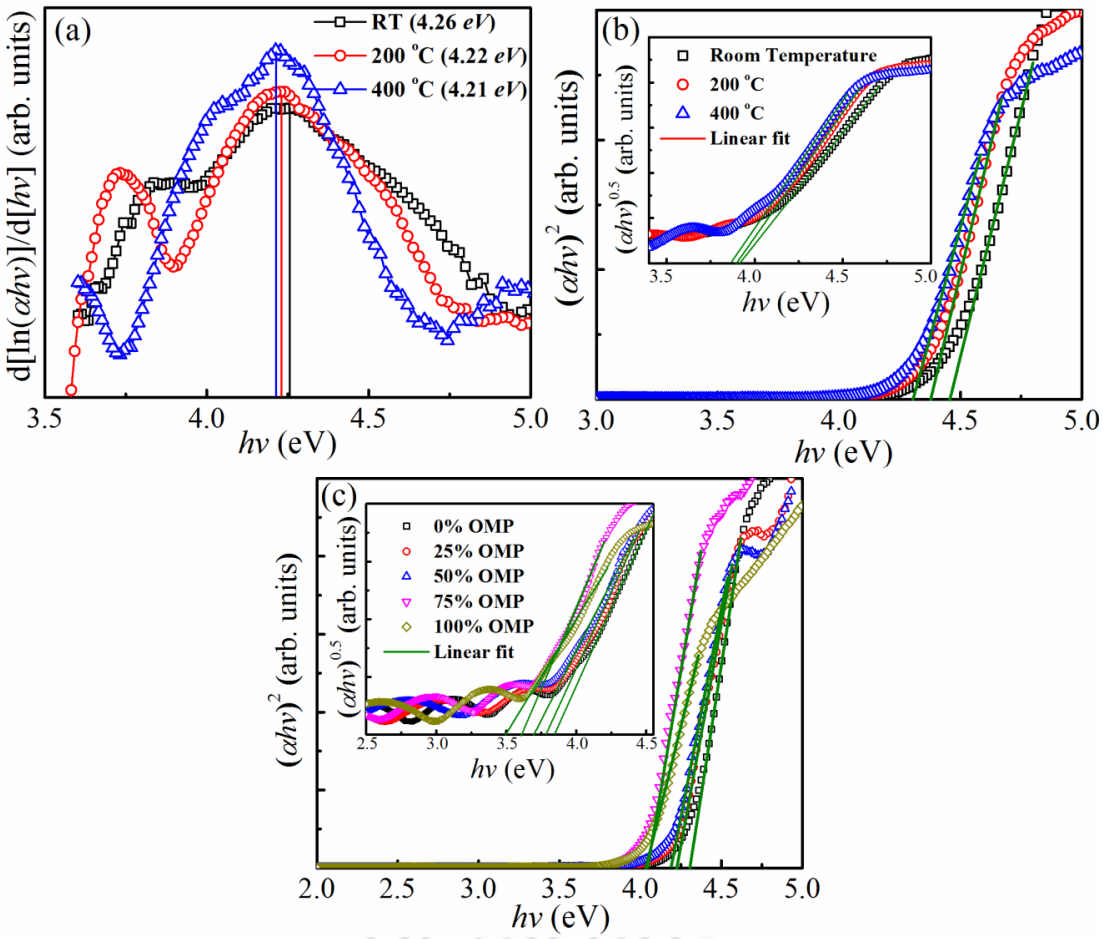

***Figure 3.12**: Variation in the (a) d[ln(αhv)]/d[hv] versus hv curve, direct bandgap absorption edges of the KNN thin films (b) deposited at different temperatures, and (c) deposited at 400 °C under different OMPs. (Inset shows the indirect bandgap curves)*

The optical bandgap (E_g) of the films obtained from the extrapolated linear portion of $(\alpha hv)^m$ versus (hv) curve, where hv is the photon energy, B is a measure of crystalline order and absorption coefficient α related to the bandgap energy as $(\alpha hv)^m = B\ (hv\text{-}E_g)$ [27]. From this relation, the allowed direct and indirect electronic transitions between the valance band state (O_{2p}) and conduction band state (Nb_{4d}) by considering the '*m*' value as

2 and 0.5, respectively. For KNN thin films, both the direct and indirect bandgap have been reported [28]. In order to confirm the bandgap of the KNN thin films, we have calculated the both the bandgap energies and compared with the bandgap estimated from the maximum value of the $d[\ln(\alpha hv)]/d[hv]$ versus hv curve (Figure 3.12(a)). The maximum value of the curve is good approximation for the optical bandgap of the material. Using this method, the obtained bandgap values of the films deposited at different temperatures under the pure argon plasma were in the range of 4.21 - 4.26 *eV*. The absorption edges of the KNN films estimated by using Tauc's relation were shown in Figures 3.12(b) &(c). The bandgap values regarding $m = 2$ ($m = 0.5$) calculated for the films deposited at temperatures RT, 200 ^{o}C, and 400 ^{o}C under pure argon plasma are 4.42 *eV* (3.89 eV), 4.36 *eV* (3.85 *eV*), and 4.32 *eV* (3.80 *eV*), respectively.

It has been observed that the bandgap energies of the films obtained using $m = 2$ are comparable to the maximum value of the $d[\ln(\alpha hv)]/d[hv]$ versus hv curve. Therefore, the present investigated thin films have direct bandgap. The direct bandgap values of the films deposited at 400 ^{o}C under various OMPs were in the range of 4.03 – 4.32 *eV*. While the indirect bandgap values of the films deposited at room temperature, 200 °C, and 400 ^{o}C films were in the range of 3.55 – 3.89 *eV,* 3.5 – 3.85 *eV,* and 3.47 – 3.8 *eV*, respectively. The decrease in optical bandgap (red shift) with higher substrate temperatures and OMP is attributed to the increase of intermediary energy levels within the bandgap, increase in crystalline nature as observed in XRD patterns and the improvement in the surface morphology and grain size of the films. Consequently, the optical constants were heavily influenced by the deposition temperature and OMP.

Photoluminescence (PL) is the light-matter interaction, which emits the light after absorption of photons. It is generally known that the intensities of the PL spectrum provide the information about the optical bandgap, defects and the quality of the deposited films. In order to investigate the effects of substrate temperature and OMP, PL spectra were obtained for all films. Figure 3.13 illustrates the PL spectra measured at room temperature in the wavelength range of 300 – 550 nm with excitation wavelength 280 nm for the films deposited at various substrate temperatures under 100% OMP. Every spectra exhibited a distinctive peak around 340 – 355 nm which corresponds to a near shortest visible blue emission. Furthermore, the characteristic peak exhibits a slight shift in the peak position with the variation in OMP and substrate temperature. This can be correlated to the grain growth in the films. It is well-known that the PL peak intensity,

peak width and shift are strongly depended on the films' density. With increasing OMP and deposition temperature, the particle size becomes larger and the ratio of the surface area to volume decreases, leading to a reduction in oxygen vacancies of the films. Hence, the films tend to be more compact with fewer defects, which cause the decrease in intensity and line width.

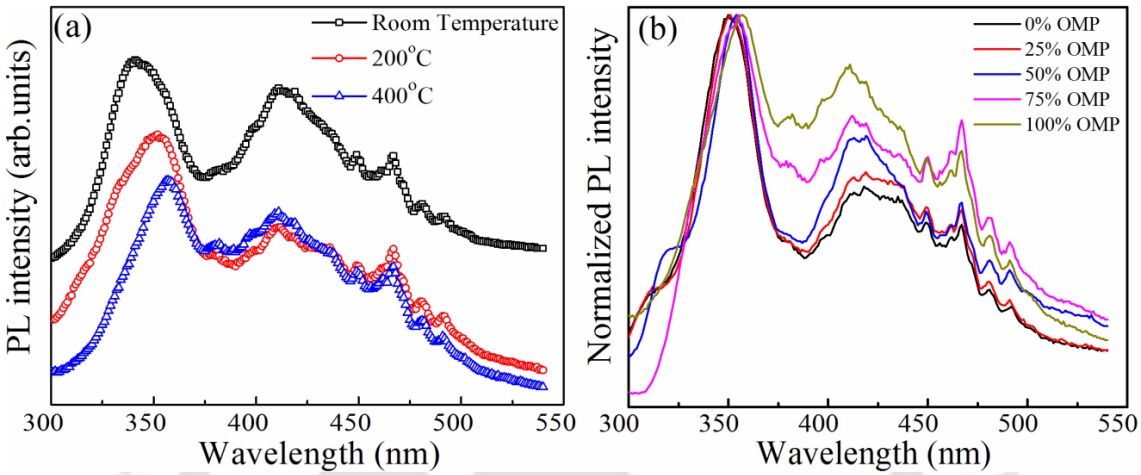

***Figure 3.13**: PL spectra of the films (a) deposited at different substrate temperatures, and (b) deposited at 400 °C under various OMPs.*

3.4.1.4 Mechanical properties of KNN thin films

Figure 3.14 depicts the variations in hardness and elastic modulus of the KNN films deposited under different OMPs as a function of different substrate temperatures. The indentation depth was set as 0.1 times the film's thickness. It is seen that both the hardness and elastic modulus improve with increasing deposition temperature and OMP.

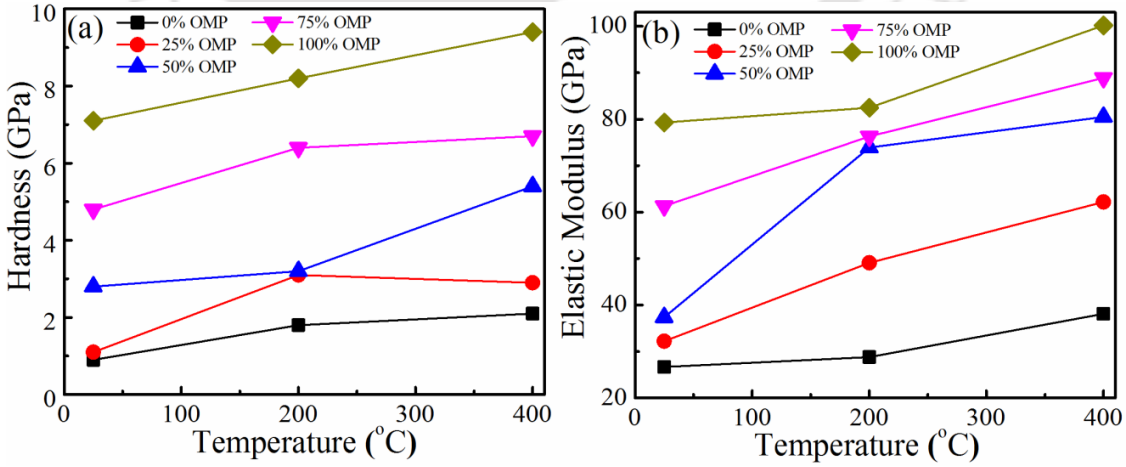

***Figure 3.14**: Variation in hardness and elastic modulus of the KNN films deposited under different OMPs as a function of temperature.*

The hardness of the films deposited at RT, 200 °C and 400 °C was in the range of 0.94 - 7.4 GPa, 1.8 - 8.2 GPa, and 2.1 – 9.4 GPa, correspondingly. Similarly, the elastic modulus of the films deposited at RT, 200 °C, and 400 °C was found to be 26.7 - 79.3 GPa, 29 - 82.5 GPa, 38.1 - 100.2 GPa, respectively. The obtained values of the hardness and the elastic modulus were comparable with those reported values in the literature [15, 18, 29]. The increase in modulus and hardness values with the increase in oxygen percentage may be due to the increase in average particle size/crystallite size. It is interesting to note that films with the average grain size of more than 300 nm exhibited better mechanical properties.

To study the effect of $K_2Nb_6O_{16}$ on the physical properties of KNN films, there is no literature is available on the mechanical properties of this phase. However, it is observed that with an increase in OMP, the weight percentage of the $K_2Nb_6O_{16}$ phase is reduced. The obtained results suggest that both elastic modulus and hardness of the films found to advance with increasing OMP. From the careful literature survey, it was understood that the physical properties of the films strongly dependent on the average particle size of the films [18, 30].

3.4.1.5 Dielectric properties

The above studies reveal that the films deposited at 400 °C under pure oxygen plasma exhibit optimal structural, optical and mechanical properties of films. Hence, a thin film capacitor Ag/KNN/Pt/TiO_2/SiO_2/Si was fabricated using above conditions and characterized.

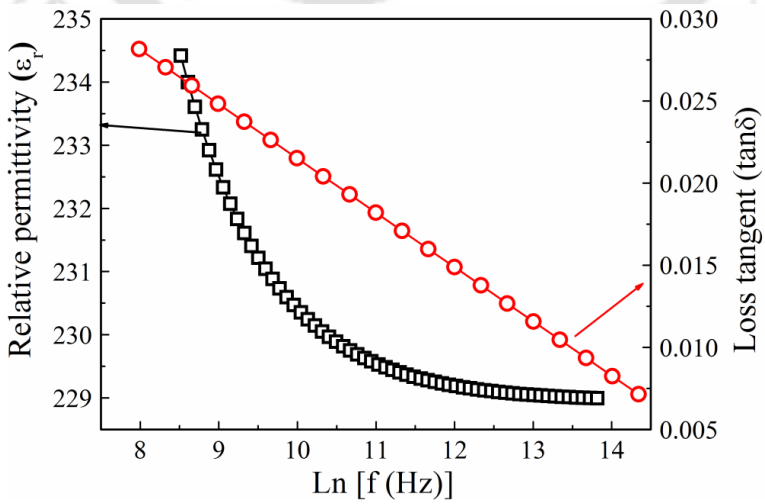

***Figure 3.15**: Dielectric properties of KNN thin films as a function of frequency.*

Figure 3.15 displays the frequency dependence of ε_r and *tanδ* for the thin film capacitor. It was observed that both the ε_r and *tanδ* decrease with increasing frequency and found to be in the range of 234 - 229 and 0.024 - 0.009, respectively. In particular, the obtained ε_r and *tanδ* at 1 MHz were 229 and 0.009, individually. Higher values of ε_r and *tanδ* at low frequencies are due to the contributions from metal electrode and the electrode interfaces. The dielectric dispersion at low frequencies occurs due to the space charges arising from vacancies or charged defects and the structural disorder is likely to be the primary cause for dielectric loss. The defects present in these thin films could constitute a local defect oriented polarization centers/dipoles, which may align themselves in the direction of the field. The observed dielectric properties are in agreement with the earlier reported values [14-15, 31-32]. The improvement of the dielectric properties of the films deposited at higher deposition temperature under moderate OMP can be attributed to the reduction in oxygen vacancies, increase in crystallinity and grain size of the films.

The KNN thin films deposited at 400 ^{o}C exhibited the better structural, microstructural, optical, mechanical and dielectric properties. Therefore, the optimized substrate temperature (400 ^{o}C) of the KNN films was chosen for further investigation.

3.4.2 Phase pure KNN thin films deposited at 400 ^{o}C and annealed at 700 ^{o}C

3.4.2.1 Crystallinity of the films

Figure 3.16(a) shows the XRD patterns of the KNN films grown at 400 ^{o}C under various OMPs. It has been observed that the as-deposited films found to be partially crystalline with the significant amount of secondary phase ($K_2Nb_6O_{16}$). But for the films annealed at 700 ^{o}C (Figure 3.16(b)), $K_{0.5}Na_{0.5}NbO_3$ phase was formed and showed a preferential orientation (100) with psuedocubic perovskite structure due to the lower surface energy of the (100) plane of KNN compared to other planes [13]. The orientation factor (*F*) for the (100) plane of the thin films calculated based on the Lotgering's theory [33],

$$F = (P - P_0)/(1 - P_0) \tag{3.4}$$

$$P = I_{(hkl)} / \sum I_{(hkl)} \tag{3.5}$$

where, *P* is the ratio of the intensity of the interested reflection of planes to the sum of all reflections, and P_0 denotes the equivalent ratio of the target with random orientation. For

the (100) plane, the orientation factor is found to be higher (0.24) for the film deposited under pure argon atmosphere and lower (0.15) for the film deposited with 50% OMP. However, the higher orientation factor did not affect the optical, electrical and dielectric properties of KNN films deposited under pure argon atmosphere, due to the secondary phase ($K_2Nb_6O_{16}$). The $K_2Nb_6O_{16}$ subordinate phase forms at a lower temperature compared to KNN phase, it may be attributed due to the deficiency of Na in the film and the variations in the sputtering yields of the elements. After annealing the films at 700 ^oC, the secondary phase was disappeared with an increase of OMP in the sputtering gas. It may be due to the suppression of volatilization of alkali elements and reduction in the oxygen vacancies.

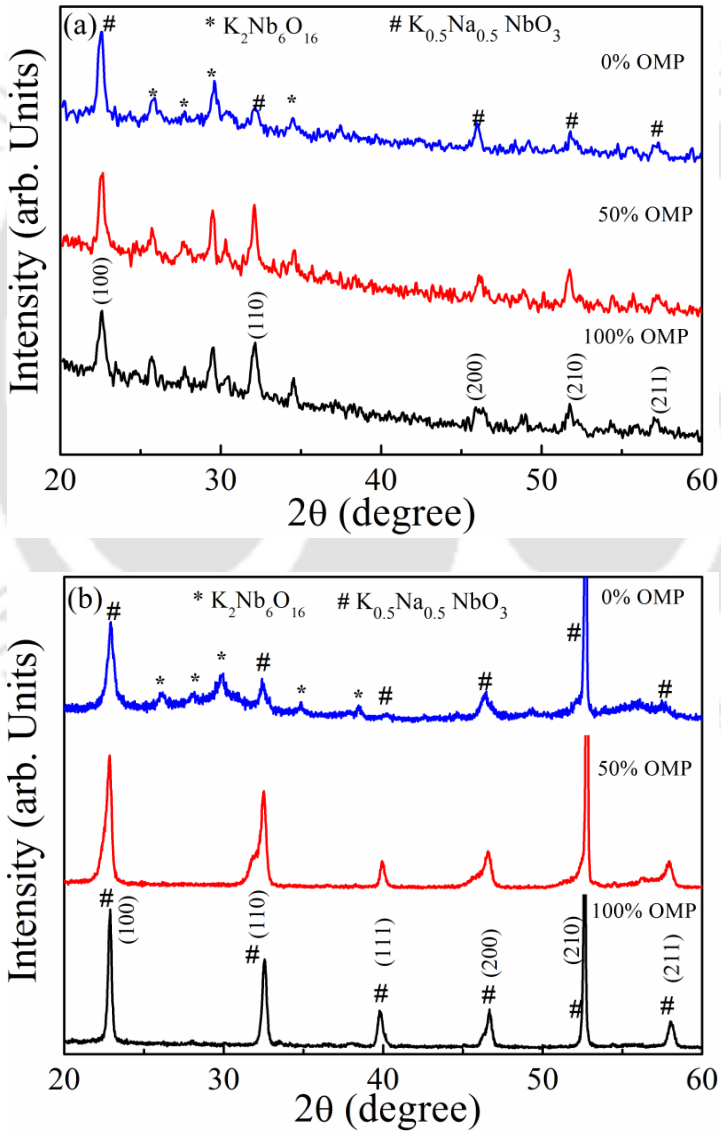

***Figure 3.16**: XRD patterns of (a) as deposited at 400 ^oC and (b) annealed at 700 ^oC of KNN thin films deposited under different OMPs.*

The intensity of all the peaks was found to increase and full width at half maxima of all the peaks decreases with OMP. The average crystallite size was found to increase from 17 nm to 30 nm, whereas strain decreases from 0.003 to 0.002 with an increase of OMP. Based on the XRD peaks (100), (110), (111) and d-spacing, the unit cell parameters and volumes are calculated and listed in Table 3.4. These values are in good agreement with the psuedocubic unit cell parameters (a = 4.0054 Å, b = 3.9551 Å, c = 4.0054 Å) reported by Ishizawa *et al.* [34]. Wiegand *et al.* [21-22] reported the lattice parameter of a = 3.970 Å for KNN thin films prepared by sol-gel process. Tanaka *et al.* [35] reported the lattice parameter of a = 3.910 Å of KNN thin films as pseudo-cubic structure. The slight differences are probably due to the compressive stress from the substrate due to thermal expansion during the deposition process.

Table 3.4: *Lattice parameters evaluated from XRD spectra of annealed KNN thin films deposited under different OMPs.*

OMP (%)	a (Å)	b (Å)	c (Å)	V (Å^3)
0	3.87702	3.93293	3.84414	58.61554
50	3.89041	3.89089	3.94475	59.71224
100	3.88370	3.88830	4.00195	60.43342

3.4.2.2 Surface morphology of the KNN thin films

Figure 3.17 shows the AFM surface morphologies of KNN thin films deposited under different OMPs and annealed at 700 ^oC in oxygen atmosphere. The microstructure of the films deposited with 0% and 50% O_2 was found to be similar with distinct and small circular grains. However, the films deposited in pure oxygen atmosphere exhibited a uniform homogeneous and dense microstructure. The average roughness and root mean square roughness found to be decrease from 7.32 nm to 3.34 nm and 9.06 nm to 4.08 nm with increasing the OMP, respectively. The average grain size also found to be increased from 24 nm to 52 nm with a rise in OMP.

The enhancement in the grain growth may be due to the improvement in crystallization of the films in pure oxygen atmosphere. To confirm the stoichiometry of the films, EDS analysis is performed on the films annealed at 700 ^oC and the chemical compositions listed in Table 3.5. It is observed that a slight deviation in the stoichiometry for the film deposited under pure argon atmosphere. This might be due to the different sputtering yields of Elements Na, K and formation of the secondary phase. As the OMP

increases, the compositions of the films are found to be closer to the target due to the suppression of secondary phase. The chemical composition of the film deposited under pure oxygen is found to be $(K_{0.52}Na_{0.48})Nb_{0.98}O_{3.02}$.

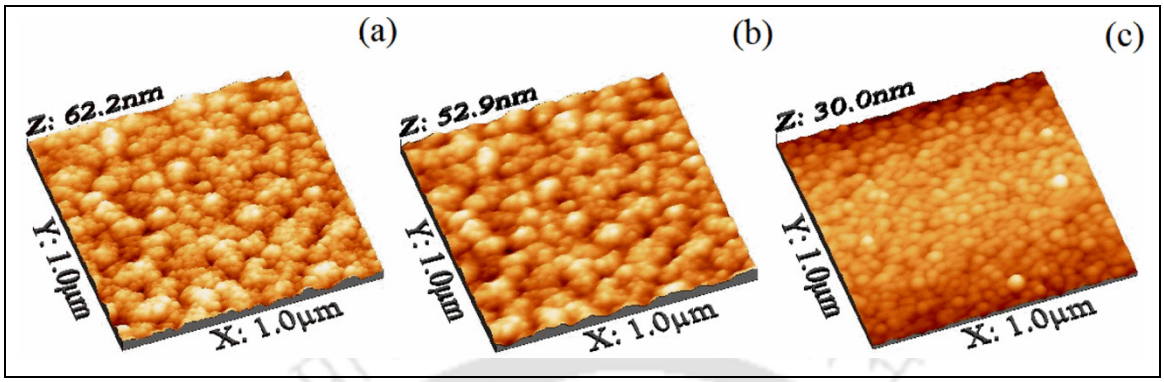

Figure 3.17: *AFM surface micrographs of the KNN thin films deposited at (a) 0%, (b) 50% and (c) 100% OMPs.*

Table 3.5: *Chemical compositions of KNN thin films deposited at 400 ^oC and annealed at 700 ^oC for 1h.*

Element	Atomic Percentages		
	0% OMP	50% OMP	100% OMP
K	7.80	8.96	10.4
Na	6.21	8.02	9.6
Nb	26.09	21.10	19.6
O	59.90	61.92	60.4
Composition	$(K_{0.39}Na_{0.31})Nb_{1.30}O_{2.99}$	$(K_{0.44}Na_{0.40})Nb_{1.05}O_{3.09}$	$(K_{0.52}Na_{0.48})Nb_{0.98}O_{3.02}$

3.4.2.3 Optical properties of KNN thin films

Optical transmittance spectra of KNN thin films deposited on quartz substrates measured in the wavelength range 200 - 1500 nm are shown in Figure 3.18. All the films found to be transparent (>70%) in the visible range and Fabry- Pérot interference behaviour was observed, which are due to the multireflections between air-film and film-substrates. These oscillations arise due to the uniform thickness and plane surface. The transmittance found to decrease to zero in the wavelength range 255 - 275 nm due to the fundamental absorption of the films. The absorption edges show a red shift with increasing the OMP for both as-deposited and annealed films. The optical constants were calculated by using envelope method [24]. The thicknesses of the films were found to be

in the range of 280 - 300 nm and 260 - 290 nm for as-deposited and annealed films, respectively.

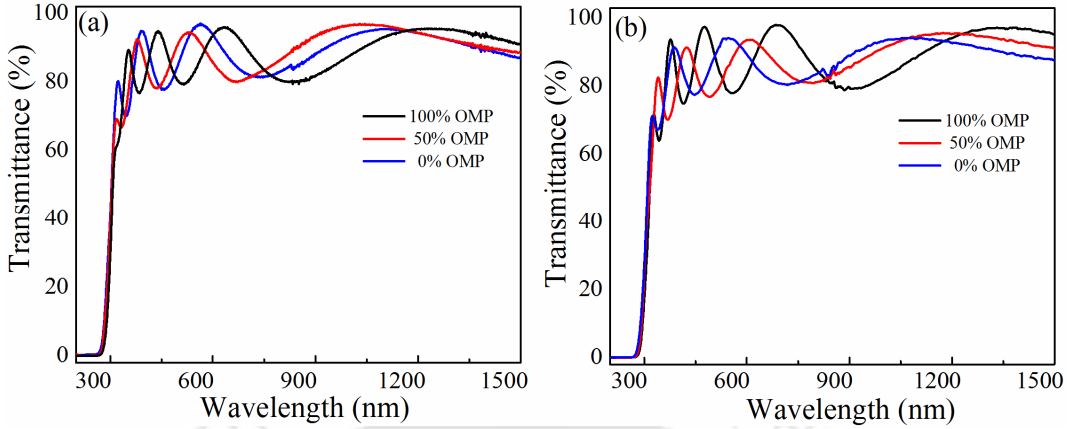

***Figure 3.18**: Transmittance spectra of (a) as deposited and (b) annealed KNN thin films deposited on quartz substrates at different OMPs.*

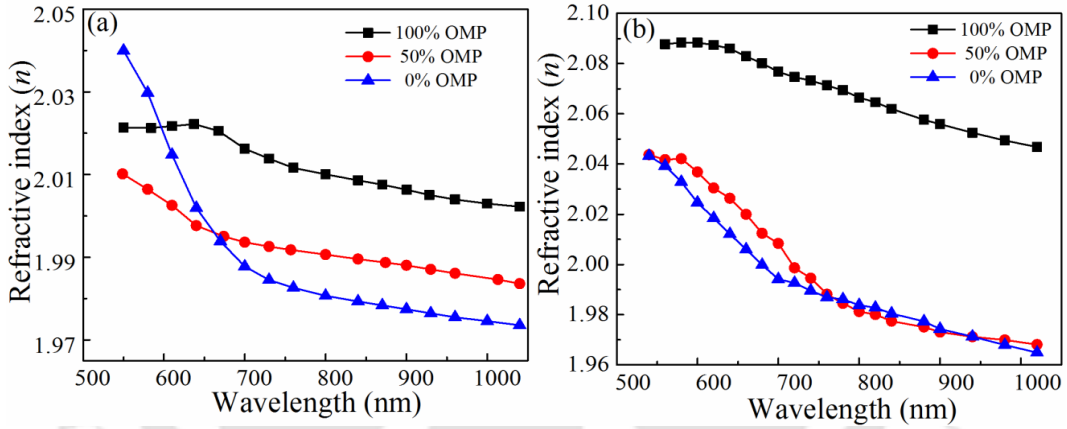

***Figure 3.19**: Variation in refractive index with the wavelength for (a) as deposited and (b) annealed KNN thin films deposited at different OMPs.*

The refractive index (n_{700}) of the as-deposited films found to be increased from 1.98 to 2.01 with increasing the OMP and enhanced from 1.99 to 2.07 for annealed films. Normally, refractive index depends on the packing density, crystallinity of the films, electronic structure, and oxygen deficiencies and A-site atom [36]. In our KNN films, atomic packing density increases with annealing as well as with OMP (Table 3.6). The improvement in the packing density may be due to the reduction in inter-atomic spacing that leads to the densification and also crystallization of the films.

The wavelength dependent refractive index $n(\lambda)$ was shown in Figure 3.19 and is analyzed with single electronic oscillator model [37-38]. According to this model, the material contains of a series of independent oscillators, which oscillates by the incident

light. The refractive index connected to the incident photon energy through the following relation,

$$n^2 - 1 = \frac{S_o \lambda_o^2}{(1 - \lambda_o^2/\lambda^2)} \tag{3.6}$$

where $S_o\lambda^2 = E_d/E_o$ and $E_o = hc/\lambda_o$. The parameters E_o, h, c and λ_o are the average oscillator energy gap, Planck's constant, velocity of light and wavelength, respectively. The dispersion energy E_d and the average oscillator strength S_o which are measure of the strength of the inter band transitions. We have calculated the parameters E_o, E_d, and S_o from the $(n^2\text{-}1)^{-1}$ versus λ^{-2} curves (Figure 3.20) and listed in Table 3.6. In the case of as-deposited films, the larger values of E_d and S_o may be due to the partial crystalline nature of the films. In the case of annealed films deposited under pure oxygen plasma, the E_o, S_o, and E_d values are comparable to six coordinated oxides, which can be attributed to the increase in crystallinity of the films [39].

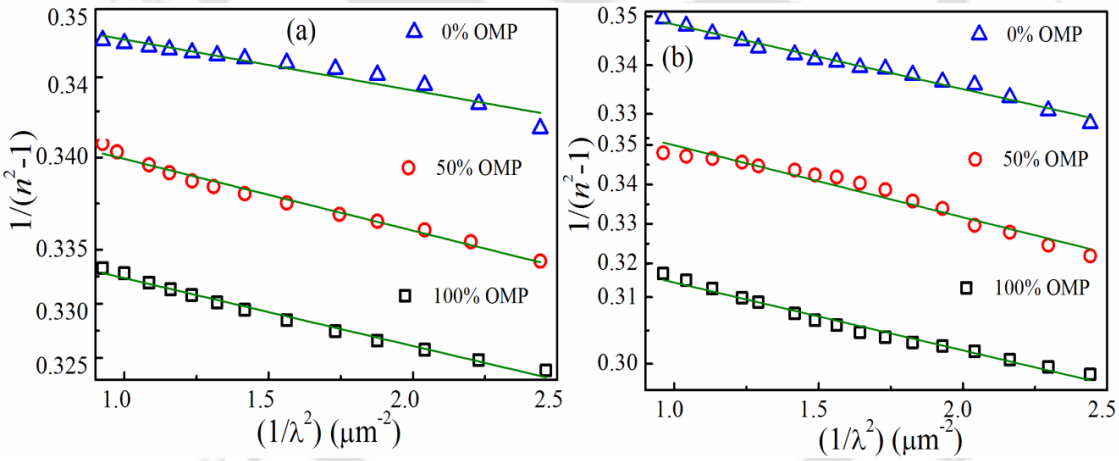

***Figure 3.20**: Fitting of the single oscillator model of KNN thin films deposited at different OMPs.*

***Table 3.6:** Optical parameters evaluated from the single - oscillator model and refractive index, packing density and Urbach energy of KNN thin films deposited at different OMPs.*

OMP (%)	As-deposited films						Annealed films					
	n_{700}	P (%)	E_o (eV)	E_d (eV)	S_o (10^{14} m^{-2})	E_U (meV)	n_{700}	P (%)	E_o (eV)	E_d (eV)	S_o (10^{14} m^{-2})	E_U (meV)
0	1.98	87.9	9.89	27.04	1.74	267	1.99	88.5	6.26	19.66	0.80	260
50	1.99	88.5	10.21	29.52	1.97	265	2.00	89.1	6.17	18.77	0.75	269
100	2.01	89.7	9.15	30.13	1.80	268	2.07	93.1	7.16	22.19	1.03	274

The optical band gap (E_g) of the films has been estimated by assuming an allowed direct electronic transition between the highest occupied state of valence band and the lowest unoccupied state of a conduction band. The absorption edges of as-deposited and annealed films were shown in Figure 3.21. It is observed that the E_g values of the annealed films found to be lower compared to as deposited films and also the E_g values decreases with increasing in OMP both for as-deposited and annealed films. This might be due to the increase of crystallinity and grain size, which leads to change in the intermediate energy levels within the gap [40]. The bandgap values are in the range of 4.34 – 4.40 *eV* and 4.29 - 4.37 *eV* for as-deposited and annealed films, respectively. These bandgap values are comparable to bulk bandgap (4.28 eV) [41] and earlier report [42]. The decrement in the bandgap might be due to the increase in crystallinity, reduction in the oxygen vacancies and improvement in the grain size.

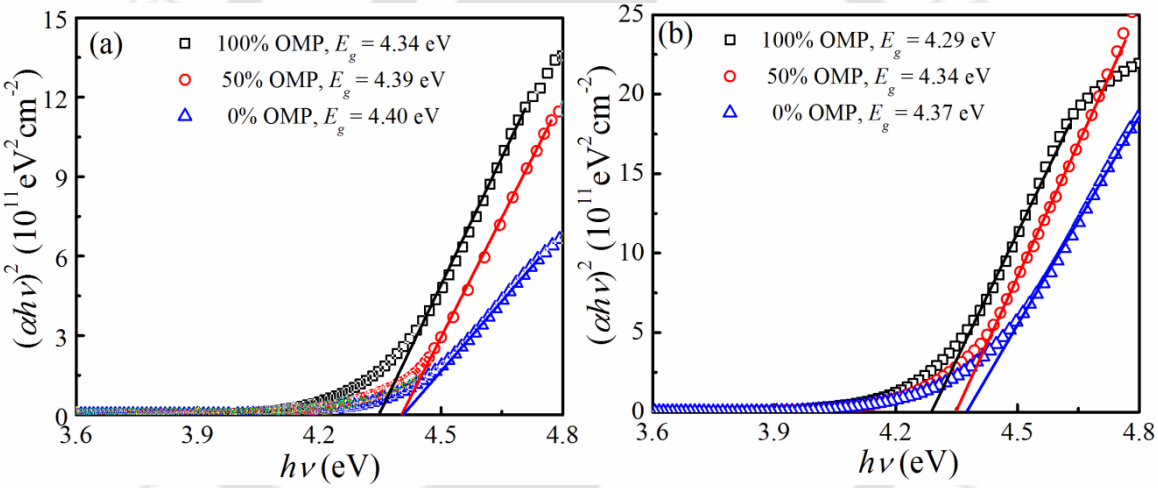

***Figure 3.21**: Absorption edges of (a) as deposited and (b) annealed KNN thin films deposited at different OMPs.*

Photon energy dependent absorption coefficient (α) can be analyzed by using the following equation [38],

$$\alpha(h\nu) = \alpha_0 \exp(h\nu / E_u) \tag{3.7}$$

where, α_0 is the pre-exponential factor and E_u is the Urbach energy, which characterizes the slope of the exponential edge. The Urbach energy values obtained from the slope of the straight line of lnα versuss $h\nu$ graph as shown in Figure 3.22. The lower value (260 *meV*) of E_u is observed for the annealed films deposited in pure argon atmosphere due to the defects induced by the oxygen vacancies and may decrease the redistribution of states

from band to tail. As a result larger optical bandgap and smaller Urbach energy observed. Further with increasing the OMP, E_u found to be increased (274 *meV*) due to the decrease of atomic structural disorder of KNN thin films. For the as-deposited films, the E_u values are in the range 265 - 268 *meV*.

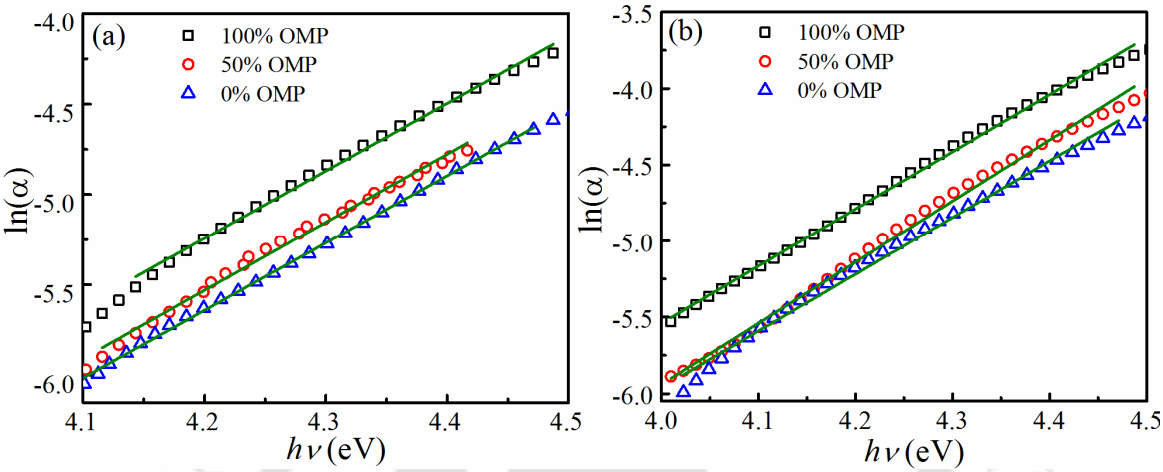

Figure 3.22: *The Urbach plots of (a) as deposited and (b) annealed KNN thin films deposited at different OMPs.*

3.4.2.4 Low frequency dielectric properties of KNN thin films

Figure 3.23 shows the frequency dependent dielectric properties of KNN thin films deposited at 400 ^oC and annealed at 700 ^oC measured in the range of 1 kHz - 1 MHz. The ε_r and *tanδ* for the film deposited in a pure oxygen (argon) atmosphere are 310 (204) and 0.034 (0.33), at 1MHz respectively. The dielectric losses of thin films are found to be in the range 3 - 33% measured at 1MHz, decreases with increasing the OMP. The decrease in the losses and enhancement in dielectric constant with increasing the OMP may be due to the reduction in oxygen vacancies and conductivity within the sample. The improvement of dielectric properties with an increase in OMP may be due to the suppression of volatilization of alkali elements. For comparison, the frequency dependent dielectric properties of as-deposited films are incorporated in the inset of Figure 3.23. It is found that both ε_r and *tanδ* follows the same trend for as-deposited as well as annealed films. In the case of as-deposited films, lower values of ε_r and higher values of *tanδ* are observed, as compared with the annealed films. This may be due to the partial crystalline nature and lesser packing density of the as-deposited films. The dielectric constants of all thin films are found to decrease with the frequency is attributed to the decrease in polarization.

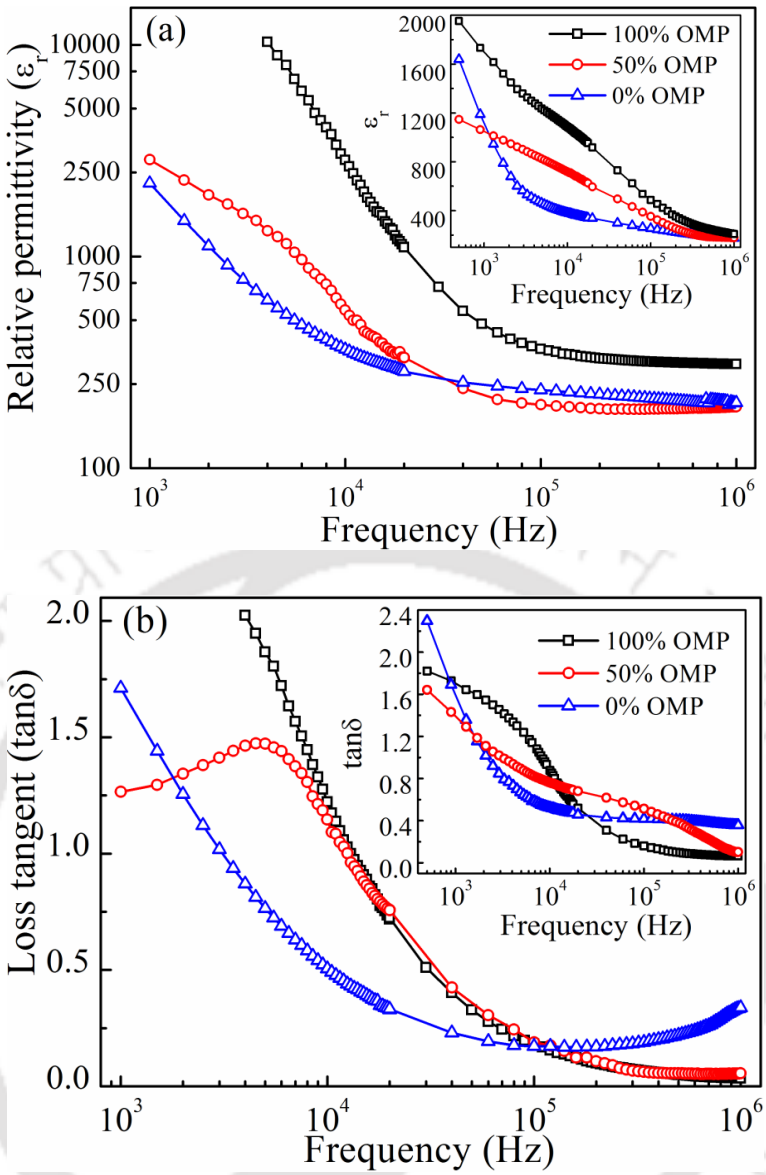

Figure 3.23: *Dielectric properties of KNN thin films measured as a function of frequency.*

Figure 3.24 shows the temperature variation of ε_r and *tanδ* of KNN films measured at 1 MHz. It can be observed that all the films showed the ferroelectric tetragonal to paraelectric cubic transition around 370 ^{o}C, and the film deposited in pure oxygen atmosphere showed the clear ferroelectric orthorhombic to ferroelectric tetragonal transition at 201 ^{o}C. It may be due to the film was well crystallized in KNN phase. The temperature dependent of dielectric properties of as-deposited KNN thin films measured at 1 MHz are shown in the inset of Figure 3.24. In case of as-deposited films, the Curie temperature is found to be in the range 330 ^{o}C - 341^{o}C, which is lower compared to the annealed films. This might be due to the partial crystalline nature of the KNN films. The Curie temperature (T_C) of the films determined based on the maximum of the dielectric

constant, which is found to be slightly lower compared to bulk KNN ceramics [43] and equivalent to earlier reports [29, 44].

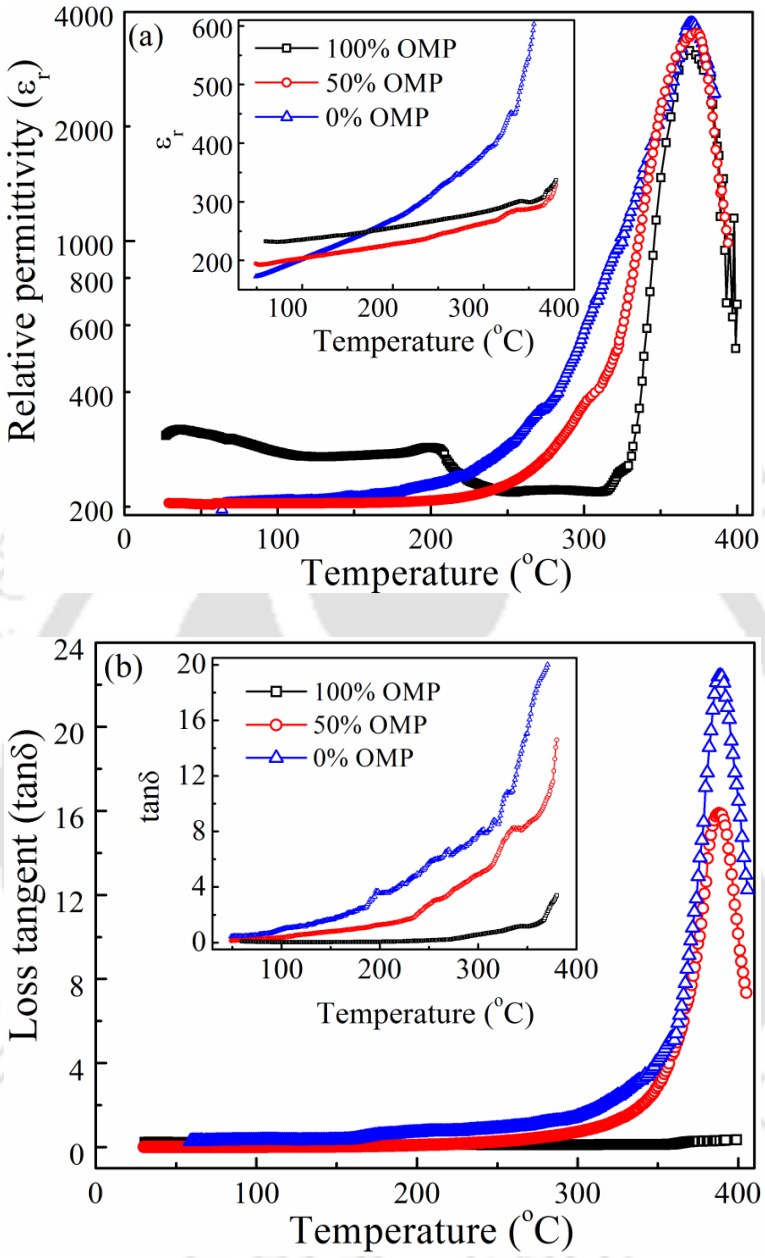

Figure 3.24: *The dielectric properties of KNN thin films measured as a function of temperature at 1MHz.*

According to the Lyddane–Sachs–Teller (LST) relation, the higher values of ε_r near T_C is due to the softening in the frequency of transverse optical phonon [12]. The temperature variation of a *tanδ* also showed the clear anomaly across the Curie temperature. With an increase in temperature, thermal energy facilitates the dipoles to orient in the field direction as a result dielectric constant increases up to Curie temperature, then after decreases due to the change in crystal structure. Further, the

increase in *tanδ* with the temperature is due to the increase in the conductivity in the sample. Across the phase transitions, the disordered domain structure causes the grains to break up and release the charge carriers. Consequently, the conductivity as well as dissipation factor increases. At high temperatures, the release of electrons from the oxygen vacancies could be the reason for higher dissipation factor, which is explained by the following equation [45].

$$O_o \rightarrow O_o \uparrow + V_o^{\bullet\bullet} + 2e^{-1} \tag{3.8}$$

For the film deposited under pure oxygen atmosphere, the variation in the dissipation factor across the phase transition is small compared to the other films due to the reduction in the oxygen vacancies.

3.4.2.5 Microwave dielectric properties of KNN thin films

The microwave dielectric properties of KNN thin films deposited onto quartz substrates measured by using SPDR method [46-47], listed in Table 3.7. The microwave dielectric properties were investigated for as-deposited and annealed KNN thin films at two different frequencies 10 GHz and 20 GHz. The improved ε_r and *tanδ* observed for the annealed films compared to as-deposited films. This might be due to the increase in packing density and refractive index with the annealing as well as higher OMP. On annealing, crystallization occurs by decrease in inter- atomic distance. This may be helpful for the increasing electron charge transfer between cations and oxygen, resulting enhancement of dipoles in the films. This enhancement of dipoles can be responsible for an increase in the polarization [48]. Further, with an increase of frequency from 10 GHz to 20 GHz, the ε_r found to decrease and *tanδ* increases slightly. This might be due to the decrease in the polarization and high conductivity at microwave frequencies.

Table 3.7: *Microwave dielectric properties of KNN thin films deposited on quartz substrates, measured by split post dielectric resonator method.*

OMP (%)	As-deposited				After annealing			
	at 10 GHz		at 20 GHz		at 10 GHz		at 20 GHz	
	ε_r	*tanδ*	ε_r	*tanδ*	ε_r	*tanδ*	ε_r	*tanδ*
0	137	0.0742	130	0.096	238	0.0469	215	0.0499
50	137	0.0612	130	0.0749	244	0.0319	220	0.0370
100	139	0.0295	131	0.0303	287	0.0103	250	0.0133

3.4.2.6 Impedance analysis of KNN thin films

The impedance plots of the KNN thin films annealed at 700 °C in oxygen atmosphere is shown in Figure 3.25. Impedance plot reveals two separate the grain and grain boundary contributions, which appear in the form of semi-circular arcs. All the films exhibit semi-circular arcs over a wide range of frequencies from 100 Hz to 1 MHz. The films deposited under 0% OMP and 50% OMP exhibit one impedance semi-circular arc, which represents the contribution from grain. Nevertheless, the film deposited in pure oxygen atmosphere shows the two semi-circular arcs, which represents the both grain and grain boundary effects presented in the film.

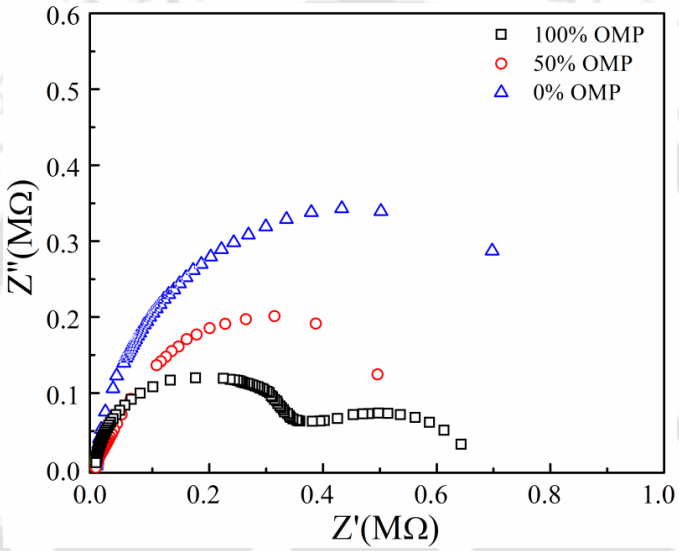

Figure 3.25: *Impedance plots of the KNN thin films deposited under different OMPs.*

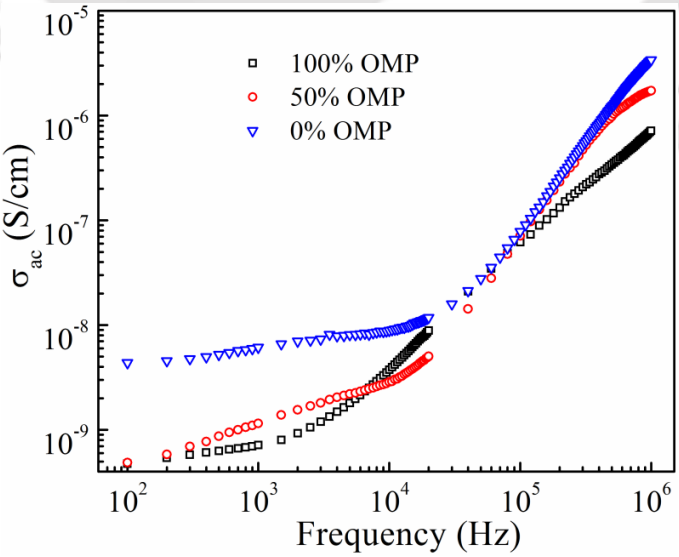

Figure 3.26: *Frequency dependent ac-conductivity of KNN thin films.*

Frequency dependant ac-conductivity of the KNN thin films, annealed at 700 ^{o}C is shown in Figure 3.26. Generally, frequency dependant ac-conductivity can be analyzed by using Jonscher power law. In the present case, it does not seem to follow the simple power law. It can be analysed by using double power law [49-51],

$$\sigma_{ac} = \sigma_0 + A\omega^{s_1} + B\omega^{s_2} \tag{3.9}$$

where, σ_{ac} is the total ac-conductivity and σ_0 is the dc-conductivity arises due to the long-range electrical transport. The exponent s_1 ($0 \leq s_1 \leq 1$) characterizes the low frequency region and corresponds to the grain boundary conductivity corresponding to the translational hopping motion. Whereas the exponent s_2 ($0 \leq s_2 \leq 2$) characterizes the high frequency region and corresponds to the grain conductivity indicating the existence of well localized or re-orientational hopping motion. In this present study, the exponent s_1 has been evaluated in the frequency range 100 Hz – 20 kHz, and the exponent s_2 evaluated between the frequency range 40 kHz -1 MHz. It is observed that the exponent s_1 found to increase from 0.43 to 1.02, whereas the exponent s_2 decreases from 1.52 to 1.36 with increase in OMP. The increment in s_1 with increasing of OMP may be due to the enhancement in the short range hopping process, which corresponds to the grain boundary conduction. Whereas the reduction in s_2 value with an increase in OMP can be attributed to the reduction in charge defects presented in the samples [50-51].

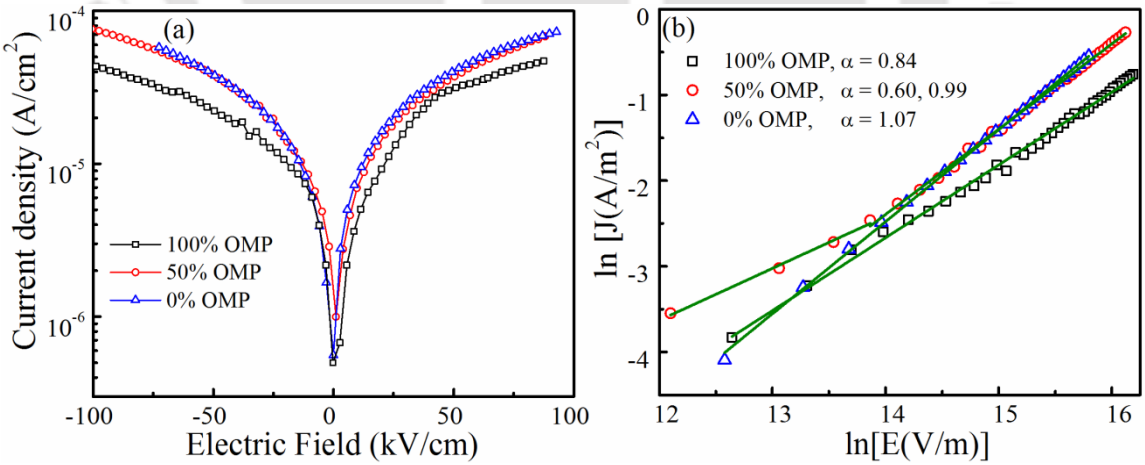

Figure 3.27: *(a) Leakage current density (J) - electric field (E) and (b) ln J- ln E curves of the KNN thin films deposited under different OMPs.*

Figure 3.27(a) shows the leakage current density characteristics of the annealed KNN films measured at room temperature. There is no significant difference in the leakage current density- electric field (*J-E*) curve was observed when the bias field is

reversed. It can be observed that the contacts were ohmic and bulk limited conduction in the films. The low leakage current density (4.98×10^{-7} A/cm^2 at 0 kV/cm) was observed for the film deposited with 100% OMP. It may be due to the fact that higher impedance and reduction in the concentration of the oxygen vacancies by the suppressing the volatilization of alkali elements in the thin-film [52].

The leakage current densities are found to be increased rapidly with rise in the electric field for all the films, and are 3.14×10^{-5} A/cm^2 at 50 kV/cm for 100%, 3.72×10^{-5} A/cm^2 at 50 kV/cm for 50% and 3.98×10^{-5} A/cm^2 at 50 kV/cm for 0% OMP. Normally conduction process in the films mainly determined from ln$J$ – ln$E$ curve. It is observed that Ag/KNN/Pt/Ti/SiO_2/Si follows an ohmic conduction ($J \propto E^{\alpha}$, α ~1) for the both sides. For the negative field, the 'α' value found to be enhanced from 0.84 to 1.07 with decreasing the OMP (Figure 3.27 (b)). The higher slope values can be due to the increase in the concentration of oxygen vacancies.

3.5 Conclusions

- $(K_{0.5}Na_{0.5})NbO_3$ ceramics were prepared by using solid state reaction method.
- The processing parameters such as calcination and sintering temperatures were optimized to obtain the single phase perovskite structure, maximum density, good dielectric and ferroelectric properties.
- The maximum relative density of 92.2%, ε_r of 614, $tan\delta$ of 0.046, P_r of 9.03μC/cm^2 and E_c of 10.83 kV/cm were obtained for the sample sintered at 1050 ^{o}C for 5h.
- The nanocrystalline KNN thin films deposited on quartz and Pt/Ti/SiO_2/Si substrates at distinctive temperatures under different OMP by RF reactive magnetron sputtering technique.
- The films deposited at substrate temperature 400 ^{o}C under pure oxygen plasma and annealed at 700 ^{o}C in oxygen atmosphere exhibited the improved structural, microstructural, optical and dielectric properties.
- The films deposited under pure oxygen plasma and annealed at 700 ^{o}C were crystallized in pure KNN phase without any secondary phases.
- The optical bandgap (4.29 *eV*) with enhanced refractive index (n_{700} = 2.07) was obtained for the annealed KNN thin film deposited under pure oxygen plasma.
- The refractive index dispersion parameters are calculated using a single oscillator model, and these parameters were heavily influenced by annealing as well as with OMP.

- The temperature dependent dielectric properties revealed that the Curie temperature of the films was found to be in the range of 369 ^{o}C – 373 ^{o}C.
- Microwave dielectric constant (*tanδ*) of annealed KNN thin film deposited under pure oxygen plasma was 287 (0.0103) and 250 (0.0133) measured at 10 GHz and 20 GHz, respectively.

3.6 References

[1] G. Shirane, R. Newnham and R. Pepinsky, *Phys. Rev.* **96** [3] (1954) 581.

[2] X. Pang, J. Qiu and K. Zhu, *J. Am. Ceram. Soc.* **94** [3] (2011) 796.

[3] L. Egerton and D. M. Dillon, *J. Am. Ceram. Soc.* **42** [9] (1959) 438.

[4] J.-F. Li, K. Wang, B.-P. Zhang and L.-M. Zhang, *J. Am. Ceram. Soc.* **89** [2] (2006) 706.

[5] R. E. Jaeger and L. Egerton, *J. Am. Ceram. Soc.* **45** [5] (1962) 209.

[6] L. Alexander and H. P. Klug, *J. Appl. Phys.* **21** [2] (1950) 137.

[7] Y. Chang, Z. Yang, X. Chao, R. Zhang and X. Li, *Mater. Lett.* **61** [3] (2007) 785.

[8] K.-i. Kakimoto, K. Akao, Y. Guo and H. Ohsato, *Jpn. J. Appl. Phys.* **44** [9B] (2005) 7064.

[9] Y. Wang, L. Hu, Q. Zhang and H. Yang, *Dalton Trans.* **44** [30] (2015) 13688.

[10] C. W. Ahn, H.-I. Hwang, K. S. Lee, B. M. Jin, S. Park, G. Park, D. Yoon, H. Cheong, H. J. Lee and I. W. Kim, *Jpn. J. Appl. Phys.* **49** [9] (2010) 095801.

[11] R. Singh, K. Kambale, A. R. Kulkarni and C. S. Harendranath, *Mater. Chem. Phys.* **138** [2-3] (2013) 905.

[12] R. H. Lyddane, R. G. Sachs and E. Teller, *Phys. Rev.* **59** [8] (1941) 673.

[13] C.-R. Cho and A. Grishin, *J. Appl. Phys.* **87** [9] (2000) 4439.

[14] B.-Y. Kim, T.-G. Seong, I.-T. Seo, M.-S. Jang, S. Nahm, J.-Y. Kang and S.-J. Yoon, *Acta Mater.* **60** [6-7] (2012) 3107.

[15] V. M. Kugler, F. Söderlind, D. Music, U. Helmersson, J. Andreasson and T. Lindbäck, *J. Cryst. Growth* **254** [3-4] (2003) 400.

[16] H. J. Lee, I. W. Kim, and B. M. Jin, *J. Korean Phys. Soc.* **56** [1] (2010) 417.

[17] A. Tian, W. Ren, L. Wang, P. Shi, X. Chen, X. Wu and X. Yao, *Appl. Surf. Sci.* **258** [7] (2012) 2674.

[18] H. Bruncková, Ľ. Medvecký and P. Hvizdoš, *Mater. Sci. Eng.: B* **178** [4] (2013) 254.

[19] S. Feng, G. Li, L. Li, and X. Li, *Rev. High Pressure Sci. Technol.* **7** (1998) 1362.

[20] T. Asanuma, T. Matsutani, C. Liu, T. Mihara, and M. Kiuchi, *J. Appl. Phys.* **95** [11] (2004) 6011.

[21] S. Weigand, S. Flege, O. Baake, and W. Ensinger, *Bull. Mater. Sci.* **35** [5] (2012) 745.

[22] S. Wiegand, S. Flege, O. Baake and W. Ensinger, *J. Mater. Sci. Technol.* **28** [6] (2012) 500.

[23] T. Li, G. Wang, D. Remiens and X. Dong, *Ceram. Int.* **39** [2] (2013) 1359.

[24] R. Swanepoel, *J. Phys. E: Sci. Instrum.* **16** [12] (1983) 1214.

[25] Y.-F. Kuo and T.-Y. Tseng, Mater. Chem. Phys. **61** [3] (1999) 244.

[26] P. Yongsiri, S. Eitssayeam, G. Rujijanagul, S. Sirisoonthorn, T. Tunkasiri and K. Pengpat, *Nanoscale Res. lett.* **7** [1] (2012) 136.

[27] J. C. Tauc, Optical Properties of Solids, *North–Holland Publishing*, Amsterdam (1972).

[28] G. H. Khorrami, A. Kompany and A. K. Zak, *Adv. Powder Technol.* **26** [1] (2015) 113.

[29] K. Shibata, K. Suenaga, A. Nomoto and T. Mishima, *Jpn. J. Appl. Phys.* **48** [12] (2009) 121408.

[30] F. Helvaci, and J. Cho, *Mater. Res. Soc. Symp. Proc.* 841 (2005) 375.

[31] J. Wu and J. Wang, *J. Appl. Phys.* **106** [6] (2009) 066101.

[32] I. Kanno, T. Mino, S. Kuwajima, T. Suzuki, H. Kotera and K. Wasa, *IEEE Trans. Ultrason. Ferroelectr. Freq. Control* **54** [12] (2007) 2562.

[33] F. K. Lotgering, *J. Inorg. Nucl. Chem.* **9** [2] (1959) 113.

[34] N. Ishizawa, J. Wang, T. Sakakura, Y. Inagaki and K.-i. Kakimoto, *J. Solid State Chem.* **183** [11] (2010) 2731.

[35] K. Tanaka, K.-i. Kakimoto and H. Ohsato, *J. Cryst. Growth* **294** [2] (2006) 209.

[36] D. Bao, H. Yang, L. Zhang and X. Yao, *Phys. Status Solidi (a)* **169** [2] (1998) 227.

[37] M. DrDomenico and S. H. Wemple, *J. Appl. Phys.* **40** [2] (1969) 720.

[38] F. Yakuphanoglu, A. Cukurovali and İ. Yilmaz, *Phys. B: Condens. Matter* **353** [3-4] (2004) 210.

[39] S. H. Wemple and M. DiDomenico, *Phys. Rev. B* **3** [4] (1971) 1338.

[40] K. V. Saravanan, K. Sudheendran, M. G. Krishna, K. C. James Raju and A. K. Bhatnagar, *Vacuum* **81** [3] (2006) 307.

[41] J. Rani, P. K. Patel, N. Adhlakha, H. Singh, K. L. Yadav and S. Prakash, *J. Mater. Sci. Technol.* **30** [5] (2014) 459.

[42] Y. B. Yao, H. T. Chan, C. L. Mak and K. H. Wong, *Thin Solid Films* **537** (2013) 156.

[43] H. Birol, D. Damjanovic and N. Setter, *J. Eur. Ceram. Soc.* **26** [6] (2006) 861.

[44] S. Y. Lee, J. S. Kim, C. W. Ahn, H. I. Hwang and I. W. Kim, *Thin Solid Films* **519** [2] (2010) 947.

[45] F. A. Kroger and H. J. Vink, *Solid State Phys.* **3** (1956) 307.

[46] J. Krupka, *Mater. Chem. Phys.* **79** [2–3] (2003) 195.

[47] A. Rambabu, S. Bashaiah and K. C. James Raju, *J. Mater. Sci.: Mater. Electron.* **25** [3] (2014) 1172.

[48] P. Li, J. F. McDonald and T. M. Lu, *J. Appl. Phys.* **71** [11] (1992) 5596.

[49] K. Funke, *Prog. Solid State Chem.* **22** [2] (1993) 111.

[50] A. Roy, K. Prasad and A. Prasad, *Process. Appli. Ceram.* **7** [2] (2013) 81.

[51] N. Ortega, A. Kumar, P. Bhattacharya, S. B. Majumder and R. S. Katiyar, *Phys. Rev. B* **77** [1] (2008) 014111.

[52] L. Chen, W. Ren, Z.-G. Ye, A. Tian, X. Wu and P. Shi, *J. Appl. Phys.* **112** [5] (2012) 052008.

Chapter 4

Dielectric and ac-conductivity studies of Dy_2O_3 doped $K_{0.5}Na_{0.5}NbO_3$ bulk and thin films

Among the lead-free piezoelectric ceramics, $K_{0.5}Na_{0.5}NbO_3$ (KNN) exhibited the promising piezoelectric and ferroelectric properties. However, it is difficult to achieve the high density in the samples prepared using solid state reaction method due to the volatilization of alkali elements. To overcome this difficulty, a suitable additives and sintering aids were added to KNN ceramics. It is well known that the partial substitution of rare-earth oxides enhance the dielectric, ferroelectric and piezoelectric properties. However, to the best of the authors knowledge, there is no study available on Dy_2O_3 doped KNN ceramics prepared by solid state reaction method. In the present chapter, we have investigated the effect of Dy_2O_3 on structural, microstructural, dielectric properties of KNN ceramics in bulk as well as in thin film form.

4.1 Literature survey

The KNN ceramics exhibits enhanced dielectric permittivity and piezoelectric coefficients with high ferroelectric curie temperatures [1]. Thus, the KNN based systems are considered as potential candidates for the microwave devices, sensors, piezoelectric actuators and ferroelectric random-access memories. KNN is a stable solid-solution of antiferroelectric $NaNbO_3$ and ferroelectric $KNbO_3$, whose ordering temperatures being 480 ^oC and 435 ^oC, respectively [2]. However, the main limitations in fabrication of such systems are control over the moisture and the low sintering temperatures because of the high volatile nature of alkaline elements present in the system [3]. Therefore, it is essential to use different preparation techniques, various sintering aids, and doping with suitable elements to obtain the improved properties and high density in KNN based systems.

The enhanced properties were reported (ε_r = 1570, T_C = 253 ^oC, d_{33} = 461 pC/N, k_p = 0.61) for the composition $(K_{0.44}Na_{0.52}Li_{0.04})(Nb_{0.84}Ta_{0.10}Sb_{0.06})O_3$ prepared by reactive-templated grain growth method, which were almost comparable to lead based ceramics [4]. Most of the enhanced properties observed in the KNN system were obtained by

replacing the alkaline, and niobium ions with Li^+, Sb^{5+}, and Ta^{5+} ions [5-7]. The doping of Li^+ ion in the A-site, and Sb^{5+}, Ta^{5+} ions in the B-site of the KNN ceramics prepared by using conventional solid state reaction method, were greatly improved the dielectric (ε_r = 1024, $tan\delta$ = 0.06) and piezoelectric (d_{33} = 390 pC/N, k_p = 49%) properties at the morphotrophic phase boundary (MPB). The enhanced dielectric and piezoelectric properties (ε_r = 1346 – 1638, T_C = 315 – 370 ^oC, d_{33} = 265 – 305 pC/N, and k_p = 45-54 %) were obtained for $BiScO_3$ and $LiSbO_3$ mixed KNN composite [8]. However, only few reports are devoted on the rare-earth doped KNN ceramics [9-13]. Wang *et al.* [9] reported very high remnant polarization P_r = 42.3 μC/cm^2 and giant coercive electric field E_c = 7.2 kV/cm in Pr_2O_3 containing KNN. Gao *et al.* [10] reported the electromechanical coefficient k_p = 38%, ε_r = 820 and d_{33} = 130 pC/N in CeO_2 doped KNN. The La_2O_3 doped $(K_{0.5}Na_{0.5})(Nb_{0.96}Sb_{0.04})O_3$ ceramics exhibited the better properties (ε_r > 700, k_p = 38%, d_{33}= 160 pC/N, g_{33} = 37.4×10^{-3} Vm/N) [11]. The bright reddish orange emission with good dielectric (ε_r = 1372, T_C = 328 ^oC) and piezoelectric (d_{33} = 230 pm/V, d_{33} = 176 pC/N, k_p = 35%) properties of 0.4 mol.% Sm_2O_3 contained $0.948(K_{0.5}Na_{0.5})NbO_3$ - $0.052LiSbO_3$ ceramics [12]. The increment in the ferroelectric, piezoelectric and photoluminescence properties of KNN ceramics were observed with the doping of Pr^{3+} [13]. The shift in the orthorhombic-tetragonal phase transition towards lower temperature side can greatly enhance the dielectric and piezoelectric properties due to the intermixture of tetragonal and orthorhombic domains, which are more significant across the MPB of KNN. However, there have been no study available on Dy_2O_3 added KNN ceramics. Therefore, an attempt has been made in the present work to investigate the temperature and frequency dependent dielectric properties of Dy_2O_3 added KNN. In this work, we report a detailed dielectric and ac-conductivity analysis of $(K_{0.5}Na_{0.5})NbO_3$+ *x* wt.% Dy_2O_3 ($0 \leq x \leq 1.5$) over a wide frequency (1 kHz - 100 MHz) and temperature range (-140 ^oC – 477 ^oC). The composition with enhanced permittivity and low dielectric loss was chosen as the ceramic target to deposit the thin films by RF magnetron sputtering technique.

Kanno *et al.* [14] reported the transverse piezoelectric properties of KNN thin films for energy harvester applications, deposited by RF magnetron sputtering. Zhu *et al.* [15] reported the dielectric, ferroelectric, and piezoelectric properties of $(K_{0.504}Na_{0.496})_{0.933}Li_{0.067}NbO_3$ thin films for the usage in intravascular ultrasound imaging applications. Improvement in the ferroelectric properties was observed in Mn-doped

KNN thin films prepared using chemical solution method [16]. The enhanced piezoelectric properties were observed for Mn-doped $(K_{0.44}Na_{0.52},Li_{0.04})(Nb_{0.84}Ta_{0.1}Sb_{0.06})O_3$ thin films prepared by using pulsed laser deposition method [17]. The KNN based thin films were prepared by various techniques and mainly focused on the dielectric, ferroelectric and piezoelectric properties. In the similar manner, most of the dielectric studies on KNN based films were confined to low frequency. In this study, we report the dielectric properties of KNN films at microwave frequencies (5, 10, and 15 GHz). Only few reports were available on optical properties of KNN based thin films such as electro-optic, optical waveguide performance and linear optical properties [18-22]. However, no work has been devoted for the nonlinear optical properties on KNN based thin films. In the present study, we have studied the linear and nonlinear optical properties of Dy_2O_3 doped KNN thin films.

4.2 Experimental details

KNN + x wt.% Dy_2O_3 ceramics have been prepared by conventional solid state reaction method with different concentrations such as x = 0, 0.5, 1.0 and 1.5. The commercially available K_2CO_3, Na_2CO_3, and Nb_2O_5 high purity chemicals were used as starting materials. Initially, these powders were heated at 150 ^oC for 1 h in air to remove the moisture present in the chemicals and weighed according to the stoichiometry. The weighed powders were mixed using planetary ball mill for 5h with distilled water as the grinding media. The obtained slurry was heated at 120 ^oC in air for overnight to remove the water content. The powders were grounded and calcined at 750^oC for 5h in air and remilled for 10h with the addition of various compositions of x = 0, 0.5, 1.0 and 1.5 wt.% of Dy_2O_3. These powders were added with few drops of polyvinyl alcohol (PVA) and pressed into pellets of 10 mm diameter and 1mm in thickness. These pellets were heated at 600 ^oC for 20 minutes to drive off the PVA, after that they were sintered at 1050 ^oC for 5h in air. The optimized composition KNN + 0.5wt.% Dy_2O_3 (KNN05D) was used as ceramic target to prepare the thin films by RF magnetron sputtering onto quartz and Pt/Ti/SiO_2/Si substrates. The sputtering chamber was evacuated to a base pressure of 1.0×10^{-6} Torr and the films deposited at a working pressure of 1.0×10^{-2} Torr with the fixed RF power 70 W in distinct argon and oxygen mixing percentages. The KNN05D thin films were deposited at a substrate temperature of 400 ^oC at different oxygen and argon plasmas and annealed at 700 ^oC in oxygen atmosphere.

4.3 Characterization of $(K_{0.5}Na_{0.5})NbO_3$ + *x* wt.% Dy_2O_3 (*x* = 0 - 1.5) ceramics

4.3.1 Crystal structure

To study the effect of Dy_2O_3 on crystal structure of KNN ceramics, the XRD patterns of KNN + *x* wt.% Dy_2O_3 (*x* = 0 - 1.5) (KNND) were fitted with Retvield refinement and shown in Figure 4.1(a). All the ceramics showed the single phase perovskite structure without any secondary phases, indicating that the Dy_2O_3 formed a solid solution with KNN matrix. For the low concentration of Dy_2O_3 ($x \leq 0.5$), the XRD pattern shows the orthorhombic crystal structure. However, for higher concentrations of Dy_2O_3, both (022) and (200) peaks become a single peak, indicating a phase transformation from orthorhombic to pseudo-cubic crystal structure. Such transformation can be clearly observed and displayed in the Figure 4.1(b) where the peak position and intensity variations of (022) and (200) Bragg reflections for various compositions between *x* = 0 and 1.5 are shown.

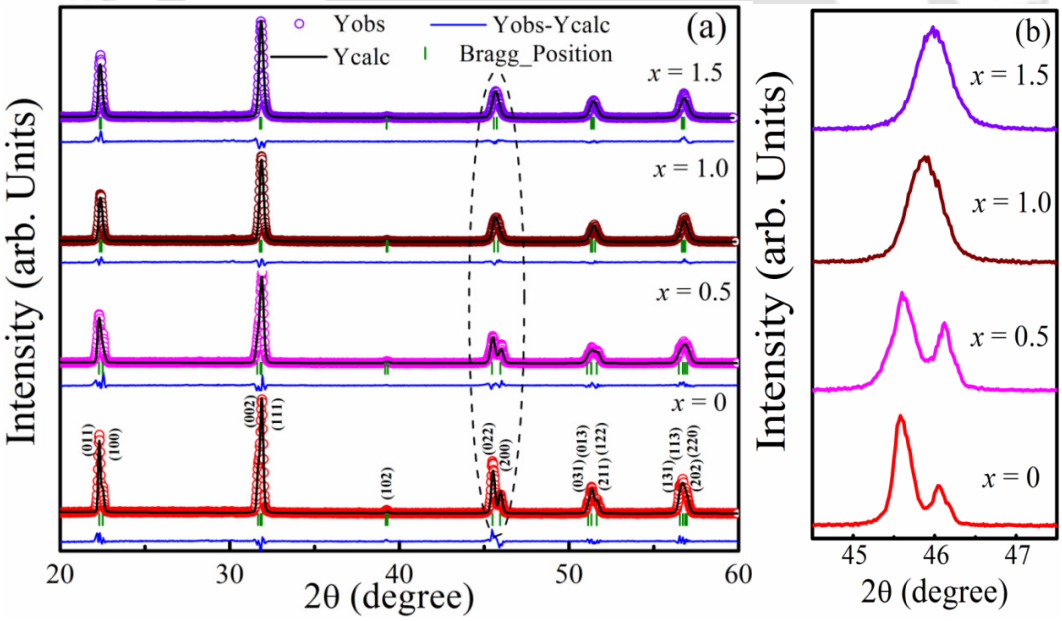

Figure 4.1: *(a) The XRD patterns together with the Retvield refined data (b) The peak position variation of (022) and (200) Brag reflections and intensity for various compositions of KNN+ x wt.% Dy_2O_3 (x = 0 - 1.5) ceramics, sintered at 1050 ^oC for 5h.*

It is also observed that the shift in the peaks towards higher angles with an increase in the concentration of Dy_2O_3. In order to understand the formation of Dy_2O_3 solid solution with KNN matrix, the lattice parameters, atomic positions of the K, Na, Nb, Dy and O atoms, and occupancy have been refined by using Fullprof software. There is

no standard JCPDS or ICSD cards were available for $(K_{0.5}Na_{0.5})NbO_3$. Therefore, the miller indices in the literature are inconsistent [23-29]. KNN ceramics exhibited the ferroelectric orthorhombic phase at room temperature and undergo similar structural transitions from orthorhombic (*Amm2*) to tetragonal (*P4mm*) around 200 ^oC and tetragonal to cubic (*Pm3m*) around 400 ^oC to that of $KNbO_3$ ceramics. Therefore, the refinement of the KNN ceramics was carried out by considering the *Amm2* space group [30]. According to this space group, the lattice parameters and unit cell volumes were calculated and listed in Table 4.1. For x = 0, the lattice parameters estimated after the refinement being a = 3.94718 Å, b = 5.66117 Å, c = 5.62514 Å with the fitting parameters χ^2 = 9.01, R_{Brag} factor = 5.60 and R_f factor = 3.17. The obtained unit cell volume V and c/a (b/a) ratio for pure KNN ceramics were 125.6949 $Å^3$, and 1.4251 (0.9936), respectively. It has been found that both V and c/a (b/a) decreases (increases) with increasing the composition reaching V = 125.3338 $Å^3$ and c/a = 1.4176 (b/a = 0.9985) for x = 1.5. Similar results were also obtained for Dy_2O_3 doped $Bi_{0.5}(Na_{0.82}K_{0.18})_{0.5}TiO_3$ ceramics [31]. This can be attributed to the difference in the ionic radius of the Na^+ (1.02Å) and Dy^{3+} (0.912Å), and one can expect that an increase in the degree of distortion of the lattice with the addition of Dy_2O_3. Therefore, the pseudo cubic nature of the crystal structure enhanced with increase of Dy_2O_3 content in the KNN matrix.

Table 4.1: *Unit cell parameters of the KNN + x wt.% Dy_2O_3 (x = 0 - 1.5) ceramics evaluated from the XRD patterns.*

x	a (Å)	b (Å)	c (Å)	V ($Å^3$)	$\alpha = \beta = \gamma$ (^{o})
0	3.94710	5.66117	5.62514	125.69490	90
0.5	3.94733	5.65552	5.62385	125.54805	90
1.0	3.95879	5.63110	5.62285	125.34673	90
1.5	3.96372	5.62738	5.61900	125.33381	90

4.3.2 Raman spectroscopy

Raman spectroscopy is a useful technique to analyze the structural and compositional studies of KNN-based systems [32-36]. It is very sensitive to structural deformations caused by impurities or deficiencies of A-site cations and the molecular vibrations of the crystal lattice in the short range ordering. Figure 4.2 shows the back-scattered Raman spectra of KNND ceramics measured at room temperature. The pure

KNN shows the orthorhombic structure with space group *Amm*2 (C_{2v}^{14}). According to the group theory, orthorhombic *Amm2* phase consists of $4A_1+4B_1+3B_2+A_2$ Raman active optical modes. The vibrational modes of NbO_6 octahedron consists of $1A_{1g}(v_1) + 1E_g(v_2) + 2F_{1u}(v_3,v_4) + 1F_{2g}(v_5) + 1F_{2u}(v_6)$. In these vibrations, $A_{1g}(v_1)$, $E_g(v_2)$, and $F_{1u}(v_3)$ are stretching modes and remaining vibrations are bending modes. From the Figure 4.2, all the vibrational modes are present for all the samples and relatively strong peaks detected around 245 cm^{-1} and 610 cm^{-1} are attributed to $F_{2g}(v_5)$ and $A_{1g}(v_1)$ modes, which are due to the nearly perfect octahedral symmetry. The peaks appeared in the region below 200 cm^{-1} corresponds to the translational modes of K^+ and Na^+/K^+ cations and rotations of the NbO_6 octahedra.

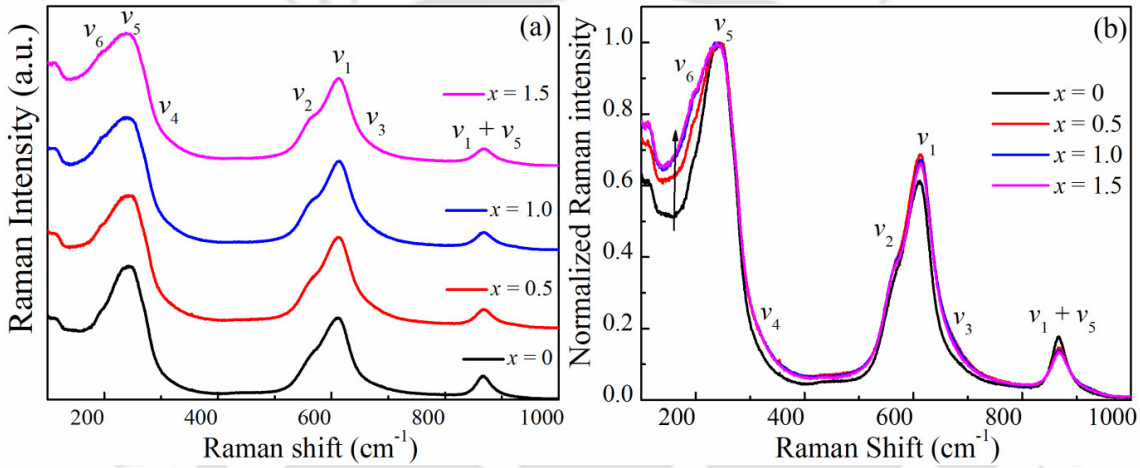

Figure 4.2: *(a) Typical Raman spectra and (b) normalized Raman intensity of KNN + x wt.% Dy_2O_3 (x = 0 - 1.5) ceramics, sintered at 1050°C for 5h.*

In order to identify the Raman modes and full width at half maximum (FWHM), the spectra was fitted with the Gaussian peaks and are listed in Table 4.2. The peak positions of v_1, v_2 and v_1+v_5 modes are shifted toward higher wavenumbers with increasing the concentration of Dy_2O_3. This is due to the change in crystal structure from orthorhombic to psuedocubic phase, which causes the changes in the vibrations of NbO_6 octahedra and increase in binding strength caused by the change in the distance between Nb^{5+} and its coordinated oxygen atoms. The FWHM of these modes also found to rise with increasing *x*, which indicates structural change in the specimens. The intensities of v_1 and v_5 modes of $x = 0.5$ sample displayed sharper and strong peaks as compared to pure KNN and other Dy_2O_3 doped ceramics. This might be due to the enhancement in polarizability with Dy_2O_3. The incorporation of smaller ionic radii of Dy^{3+} into KNN lattice will increase the distance between the atoms and leads to the enhancement in

polarizability as well as vibrational intensity of the corresponding modes. Further, with rise in the Dy_2O_3 concentration above 0.5 wt.%, the v_5 mode shifted towards lower wavenumber due to the improvement of crystal distortion in KNN matrix. The intensity of v_1+v_5 mode decreases and shifted toward higher wavenumber with enhanced FWHM was observed with increasing x concentration may be due to the change in the stoichiometry. The incorporation of Dy_2O_3 in KNN matrix causes the change in the translational modes of A-site cations (K^+ and Na^+) and rotations of NbO_6 octahedra, thus the enhancement in the intensity of v_6 mode and low frequency bands were observed.

Table 4.2: *Variation in the Raman shift and FWHM of the modes for KNN + x wt.% Dy_2O_3 (x = 0 - 1.5) ceramics.*

$x = 0$		$x = 0.5$		$x = 1.0$		$x = 1.5$	
Raman shift(cm^{-1})	FWHM (cm^{-1})	Raman shift(cm^{-1})	FWHM (cm^{-1})	Raman shift(cm^{-1})	FWHM (cm^{-1})	Raman shift(cm^{-1})	FWHM (cm^{-1})
204.22	45.01	203.90	53.03	201.46	55.45	201.30	55.67
246.96	56.18	250.89	56.41	248.80	56.83	248.63	57.85
564.93	50.85	567.21	54.56	569.45	57.93	571.41	63.22
612.39	41.94	613.39	42.63	613.92	43.02	614.58	42.80
668.95	58.55	656.93	76.30	655.90	76.62	659.57	78.73
866.97	28.46	867.99	34.88	868.41	38.65	868.56	38.92

4.3.3 Microstructural analysis

Figure 4.3 shows the surface micrographs of the KNND ceramics sintered at 1050 ^oC for 5h. It is observed that all the samples showed a dense microstructure with the less pores. The density of the samples was measured using Archimedes method and is in the range of 92 - 93% of the theoretical density (4.51 g/cm^3). The density of the samples found to be increased with the Dy_2O_3 and a maximum density of 93.56% is obtained for x = 1.0 sample, there after it decreases for x = 1.5 (Table 4.3).

The x = 0 sample (pure KNN) exhibited the well crystallized and non-uniform grains with an average grain size of 2.3 µm. Further, the average grain size significantly decreases with the increase in the Dy_2O_3 content and the average grain size for x = 1.5 composition is found to be 0.23 µm. The reduction in grain size with Dy_2O_3 concentration can be understood as follows; during sintering, the Dy^{3+} ions isolates at the grain

boundaries of the KNN matrix and leads to decrease in mobility and diffusion. This causes the reduction in mass transportation, as a result the grain size of the ceramics decreases [37, 38].

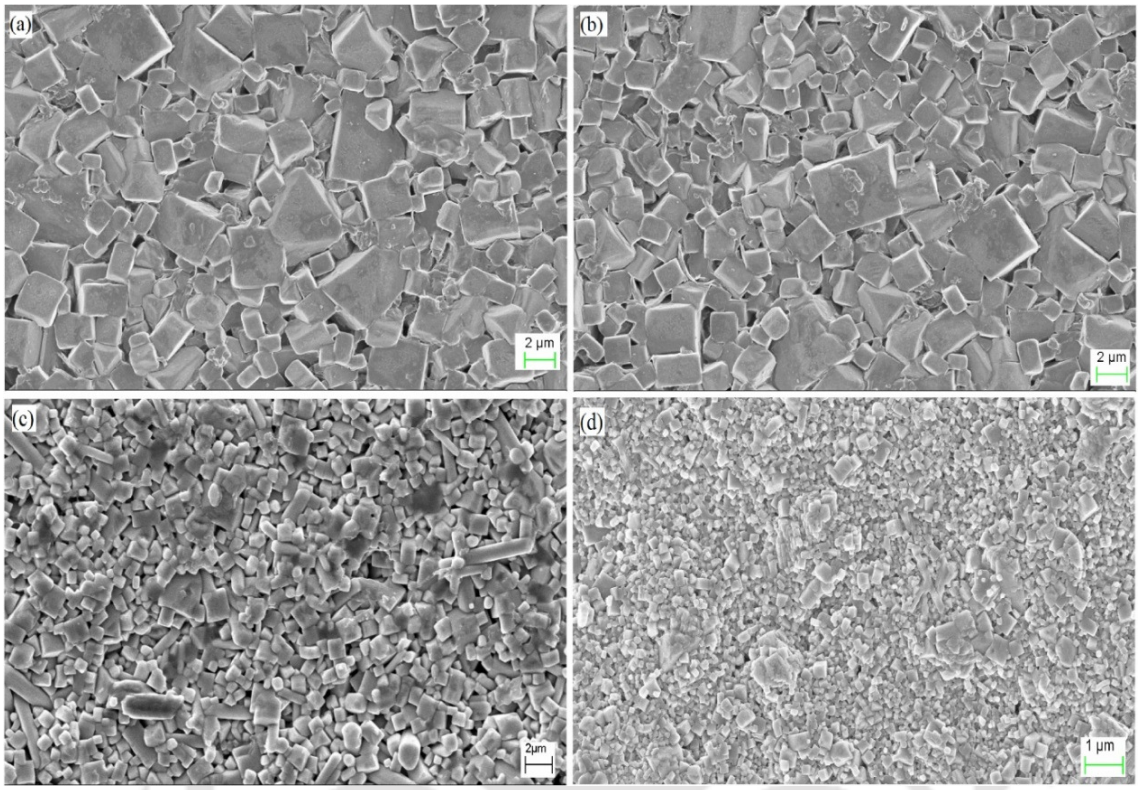

Figure 4.3: *Surface micrographs of the KNN+ x wt.% Dy_2O_3 ceramics, sintered at 1050 ^oC for 5 h; (a) x = 0 (b) x = 0.5 (c) x = 1.0 and (d) x = 1.5.*

Table 4.3: *Density and average grain sizes of KNN + x wt.% Dy_2O_3 (x = 0 - 1.5) ceramics, sintered at 1050 ^oC for 5h.*

x wt.% (Dy_2O_3)	Density (g/cm^3)	Relative density (%)	Grain size (µm)
0	4.16	92.23	2.30
0.5	4.20	93.12	1.67
1.0	4.22	93.56	1.12
1.5	4.21	93.34	0.23

4.3.4 Dielectric properties

4.3.4.1 Low frequency dielectric properties

Figure 4.4 shows the temperature variation of the relative permittivity (ε_r) and loss tangent ($tan\delta$) of pure KNN and KNN doped with various compositions ($0 \leq x \leq 1.5$) of Dy_2O_3 ceramics recorded at various frequencies between 1 kHz to 1 MHz. The relative permittivity of the samples was calculated from the measured capacitance. Pure KNN

ceramics (x = 0) exhibited two cusps across $T_{O\text{-}T}$ = 207 °C and $T_{T\text{-}C}$ = 388 °C associated with the crystallographic transitions occurring from orthorhombic phase to tetragonal and ordered ferroelectric tetragonal to disordered paraelectric cubic phase transitions (Cure temperature), respectively. These values are consistent with the previously reported values of $T_{O\text{-}T}$ = 193 °C and $T_{T\text{-}C}$ = 400 °C [39].

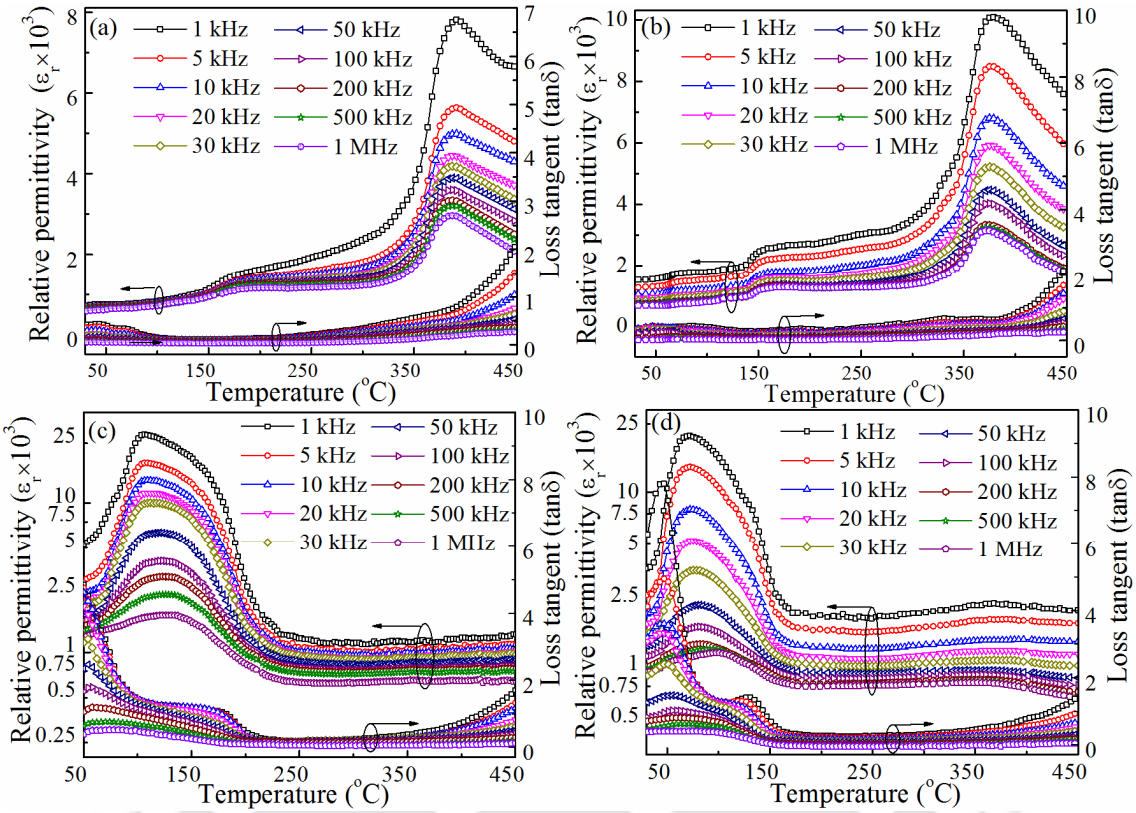

Figure 4.4: *Temperature dependence of ε_r and tanδ of KNN + x wt.% Dy_2O_3 ceramics recorded at various frequencies; (a) x = 0 (b) x = 0.5 (c) x = 1.0 and (d) x = 1.5.*

A progressive improvement in the ε_r values has been noticed with the extent of Dy_2O_3 incorporation into KNN matrix reaching a maximum value of 3151 (at 1MHz) at temperature of 372 °C for critical composition of x_c = 0.5. Beyond this composition level, the ε_r values continues to diminish and reaches a minimum value of 1168 (at 1MHz) at 97 °C for x = 1.5. With the rising of Dy_2O_3 concentration, both the transition temperatures shifted towards the lower temperature side. The enhancement in ε_r up to x = 0.5 can be ascribed due to the substitution of the lower ionic radii Dy^{3+} ions inside the 'A' sites of Na^+ (1.02Å) having higher ionic radius. In the present study, the A-site substitution by the Dy^{3+} (0.912Å) ions can be understood using the following equation involving the defect chemistry:

$$Dy_2O_3 \xrightarrow{K_{0.5}Na_{0.5}NbO_3} 2Dy_{Na}^{\bullet\bullet} + 4V_{Na}^{'} + 3O_o \qquad (4.1)$$

According to the above equation, when the Dy^{3+} ions occupy the A-site cation of Na^+, the compositional heterogeneity may occur inside the KNN lattice. Since, the higher valence Dy^{3+} ions are replacing the lower valance Na^+ ions, in order to maintain an overall charge neutrality, Dy^{3+} acts as a donor due to the existence of excess amount of electrons and one can expect same number of Na-vacant sites [37]. Such process may cause the development of some strain which finally assist to increase the net dipole moment within the unit cell. Due to the increment of net dipole moment, the maximum relative dielectric permittivity reaches a maximum value across $T_{T\text{-}C}$ and lower dielectric loss obtained at room temperature for x = 0.5. Beyond this critical composition (x > 0.5), the higher concentration of Dy_2O_3 in the KNN matrix might have caused severe distortion of the unit cell and leading to the increment in ε_r as well as $tan\delta$ at room temperature. It has been observed that a strong dispersion in the dielectric permittivity and in the ferroelectric to paraelectric transition temperature ($T_{T\text{-}C}$) shifted towards high temperature side with a rise in the frequency for x = 1.0 and 1.5 samples. Also, the magnitude of this transition reduces continuously with rise in the frequency. Such a shift in the temperature of maximum relative permittivity with increasing the frequency is a typical signature of relaxor ferroelectricity [40-45]. The existence of the relaxor ferroelectric behavior is linked with the formation of polar clusters, which possess different relaxation times. Due to late dielectric response of such polar nanoregions, the transition temperature $T_{T\text{-}C}$ (i.e. T_C) shifts towards high temperature side. However, for x = 0 and 0.5 samples, no shift is noticed in the position of $T_{T\text{-}C}$ with increasing the frequency. In case of normal ferroelectrics for $T > T_{T\text{-}C}$, the reciprocal behaviour of ε_r versus T usually follows the Curie-Weiss law [46].

$$1/\varepsilon_r = (T - T_{cw})/C \tag{4.2}$$

where, 'C' is the Curie-Weiss constant and 'T_{CW}' is the Curie-Weiss temperature. For a typical relaxor ferroelectric, nonlinear behavior of $\varepsilon_r^{-1}(T)$ arises above the T_C which signifies the deviation from the Curie-Weiss law. The difference in the reciprocal value of the relative dielectric permittivity and peak maximum of ε_r should follow the Uchino and Nomura formula [47].

$$(1/\varepsilon_r) - (1/\varepsilon_r^m) = (T - T_m)^\gamma / C \tag{4.3}$$

where, 'γ' is a measure of the degree of diffuseness in the transition. For normal ferroelectric systems the diffuseness coefficient 'γ' (equation 4.3) should be equal to 1. But, for relaxor ferroelectrics 'γ' varies between 1 and 2 [48]. Accordingly, the 'γ' value has been evaluated for different compositions by finding the slope of the above function under logarithmic scale i.e. log $[(\varepsilon_r^{-1}) - (\varepsilon_r^{m})^{-1}]$ versus log $(T\text{-}T_m)$ as shown in Figure 4.5.

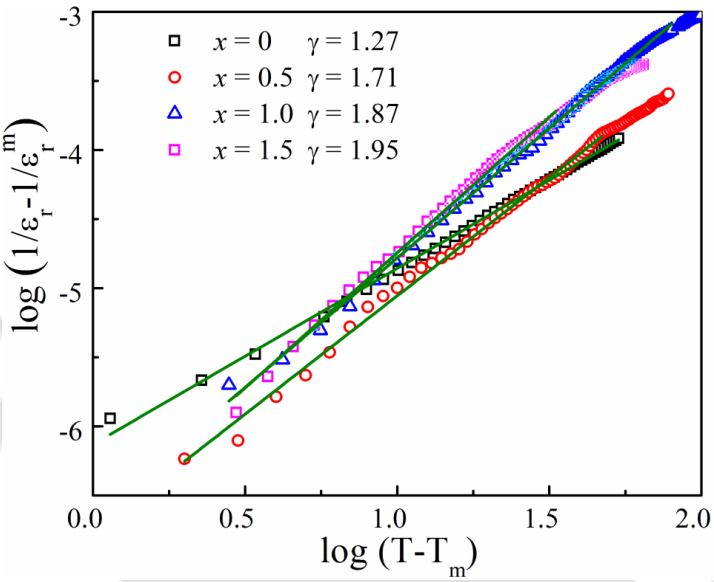

Figure 4.5: *The logarithmic variation of $[(\varepsilon_r^{-1}) - (\varepsilon_r^{m})^{-1}]$ as a function of $(T\text{-}T_m)$ measured at 1 MHz for various compositions of KNN+ x wt.% Dy_2O_3 (x = 0 - 1.5) system.*

The estimated 'γ' values lies in the range of 1.27 - 1.95 for x = 0 - 1.5, respectively, which signifies that the system exhibiting relaxor behaviour. In the present case, the degree of relaxor behaviour found to be enhanced with increasing the Dy_2O_3. The sample with x = 0 shows the γ value 1.27, but on the contrary, there is no peak shift observed with increasing the frequency from 1 kHz to 1 MHz. The improvement in the γ value with increasing Dy_2O_3 composition may be due to the strong distortion caused by the difference in valence and ionic radii of Dy^{3+} and Na^{+} in the A-site of KNN crystal structure. Such distortion of the crystal structure may cause the formation of local polar nanoregions and local electric fields owing to the charge imbalance [41, 48]. The response of these polar nanoregions to the applied ac signal mostly decides the relaxor behaviour.

The variation of both structural transitions and room temperature dielectric properties as a function of composition is listed in Table 4.4. For the compositions x = 1.0 and 1.5, $T_{T\text{-}C}$ reaches the lower values of 130 ^{o}C and 97 ^{o}C, respectively, and $T_{O\text{-}T}$ almost suppressed and pushed to below the room temperature. This indicates that the KNND

system (for x =1.0 and 1.5) should exhibit the tetragonal phase mixed with orthorhombic crystal structure at room temperature. As a result, the ε_r values enhanced significantly with increasing Dy_2O_3 upto x = 1.0, and then decreases for x = 1.5. It is also observed that the large decrease in ε_r values at the Curie temperature, owing to the maximum crystallographic distortion at higher Dy_2O_3 concentration. As the Dy_2O_3 wt.% rises in the KNN matrix, one can expect the disturbance of long-range ferroelectric ordering by increasing the compositional disorder. This process finally forces $T_{T\text{-}C}$ to decrease and favors the formation of polar nanoregions [40, 48-49]. At higher levels of Dy_2O_3, diffuse phase transition was observed, which is confirmed by the increased broadness of the peaks. The smaller grain size can also be the reason for diffuse phase transitions [38]. Such diffusive phase transitions are indicative of the existence of relaxor behavior [41, 48]. The temperature variation of loss tangent for different 'x' compositions also shows the similar anomalies across $T_{O\text{-}T}$ and $T_{T\text{-}C}$. The overall dielectric loss is found to be enhanced with an increase in Dy_2O_3 ($x \geq 1.0$) concentration.

Table 4.4: *Variation in the transition temperatures, ε_r and tanδ for different compositions of KNN added with Dy_2O_3.*

x wt.% (Dy_2O_3)	$T_{O\text{-}T}$ (°C)	$T_{T\text{-}C}$ (°C)	ε_r (1 MHz)	$tan\delta$ (1 MHz)
0	207	395	578	0.048
0.5	171	372	677	0.042
1	-	130	1121	0.380
1.5	-	97	899	0.387

The frequency variation of the peak maximum in the dielectric permittivity has been analyzed using Vogel-Fulcher (V-F) law [49-52],

$$f = f_0 \exp((-E_A)/k_B(T_m - T_f)) \quad (4.4)$$

where, f_0 is the Debye frequency, E_A the activation energy, k_B the Boltzmann constant, T_m is the temperature at which maximum ε_r is obtained, and T_f is the freezing temperature of dipoles.

The scattered symbols shown in the Figure 4.6 (a & b) are the transition temperatures corresponding to the maximum value of the dielectric permittivity (across the $T_{T\text{-}C}$ (T_m)) and the solid line is corresponding to the least square fit to the V-F equation [equation 4.4]. The V-F law is most extensively used to describe the relaxor behavior in

the weakly coupled ferroelectrics where the compositional disorder plays a significant role. The experimentally observed frequency dependence of T_m values and the least-square fit to the V-F law represented by the solid line is in good agreement with each other. This analysis revealed the following fitting parameters, $f_0 = 1.16 \times 10^{12}$ Hz, $T_f = 90$ ^oC, and $E_A = 32.1$ meV for x =1.0 and $f_0 = 6.67 \times 10^{12}$ Hz, $T_f = 59$ ^oC, and $E_A = 31.7$ meV for x =1.5, respectively. The insets of Figure 4.6(a & b) shows the variation of ln(f) versus 1000/(T_C - T_f) for the composition $x \geq 1.0$ wt.% of Dy_2O_3 samples, sintered at 1050^{o}C. The linear behavior of ln(f) against 1000/(T_C - T_f) further confirms the validity of the V-F relation.

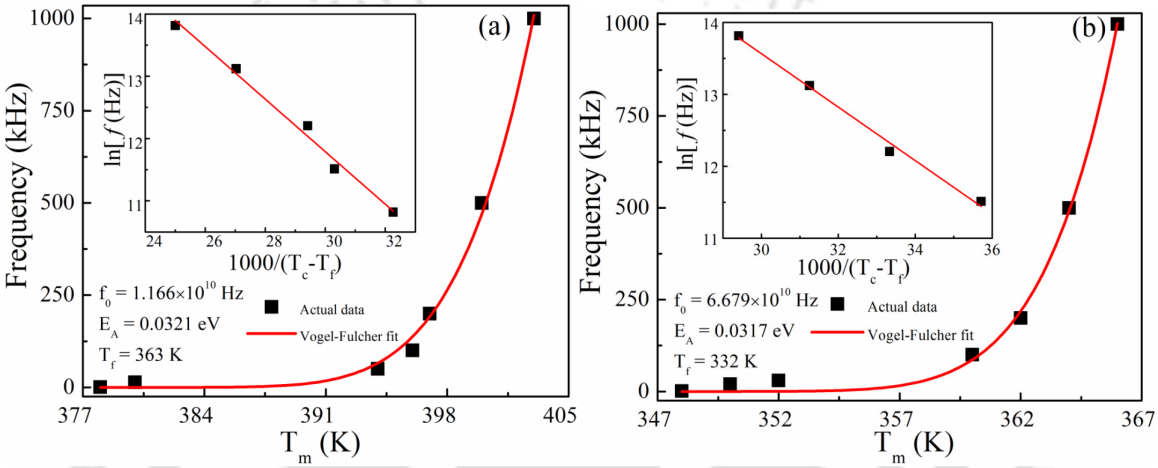

Figure 4.6: *Temperature dependence of the frequency of KNND ceramics (a) x = 1.0 and (b) x = 1.5. The solid symbols indicate the experimental data and a solid line represents the fitting by using Vogel-Fulcher law.*

The variation of ac-conductivity as a function of temperature $\sigma_{ac}(T)$ for different compositions measured at a constant frequency of 1 MHz is shown in Figure 4.7(a). The ac-conductivity shows the clear anomalies across the crystallographic phase transitions around $T_{O\text{-}T}$ = 207 ^oC for x = 0 and further decreases with an increase in x wt.% of Dy_2O_3. The activation energy (E_A) of the samples was estimated from the slope of the lnσ_{ac} versus 1000/T curve, which is depicted in Figure 4.7(b). In the temperature interval of 37 ^oC – 197 ^oC, two different slopes were observed in lnσ_{ac} versus 1000/T graph for x = 0 and 0.5, with the activation energies of 62 - 68 *meV* and 256 - 347 *meV*, for lower and high temperature regimes, respectively. In the high temperature regime, the E_A exhibited higher values as compared to low temperature regime and is due to the significant crystallographic phase change is significant in this regime. Therefore, the ferroelectric properties were also strongly affected the ac-conductivity of the specimens. At higher

temperature, the release of more number of charge carriers from the oxygen vacancies could be the reason for the higher activation energy [53].

$$O_o \rightarrow O_o \uparrow + V_o^{\bullet\bullet} + 2e^{-1} \tag{4.5}$$

According to the above equation, free electrons remain stay in the samples, due to the oxygen vacancies, which enhance the total conductivity progressively with increasing temperature. For x = 1.0 and 1.5 samples, the calculated E_A values lie in the range of 55-87 *meV*. Usually, the lower activation energy is obtained in low temperature regime and can be attributed due to the hopping of charge carriers from one localized state to another in a disordered manner [54].

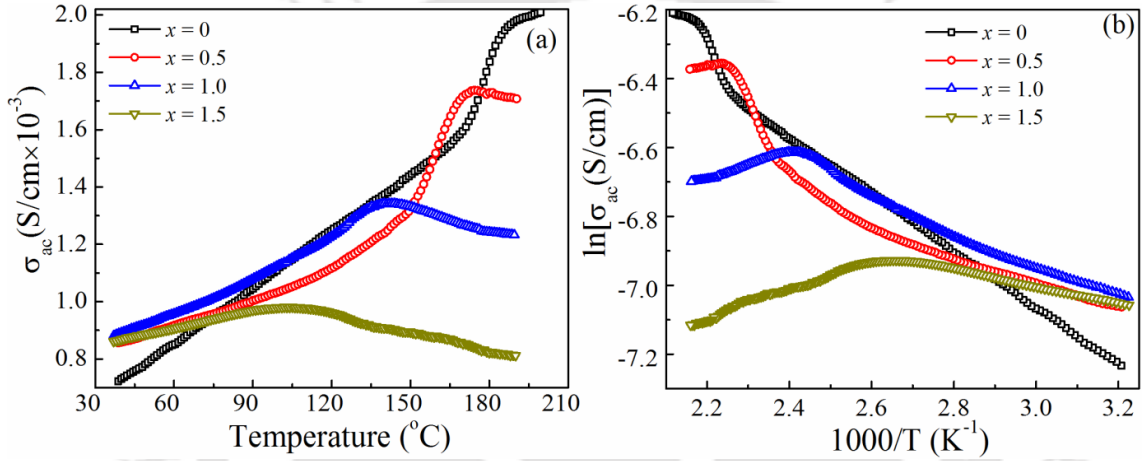

Figure 4.7: *(a) Temperature dependence of ac-conductivity and (b) lnσ_{ac} versus 1000/T in the regime 37 °C – 197 °C of various compositions for x = 0 - 1.5 of KNN+ x wt.% Dy_2O_3.*

To study the effect of Dy_2O_3 on hopping mechanism in detail, the temperature dependent ac-resistivity data is analyzed using Mott's variable range hopping (VRH) conduction mechanism. According to VRH mechanism, the probability of hopping of electrons from one localized state to another state, whose energy levels are equal is higher compared to the different energy levels. The hopping length (R_H) decreases with increasing temperature and the density of states ($N(E_F)$) is assumed to be constant in the temperature range. The high temperature dependent (37 °C – 197 °C) resistivity was analyzed by following Mott's law,

$$\rho_{ac} = \rho_0 \exp(T_0 / T)^{1/4} \tag{4.6}$$

where, ρ_0 and T_0 are being pre-exponential factor and characteristic temperature coefficient, which depends on the density of states at Fermi level, respectively [55-57]. In

order to simplify the equation (4.6), take the natural logarithm on both sides and rewritten as below,

$$\ln \rho_{ac} = \ln \rho_0 + \left(\frac{T_0}{T}\right)^{\frac{1}{4}} \tag{4.7}$$

Again apply the natural logarithm on both sides of equation (4.7),

$$\ln\left[\ln\left(\frac{\rho_{ac}}{\rho_0}\right)\right] = \frac{1}{4}\ln T_0 - \frac{1}{4}\ln T \tag{4.8}$$

The linear variation of $\ln\rho_{ac}$ against $T^{-1/4}$ provides the signatures of variable range hopping process among the ions Nb^{5+}-Dy^{3+}-$[Na^{1+}]_{0.5}$ or Nb^{5+}-Dy^{3+}-$[K^{1+}]_{0.5}$. The parameters T_0 and ρ_0 have been evaluated from the slopes and intercepts of the Figure 4.8(a). The values of T_0 are 2.31×10^6 and 2.23×10^4 measured at 1 MHz for x = 0 and 0.5, respectively. The higher values of T_0 for lower concentration of x are attributed due to the strong localization of charge carriers and lower conductivity [58]. Further, with rise in the concentration of Dy_2O_3, the T_0 value found to be decreased due to the more number of defect states present in x = 1.5 sample. The values of slopes obtained from the logarithmic graphs $\ln[\ln(\rho_{ac}/\rho_0)]$ versus $\ln(T)$ are shown in Figure 4.8(b).

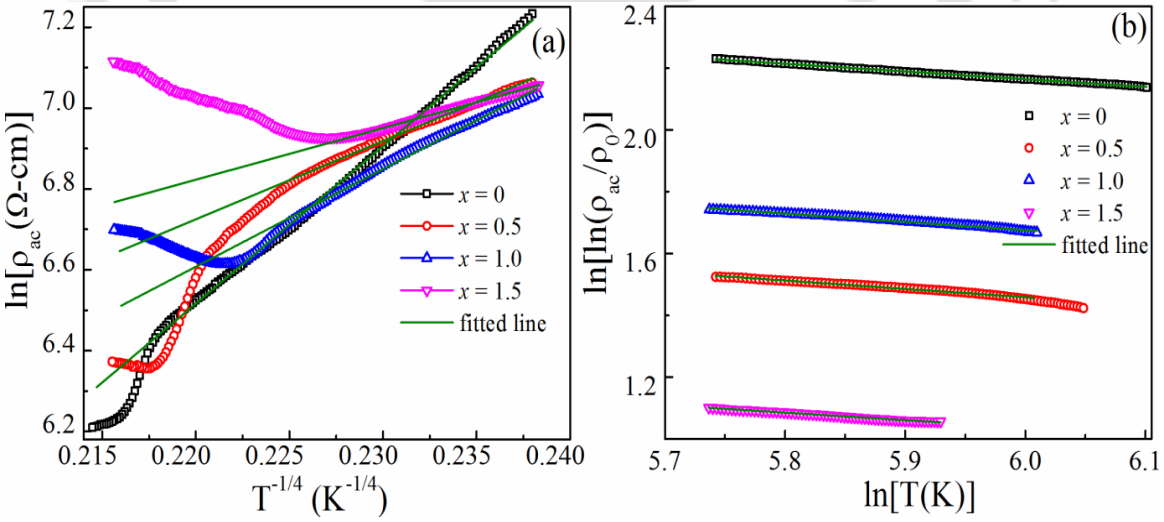

Figure 4.8: *Variation of (a) $\ln\rho_{ac}$ with $T^{-1/4}$ and (b) $\ln[\rho_{ac}/\rho_0]$ with lnT in the temperature regime 37 ^oC – 197 ^oC for KNN+ x wt.% Dy_2O_3(x = 0 - 1.5) ceramics.*

It has been observed that the pure KNN ceramics (x = 0) exhibited the slope value of -0.25. Whereas for x = 0.5, 1.0 and 1.5 the obtained slopes were slightly deviated and are -0.26, -0.26 and -0.245, respectively. Generally, depending upon the nature of the hoping process the power of exponential values varies. For the variable range hopping process,

the typical exponential value should be approximately -0.25. Both ρ_0 and T_0 depends upon the density of states of electrons at the Fermi level [57-59].

$$N(E_F) = 16\alpha^3 / k_B T_0 \tag{4.9}$$

In the equation (4.9) the decay length α^{-1} signifies the spatial extension of the wave function $e^{-(\alpha R)}$ associated with the localized states. The average hoping length is determined by using the following equation [58, 59].

$$R_H = 0.75 \times [3/(2\pi\alpha N(E_F) k_B T)]^{1/4} \tag{4.10}$$

The energy of hopping between two localized states either between the successive sites or centered at different locations is related with the $N(E_F)$ with the following equation [58, 59].

$$W_H = [3/(4\pi R^3 N(E_F))] \tag{4.11}$$

Using the values of ρ_0 and T_0 obtained from slope and intercept of Figure 4.8 (a), one can extract the values of all the other parameters given in the above equations provided that one should has an idea of approximate range of $N(E_F)$. However, the value of decay length α^{-1} (= ξ) is not known correctly for the KNN based ceramics. Ambegaokar and Hill *et al.* [55, 60] reported the ξ in the range of 1 nm. Han *et al.* [61] reported the ξ as the distance between the nearest B atoms of the ABO_3 perovskite structure. In the present case, the distance between Nb ions assumed approximately as 0.6 nm. Therefore, the values of $N(E_F)$ can be obtained by considering the decay length ξ as 1 nm and 0.6 nm.

Table 4.5: *The calculated Mott's VRH parameters of KNN+ x wt.% Dy_2O_3 (x = 0 - 1.5) ceramics, obtained in the temperature range of 37 ^oC-197 ^oC.*

x	T_0 (^oC)	$N(E_F)$(10^{20} eV^{-1} cm^{-3})		R_H (nm)		W_H (meV)	
		ξ=1 nm	ξ=0.6 nm	ξ=1 nm	ξ=0.6 nm	ξ=1 nm	ξ=0.6nm
0	2316393	0.80	3.71	2.89-2.69	1.97-1.80	118-152	81-106
0.5	223511	8.29	38.43	1.61-1.50	1.10-1.03	66-85	45-55
1	510336	3.63	16.84	1.98-1.84	1.35-1.26	81-104	55-68
1.5	22542	81.38	376.99	0.91-0.85	0.62-0.59	37-48	25-29

By using the values of α and $N(E_F)$, the average hopping length R_H and hopping energy W_H has been evaluated. The calculated parameters using VRH model were listed in Table 4.5. It is observed that the hopping energy calculated using ξ = 0.6 nm is comparable to the activation energy calculated using Arrhenius relation. However, the average hopping length found to be higher than the decay length of the wave function between the localized states. Therefore, in order to study the ac-conductivity of KNND ceramics in detail, we have analyzed the VRH mechanism in the low temperature range between -140 ^oC – 33 ^oC and is presented in the next section.

4.3.4.2 Broadband dielectric properties

The low temperature dependant (-140 ^oC – 400 ^oC) dielectric properties of KNND ceramics measured at different frequencies from 1 MHz to 100 MHz are shown in Figure 4.9. For x = 0 sample, three anomalies were observed in both ε_r and $tan\delta$ around -60 ^oC, 199 ^oC, and 374 ^oC, which are the structural transitions from rhombohedral to orthorhombic ($T_{R\text{-}O}$), orthorhombic to tetragonal ($T_{O\text{-}T}$), and tetragonal to cubic ($T_{T\text{-}C}$) states, respectively. With increasing the Dy_2O_3 concentration, all the transition temperatures were shifted towards lower temperatures, which are similar to the phase transition temperatures obtained in the low frequency dielectric studies. The incorporation of Dy_2O_3 into KNN matrix was shifted the crystallographic phase transitions $T_{O\text{-}T}$ and $T_{T\text{-}C}$ towards lower temperatures as compared to x = 0 sample. It can be explained as decrease in the long range ordering and increase in the short range harmonic restoring force constant within the system according to the relation, $T_{T\text{-}C} = (K_L\text{-}K_S)/B$, where K_L and K_S are the long range and short range force constants, and B is the anharmonic coefficient [62, 63].

The improvement in relative permittivity (ε_r) from 455 to 994 with increasing the Dy_2O_3 concentration can be attributed to the enhancement in the polarizability by the replacement of the higher ionic radius of Na^+ (1.02Å) inside the 'A' site of KNN matrix with lower ionic radii of Dy^{3+} (0.91Å) ions. Beyond x = 1.0 composition, the ε_r found to be diminished and $tan\delta$ enhanced due to the higher distortion in the crystal structure as well as shift in the Curie temperature toward room temperature. The samples with $x \geq 0.5$ exhibited the small shift in Curie temperature with an increase in the frequency from 1 MHz to 100 MHz, which is similar to the low frequency dielectric properties. Therefore, KNND ceramics exhibited relaxor behaviour even at higher frequencies.

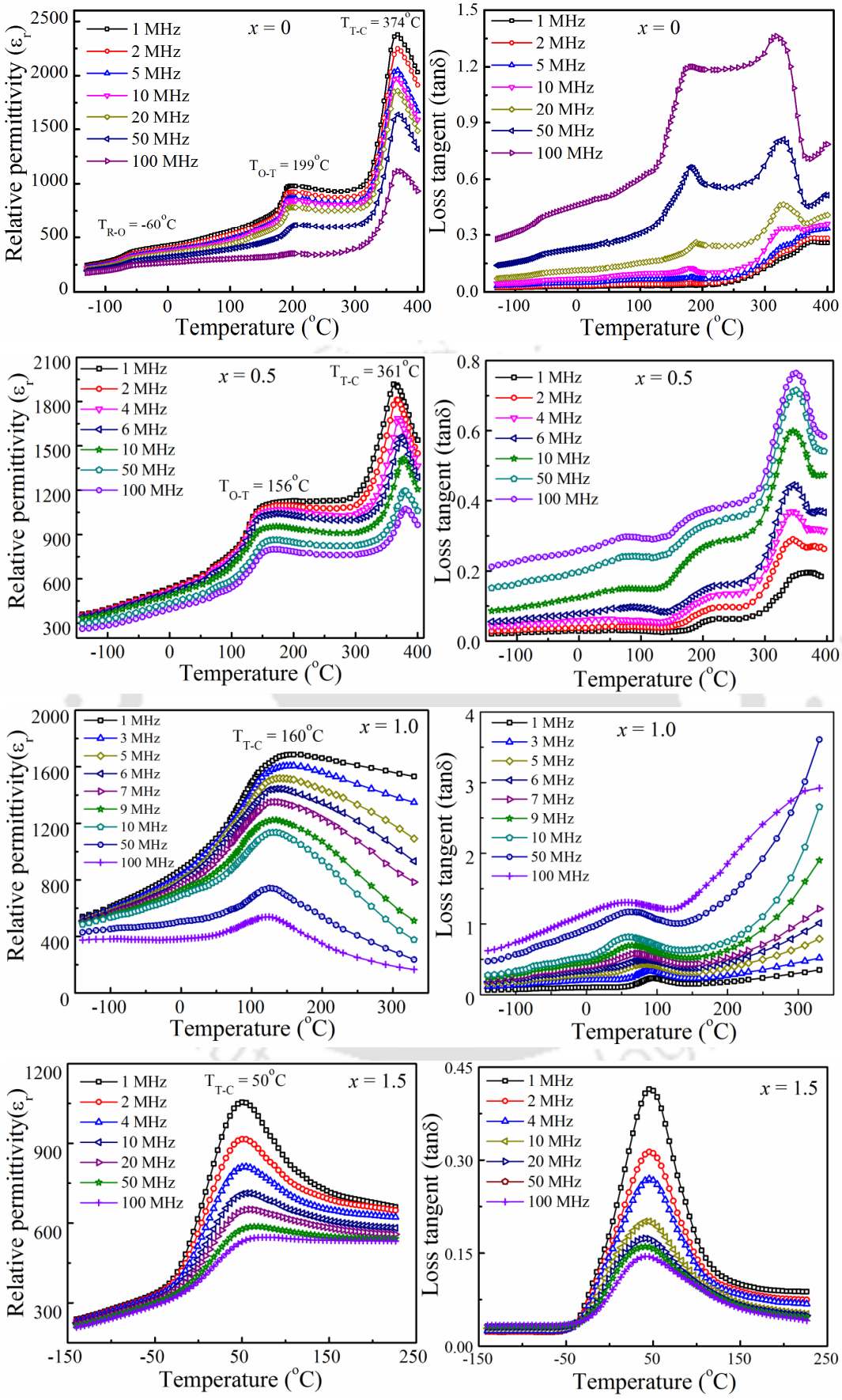

Figure 4.9: *Temperature dependent dielectric properties of KNN + x wt.% Dy_2O_3 (x = 0 - 1.5) ceramics, measured at different frequencies.*

In the earlier section, we have studied effect of Dy_2O_3 on ac-conductivity of KNN ceramics in the high temperature range. However, it is essential to study the conductivity of KNN ceramics in low temperatures to find out the hopping nature of charge carriers and dielectric relaxations. Therefore, the low temperature (-140 ^oC – 33 ^oC) ac-conductivity of KNND ceramics is analyzed using VRH mechanism.

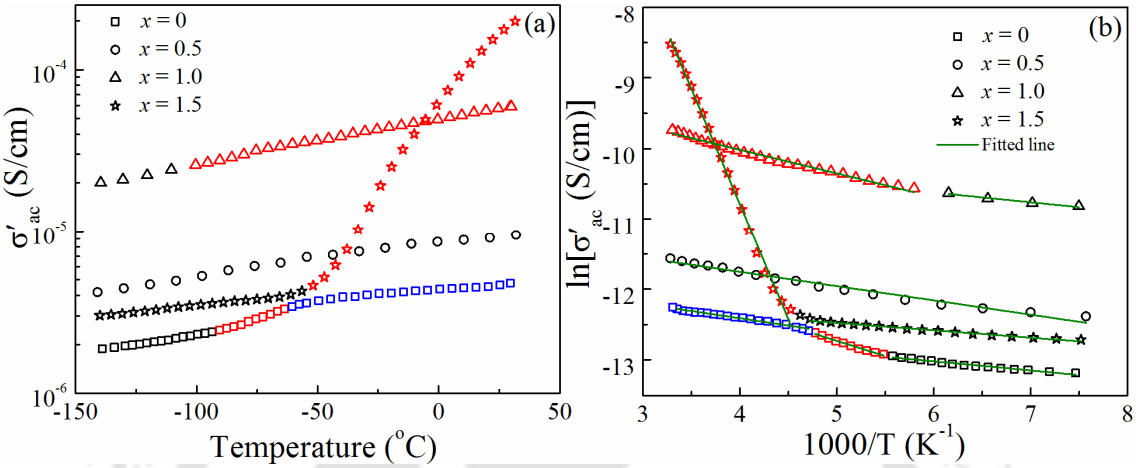

Figure 4.10: *(a) The temperature dependent ac-conductivity and (b) variation in the $ln[\sigma'_{ac}]$ with 1000/T of KNN + x wt.% Dy_2O_3 (x = 0 - 1.5) ceramics. (Colours, black: regime 1, Red: regime 2, blue: regime 3)*

The temperature dependent ac-conductivity of KNND ceramics displayed the clear anomalies around the structural phase transitions and is shown in Figure 4.10(a). The activation energy (E_A) of the KNND ceramics was estimated in different temperature regimes where the linear behaviour exhibited in the ln σ'_{ac} versus 1000/T graph (Figure 4.10 (b)) using Arrhenius relation $\sigma'_{ac} = \sigma_0 \exp(-E_A/k_BT)$. The obtained activation energies of all the samples measured in different temperature regimes such as regime 1 (R1), regime 2 (R2), and regime 3 (R3) were listed in Table 4.6. The lower activation energies (8 - 18 *meV*) in the low temperature regimes can be due to the randomly hopping of charge carriers between the localized states [54]. The higher activation energies 41 *meV* and 287 *meV* observed for the samples x = 0 and 1.5, respectively, in the temperature range over the structural change. Across this temperature, the change in crystal structure causes the release of charge carriers from grains or grain boundaries; hence the conductivity as well as activation energy enlarges.

As discussed in the earlier section, the linear variation of ρ'_{ac} versus $T^{1/4}$ for different temperature regimes displayed in Figure 4.11, which gives the typical signatures of VRH mechanism in the KNND ceramics. In order to confirm the VRH conduction

mechanism, $\ln[\ln(\rho'_{ac}/\rho_0)]$ versus $\ln T$ plotted according to the equation (4.8), which is shown in Figure 4.12.

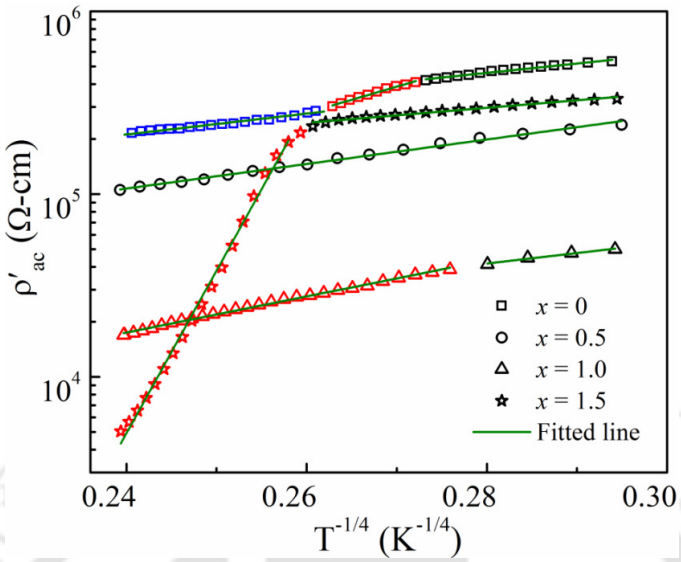

Figure 4.11: *Temperature dependence of ac-resistivity measured in the temperature range -140 ^oC – 33 ^oC of KNN + x wt.% Dy_2O_3 (x = 0 - 1.5) for different regimes. (Colours, black: regime 1, Red: regime 2, blue: regime 3)*

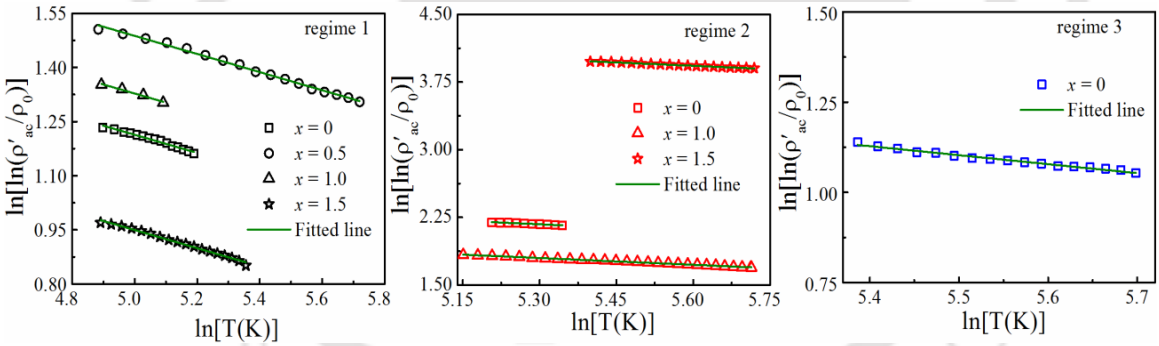

Figure 4.12: *Double logarithmic variation ρ'_{ac}/ρ_0 with lnT yields the slope of -0.25 in the different temperature regimes of KNN + x wt.% Dy_2O_3 (x = 0 - 1.5) ceramics.*

Interestingly, all the samples in different regimes exhibited the slope of -0.25, indicating that the variable range hopping presented among the ions Nb^{5+}-Dy^{3+}-$[Na^{1+}]_{0.5}$ or Nb^{5+}-Dy^{3+}-$[K^{1+}]_{0.5}$. Further, using the T_0 values obtained from the slopes of the Figure 4.11 and decay length ξ (0.6 nm), the values of $N(E_F)$, R_H, and W_H were calculated and presented in Table 4.6. The obtained parameters should satisfy the criteria to follow the VRH conduction mechanism $\alpha R_H \geq 1$ and $W_H > k_B T$ [58]. All the samples satisfied the above conditions except x = 1.5, and it can be ascribed to the increased crystal distortion

with more number of defect states and shift in the Curie temperature toward room temperature.

Table 4.6: *The VRH parameters of KNN+ x wt.% Dy_2O_3 (x = 0 - 1.5) ceramics, measured in the temperature range of -140 ^oC - 33 ^oC.*

x	Regime	E_A (meV)	T_0 (^oC)	$N(E_F)$ (10^{20} eV^{-1} cm^{-3})	R_H (nm)	W_H (meV)
	R1	13	18746	452.23	0.73 - 0.68	12-16
0	R2	41	1.19×10^6	7.18	1.91 - 1.85	45-50
	R3	16	19889	426.58	0.66 - 0.60	18-24
0.5	R1	18	56580	151.28	0.96 - 0.78	16-31
1.0	R1	11	29780	286.19	0.82 - 0.78	14-16
	R2	28	268039	32.05	1.33 – 1.16	30-46
1.5	R1	8	6341	1300.26	0.56 - 0.50	9-14
	R2	287	1.81×10^9	4.75×10^{-3}	11.37-10.49	329 – 419

The obtained W_H and R_H values by considering the ξ = 0.6 nm were comparable to the activation energy calculated using Arrhenius relation and distance between the Nb ions, respectively. We found that $N(E_F)$ increases, whereas hopping distance and hopping energy decreases with the incorporation of Dy_2O_3 content in the KNN matrix. This indicates that Dy^{3+} assisted the hopping of charge carriers from one localized site to another. It is observed that, the Mott's VRH conduction mechanism is more prominent in low temperature rather than high temperature region.

4.3.4.3 Voltage dependent dielectric properties

The DC voltage dependant relative permittivity characteristics of the KNN + x wt.% Dy_2O_3 (x = 0 - 1.5) ceramics with the applied DC voltage range from +5 V to -5 V and measured at 1 MHz were shown in Figure 4.13. The relative permittivity exhibits a strong nonlinear behaviour with respect to the sweep direction of the applied bias voltage due to the switching of domains, confirming the ferroelectricity in the KNND ceramics. All the samples displayed the asymmetry in ε_r maxima values and the centres of the butterfly loops are not located at zero bias voltage, but shifted toward the positive bias voltage. It might be due to the fact that the difference in the internal bias field at the interface between the both electrodes and bulk ceramics.

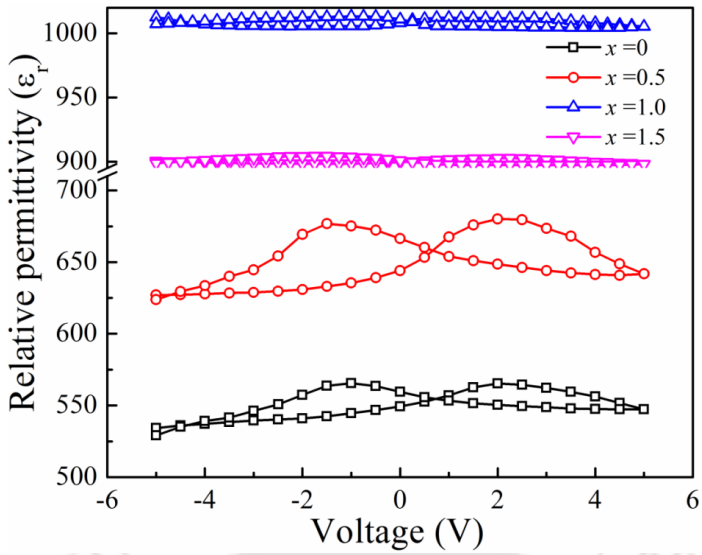

Figure 4.13: *DC Voltage dependence of the relative permittivity of KNN + x wt.% Dy_2O_3 (x = 0 - 1.5) ceramics, measured at 1MHz.*

The Large hysteresis loops were observed for both x = 0 and 0.5 samples, but the width of hysteresis loop decreased with increasing the Dy_2O_3 concentration. It may be attributed to the accumulation of large number of charge carriers for higher Dy_2O_3 concentration, at the interface between dielectric and the electrode. The tunability is determined by finding the change in ε_r at zero bias voltage (0V) compared to ε_r with non-zero bias voltage (5V) [62]. The tunability was found to be higher (3.95%) for the sample with x = 0.5. Therefore, the polarization-electric field (*P-E*) measurement have been performed on both x = 0 and 0.5 samples due to their larger hysteresis loops and tunability.

4.3.4.4 Ferroelectric properties

The *P-E* loops of pure KNN and KNN + 0.5 wt.% Dy_2O_3 samples measured at room temperature are shown in Figure 4.14. Both the samples exhibited the well saturated hysteresis loops, and the values of remnant polarization ($2P_r = P_{r+} - P_{r-}$) found to be increased, whereas the coercive field ($2E_c = E_{c+} - E_{c-}$) decreased for the Dy_2O_3 doped KNN ceramics. It can be explained as the increment of number of switchable domains available in Dy_2O_3 doped KNN sample. The maximum value of $2P_r$ (27.36 $\mu C/cm^2$) is obtained for the doped sample as compared to the pure KNN, which is due to the uniform grain size, high relative permittivity, and low dielectric loss (ε_r = 677 and $tan\delta$ = 0.04 at 1MHz). The enhanced dielectric properties, improved tunability and ferroelectric properties of the Dy_2O_3 doped KNN ceramics make them suitable for tunable RF circuits and high performance piezoelectric applications.

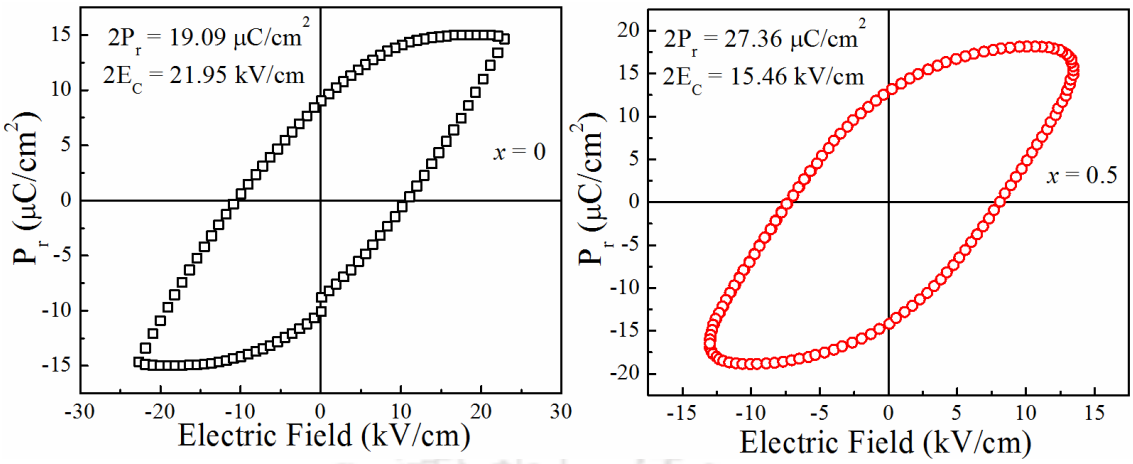

Figure 4.14: *The P-E loops of KNN + x wt.% Gd_2O_3 (x = 0 and 0.5) ceramics sintered at 1050 °C.*

Therefore, KNN + 0.5wt.% Dy_2O_3 (KNN05D) is identified as the best composition for the deposition of thin films by using RF magnetron sputtering technique.

4.4 $(K_{0.5}Na_{0.5})NbO_3$+0.5 wt.% Dy_2O_3 thin films

4.4.1 Crystallinity of the thin films

The as-deposited KNN05D thin films are partially crystallized and the phase pure films obtained after annealing. Figure 4.15 shows the X-ray diffraction pattern of the annealed KNN05D thin films grown on the quartz substrates deposited under various OMPs.

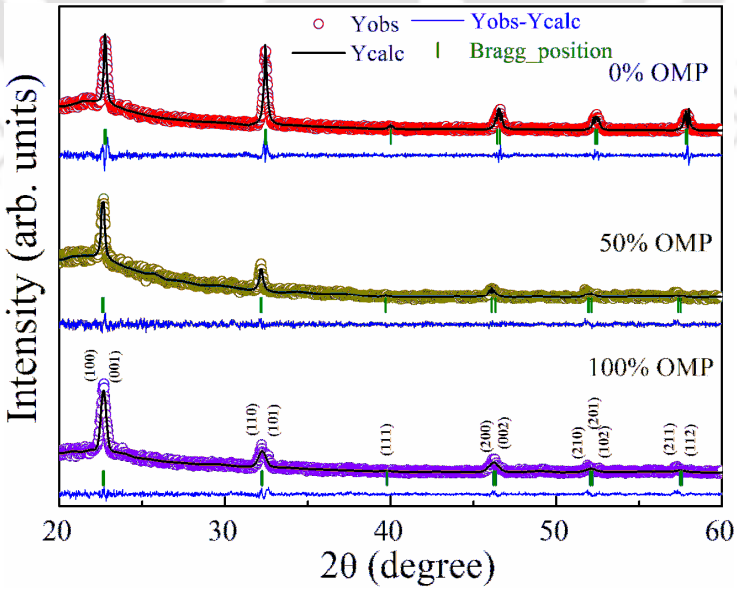

Figure 4.15: *The XRD pattern along with Retvield refinement of the annealed KNN05D thin films, deposited under different OMPs.*

The Rietveld refinements were undertaken to study the crystal structure and lattice parameters of KNN05D thin films. The refinement was performed by considering the *P4mm* space group using FullProf program [64]. The film deposited under pure argon plasma exhibited perovskite structure having a single phase with (110) orientation, and no secondary phase were observed. However, with an increase in OMP, the preferential orientation of the KNN05D films changed from (110) to (001) plane due to the lower surface energy of the (001) plane as compared to other planes [65]. The orientation factor for both the (001) and (110) reflections were estimated by the Lotgering factor (*F*) using the equation (3.4). The *F* for the (001) plane ($F_{(001)}$) of the film deposited under pure argon plasma is 0.20 and it is enhanced linearly to 0.46 with a rise in the oxygen concentration in the sputter gas, whereas the $F_{(110)}$ decreases from -0.16 to -0.43 with an increase of OMP.

The lattice parameters of the KNN05D thin films have been refined using FullProf software and listed in Table 4.7. The unit cell volume (*V*) and tetragonality ratio (*c/a*) for the films deposited under pure argon atmosphere are 59.2764 $Å^3$ and 1.0031, respectively. Both the *V* and *c/a* ratio found to be enhanced with an increase in OMP, and obtained maximum value of 60.2717 and 1.0036 for film deposited in pure oxygen plasma, which can be attributed to the reduction in the oxygen vacancies.

Table 4.7: *Lattice parameters and Lotgering factor extracted from the XRD pattern of KNN05D thin films deposited under different OMPs.*

OMP (%)	*a* (Å)	*b*(Å)	*c*(Å)	*V*($Å^3$)	*c/a*	$F_{(001)}$	$F_{(110)}$
0	3.8949	3.8949	3.9073	59.2764	1.0031	0.20	-0.16
50	3.9154	3.9154	3.9297	60.2472	1.0036	0.38	-0.41
100	3.9161	3.9161	3.9302	60.2717	1.0036	0.46	-0.43

4.4.2 Raman spectroscopy of thin films

Figure 4.16 shows the Raman spectra of KNN05D thin films deposited under different OMPs and annealed at 700 ^oC for 1h. At room temperature, KNN05D ceramic target shows the orthorhombic phase with *Amm2* space group [32-36]. The ceramic target exhibited the v_1 (~613 cm^{-1}) and v_5 (~251 cm^{-1}) modes are relatively strong and these modes are sensitive to the change in the macro symmetry of the NbO_6 octahedra.

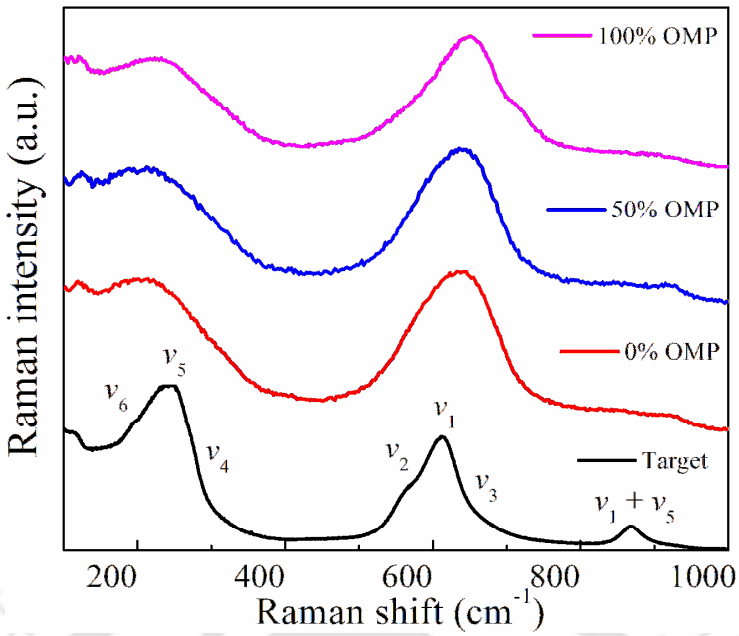

Figure 4.16: *Raman spectra of KNN05D ceramic target and annealed thin films deposited at various OMPs.*

For the clear identification of Raman modes, the spectra was deconvoluted into different Gaussian peaks and change in the modes position and FWHM as a function of OMP are listed in Table 4.8. As the OMP increases, the peak positions of v_1 and v_5 modes are observed to be shifted towards higher wavenumbers, whereas the FWHM of these modes are found to be decreased. Normally, the Raman shifts toward the higher wavenumber side is related to the crystal stress, tetragonality and polarization, whereas the FWHM represents the degree of crystallinity [66]. This is in agreement with the XRD observations.

Table 4.8: *The variation in the spectral band position and FWHM of v_1 and v_5 modes of the KNN05D thin films annealed at 700 ^oC for 1h.*

OMP (%)	v_5 mode		v_1 mode	
	Position(cm^{-1})	FWHM(cm^{-1})	Position(cm^{-1})	FWHM(cm^{-1})
Target	250.89±0.34	56.41±0.41	613.39±0.20	42.63±0.56
0	211.03±1.53	168.89±2.08	640.80±3.19	103.51±2.28
50	217.64±4.43	150.08±5.91	642.61±2.39	101.45±2.92
100	242.28±2.69	116.60±6.50	656.29±0.85	77.37±3.23

4.4.3 Microstructural analysis

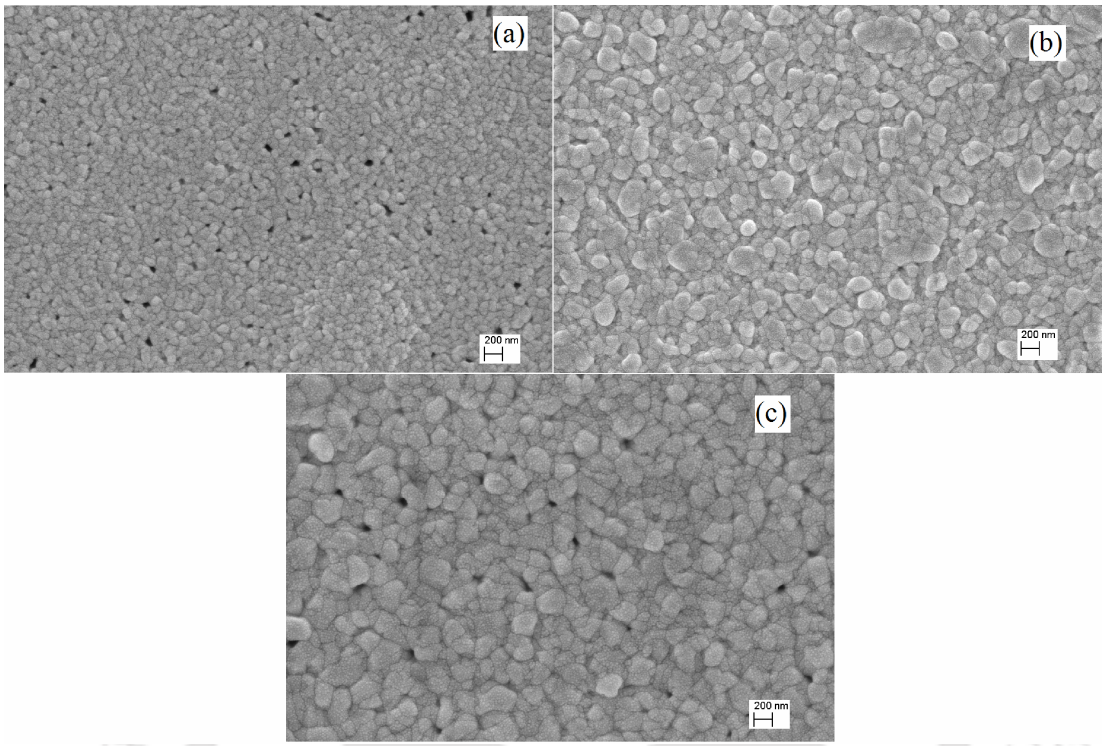

Figure 4.17: *FESEM images for the KNN05D films deposited under (a) 0%, (b) 50%, and (c) 100% OMP and annealed at 700 ^oC for 1h.*

The FESEM images of the KNN05D thin films deposited under different OMPs Figure 4.17. The film deposited under pure argon plasma show the small and non-uniform grain size of 103 nm. The high deposition rate in the pure argon plasma makes the sputtered atoms in the form of islands; therefore, particle size was found to be small with a significant amount of pores. With an increase in the OMP in the sputtering gas, the enhanced kinetics facilitated by thermal energy and more reaction time of sputtered species due to the lower deposition rate can help to improve the grain size. Therefore, the average grain size of the films increased to 195 nm and 210 nm for the films deposited at 50% and 100% OMP, respectively.

4.4.4 Optical studies

4.4.4.1 Linear optical properties

The optical transmittance spectra of the annealed KNN05D films deposited onto quartz substrates at various OMPs in the wavelength regime of 200-900 nm is shown in Figure 4.18. The transmittance of the KNN05D films found to be decreased to nearly zero in the region 290-330 nm and above 330 nm; the films are exhibiting transmittance

approximately 80%. The appearance of well resolved interference fringes confirms the good surface quality of the films.

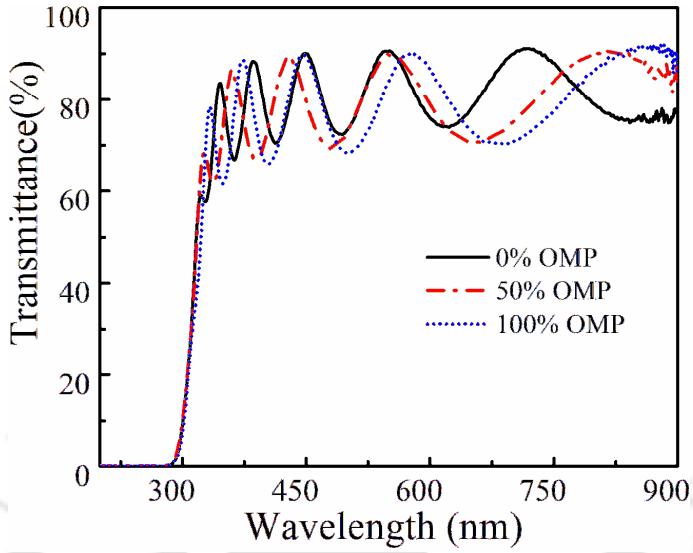

Figure 4.18: *Transmittance spectra of KNN05D thin films deposited at different OMPs and annealed at 700 °C for 1h.*

In general, the real part of the refractive index *n*, is related to the crystallinity, optical density, oxygen deficiencies and electronic structure [67]. The imaginary part of the refractive index, extinction coefficient (*k*), represents the absorption of the light. The refractive index, *n* and thickness of the films are calculated using Swanepoel's envelope method [68]. The refractive index at 700 nm (n_{700}) of the films was found to be in the range of 2.08-2.21 for annealed films, and increased with the rise in the OMP (Figure 4.19 (a)).

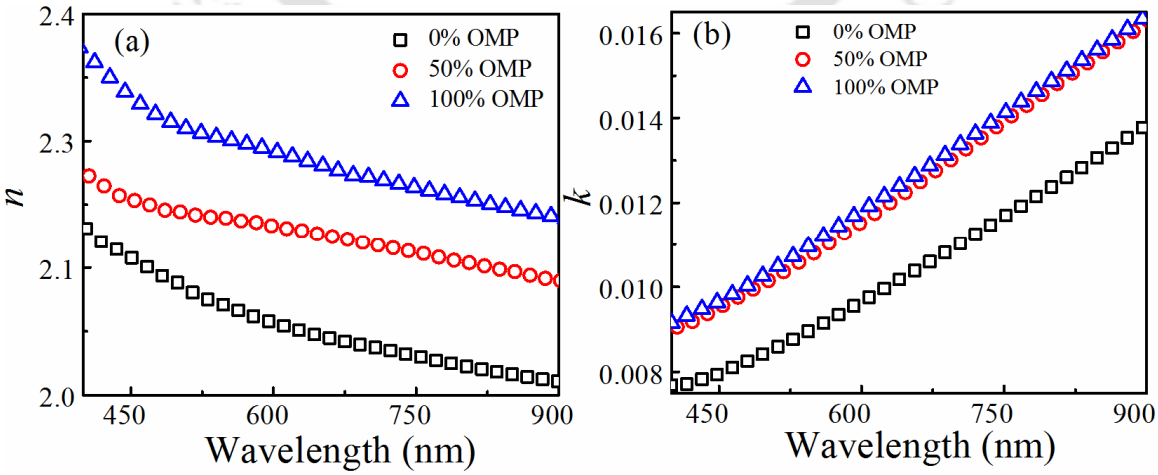

Figure 4.19: *(a) refractive index and (b) extinction coefficient as a function of wavelength of annealed KNN05D thin films deposited at different OMPs.*

The thickness of the films estimated using Swanepoel's method lies in the range of 410 – 430 nm, which is consistent with the profilometer results. The optical packing density (*P*) of the films estimated using the equation (3.3), is in the range of 92.73-99.50% and increases linearly with the OMP. The enhanced packing density and reduction in the oxygen vacancies might be the reason for the larger *n* value for the film deposited under pure oxygen atmosphere. The *k* values estimated using the relation $k = \alpha\lambda/4\pi$, where, α is the linear absorption coefficient and λ is the wavelength. The variations in the *k* values of the films deposited under different OMPs are shown in Figure 4.19(b) and it is found to be increasing from 1.5×10^{-2} to 1.9×10^{-2} (at 700 nm) with a rise in the OMP due to the high packing density and larger grain size.

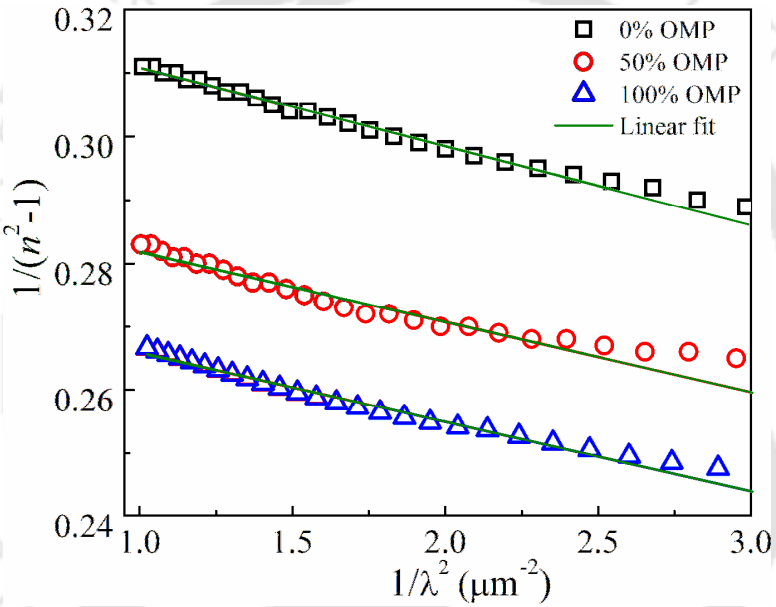

Figure 4.20: *The $(n^2-1)^{-1}$ versus λ^{-2} plot for the single oscillator model fitting of KNN05D thin films deposited at various OMPs.*

It is clearly seen that the observed dispersion is observed in the refractive index in the lower wavelength region and becomes fairly flat above 500 nm. Therefore, the dispersion in the refractive index is analyzed using Wemple and DiDomenico (W-D) single oscillator model [69-70]. The equation (3.6) of chapter 3 is used to analyze the W-D model, where the linear variation between the $(n^2-1)^{-1}$ versus λ^{-2} plot, confirms the validity of this model. The parameters such as E_o, E_d, S_o, and n_∞ values are extracted from the slope and intercept of the corresponding straight line as shown in Figure 4.20. The obtained values are listed in Table 4.9. The obtained E_o and E_d values of the thin films are consistent with the six coordinated oxides [71]. The refractive index dispersion parameter (E_o/S_o) found to be decreased with the rise in OMP and the value of E_o/S_o for the films

deposited under pure oxygen atmosphere exhibited the value of 6.84×10^{-14} *eV*. m^2, which is consistent with most probable value of $6 \pm 0.5\times10^{-14}$ *eV*. m^2 [69].

Table 4.9: *Optical parameters of annealed KNN05D thin films deposited under various OMPs.*

OMP (%)	n_{700}	E_o (*eV*)	E_d (*eV*)	S_o (10^{14} m^{-2})	n_∞	E_o/S_o (10^{-14} *eV*. m^2)	Thickness (nm)
0	2.08	6.36	19.70	0.81	2.02	7.84	430
50	2.16	6.37	21.76	0.89	2.10	7.10	415
100	2.21	6.24	22.55	0.91	2.14	6.84	410

The optical bandgap of the KNN05D thin films was measured using Tauc relation [72]. The direct bandgap (E_g) of the annealed KNN05D films calculated from the extrapolated linear portion of $(\alpha hv)^2$ versus (hv) curve, which is shown in Figure 4.21. The marginal reduction in the E_g was observed with the rise in the OMP is due to the increase in the grain size as well as crystallinity of the films. The obtained E_g values were in the range of 4.28 - 4.30 *eV* and are slightly lower as compared to that of pure KNN thin films (4.29 - 4.37 *eV*). The obtained bandgap values are in good agreement with the average oscillator energy values (E_o= 1.46-1.48E_g) [70].

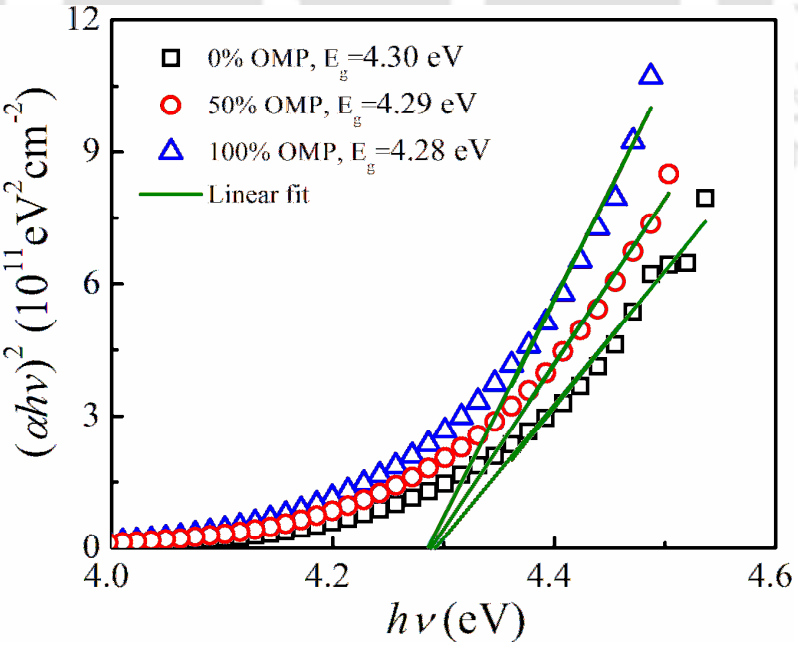

Figure 4.21: *Tauc's absorption edges of annealed KNN05D thin films deposited under different OMPs.*

4.4.4.2 Nonlinear optical properties

The intensity dependent (nonlinear) optical properties of KNN05D thin films were studied using modified single beam z-scan technique [73]. In this technique, sample transmittance is measured as a function of sample position with respect to the focal plane, in the longitudinal direction. The experimental procedure for the measurement using z-scan technique is explained in chapter 2 (section 2.3.10.2). The beam waist (ω_0) and Rayleigh length ($z_0 = \pi\omega_0^2/\lambda$) of the focused, beam was estimated to be 22.58 μm and 2.53 mm, respectively. The peak intensity (I_0) at the focus is estimated as, 7.47 kW/cm^2. The nonlinear absorption coefficient (β_{eff}) estimated from the open aperture (OA) z-scan curve, which is obtained from the integrated intensity over the entire image as a function of sample position with respect to focal plane. The closed aperture (CA) z-scan curve is obtained from the integrated intensity of the partially masked images of open z-scan. The nonlinear refractive index (n_2) extracted by dividing the closed aperture signal with open aperture signal.

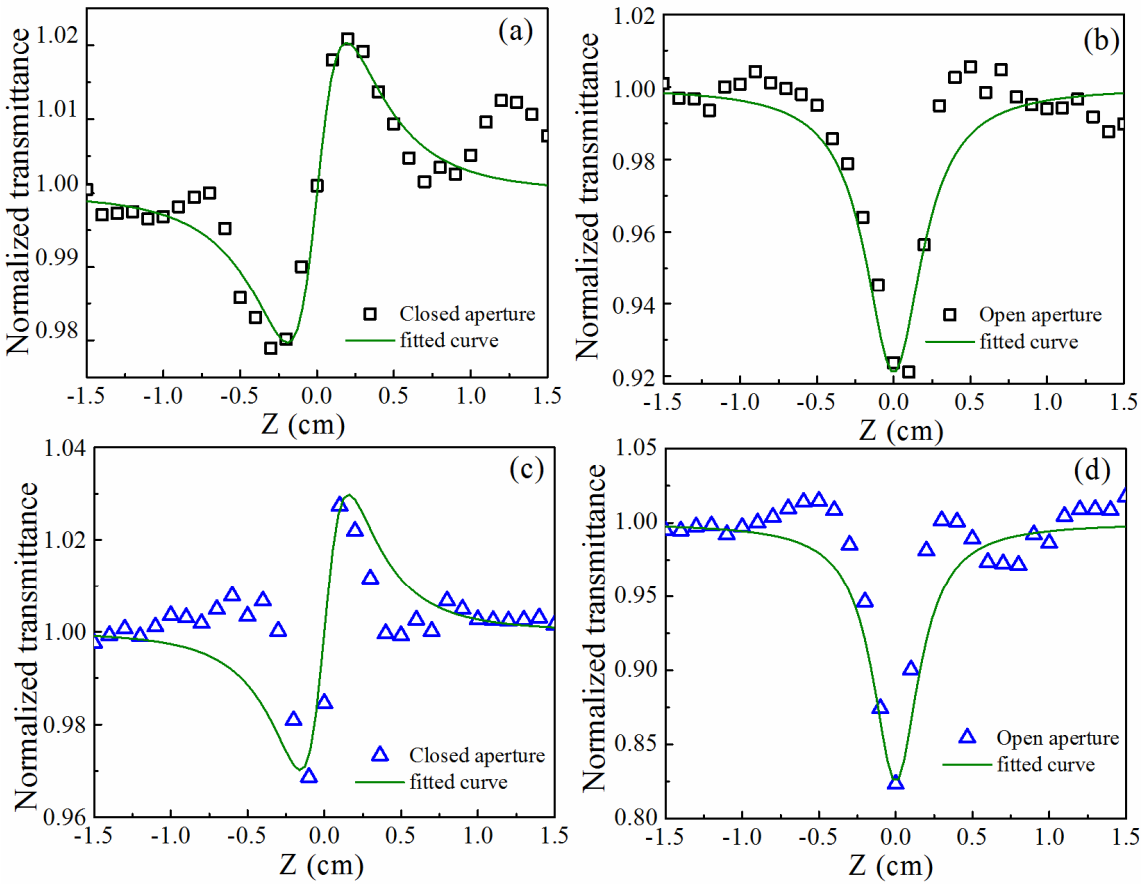

Figure 4.22: *Z-scan plots for the annealed KNN05D thin films deposited under pure argon plasma ((a), (b)) and pure oxygen plasma ((c), (d)). The symbols are the experimental data, and the solid lines are theoretical fit curves.*

The CA and OA z-scan curves of the annealed KNN05D thin films deposited under pure argon and pure oxygen plasmas are shown Figure 4.22. The OA curve of the films exhibited the transmittance minima at z = 0, confirming the reverse saturation nonlinear absorption process in the films. The CA curve of the KNN05D films exhibited a pre-focal valley followed by a post-focal peak, indicating the positive nature of the nonlinear refractive index as a result of self-focusing behavior in the films. The measured values of n_2, β_{eff}, $\chi_R^{(3)}$, $\chi_I^{(3)}$, and $|\chi^{(3)}|$ using the equations (2.36-2.39) are listed in the Table 4.10. Both the films (0 and 100% OMP) showed the strong optical nonlinearity and the larger value of n_2 (7.04×10^{-6} cm^2/W) observed for the 100% OMP film is attributed to the higher optical packing density, linear refractive index and tetragonality ratio. The nonlinear absorption coefficient also found to be increased from 0.735 to 1.70 cm/W with the rise in OMP due to the large value of the linear absorption coefficient (α = 2438 cm^{-1}) in 100% OMP film as compared to 0% OMP film (1999 cm^{-1}). The higher packing density in the sample causes the large absorption of laser energy and thermal agitation of particles leads to the change in the temperature; therefore, the optical nonlinearity found to be enhanced. It is also observed that the both $\chi_R^{(3)}$ and $\chi_I^{(3)}$ found to be improved with increasing the OMP. The larger value of third order nonlinear susceptibility ($|\chi^{(3)}|$ = 1.40 $\times10^{-3}$ esu) was obtained for the film deposited under pure oxygen atmosphere. The obtained larger nonlinear optical properties of KNN05D thin films suggest that the Dy_2O_3 doped KNN thin films are the potential candidate for the applications in nonlinear photonic devices.

Table 4.10: *Nonlinear optical properties of KNN05D thin films deposited under pure argon and oxygen plasmas, measured using z-scan method.*

OMP (%)	n_2 (10^{-6} cm^2/W)	β_{eff} (cm/W)	$\chi_R^{(3)}$ (10^{-3} esu)	$\chi_I^{(3)}$ (10^{-3} esu)	$\|\chi^{(3)}\|$ (10^{-3} esu)
0	4.92	0.73	0.55	0.41	0.69
100	7.04	1.70	0.89	1.08	1.40

4.4.5 Dielectric properties

4.4.5.1 Low frequency dielectric properties

The dielectric properties of the KNN05D thin films were measured over the frequency range from 1 kHz to 1 MHz and are displayed in Figure 4.23. All the films exhibited the strong dispersion in ε_r in the frequency range of 1 kHz-100 kHz and decreases

monotonically with increasing the frequency. A stable frequency dependent ε_r was observed over the frequency range of 100 kHz-1MHz. The larger value of ε_r (343) and lower *tanδ* (0.045) are observed for the film deposited under 100% OMP, measured at frequency 1MHz. The obtained *tanδ* values are in the range of 4% - 11%.

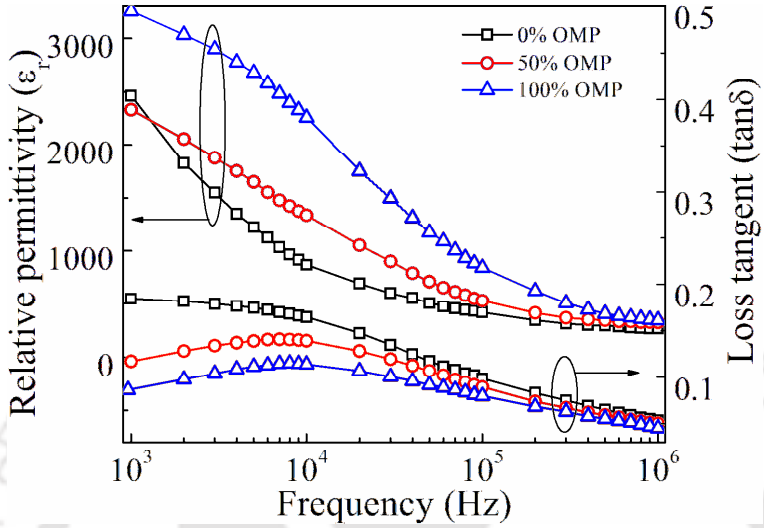

Figure 4.23: *The dielectric properties of KNN05D thin films measured in the frequency range of 1 kHz-1 MHz.*

Li *et al*. [74] reported the dielectric properties (ε_r = 551 and *tanδ* = 0.03 at 100 kHz) of KNN thin films deposited on $LaNiO_3$ using RF magnetron sputtering method. Blomqvist *et al.* [75] also reported the ε_r = 470 and *tanδ* = 0.01 (at 100 kHz) of epitaxial KNN thin films grown on $LaAlO_3$ substrates. However, the obtained dielectric properties were found to be higher than the values as compared to other reports [76-77].

4.4.5.2 Microwave dielectric properties

The microwave dielectric properties of KNN05D thin films were measured using SPDR method at the spot frequencies 5, 10 and 15 GHz. The relative permittivity and loss tangent of the films were calculated based on the thickness and resonant frequencies in iterative method by using equations (2.40 & 2.41) of chapter 2 [78]. The measured ε_r and *tanδ* of the KNN05D thin films at microwave frequencies were listed Table 4.11. The microwave relative permittivity of the KNN05D thin films deposited on quartz substrates increases with rise in OMP. It might be due to the larger grain size, higher packing density and tetragonality ratio. Generally, the high values of relative permittivity in ABO_3 perovskite materials is mainly attributed to the higher *c/a* ratio, which is caused by the large ionic polarization facilitated by lattice vibrations of BO_6 octahedra. The blue shift in the v_1 mode and decrease in the FWHM indicates the enhancement in the polarization

with rise in the OMP. The films deposited under low OMP exhibited the high dielectric losses that might be due to the existence of oxygen deficiencies, which further reduced with the rise in OMP. Therefore, the loss tangent values decrease with increasing the OMP. It is also observed that the relative permittivity decreases from 332 to 281, whereas loss tangent values increase from 0.012 to 0.019 with increase in the frequency from 5 GHz to 15 GHz for the film deposited in pure oxygen atmosphere. The improved microwave dielectric properties with OMP also observed for the BST thin films [79]. The best microwave dielectric properties of KNN05D thin films are obtained as compared to the pure KNN thin films [20], which is due to the higher tetragonality ratio (1.0036) in the films. The higher relative permittivity and low loss tangent are the essential parameters for the fabrication of high-performance piezoelectric devices and microwave tunable devices.

Table 4.11: *Microwave dielectric properties of KNN05D thin films, measured by using SPDR technique.*

OMP (%)	5 GHz		10 GHz		15 GHz	
	ε_r	$tan\delta$	ε_r	$tan\delta$	ε_r	$tan\delta$
0	304	0.017	274	0.023	255	0.036
50	317	0.016	294	0.019	271	0.028
100	332	0.012	307	0.014	281	0.019

4.4.6 Leakage current characteristics

The leakage current characteristics (*J-E*) of annealed KNN05D thin films deposited under different OMPs, measured at room temperature are displayed in Figure 4.24(a). The current density of all the films increases exponentially with an applied electric field and relatively low value of leakage current density (9.90×10^{-9} A/cm^2) at high electric field (150 kV/cm) observed for the 100% OMP film, which is attributed to the better crystallinity and dense microstructure. At lower OMPs, the leakage current density is found to be enhanced to 9.92×10^{-9} A/cm^2 and 1.17×10^{-8} A/cm^2 (at 150 kV/cm) for the films deposited under 50% OMP and 0% OMP, respectively. This can be attributed to the presence of oxygen vacancies and large number of grain boundaries. The obtained leakage current found to be lower as compared to the highly (001) oriented KNN thin films deposited on $LaNiO_3$ substrates (~10^{-6} A/cm^2 at 150 kV/cm) and on SRO/STO substrate (10^{-7} A/cm^2 at 150 kV/cm) prepared by RF magnetron sputtering method [74,

80], and even found to be lower compared to the films deposited using PLD [81] and cobalt doped KNN thin films prepared using chemical solution deposition method [82].

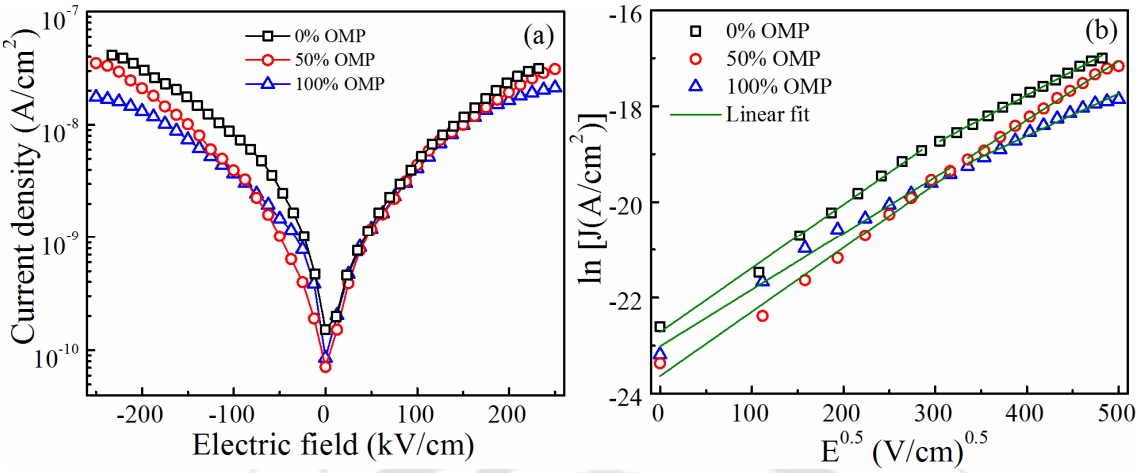

Figure 4.24: *(a) Leakage current densities, (b) Poole-Frenkel Emission conduction fitting of the KNN05D thin films deposited at different OMPs.*

In addition, the log*J*–log*E* plots were employed to confirm the conduction mechanism in KNN05D thin films deposited at different OMPs. In the positive electric field side, two different slopes were observed and in the range of 1.33-1.49 in the low electric fields (≤ 75 kV/cm) and 1.91-2.26 in the high electric fields. It indicates that the space charge limited current (SCLC) ($J \propto E^{\gamma}$, $\gamma > 1$) conduction mechanism is dominant in the high field region [83]. However, for the negative side, the obtained slopes are in the range of 1-1.36 and 1.73-2.35 for the low and high field regions, respectively. Therefore, ln(J) - $E^{0.5}$ plots were analyzed to know the conduction mechanism is either Schottky emission (SE) or Poole–Frenkel emission (PFE) conduction mechanism, where the linear variation in the ln(J) versus $E^{0.5}$ is the validity of the both mechanisms (Figure 4.24(b)). These conduction mechanisms are explained using following relation [84],

$$J = J_0 \exp\left(\frac{\beta E^{0.5}}{k_B T}\right) \tag{4.12}$$

where, J_0 is a pre-exponential constant, E is the applied electric field, k_B is Boltzmann's constant, T is the absolute temperature, and β can be obtained from the slope of the ln(J) versus $E^{0.5}$ curve, which is related to the high frequency relative permittivity (ε_∞) according to the following equation,

$$\beta = \left(\frac{e^3}{\alpha \pi \varepsilon_0 \varepsilon_\infty}\right)^{0.5} \tag{4.13}$$

here, *e* is the charge of electron; ε_0 is vacuum permittivity, and the constant $\alpha = 1$ for PFE and $\alpha = 4$ for SE conduction mechanisms. The refractive index of the films calculated from ε_∞ using the relation, $n = \varepsilon_\infty^{0.5}$. The calculated *n* values lie in the range of 1.96 - 2.26 (2.26 - 2.45) by considering α value as 1, whereas the *n* values for the $\alpha = 4$ are in the range of 0.97 - 1.12 (1.12 - 1.22) for the positive (negative) electric field side, respectively. It is also observed that *n* value found to be increases with a rise in OMP. The estimated *n* values using PFE conduction mechanism are comparable to optical findings (2.05-2.18) and consistent with the earlier reports [18]. Therefore, it is concluded that the PFE conduction mechanism is dominant in the KNN05D thin films. The obtained results suggest that the Dy_2O_3 doped KNN thin films are suitable candidates for the applications in nonlinear optical devices and high frequency devices.

4.5 Conclusions

- KNN + *x* wt.% Dy_2O_3 ($x = 0$ - 1.5) ceramics have been prepared by solid state reaction method.
- Frequency and temperature dependent dielectric properties were revealed that the composition with $x = 0.5$ exhibited the better dielectric properties and relaxor behaviour was observed in $x \geq 1.0$ compositions.
- The relaxor behaviour of the KNN + *x* wt.% Dy_2O_3 ($x = 1.0$ and 1.5) ceramics is analyzed using modified Curie-Weiss law and Vogel-Fulcher law.
- The improved dielectric properties ($\varepsilon_r = 677$ and $tan\delta = 0.04$ at 1MHz), ferroelectric properties ($2P_r = 27.36$ μC/cm^2 and $2E_c = 15.46$ kV/cm) and tunability (3.95%) were observed for the KNN + 0.5 wt.% Dy_2O_3 composition.
- KNN + 0.5 wt.% Dy_2O_3 thin films deposited by using RF magnetron sputtering technique.
- The improved refractive index ($n_{700} = 2.21$), optical packing density (99.5%), and lower optical bandgap (4.28 *eV*) were obtained for the film deposited under pure. oxygen plasma.
- The nonlinear optical properties of the KNN05D thin films measured using modified z-scan technique. The large values of optical nonlinear refractive index (7.04×10^{-6} cm^2/W), nonlinear absorption (1.70 cm/W), and third order nonlinear susceptibility (1.40×10^{-3} esu) showed that the Dy_2O_3 doped KNN thin films are promising candidates for nonlinear photonic devices.

- The SPDR technique is employed to measure the microwave dielectric properties of KNN05D thin films and the enhanced microwave dielectric properties were observed for the annealed films deposited under pure oxygen plasma.
- The PFE conduction mechanism is dominant conduction mechanism in the KNN05D thin films and low leakage current density (9.90×10^{-9} A/cm^2 at 150 kV/cm) was observed for the 100% OMP film.

4.6 References

[1] E. Buixaderas, V. Bovtun, M. Kempa, M. Savinov, D. Nuzhnyy, F. Kadlec, P. Vaněk, J. Petzelt, M. Eriksson and Z. Shen, *J. Appl. Phys*. **107** [1] (2010) 014111.

[2] G. Shirane, R. Newnham and R. Pepinsky, *Phys. Rev*. **96** [3] (1954) 581.

[3] P. Dubernet and J. Ravez, *Ferroelectr.* **211** [1] (1998) 51.

[4] Y. Saito, H. Takao, T. Tani, T. Nonoyama, K. Takatori, T. Homma, T. Nagaya and M. Nakamura, *Nat.* **432** [7013] (2004) 84.

[5] L. Zhengfa, L. Yongxiang and Z. Jiwei, *Curr. Appl. Phys.* **11** [3] (2011) S2.

[6] B.-Q. Ming, J.-F. Wang, P. Qi and G.-Z. Zang, *J. Appl. Phys*. **101** [5] (2007) 054103.

[7] J. Wu, D. Xiao, Y. Wang, J. Zhu, L. Wu and Y. Jiang, *Appl. Phys. Lett.* **91** [25] (2007) 252907.

[8] J. Minhong, D. Manjiao, L. Huaxin, W. Shi and L. Xinyu, *Mater. Sci. Eng. B* **176** [2] (2011) 167.

[9] Z. Wang, Y. Zhuo, D. Xiao, W. Wu, C. Zhang, X. Huang and J. Zhu, *Curr. Appl. Phys.* **11** [3] (2011) S143.

[10] D. Gao, K. W. Kwok, D. Lin and H. L. W. Chan, *J. Mater. Sci.* **44** [10] (2009) 2466.

[11] J. Yoo and B. Seo, *Ferroelectr.* **425** [1] (2011) 106.

[12] J. Hao, Z. Xu, R. Chu, W. Li and J. Du, *J. Appl. Phys*. **117** [19] (2015) 194104.

[13] Y. Wei, Z. Wu, Y. Jia, J. Wu, Y. Shen and H. Luo, *Appl. Phys. Lett.* **105** [4] (2014) 042902.

[14] I. Kanno, T. Ichida, K. Adachi, H. Kotera, K. Shibata and T. Mishima, *Sens. Actuators A: Phys.* **179** (2012) 132.

[15] B. Zhu, Z. Zhang, T. Ma, X. Yang, Y. Li, K. K. Shung and Q. Zhou, *Appl. Phys. Lett.* **106** [17] (2015) 173504.

[16] L. Wang, W. Ren, P. Shi, X. Chen, X. Wu and X. Yao, *Appl. Phys. Lett.* **97** [7] (2010) 072902.

[17] M. Abazari, T. Choi, S. W. Cheong and A. Safari, *J. Phys. D: Appl. Phys.* **43** [2] (2010) 025405.

[18] M. Blomqvist, S. Khartsev, A. Grishin and A. Petraru, *Integr. Ferroelectr.* **54** [1] (2003) 631.

[19] M. Blomqvist, S. Khartsev and A. Grishin, *Integr. Ferroelectr.* **80** [1] (2006) 97.

[20] M. Peddigari, B. Sindam, K. C. J. Raju and P. Dobbidi, *J. Am. Ceram. Soc.* **98** [5] (2015) 1444.

[21] P. Mahesh and D. Pamu, *Thin Solid Films* **562** (2014) 471.

[22] Y. B. Yao, H. T. Chan, C. L. Mak and K. H. Wong, *Thin Solid Films* **537** (2013) 156.

[23] K. Wang and J.-F. Li, *Appl. Phys. Lett.* **91** [26] (2007) 262902.

[24] B.-P. Zhang, J.-F. Li, K. Wang and H. Zhang, *J. Am. Ceram. Soc.* **89** [5] (2006) 1605.

[25] D. Lin, K. W. Kwok, H. Tian and H. W. L.-w. Chan, *J. Am. Ceram. Soc.* **90** [5] (2007) 1458.

[26] M. Matsubara, K. Kikuta and S. Hirano, *J. Appl. Phys.* **97** (2005) 114105.

[27] S. Zhang, R. Xia, T. R. Shrout, G. Zang and J. Wang, *J. Appl. Phys.* **100** [10] (2006) 104108.

[28] Y. Zhen and J.-F. Li, *J. Am. Ceram. Soc.* **89** [12] (2006) 3669.

[29] R. Zuo, J. Rödel, R. Chen and L. Li, *J. Am. Ceram. Soc.* **89** [6] (2006) 2010.

[30] A. W. Hewat, *J. Phys. C: Solid State Phys.* **6** [16] (1973) 2559.

[31] C. Zhi-Hui, D. Jian-Ning, M. Lin, Y. Ning-Yi and Z. Wei-Wei, *Ferroelectr.* **425** [1] (2011) 63.

[32] K.-i. Kakimoto, K. Akao, Y. Guo and H. Ohsato, *Jpn J Appl. Phys.* **44** [9B] (2005) 7064.

[33] R. Singh, K. Kambale, A. R. Kulkarni and C. S. Harendranath, *Mater. Chem. Phys.* **138** [2-3] (2013) 905.

[34] H. J. Trodahl, N. Klein, D. Damjanovic, N. Setter, B. Ludbrook, D. Rytz and M. Kuball, *Appl. Phys. Lett.* **93** [26] (2008) 262901.

[35] Y. Wang, L. Hu, Q. Zhang and H. Yang, *Dalton Trans.* **44** [30] (2015) 13688.

[36] W. L. Zhu, J. L. Zhu, Y. Meng, M. S. Wang, B. Zhu, X. H. Zhu, J. G. Zhu, D. Q. Xiao and G. Pezzotti, *J. Phys. D: Appl. Phys.* **44** [50] (2011) 505303.

[37] P. Fu, Z. Xu, R. Chu, W. Li, Q. Xie, Y. Zhang and Q. Chen, *J. Alloy. Compd.* **508** [2] (2010) 546.

[38] D. Lin, K. W. Kwok and H. L. W. Chan, *J. Phys. D: Appl. Phys.* **40** [21] (2007) 6778.

[39] E. Buixaderas, V. Bovtun, M. Kempa, M. Savinov, D. Nuzhnyy, F. Kadlec, P. Vaněk, J. Petzelt, M. Eriksson and Z. Shen, *J. Appl. Phys.* **107** [1] (2010) 014111.

[40] H. Yu and Z.-G. Ye, *J. Appl. Phys.* **103** [3] (2008) 034114.

[41] H. Cheng, W. Zhou, H. Du, F. Luo, D. Zhu, D. Jiang and B. Xu, *J. Alloy. Compd.* **579** (2013) 192.

[42] S. Xiao, S. Deng, J. Zhang, Y. Zhou, J. Tang, Y. Wang, L. Wang, H. Qi and J. Wang, *Ceram. Int.* **38** [7] (2012) 6071.

[43] V. V. Shvartsman, D. C. Lupascu and D. J. Green, *J. Am. Ceram. Soc.* **95** [1] (2012) 1.

[44] L. E. Cross, *Ferroelectr.* **151** [1] (1994) 305.

[45] H. Du, W. Zhou, F. Luo, D. Zhu, S. Qu and Z. Pei, *Ferroelectr.* **401** [1] (2010) 141.

[46] G. H. Jonker, *Mater. Res. Bull.* **18** [3] (1983) 301.

[47] K. Uchino and S. Nomura, *Ferroelectr.* **44** [1] (2011) 55.

[48] H. Du, W. Zhou, F. Luo, D. Zhu, S. Qu and Z. Pei, *J. Appl. Phys.* **105** [12] (2009) 124104.

[49] A. A. Bokov and Z. G. Ye, *J. Mater. Sci.* **41** [1] (2006) 31.

[50] D. Viehland, S. J. Jang, L. E. Cross and M. Wuttig, *J. Appl. Phys.* **68** [6] (1990) 2916.

[51] X. Long and Z.-G. Ye, *Appl. Phys. Lett.* **90** [11] (2007) 112905.

[52] V. Bobnar, J. Bernard and M. Kosec, *Appl. Phys. Lett.* **85** [6] (2004) 994.

[53] F. A. Kröger and H. J. Vink, Solid State Physics, *Academic Press*, New York (1956).

[54] A. K. Roy, A. Singh, K. Kumari, K. Amar Nath, A. Prasad and K. Prasad, *ISRN Ceram.* **2012** (2012) 1.

[55] R. M. Hill, *Phys. status solidi (a)* **34** [2] (1976) 601.

[56] J. J. Hauser, *Phys. Rev. B* **9** [6] (1974) 2623.

[57] S. Upadhyay, O. Parkash and D. Kumar, *J. Electroceram.* **18** [1-2] (2007) 45.

[58] I. Rawal and A. Kaur, *J. Appl. Phys.* **115** [4] (2014) 043717.

[59] S. De, S. Niranajana, B. Satyanarayana and M. Rao, *J. Optoelectron. Adv. Mater. Rapid Commun.* **3** [12] (2009) 1365.

[60] V. Ambegaokar, B. I. Halperin and J. S. Langer, *Phys. Rev. B* **4** [8] (1971) 2612.

[61] H. Han, C. Davis and J. C. Nino, *J. Phys. Chem. C* **118** [17] (2014) 9137.

[62] X. Chou, J. Zhai, H. Jiang and X. Yao, *J. Appl. Phys.* **102** [8] (2007) 084106.

[63] Y. Chen, X.-L. Dong, R.-H. Liang, J.-T. Li and Y.-L. Wang, *J. Appl. Phys.* **98** [6] (2005) 064107.

[64] N. Ishizawa, J. Wang, T. Sakakura, Y. Inagaki and K.-i. Kakimoto, *J. Solid State Chem.* **183** [11] (2010) 2731.

[65] C.-R. Cho, and A. Grishin, *J. Appl. Phys.* **87** [9] (2000) 4439.

[66] F. Rubio-Marcos, A. Del Campo, P. Marchet, and J. F. Fernandez, *Nat. Commun.* **6** (2015) 6594.

[67] D. Bao, H. Yang, L. Zhang, and X. Yao, *Phys. Stat. Sol. (a)* **169** [2] (1998) 227.

[68] R. Swanepoel, *J. Phys. E: Sci. Instrum.* **16** [12] (1983) 1214.

[69] M. DiDomenico Jr., and S.H. Wemple, *J. Appl. Phys.* **40** (1969) 720.

[70] F. Yakuphanoglu, A. Cukurovali, and İ. Yilmaz, *Physica B* **353** [3-4] (2004) 210.

[71] S. H. Wemple, and M. DiDomenico, *Phys. Rev. B* **3** [4] (1971) 1338.

[72] J. C. Tauc, Optical Properties of Solids, F. Abeles ed. *North-Holland Publishing*, Amsterdam (1972).

[73] I. Kumar, and A. Khare, *Opt. Laser Technol.* **77** (2016) 51.

[74] T. Li, G. Wang, D. Remiens, and X. Dong, *Ceram. Int.* **39** [2] (2013) 1359.

[75] M. Blomqvist, J.-H. Koh, S. Khartsev, A. Grishin and J. Andréasson, *Appl. Phys. Lett.* **81** [2] (2002) 337.

[76] X. Yan, W. Ren, X. Wu, P. Shi, and X. Yao, *J. Alloy. Compd.* **508** [1] (2010) 129.

[77] L. Yao, K. Zhu, J. Wang, J. Liu, J. Qiu, M. Cheng, and Q. Gu, *Ferroelectr.* **493** [1] (2016) 47.

[78] J. Krupka, A. P. Gregory, O. C. Rochard, R. N. Clarke, B. Riddle, and J. Baker-Jarvis, *J. Eur. Ceram. Soc.* **21** [15] (2001) 2673.

[79] K. V. Saravanan, K. Sudheendran, M. G. Krishna, and K. C. James Raju, *Ferroelectr.* **356** [1] (2007) 158.

[80] T. Li, G. Wang, K. Li, G. Du, Y. Chen, Z. Zhou, D. Rémiens, and X. Dong, *Ceram. Int.* **40** [1] (2014) 1195.

[81] A. Tian, W. Ren, L. Wang, P. Shi, X. Chen, X. Wu, and X. Yao, *Appl. Surf. Sci.* **258** [7] (2012) 2674.

[82] L. Wang, W. Ren, P. Shi, X. Wu, *J. Alloy. Compd.* **608** (2014) 202.

[83] A. Rose, *Phys. Rev.* **97** [6] (1955) 1538.

[84] J. G. Simmons, *Phys. Rev.* **155** [3] (1967) 657.

Chapter 5

Dielectric and ac-conductivity studies of Gd_2O_3 doped $(K_{0.5}Na_{0.5})NbO_3$ bulk and thin films

Due to the hygroscopic and volatile nature of alkali elements, it is difficult to get the high density, good dielectric, ferroelectric and piezoelectric properties of KNN ceramics by using solid state reaction method. In order to improve the dielectric and ferroelectric properties, KNN ceramics were doped with suitable elements and added with various sintering aids. In the present chapter, we have studied the effect of rare-earth oxide Gd_2O_3 on structural, microstructural, dielectric properties of KNN ceramics and optimized the best composition to deposit the thin films.

5.1 Literature survey

The KNN ceramics exhibited the improved dielectric properties, ferroelectric properties and piezoelectric properties prepared using hot pressing, spark plasma sintering techniques compared to conventional solid state sintering method [1-2]. However, those techniques are very expensive to produce the large number of samples. Therefore, in order to enhance the performance of KNN ceramics, it is essential to use different additives or suitable dopants. The improved sinterability with the reduced piezoelectric properties of KNN ceramics were observed by the addition of sintering aids like MnO_2, $K_4CuNb_8O_{23}$ and $K_{1.94}Zn_{1.06}Ta_{5.19}O_{15}$ [3-5]. Saito *et al.* [6] reported the most enhanced properties (ε_r = 1570, T_C = 253 ^oC, d_{33} = 461 pC/N, k_p = 61%) for the KNN ceramics doped with Li^+, Sb^{5+}, and Ta^{5+} ions. Most of the enhanced properties were observed in the KNN system either in the composite form or doped with different elements due to the existence morphotrophic phase boundary (MPB) and the co-existence of tetragonal and orthorhombic phases near room temperature [7-11]. Ahn *et al.* [11] proposed the relation between the longitudinal piezoelectric constant (d_{33}) and tetragonal to orthorhombic transition temperature ($T_{O\text{-}T}$) as d_{33} = (306.21-1.02 $T_{O\text{-}T}$) pC/N. Therefore, the shift in the $T_{O\text{-}T}$ toward room temperature with the enhanced permittivity is required for high performance piezoelectric applications. Few authors also reported the improved dielectric, ferroelectric and piezoelectric properties of rare-earth doped KNN ceramics. Wang *et al.* [12] reported the improved ferroelectric properties (P_r = 42.3 μC/cm^2 and E_c

= 7.2 kV/cm) in Pr_2O_3 doped KNN ceramics. Improved electrical properties (ε_r = 820 and k_p = 38%) and piezoelectric properties (d_{33}= 130 pC/N) were observed in CeO_2 doped KNN ceramics [13]. The La_2O_3 doped $(K_{0.5}Na_{0.5})(Nb_{0.96}Sb_{0.04})O_3$ ceramics also exhibited the enhanced properties (ε_r > 700, k_p = 38%, d_{33}= 160 pC/N, g_{33} = 37.4×10^{-3} Vm/N) [14]. Hao *et al.* [15] reported the photoluminescence (PL) properties with good dielectric (ε_r = 1372, T_C = 328 ^oC) and piezoelectric (d_{33} = 230 pm/V, d_{33} = 176 pC/N, k_p = 35%) properties of 0.4 mol% Sm_2O_3 doped $0.948(K_{0.5}Na_{0.5})NbO_3$ - $0.052LiSbO_3$ ceramics prepared by solid state reaction method. Wei *et al.* [16] reported the 1.2-1.3 times enhancement in the PL intensity, ferroelectric and piezoelectric (P_r = 13.75 μC/cm^2, d_{33} = 108.4 pC/N, k_p = 29%) properties were observed in 0.3% Pr^{3+} doped KNN ceramics. However, there have been no reports on Gd_2O_3 doped KNN bulk and thin films. KNN thin films deposited by using different methods are mainly focused on the dielectric, ferroelectric, piezoelectric properties and linear optical properties [17-25]. However, there is no literature available on the nonlinear optical properties and microwave dielectric properties of the KNN based thin films.

Therefore, in the present chapter, we have investigated the temperature (-140 ^oC – 450 ^oC) and frequency (1 kHz - 1 GHz) dependent dielectric properties and ac-conductivity studies of $(K_{0.5}Na_{0.5})NbO_3$+ x wt.% Gd_2O_3 ($0 \leq x \leq 1.5$) ceramics. The composition with good dielectric and ferroelectric properties was chosen to make the target to deposit the thin film by RF reactive magnetron sputtering and studied their liner, nonlinear and microwave dielectric properties.

5.2 Experimental details

Standard solid state reaction method has been adopted for the synthesis of KNN+ x wt.% Gd_2O_3 system (x = 0 - 1.5). For this commercially available high purity chemicals of potassium carbonate, sodium carbonate, gadolinium oxide, and niobium oxide have been used as precursors. The powders were heated individually at 150 ^oC for 1h in air to remove the moisture present in the chemicals. The stoichiometric amounts of the raw materials were mixed by using ball milling method for 5h with distill water as the grinding media. The obtained slurry was heated at 120 ^oC in air for overnight to remove the water content. These powders are calcined at 750 ^oC for 5 h in air and remilled for 10h with an inclusion of various compositions of x = 0.3, 0.5, 1.0 and 1.5 wt.% of Gd_2O_3. The obtained powders are pressed into pellets of 10 mm diameter and 1mm of thickness using polyvinyl alcohol as a binding agent. These pellets were sealed in an alumina

crucible and sintered at 1050 °C for 5h in air. The optimized composition KNN + 1.0 wt.% Gd_2O_3 (KNN1G) was used as ceramic target to prepare the thin films by RF reactive magnetron sputtering onto quartz and Pt/Ti/SiO_2/Si substrates. The sputtering chamber was evacuated to base pressure of 1.0×10^{-6} Torr and the films deposited at a working pressure 1.0×10^{-2} Torr with the sputtering power 70 W in distinct argon and oxygen mixing percentages (OMP). The KNN1G thin films were deposited at a substrate temperature of 400 °C at different oxygen and argon plasmas and annealed at 700 °C in oxygen atmosphere. The rate of deposition was estimated in different OMPs and deposited for different times to get same thickness for all the films.

5.3 $(K_{0.5}Na_{0.5})NbO_3$+ *x* wt.% Gd_2O_3 (*x* = 0 - 1.5) ceramics

5.3.1 XRD analysis

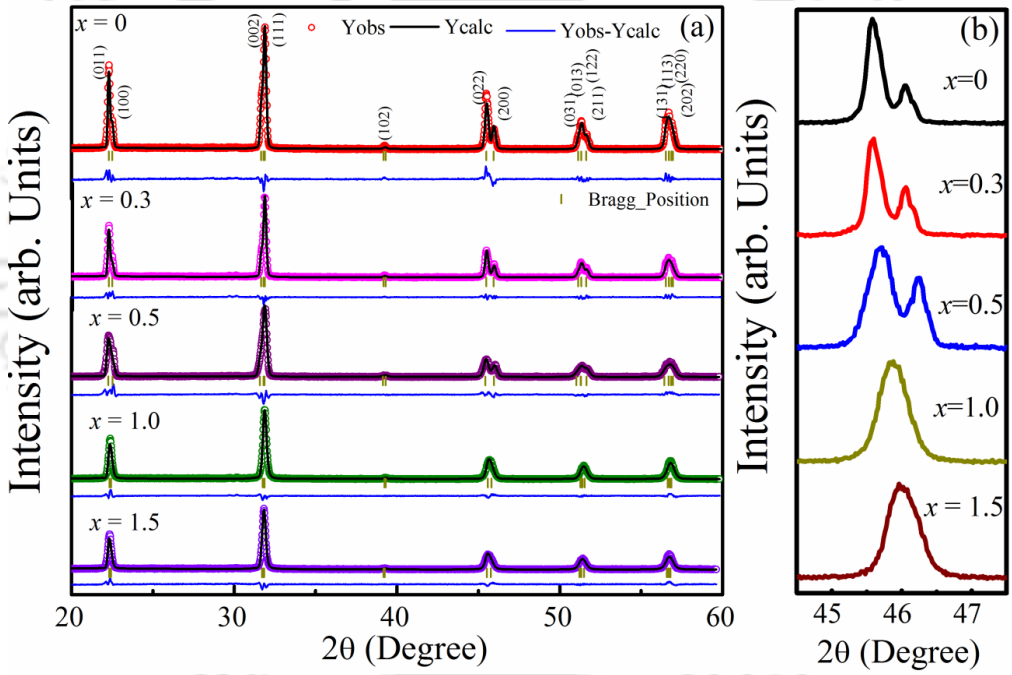

Figure 5.1: *(a) The X-ray diffraction patterns together with the Retvield refined data, and (b) peak position variation of (022) and (200) Brag reflections and intensity for various compositions of KNN+ x wt.% Gd_2O_3 (x = 0 - 1.5) sintered pellets.*

The X-ray diffraction (XRD) pattern along with the Rietveld refinement data of KNN + *x* wt.% Gd_2O_3 (*x* = 0 - 1.5) pellets sintered at 1050 °C for 5 h in air are shown in Figure 5.1(a). For the low concentration of Gd_2O_3 the XRD pattern shows the orthorhombic crystal structure. However, for higher compositions a phase transformation from orthorhombic to pseudo-cubic crystal structure is clearly evident. Such transformation can be clearly seen in the Figure 5.1(b), where the peak position and

intensity variations of (022) and (200) Bragg reflections for various compositions between x = 0 and 1.5 are shown. With increasing the concentration of Gd_2O_3, both the peaks were merged into single peak and shifted towards higher angle side. The refinement was carried out by considering *Amm2* space group [26]. The lattice parameters, atomic positions of the K, Na, Nb, Gd and O atoms, and occupancy have been refined. The corresponding parameters estimated after the refinement being a = 3.9471 ± 0.001Å, b = 5.66117 ± 0.001Å, c = 5.62514 ± 0.002Å for x = 0. The fitting parameters $\chi^2 \approx 9.01$, R_{Brag} factor ≈ 5.60 and R_f factor ≈ 3.17 for the composition x = 0. For pure KNN case we have obtained the unit cell volume V = 125.70 Å^3 and c/a = 1.425. It has been found that both V and c/a decreases with increasing the composition reaching V = 125.41 Å^3 and c/a = 1.424 for x = 1.5. Due to the difference in the ionic radius of the Na^+ (1.02Å) and Gd^{3+} (0.938Å) one can expect increasing degree of distortion of the lattice with the addition of Gd_2O_3 content. Therefore, the pseudo-cubic nature of the crystal structure increases with increasing the Gd_2O_3 content in the KNN matrix.

5.3.2 Raman spectroscopy

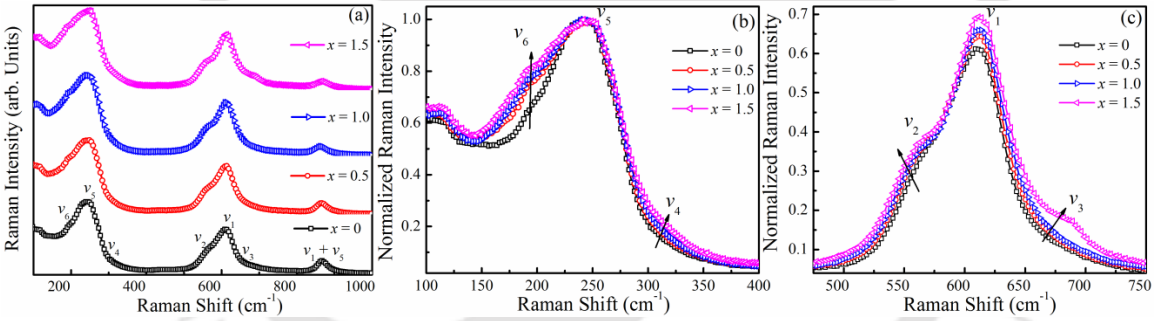

Figure 5.2: *(a) Raman spectra of KNN + x wt.% Gd_2O_3 (x = 0 -1.5) ceramics as function of x. The plots (b) and (c) are the normalized intensities of the v_5 and v_1 modes, respectively.*

Figure 5.2 shows the back-scattered Raman spectra of KNN+ x wt% Gd_2O_3 (x = 0 - 1.5) ceramics measured at room temperature. The pure KNN shows the orthorhombic structure with space group *Amm*2. According to the group theory, orthorhombic *Amm*2 phase consists of $4A_1+4B_1+3B_2+A_2$ Raman active optical modes. All these modes are also infrared active except A_2 mode. The vibrational modes of NbO_6 octahedron consists of $1A_{1g}(v_1)+1E_g(v_2)+2F_{1u}(v_3,v_4)+1F_{2g}(v_5)+1F_{2u}(v_6)$. In these vibrations, $A_{1g}(v_1)$, $E_g(v_2)$, and $F_{1u}(v_3)$ are stretching modes and remaining vibrations are bending modes [27-31]. All the vibrational modes correspond to KNN are present and relatively strong peaks detected around 245 cm^{-1} and 610 cm^{-1}, which are due to the nearly perfect octahedral

symmetry. The peaks appeared in the region below 200 cm^{-1} corresponds to the translational modes of K^+ and Na^+/K^+ cations and rotations of the NbO_6 octahedran. The higher concentrations of Gd_2O_3 may induce the changes in the vibrational modes of NbO_6 octahedron. In order to identify the Raman modes and full width at half maximum (FWHM), the spectra was fitted with the sum of Gaussian peaks.

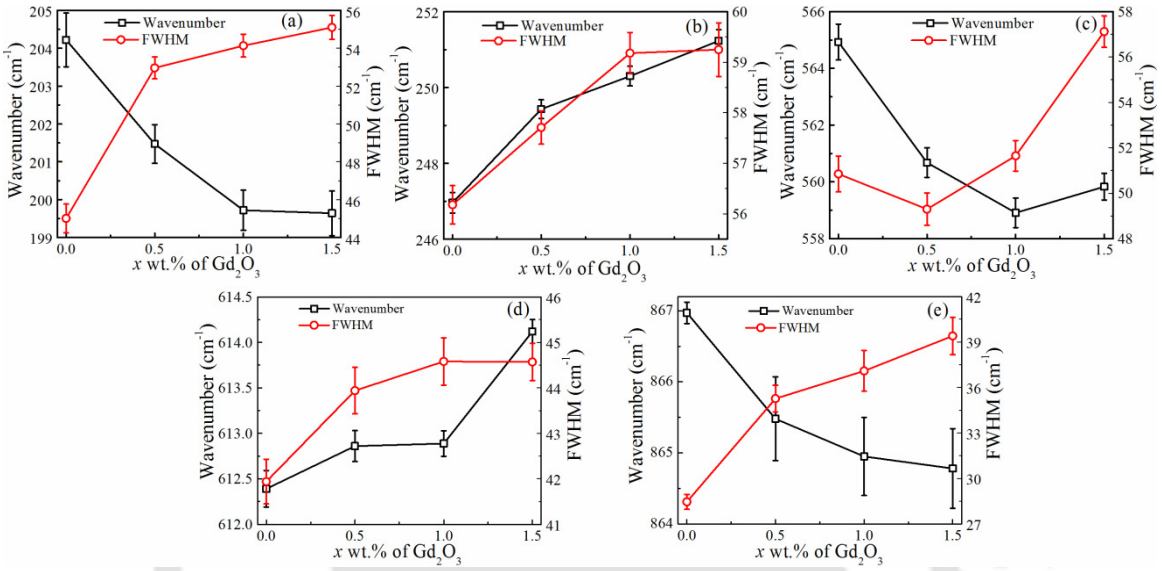

Figure 5.3: *Variation in the Raman shift and FWHM of the modes (a) v_6, (b) v_5, (c) v_2, (d) v_1, and (e) v_1+v_5 for KNN + x wt.% Gd_2O_3 (x = 0 - 1.5) ceramics as a function of x.*

As shown in Figure 5.3, the peak positions of v_1 and v_5 modes are shifted toward higher wavenumbers with increasing the Gd_2O_3 concentration. This might be due to the change in crystal structure from orthorhombic to psuedocubic phase causes the changes in the vibrations of NbO_6 octahedra. The blue shift in the v_1 and v_5 peaks are due to the increase in compressive strain and binding strength caused by shortening of the distance between Nb^{5+} and its coordinated oxygen atoms [27-32]. The incorporation of small Gd^{3+} ions into the A-site of the perovskite structure causes the distortion of O-Nb-O angles and leads to increase the force constant [27]. The FWHM of the both v_1 and v_5 modes also found to increase with increasing x, which indicates structural change in the specimens. It is also observed that, the normalized intensities of the v_1, v_2, and v_5 modes become stronger with increasing the Gd_2O_3 concentration. Particularly, the intensities of v_1 and v_5 modes of doped samples displayed sharper and strong peaks as compared to pure KNN ceramics. This might be due to the increasing of polarizability with the Gd_2O_3 concentration. The incorporation of smaller ionic radii of Gd^{3+} into KNN lattice will increase the distance between the atoms and leads to the enhancement in polarizability as well as vibrational intensity of the corresponding modes. The relative peak intensity of

v_1+v_5 mode is found to be decreases gradually. The peak position slightly shifted to lower wavenumber and FWHM found to increase with increasing of Gd_2O_3 concentration. Ahn *et al*. [30] reported that v_1+v_5 mode is very sensitive to the stoichiometry, excess amounts of K and Na deficiencies. The change in stoichiometry by the addition of Gd_2O_3 in the KNN matrix may lead to change the vibrations of v_1+v_5 mode. Interestingly, the peak intensities of the vibrational mode v_6 and the low frequency band at 110 cm^{-1} were found to increase with an increase in Gd_2O_3 concentration (Figure 5.2(b)). Yao *et al*. [25] reported the phase transition temperatures based on the change in the relative intensities of the two dominant modes (v_1 and v_5) with respect to the low frequency bands. The relative intensities (I_R) of the modes v_1 and v_5 with respect to the frequency band located at 110 cm^{-1} are listed in Table 5.1. The I_R for the modes v_1 (610 cm^{-1}) and v_5 (245 cm^{-1}) can be defined as:

$$I_R = \frac{I_{610}}{I_{110}} and \frac{I_{245}}{I_{110}} \tag{5.1}$$

The relative intensity of the v_5 mode found to be decreased whereas the intensity of v_1 mode enhanced with increasing the concentration of Gd_2O_3. This might be due to the increase in the lattice distortion as well as increase in the polarizability by the incorporation of Gd_2O_3 into the KNN lattice.

Table 5.1: *Relative intensities of the dominant bands v_1 mode and v_5 mode with respect to low frequency band 110 cm^{-1} of KNN + x wt.% Gd_2O_3 (x = 0 - 1.5) ceramics.*

x	I_{245}/I_{110}	I_{610}/I_{110}
x = 0	1.644	1.008
x = 0.5	1.572	1.015
x = 1.0	1.569	1.043
x = 1.5	1.500	1.046

5.3.3 Microstructural analysis

The surface morphology of the KNN+ *x* wt.% Gd_2O_3 (*x* = 0 - 1.5) ceramics sintered at 1050 ^oC for 5h are shown in Figure 5.4. All the samples are found to be highly densified and are in the range 92.23 – 95.34% of the theoretical density (4.51g/cm^3). The maximum density (4.30 g/cm^3) was obtained for the *x* = 1.0 sample. The average grain size of the samples found to be gradually decreased with an increase in the concentration

of Gd_2O_3. The average grain size of the pure KNN (x = 0) ceramics is 2.26 ± 1.07µm, which is further decreases to 0.35 ± 0.13µm for x = 1.5 sample.

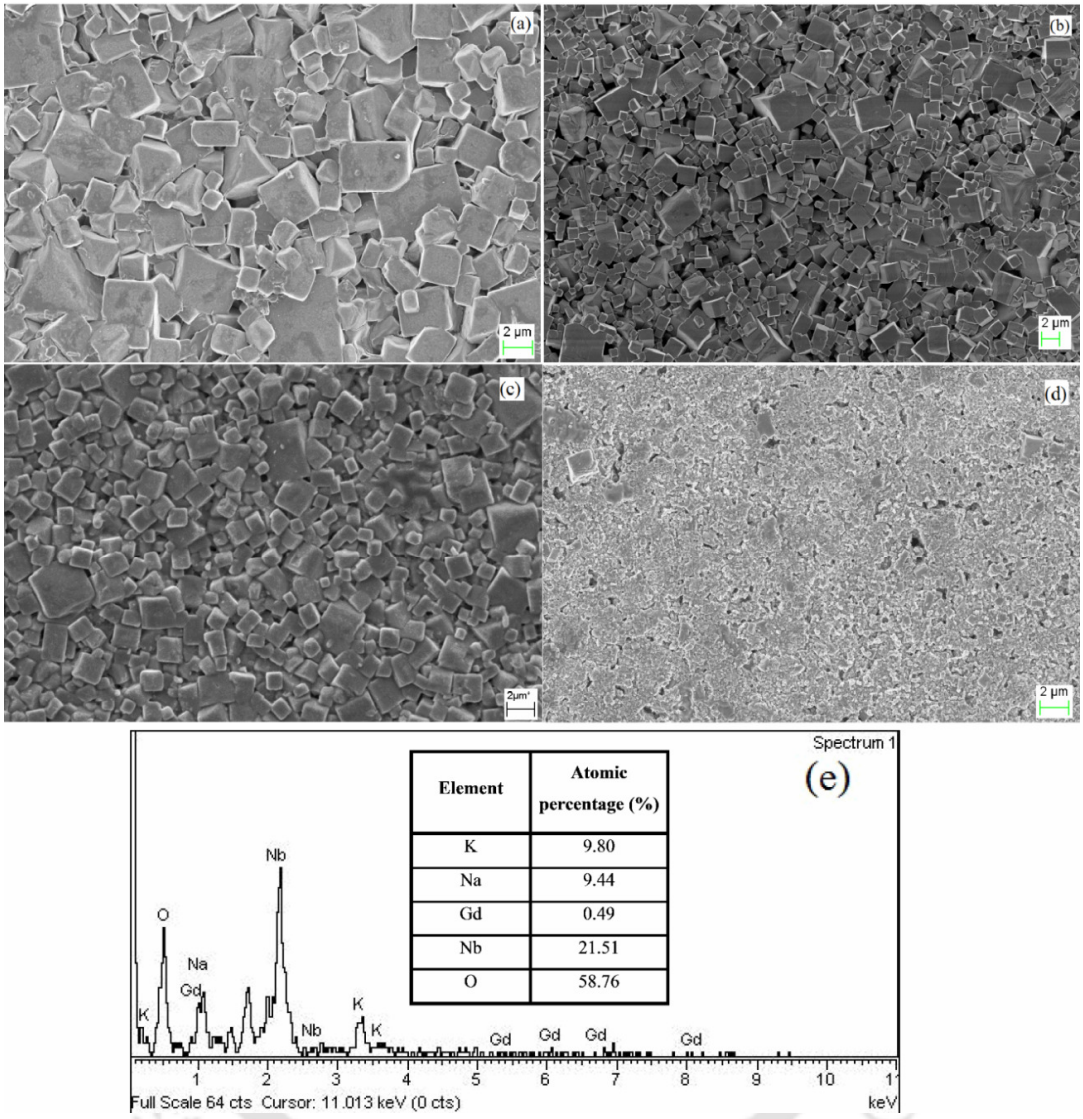

Figure 5.4: *Surface micrographs of the KNN + x wt.% Gd_2O_3 ceramics with (a) x = 0, (b) x = 0.5, (c) x = 1.0, (d) x = 1.5 and (e) EDS spectra of x = 1.0 sample, sintered at 1050 ^oC.*

As the concentration of Gd_2O_3 increases, it can be segregated at the grain boundaries that lead to decrease the mobility and reduce the mass transportation [33]. Therefore, the grain growth found to be inhibited and sub-micrometre grains are formed for x = 1.5 sample. Matsubara *et al.* [34] reported that the small and uniform grain microstructure can enhance the mechanical strength of piezoelectric ceramics. In the present case, KNN+ x wt.% Gd_2O_3 ($x \geq 0.5$) samples have small and homogeneous microstructure, which are suitable for high performance piezoelectric ceramic applications. In order to determine the stoichiometry of the KNN + 1.0 wt.% Gd_2O_3

sintered ceramic, the energy dispersive spectrum analysis is performed and is shown in Figure 5.4(e). The atomic percent of Na, K, Gd and Nb was normalized according to the ABO_3 stoichiometry. It is observed that, the atomic percent of Na (9.44%) found to be lower compared to K (9.80%) in the A-site of the ABO_3 stoichiometry. This might be due to the volatilization of Na atoms during the sintering or the replacement of Gd (0.49%) atoms in the A-site.

5.3.4 Dielectric properties

5.3.4.1 Low frequency dielectric properties

The temperature variation of the relative permittivity (ε_r) of pure KNN and various compositions ($0.3 \leq x \leq 1.5$) of Gd_2O_3 added KNN samples recorded at a constant frequency f = 1 MHz and shown in Figure 5.5(a). Pure KNN system (x = 0) exhibit two cusps across 207 ^oC and 395 ^oC associated with the crystallographic transitions occurring from orthorhombic phase to tetragonal and ordered-ferroelectric tetragonal to disordered-paraelectric cubic phase transitions, respectively. These values are consistent with previously reported values of $T_{O\text{-}T}$ = 193 ^oC and $T_{T\text{-}C}$ = 400 ^oC [35]. A progressive increase in the ε_r values has been noticed with the extent of Gadolinium incorporation into KNN matrix reaching a maximum value of ε_{rmax} = 4147 at $T_{T\text{-}C}$ = 357 ^oC for critical composition of x_c = 0.5. Beyond this composition level ε_r values continues to decrease and reaches a minimum value of ε_r = 1710 at 287 ^oC for x = 1.5. With the increasing of Gadolinium concentration, both the transition temperatures shift towards the lower temperature side. The increase of ε_r up to x = 0.5 can be ascribed due to the incorporation of the lower ionic radii Gd^{3+} ions inside the 'A' sites of Na^+ (1.02Å) having higher ionic radius. In the present study, the A-site substitution by the Gd^{3+} (0.938Å) ions can be understood using the following equation (5.2) involving the defect chemistry:

$$Gd_2O_3 \xrightarrow{K_{0.5}Na_{0.5}NbO_3} 2Gd^{\bullet\bullet}_{Na} + 4V'_{Na} + 3O_o \qquad (5.2)$$

According to the equation (5.2), when the Gd^{3+} ions occupy the A-sites of Na^+ the compositional heterogeneity may occur inside the KNN lattice. Since the higher valence Gd^{3+} ions are replacing the lower valance Na^+ ions, in order to maintain an overall charge neutrality, Gd^{3+} acts as a donor due to the existence of excess amount of electrons and one can expect same number of Na-vacant sites (V'_{Na}). This process may cause the development of some strain which finally assist to increase the correlation length between dipoles and facilitates the orientations of the domains. Due to the increment of net dipole

moment, the relative permittivity reaches a maximum value across $T_{T\text{-}C}$ for x = 0.5. Beyond the composition x = 0.5, ε_r value found to be decreased continuously at the Curie temperature. However, room temperature relative permittivity value found to be enhanced with Gd_2O_3 composition. The higher ε_r (1112) and lower *tanδ* (0.03) values are obtained at room temperature for the composition x = 1.0.

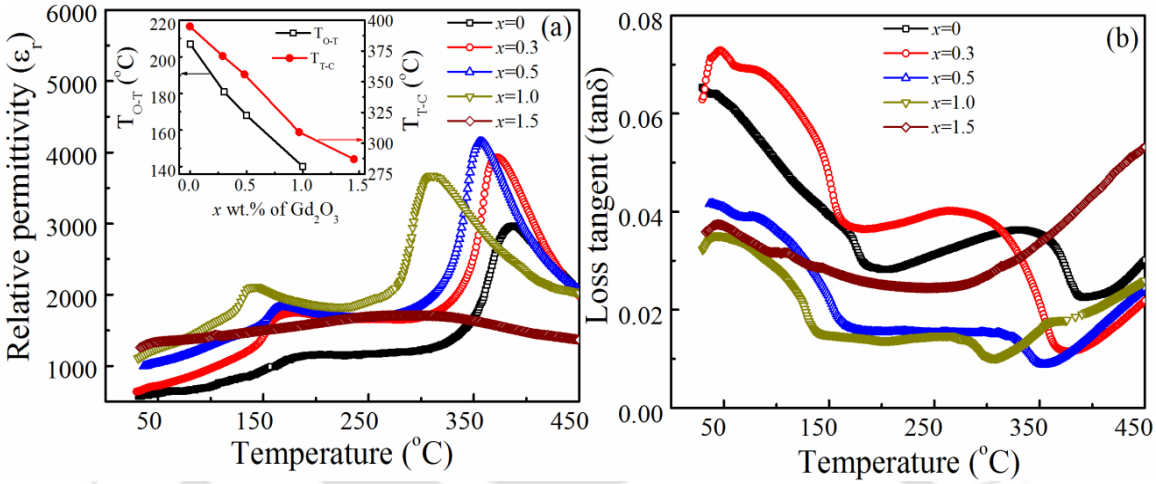

Figure 5.5: *(a) The temperature dependence of ε_r and (b) tanδ plots of various compositions of KNN+ x wt.% Gd_2O_3 (x = 0 - 1.5) ceramics measured at 1 MHz. The inset shows the variation of transition temperatures both $T_{O\text{-}T}$ and $T_{T\text{-}C}$ as a function of composition.*

The inset of Figure 5.5(a) shows the variation of both structural transitions $T_{O\text{-}T}$ and $T_{T\text{-}C}$ as a function of composition. For the composition x = 1.5, $T_{T\text{-}C}$ reaches its minimum value of 287 °C and $T_{O\text{-}T}$ almost suppressed and pushed below the room temperature. This indicates that KNN + 1.5 wt.% Gd_2O_3 system should exhibit either entirely tetragonal phase or the tetragonal phase mixed with orthorhombic crystal structure. Such a large decrease in the relative permittivity values occurs owing to the maximum crystallographic distortion at higher Gd_2O_3 concentration. Generally, as the Gd_2O_3 wt.% increases in the KNN matrix, one can expect the disturbance of long-range ferroelectric ordering by increasing the compositional disorder. Therefore, as x increases, the curie temperature of the system found to be decreases according to the equation, $T_{T\text{-}C} = (K_L\text{-}K_S)/B$, where K_L is the long range force constant, K_S is the short range harmonic restoring force constant, and B is the anharmonic coefficient [36-37]. The increased broadness of the peak with the rise of the Gd_2O_3 content indicates that the transition of ε_r *(T)* is diffusive in nature. Such diffusive phase transitions are indicative of the existence of relaxor behavior [38-40]. Figure 5.5(b) shows the temperature variation of loss tangent for different compositions, showing the clear anomalies across $T_{O\text{-}T}$ and $T_{T\text{-}C}$. For the low

concentration of Gd_2O_3, the loss tangent found to be decreased. This might be due to the excessive positive charge (Gd^{3+}) in the Na^+ can be cause of the formation of Na-vacancies, which can interact with the oxygen vacancies and decreases their mobility. Further, with increasing the concentration of Gd_2O_3, the loss tangent found to be increased. This might be due to the amount of Gd_2O_3 increases in the KNN matrix may cause severe distortion of the unit cell and leading to increase the loss tangent. The overall dielectric loss is less than 8% and above 377 ^oC the loss tangent increases continuously with increasing temperature. Hence the composition x = 0.5 exhibited the high ε_r and low $tan\delta$ values at the Curie temperature, therefore this composition was examined in the frequency range from 500 Hz to 1 MHz.

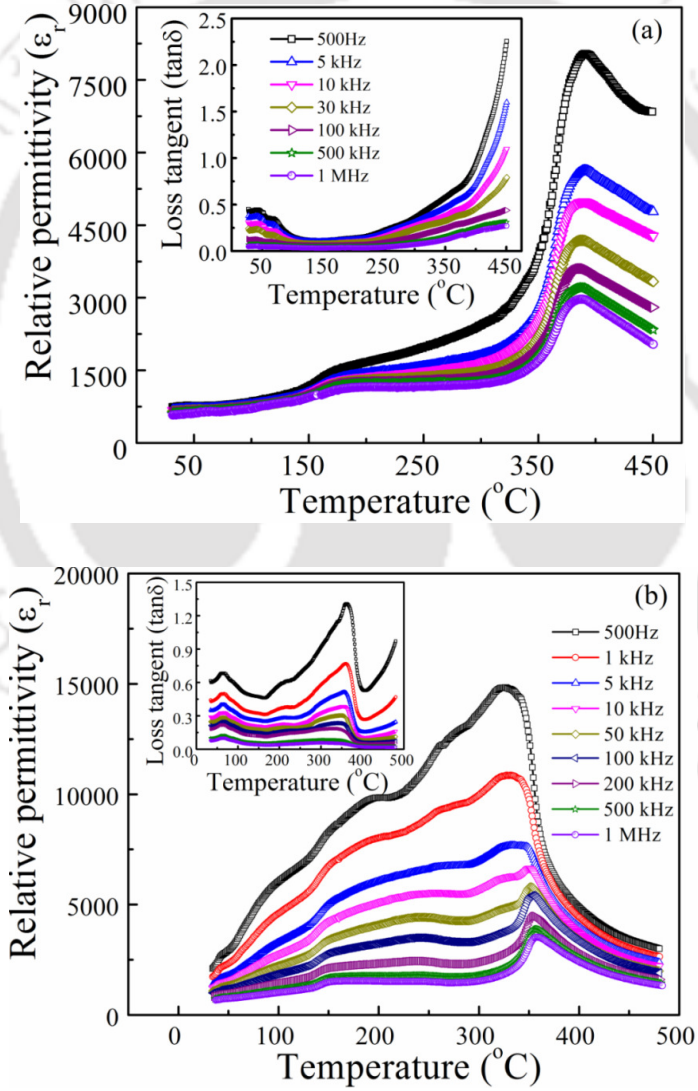

Figure 5.6: *Temperature dependence of the relative permittivity and loss tangent of (a) pure KNN (x = 0) and (b) x = 0.5 wt.% substituted KNN ceramics recorded at various frequencies.*

Figure 5.6 shows the temperature dependence of the ε_r and *tanδ* (inset) at various frequencies between 500 Hz to 1 MHz for $x = 0$ and 0.5. Strong frequency dispersion and clear shift in the $T_{T\text{-}C}$ towards high temperature side with increasing the frequency was observed in both ε_r and *tanδ* for $x = 0.5$. Also the magnitude of this transition decreases continuously with increasing the frequency. Such an increase of temperature maximum of relative permittivity with increasing the frequency is a typical signature of relaxor ferroelectricity [41-44]. The existence of the relaxor ferroelectric behavior is linked with the formation of polar clusters, which possess different relaxation times. Due to the delay in the dielectric response of such frozen polar nanoregions the transition temperature $T_{T\text{-}C}$ shifts towards high temperature side. However, for $x = 0$ no shift is noticed in the position of $T_{T\text{-}C}$ with increasing the frequency.

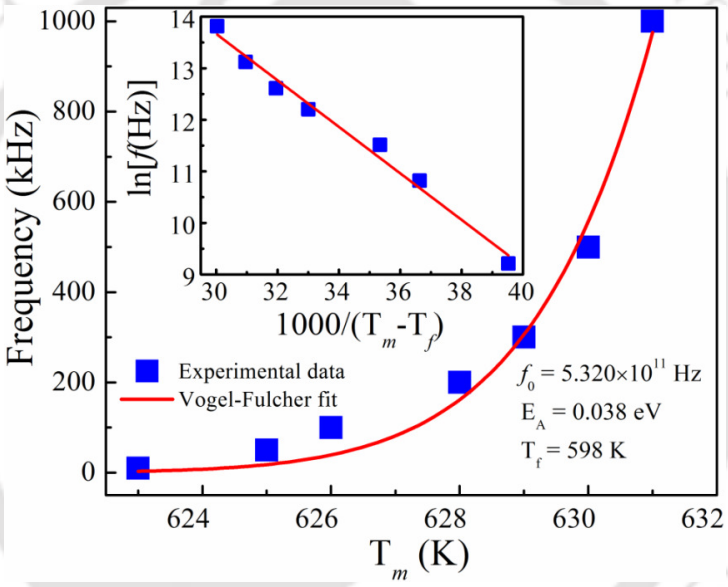

Figure 5.7: *Temperature dependence of the frequency for KNN + 0.5wt.% Gd_2O_3 ceramics. The solid symbols indicate the experimental data and a solid line represents the fitting by using Vogel-Fulcher law.*

The frequency variation of the peak maximum in the relative permittivity of $x = 0.5$ sample has been analyzed using Vogel-Fulcher (V-F) law (equation (4.4)). This V-F law is used to analyze the relaxor behaviour of compositional disordered ferroelectrics [42-45]. The scattered symbols shown in the Figure 5.7 are the transition temperatures corresponding to the maximum value of the ε_r (across the $T_{T\text{-}C}$) and the solid line is the corresponding least square fit to the V-F equation. The experimentally observed frequency dependence of T_m values and the least-square fit to the V-F law represented by the solid line is in good agreement with each other. The obtained fitting parameters are $f_0 = 5.32 \times 10^{11}$ Hz, $T_f = 325$ °C, $E_A = 38$ *meV*. The linear behavior of ln(*f*) against 1000/

(T_m-T_f) further confirms the validity of the V-F relation (inset of Figure 5.7). Generally, the degree of relaxor behavior can be described by a parameter $\Delta T_{Relaxor}$, which is defined as the difference between the position of dielectric peak maximum measured at frequencies 10 kHz and 1 MHz (i.e. $\Delta T_{Relaxor} = (T_m)_{1\ MHz} - (T_m)_{10\ kHz}$). For $x = 0.5$ the value of $\Delta T_{Relaxor}$ = 8 ^oC and $\Delta T_{Relaxor}$ = 0 for x = 0 which clearly indicates that the relaxor behavior in KNN system is caused by the addition of the rare-earth oxide Gd_2O_3.

Therefore, in order to confirm the relaxor behavior of KNN + x wt.% Gd_2O_3 (x = 0 - 1.5) ceramics, the high temperature relative permittivity data was analyzed. For normal ferroelectrics above the Curie temperature, the relative permittivity should follow the Curie-Weiss law [46]. For a typical relaxor ferroelectric, nonlinear behavior of $\varepsilon_r^{-1}(T)$ arises above the $T_{T\text{-}C}$ which signifies the deviation from the Curie-Weiss law. The difference in the reciprocal value of the ε_r and peak maximum of relative permittivity (ε_r^m) should follow the Uchino and Nomura formula [47],

$$\frac{1}{\varepsilon_r} - \frac{1}{\varepsilon_r^m} = \frac{(T - T_m)^\gamma}{C} \tag{5.3}$$

where, C is the Curie-Weiss constant. For normal ferroelectric systems the diffuseness coefficient 'γ' should be equal to the unity. But, for relaxor ferroelectrics 'γ' varies from 1 to 2 [48]. Thus, the coefficient 'γ' is a measure of the degree of diffuseness in the transition [49].

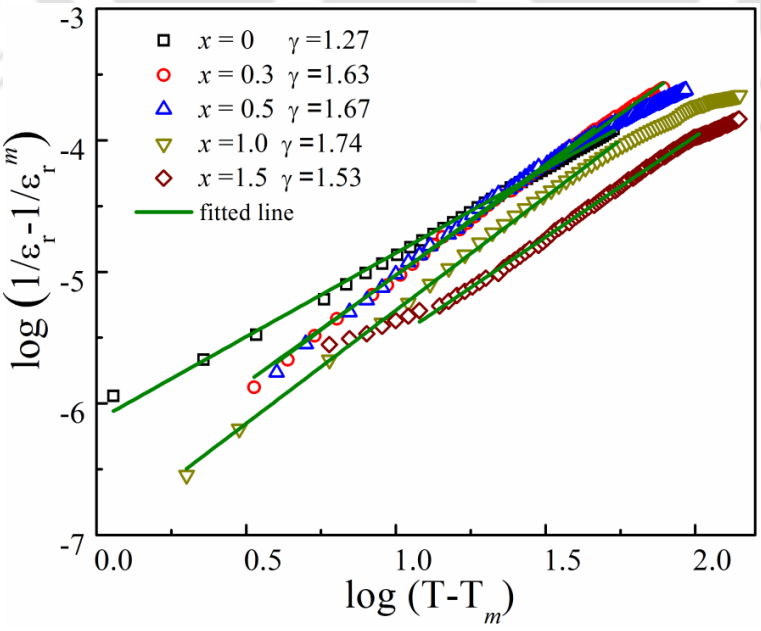

Figure 5.8: *The logarithmic variation of ($1/\varepsilon_r$ - $1/\varepsilon_r^m$) as a function of (T-T_m) measured at 1 MHz for various compositions of KNN+ x wt.% Gd_2O_3 (x = 0-1.5) system.*

Accordingly, the 'γ' value has been evaluated for different compositions (x) of Gd_2O_3 contained KNN system by finding the slope of the equation (5.3) under logarithmic scale i.e. log $(1/\varepsilon_r\text{-}1/\varepsilon_r^m)$ versus log $(T\text{-}T_m)$ shown in Figure 5.8. Consequently, the estimated 'γ' values lies in the range 1.27-1.74 for x = 0 -1.5 respectively, which signifies that the system exhibiting relaxor behaviour. Also, in the present case the degree of relaxor behaviour increases with increasing the Gd_2O_3 concentration. For the x = 0 sample shows the γ value 1.27, however, there is no peak shift observed with increasing the frequency from 500 Hz to 1 MHz. Due to the difference in valence and ionic radii of Gd^{3+} and Na^{+} may cause the disorder at A-site of KNN matrix and also leads to the formation of local electric fields owing to the charge imbalance [38, 48]. The increase in the γ value with increasing Gd_2O_3 composition may be due to change in crystal structure and the formation polar nanoregions. In the present case the degree of relaxor behavior decreases for x > 1. The origin of such behavior is associated with the intermixture of crystallographic phases. Our results indicate that at room temperature the system is exhibiting neither the orthorhombic phase nor tetragonal structure for all the samples with x > 1, thus, the 'γ' values decreases for x = 1.5. The peak in the temperature dependence of dielectric constant pertaining to the orthorhombic to tetragonal phase transition is appearing across the room temperature for x = 1.5 (Figure 5.5). Thus, we expect that the percolation limit of intermixture stage of orthorhombic and tetragonal phases play as important role in deciding the global dielectric behavior. The temperature dependent high frequency (1 MHz-1 GHz) dielectric properties of all the compositions were discussed in the next section.

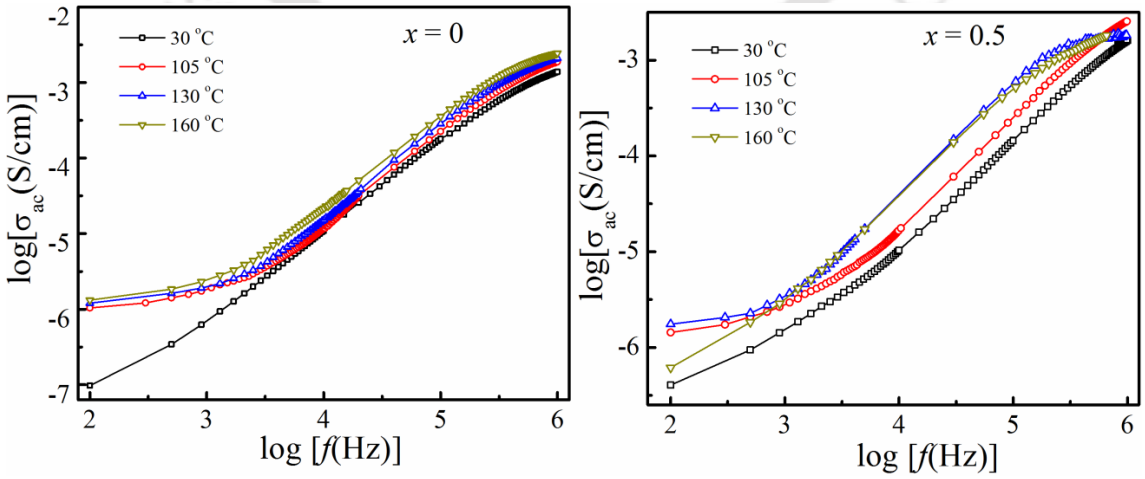

Figure 5.9: *Frequency dependence of the ac-conductivity measured at different temperatures for (a) x = 0 and (b) 0.5 of KNN+ x wt.% Gd_2O_3 ceramics.*

We have also studied the frequency dependence of ac-conductivity at different temperatures for samples with $x = 0$ and 0.5. For all the samples the σ_{ac}, starts dispersing below the critical frequency $f_c \leq 10$ kHz as shown in Figure 5.9. The conductivity plots merges beyond f_c and exhibiting almost linear behaviour. The conductivity follows frequency independent behaviour for $f < f_c$ except for $T = 30$ ^oC while for $f > f_c$ all the temperatures the σ_{ac} becomes frequency dependant. For the $x = 0.5$ sample, the σ_{ac} exhibits almost linear behaviour in the entire frequency regime (100 Hz- 1 MHz). At higher temperatures, the frequency independent behaviour of σ_{ac} for $f < f_c$ can be attributed due to the long-range translation motion of ions contributing to the dc-conductivity. Such type of dc-conductivity was first explained by Funke using the jump relaxation model [50]. According to the model proposed by Funke, the conductivity at the low frequencies are associated with the successful jumps to its nearest neighbour vacant sites due to the available of long time period. Such successive jumps result in a long-range translational motion of ions contributing to dc-conductivity. Also, for all the compositions the overall conductivity increases with increase in temperature. This is due to the fact that the samples sintered at high temperature can exhibit low level of oxygen content; therefore there will be finite amount of probability to create the oxygen vacancies following the Kröger-Vink equation [51].

$$O_o \rightarrow O_o \uparrow + V_o^{\bullet\bullet} + 2e^{-1} \tag{5.4}$$

According to this model, free electrons remain stay in the samples, due to the oxygen vacancy which in-turn enhance the total conductivity progressively with increasing temperature. As the frequency increases, the ratio between unsuccessful hops to successful hops increases, due to this process the depressiveness in the conductivity values occurs. It is well known that the frequency dependence of the conductivity follows the Jonsher equation [52],

$$\sigma_{ac}(\omega) = \sigma_0 + A\omega^s \tag{5.5}$$

where, $\sigma_{ac}(\omega)$ is the total conductivity, σ_0 is the dc conductivity, and the term $A\omega^s$ corresponds to the short range hopping of ions [53-54]. Here the pre exponential factor '*A*' is the temperature dependant component and the exponent '*s*' is found to take the values between 0 and 1. The factor '*s*' usually determines the interaction between the dipoles participating in the polarization process. These two parameters '*s*' and '*A*' are

temperature dependants and also depend on the intrinsic property of the material [54]. Table 5.2 lists the estimated values of '*s*' and log*A* from Figure 5.9 for various temperatures of pure KNN ($x = 0$) and 0.5wt.% Gd_2O_3 contained KNN system.

Table 5.2: *The variation of log A and s parameters evaluated at different temperatures of KNN+ x wt.% Gd_2O_3 ceramics for x = 0 and x = 0.5.*

Temperature (^oC)	Log *A*		*s*	
	$x = 0$	$x = 0.5$	$x = 0$	$x = 0.5$
30	-7.84	-8.66	0.83	0.98
105	-7.80	-8.03	0.85	0.90
130	-7.33	-7.55	0.78	0.86
160	-6.91	-6.54	0.72	0.65

According to the many body interaction model, $s = 1$ implies pure Debye relaxation, where the interaction between the neighbouring dipoles is negligible [55]. In the present case, for the compositions $x = 0$ and 0.5, the value of '*s*' found to be less than '1' indicating the non-Debye type relaxation. The increase in '*A*' with increasing the temperature is attributed to the increment in the polarizability. For the case of pure KNN, the value of '*s*' increases to 0.85 for initial temperatures up to 105 ^oC because of small polaron hopping mechanism [54]. Earlier reports suggest that the formation of small polaron can takes place in pure KNN system whose conduction-band consist of the incomplete '*d*' or '*f*' orbital. In the present case, the incomplete "*d*" orbital created due to the reduction of Nb^{5+} into Nb^{4+}, may be responsible for the small polaron formation. As the temperature increases, the dissociation of polaronic states takes place and leads to the charge carriers interact with positive ions in the lattice, which leading to the formation of large polaron. As a consequence, we observed the small values of '*s*' with increasing the temperature. However, for $T > 105$ ^oC the '*s*' values decreases due to the large polaron hopping. These large polarons can scatter with the existing ions and phonons in the crystal lattice and causes change in the conductivity. Thus, the value of '*s*' decreases with increasing the temperature. For $x = 0.5$, the 's' value close to 1 at low temperatures and found to be decreased with increasing the temperature, which could be due to the large polaron hopping [56]. Since the charge carrier of large polaron extends over multiple sites. Consequently the charge carriers can adjust continuously to the alternations of the atomic positions and thereby move between the sites and leading to the increase of the conductivity with temperature [56].

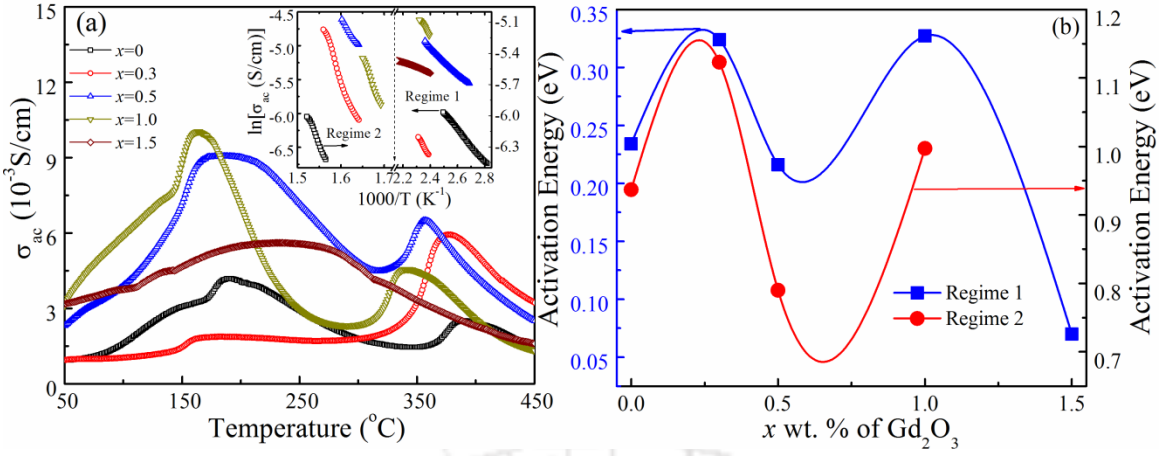

Figure 5.10: *(a) Temperature dependence of ac-conductivity of different compositions for x = 0-1.5 of KNN+ x wt.% Gd_2O_3. The inset shows variation of lnσ_{ac} versus 1000/T in two different regimes 1 (82 °C-137 °C) and 2 (297 °C-397 °C). (b) The variation of activation energy (E_A) for different compositions in both the temperature regimes 1 and 2.*

Figure 5.10(a) shows the temperature variation of ac electrical conductivity σ_{ac} (T) for different compositions measured at frequency 1 MHz. All the samples exhibited the clear anomalies across the crystallographic phase transitions. We have estimated the activation energy (E_A) by using Arrhenius relation $\sigma_{ac} = \sigma_0 \exp(-E_A/k_BT)$ from the slope of the ln σ_{ac} versus 1000/T which is shown in the inset of Figure 5.10(a). Two different temperature regimes have been identified where the ln σ_{ac} versus 1000/T exhibits the linear behaviour. For the regime 1 (R1) (82 °C - 137 °C), the calculated E_A values lie in the range 0.07 - 0.32 *eV*, whereas for regime 2 (R2) (297 °C - 397 °C) the E_A values lies in the range 0.79 - 1.12 *eV*. The variation of activation energy values calculated as a function composition '*x*' is shown in the Figure 5.10(b). Usually, the lower E_A values obtained in R1 can be attributed due to the carrier transport through hopping between localized states in a disordered manner. For all the compositions in the R2, the E_A was found to exhibit higher values as compared to R1. Because the temperature range over which the ferroelectric to paraelectric phase change is significant in R2. It is expected that ferroelectric properties strongly affect the values of the ac conductivity. Because across the Curie temperature the domain structure causes the grains to breakup and releases charge carriers, consequently the conductivity increases. At higher temperatures, the electrons could be released from the oxygen vacancies according to the equation (5.4).

In order to study the hopping mechanism in detail, we have measured the high temperature resistivity in both pure and doped system and analyzed using Mott's variable range hopping (VRH) mechanism. Figure 5.11(a) and (b) shows the lnρ_{ac} versus $T^{-1/4}$ for

both x = 0 and x = 0.5 samples in the regimes R1 and R2, respectively. The resistivity data is fitted to the equation,

$$\rho_{ac} = \rho_0 \exp(T_0 / T)^{1/4} \tag{5.6}$$

where, ρ_0 and T_0 being pre-exponential factor and characteristic temperature coefficient depends on the density of states at Fermi level, respectively [57-60]. The linear variation of $\ln\rho_{ac}$ against $T^{-1/4}$ in both the regimes R1 and R2 provides the signatures of variable range hopping process in the pure and Gd_2O_3 doped KNN system.

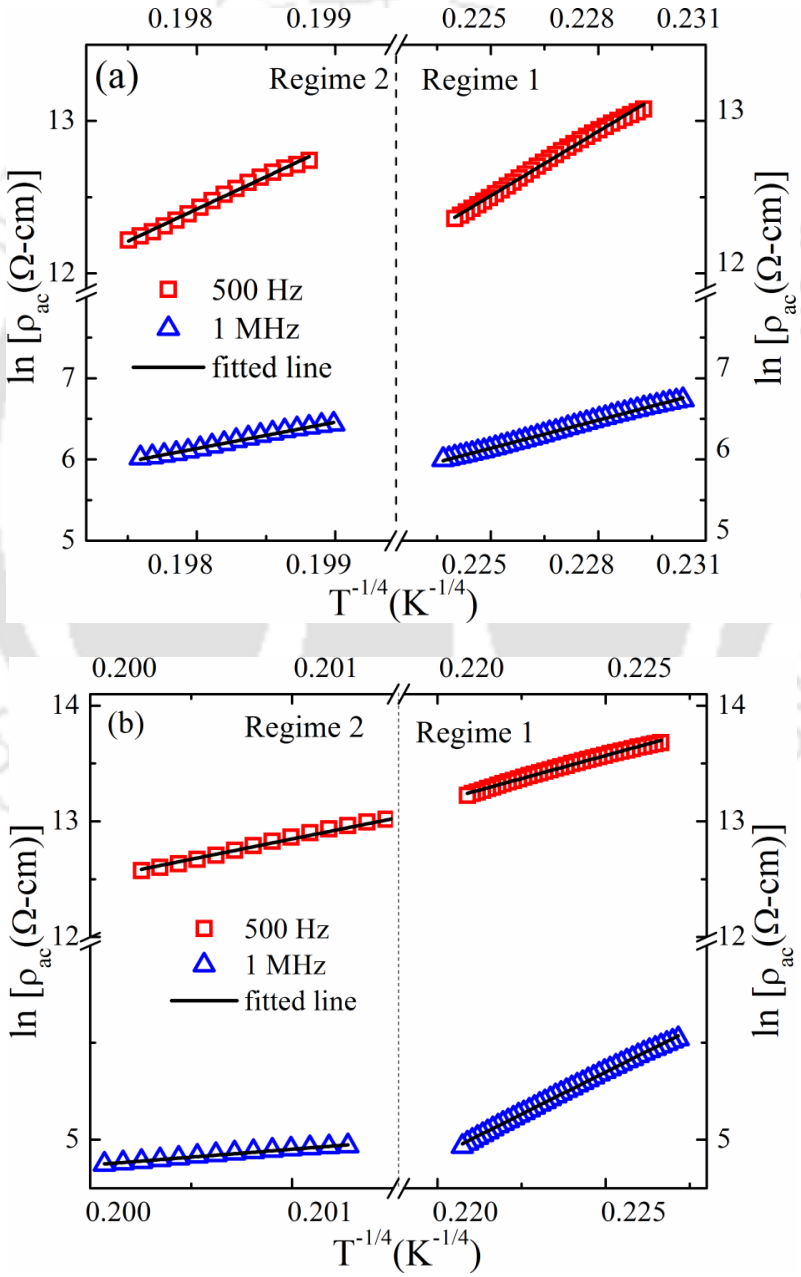

Figure 5.11: *Variation of $\ln\rho_{ac}$ with $T^{-1/4}$ in the temperature regimes R1 and R2 for (a) x = 0, and (b) x = 0.5.*

According to the VRH model, the probability of the electron hopping between the states due to the thermal activation is more for those energy levels close to each other compared to far in energy levels. The characteristic hopping length R_H decreases with increasing temperature. The parameters ρ_0 and T_0 have been evaluated from the slopes and intercepts of the graphs 5.11. The characteristic temperature T_0 evaluated from the slope of the $\ln\rho_{ac}$ versus $T^{-1/4}$ being 3.21×10^{10} and 1.52×10^{10} measured at 500 Hz in the regime R2 for x = 0 and 0.5, respectively. Further, it is observed that with increasing the frequency up to 1 MHz, the T_0 values decreased due to the increase in the conductivity. The higher values of T_0 at low frequencies are attributed due to the strong localization of charge carriers and lower conductivity [61].

The values of slopes obtained from the logarithmic graphs $\ln[\ln(\rho_{ac}/\rho_0)]$ versus $\ln T$ are shown in Figure 5.12. For pure KNN the obtained average slope values are -0.25 and -0.24 (at 1 MHz) for R1 and R2, respectively. For x = 0.5, the average slopes found to be -0.25 and -0.27 (at 1 MHz) for R1 and R2, respectively. Generally, depending upon the nature of the hoping process the power of exponential values varies. For the variable range hopping process the typical exponential value should be approximately -0.25. It is interesting to know that for pure KNN and KNN + 0.5wt.% Gd_2O_3 ceramics followed the VRH mechanism in the R1 regime and slightly deviated in high temperature regime R2. The variable range hopping process can expected among the ions Nb^{5+}-Gd^{3+}-$[Na^{1+}]_{0.5}$ or Nb^{5+}-Gd^{3+}-$[K^{1+}]_{0.5}$.

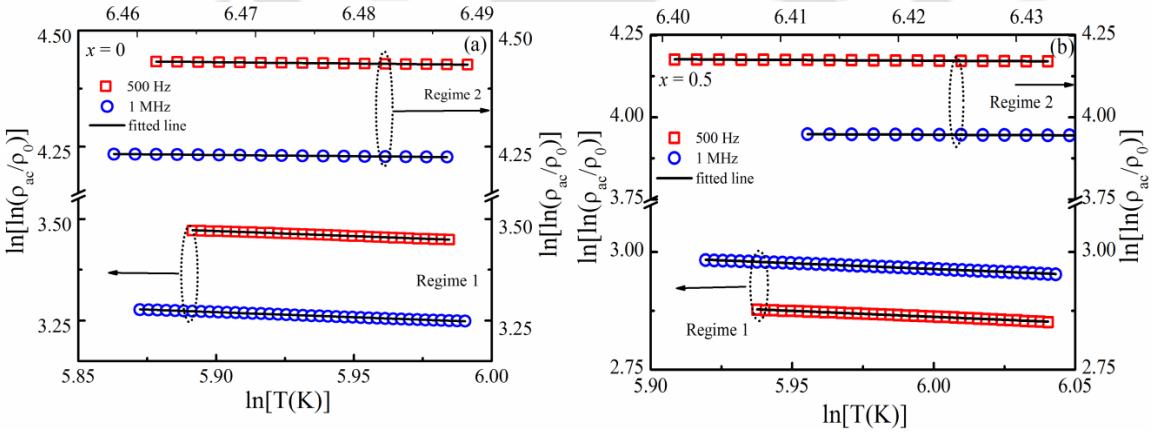

Figure 5.12: *The double logarithmic plots of resistivity ($ln[ln(\rho_{ac}/\rho_0)]$) versus lnT in the temperature regimes R1 and R2 for (a) x = 0 and (b) x = 0.5.*

The density of states of electrons near the Fermi level ($N(E_F)$), average hopping length (R_H), and hopping energy (W_H) calculated using equations (4.9 - 4.11) of chapter 4

[61-63]. The electron density of states at the Fermi level $N(E_F)$ can be obtained by considering the decay length α approximately 0.6 - 1 nm [57, 64-65]. From the values of α and $N(E_F)$ the average hopping length R_H has been evaluated. For x = 0 and 0.5 the hopping length lies in the range 7.94 nm – 29.24 nm and 5.55 nm – 26.41 nm, respectively. The various parameters evaluated from the resistivity data are listed in Table 5.3. For x = 0.5 sample the $N(E_F)$ values found to be higher compared to the pure KNN system i.e. x = 0 because the addition of Gd_2O_3 may induce defect dipoles that provide a large number of localized states near to the E_F. As a result of the number of states increases the hopping length R_H and hopping energy W_H are found to be decreased with the addition of Gd_2O_3 in KNN core matrix.We found that $N(E_F)$ decreases with increasing temperature but increases with increase in frequency for the x = 0.5. At low frequencies, the value of hopping distance and hopping energy decreases with the incorporation of Gadolinium content. This indicates that Gd^{3+} assisted the hopping of charge carriers from one localized site to another. Further, we have analyzed the ac-conductivity of the KNN+ x wt.% Gd_2O_3 by using VRH mechanism in the very low temperature range between -140 – 30 ^oC and discussed in the next section.

Table 5.3: *The calculated Mott's parameters of KNN+ x wt.% Gd_2O_3 ceramics for x = 0 and 0.5.*

Frequency (Hz)	T_0 (10^8 ^oC)		$N(E_F)$(10^{17} eV^{-1} cm^{-3})		R_H (nm)		W_H (eV)	
	x =0	x =0.5	x =0	x =0.5	x = 0	x =0.5	x =0	x=0.5
500 Hz (R1)	3.905	0.403	4.74	44.32	8.86	5.55	0.722	0.314
1MHz (R1)	1.753	0.563	0.057	36.07	29.24	5.84	1.656	0.331
500 Hz (R2)	321.82	152.42	10.60	0.086	7.94	26.41	0.449	1.496
1MHz (R2)	109.79	20.12	0.197	1.04	21.49	14.18	1.217	0.803

5.3.4.2 Broadband dielectric properties

The frequency dependent real (ε') and imaginary (ε'') parts of the complex permittivity were measured over a frequency range 1 MHz to 1GHz for different compositions of KNN+ x wt.% Gd_2O_3 (x = 0 - 1.5) are shown in Figure 5.13. The real part describes an easy response of the dipoles to the applied electric field or polarization in the medium, while the imaginary part is associated with dissipation of energy into the medium.

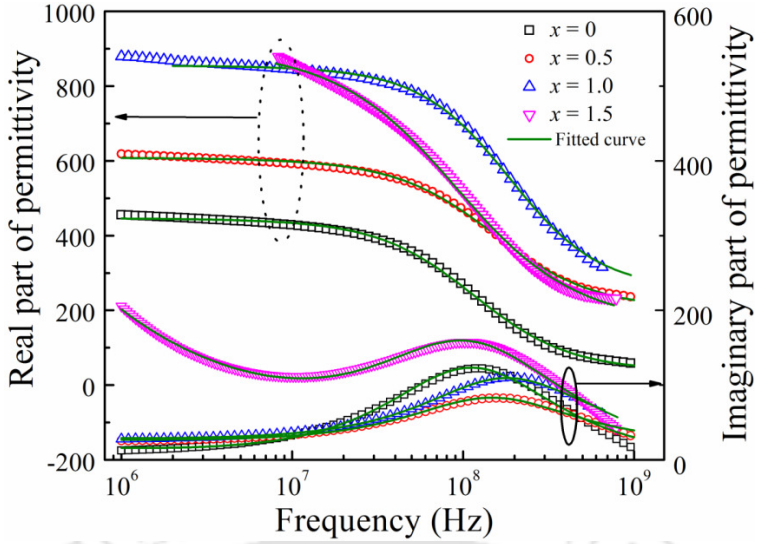

Figure 5.13: *Frequency dependence of real and imaginary part of permittivity of KNN + x wt.% Gd_2O_3 (x = 0 - 1.5) ceramics, sintered at 1050 ^oC, and measured at room temperature. The lines are fitting curves by using equation (2.21).*

Table 5.4: *The evaluated H-N parameters of KNN + x wt.% Gd_2O_3 (x = 0 - 1.5) ceramics measured at room temperature.*

x wt.%	α	$\Delta\varepsilon$	τ (10^{-9} sec)	Grain size (μm)
$x = 0$	0.888 ± 0.015	448 ± 9	1.45 ± 0.09	2.26 ± 1.07
$x = 0.5$	0.880 ± 0.013	409 ± 14	1.07 ± 0.07	1.71 ± 0.59
$x = 1.0$	0.914 ± 0.010	604 ± 17	0.87 ± 0.02	1.36 ± 0.46
$x = 1.5$	0.739 ± 0.018	946 ± 16	1.41 ± 0.09	0.35 ± 0.13

The frequency dispersion behavior of KNN + *x* wt.% Gd_2O_3 ceramics were analyzed by fitting the experimental dielectric permittivity data with Havriliak - Negami function using equation (2.21) [66]. The obtained data of KNN+ *x* wt.% Gd_2O_3 (*x* = 0 - 1.5) ceramics has been analyzed through H–N function using WinFit software program [67] and the extracted values have been given in Table 5.4. The value of β found to be constant 1, and α change with the Gd_2O_3 concentration, revealed that the relaxation process, which obeys the Cole - Cole relaxation at room temperature. For *x* = 0, the dielectric spectra found to be asymmetric and the spectra becomes symmetric with increasing the Gd_2O_3 concentration upto *x* = 1.0. Again the asymmetric behavior observed for *x* = 1.5 can be due to the enhancement of crystallographic distortion and also increasing the contribution of the conductivity in the imaginary part of the permittivity. The symmetry parameter α found to be increases from 0.888 to 0.914 with an increase in the *x* upto 1.0, then it decreases to 0.739 for *x* = 1.5.Whereas the high frequency

relaxation time (τ) found to be decreases from $1.45\times10^{-9} \pm 8.9\times10^{-11}$ s to $8.78\times10^{-10} \pm 2.5\times10^{-11}$ s with increasing the x upto 1.0, and then increases to $1.41\times10^{-9} \pm 9.6\times10^{-11}$s for x = 1.5. The decreasing trend of τ observed for low concentration of x may be due to the reduction in the A-site vacancies induced by volatilization of alkali elements during the sintering. On the other hand, lower τ of doped samples may be due to the relaxation facilitated by smaller grains as compared to large grains of pure KNN ceramics [68].

The temperature dependant dielectric properties of KNN+ x wt.% Gd_2O_3 (x = 0 - 1.5) ceramics measured at different frequencies from 1MHz to 400 MHz are shown in Figure 5.14. Similar to low frequency dielectric properties, pure KNN exhibited the structural transitions around T_{O-T} = 199°C, and T_{T-C} = 374°C, and another low temperature structural transition near T_{R-O} = - 60 °C, which could be attributed to the crystallographic phase transition from rhombohedral to orthorhombic state. The incorporation of Gd_2O_3 into KNN matrix enhanced the relative permittivity and shifted the crystallographic phase transitions T_{O-T} and T_{T-C} towards lower temperatures 85 °C and 243 °C, respectively. The compositions x = 1.0 and 1.5 were exhibited the shift in the T_{T-C} with increasing the frequency, even in the high frequency range 1 MHz - 100 MHz. However, no shift in the T_{T-C} observed for pure and x = 1.0 in this frequency range. The relaxor parameter $\Delta T_{Relaxor}$ found to be 7 °C and 57 °C measured in the frequency between 1 MHz and 100 MHz. Therefore, relaxor behavior of KNN ceramics was enhanced with increasing the Gd_2O_3 wt.%. The sample with x = 1.0, exhibited a high relative permittivity (879 at 1MHz) by shifting the T_{O-T} toward room temperature and low dielectric loss (<5%) in the wide temperature range (-140 °C – 150 °C) with the high Curie temperature 307 °C can be suitable for high temperature piezoelectric applications. With increasing the x wt.% of Gd_2O_3 causes the crystal cell distortion and increases the dielectric loss. This can enhance the conductivity for the excess amount of Gd_2O_3. The temperature dependent *tanδ* also shows the anomalies at the phase transitions similar to ε_r.

The low temperature dependent (-140 °C – 35 °C) ac-conductivity measurements have been performed on KNN + x wt.% Gd_2O_3 (x = 0 - 1.5) ceramics. The Activation energies (E_A) have been calculated by using Arrhenius relation $\sigma_{ac} = \sigma_0 \exp(-E_A/k_BT)$ from the slope of $\ln\sigma_{ac}$ versus $1000/T$ plot from different regimes shown in Figure 5.15. The obtained E_A values are listed in Table 5.5. The E_A values are higher in the crystallographic phase transition region as compared to other regimes, which are due to the disordered domains, that causes the grains to break up and release more number of charge carriers.

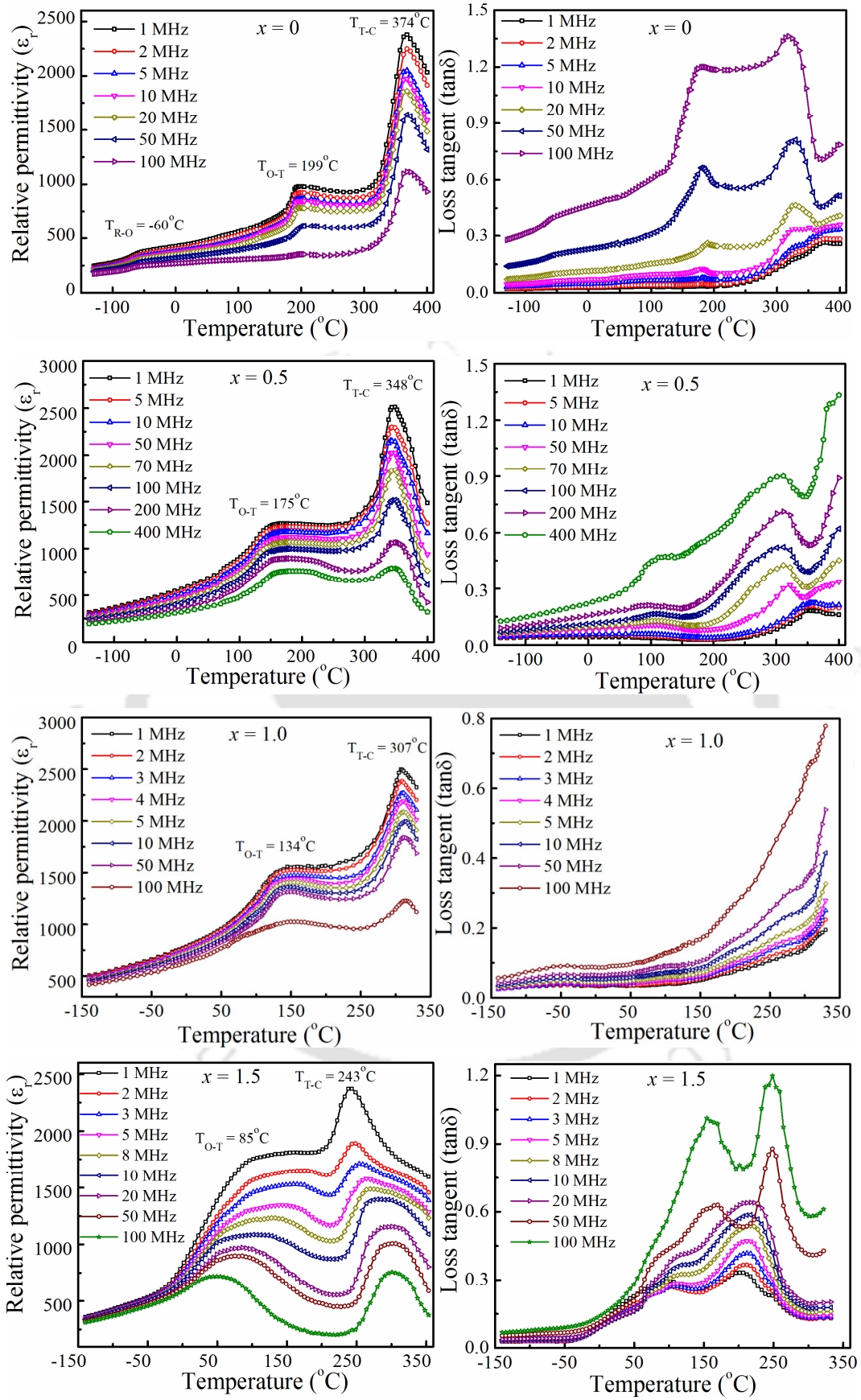

Figure 5.14: *Temperature dependence of ε_r and loss tangent of KNN + x wt.% Gd_2O_3 (x = 0 - 1.5) ceramics, sintered at 1050 °C and measured at different frequencies.*

.

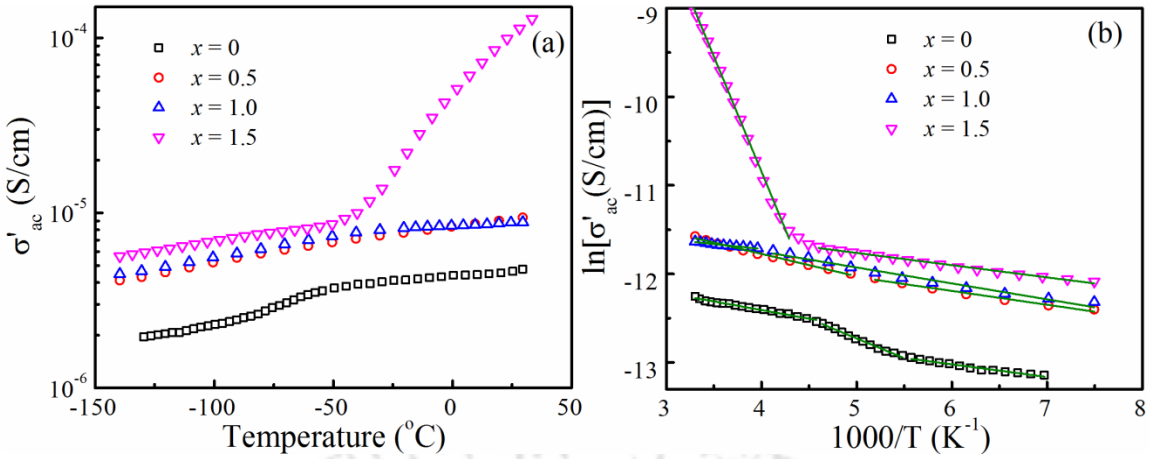

Figure 5.15: *(a) Temperature dependence of ac conductivity and (b) Arrhenius plots of conductivity of KNN + x wt.% Gd_2O_3 (x = 0 -1.5) ceramics measured in the temperature range -140 °C - 35 °C.*

Table 5.5: *Activation Energy (E_A) and Mott's various parameters extracted from different regimes (R3, R4, and R5) in the temperature range of -140 °C - 35 °C.*

x	Regime	E_A (*eV*)	$N(E_F)$ (10^{22} eV^{-1} cm^{-3})	R_H (nm)	W_H (*eV*)
x = 0	R3 (-130 - -84 °C)	0.013	4.522	0.733 - 0.681	0.012 - 0.016
	R4 (-81 - -54 °C)	0.041	0.071	1.912 - 1.848	0.045 - 0.050
	R5 (-50 – 30 °C)	0.016	4.265	0.663 - 0.607	0.018 - 0.024
x = 0.5	R3 (-140 - -80 °C)	0.014	2.220	0.877 - 0.800	0.015 - 0.020
	R4 (-70 – 30 °C)	0.022	1.185	0.924 - 0.836	0.024 - 0.033
x = 1.0	R3 (-140 - -30 °C)	0.017	1.644	0.930 - 0.793	0.017 - 0.027
x = 1.5	R3 (-140 - -50 °C)	0.012	4.227	0.746 - 0.657	0.013 - 0.019
	R4 (-40 – 35 °C)	0.224	1.404×10^{-4}	8.555 - 7.989	0.261 - 0.321

The temperature dependence (-140 °C – 35 °C) of Mott's VRH conduction in KNN + *x* wt.% Gd_2O_3 (*x* = 0 - 1.5) ceramics are analyzed by using the equations (4.8 - 4.11). Figure 5.16 shows the ln[ln(ρ_{ac})] versus ln(*T*) for all the samples at different temperature regimes measured in the range of -140 °C - 35 °C. Interestingly, all the samples show the linear behaviour with slope equal to -0.25 in different regimes. The decay lenght α^{-1} can be assumed as the nearest distance between Nb ions approximately 0.6 nm and estimated the $N(E_F)$ values and listed in Table 5.5. In the low temperature regime (R3), the $N(E_F)$ of KNN + *x* wt.% Gd_2O_3 ceramics are found to be decreased with

increasing in Gd_2O_3 concentration upto x = 1.0. The lower values of $N(E_F)$ obtained for low concentration of x may be due to the reduction in the A-site defects caused by volatilization of alkali elements during the sintering process. The decrease in the grain size also could be the reason for small value of $N(E_F)$. For x = 1.5 sample, the $N(E_F)$ found to be enhanced due to the increase of crystal distortion and defect states at the Fermi level. The lower values of $N(E_F)$ for x = 0 and 1.5 compared to other compositions in the temperature regime R4 can be due to the change in crystal structure. After knowing the values of $N(E_F)$, the conduction behaviour of the KNN + x wt.% Gd_2O_3 (x = 0 - 1.5) is further analyzed in terms of hopping length (R_H) between two sites with same energy level and the average hopping energy (W_H) by using the equations (4.10 & 4.11) and listed in Table 5.5.

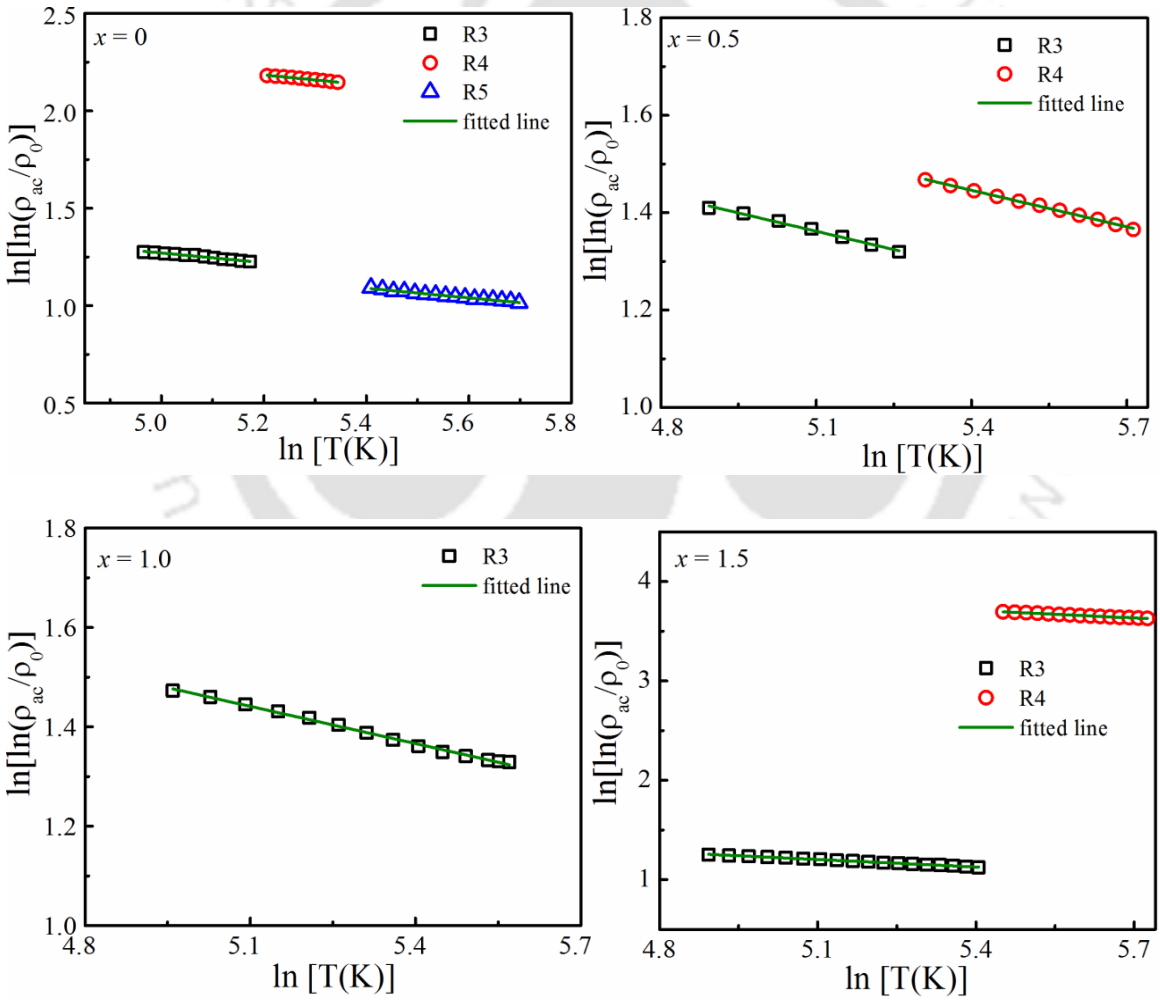

Figure 5.16: *Variation of double logarithmic plots of resistivity with lnT in the temperature range of -140 °C - 35 °C at different temperature regimes of KNN + x wt.% Gd_2O_3 (x = 0 - 1.5) ceramics.*

The obtained Mott's parameters for the VRH conduction mechanism at different temperature regimes satisfied the condition $W_H \geq k_B T$ and $\alpha R_H \geq 1$ [57]. It is observed that the R_H found to be decreases whereas W_H increases with increasing the temperature and is attributed to the increase in disorder in the system. For x = 0 sample, in the temperature regime R5 the R_H found to be in the range of 0.57 nm- 0.62 nm, which is almost equal to the distance between Nb atoms. In the low temperature regime R3, both R_H and W_H found to increase with an increase in Gd_2O_3 concentration upto x = 1.0, and decreases for x = 1.5. The higher values of R_H and W_H for x = 0 and 1.5 samples in the regime R4 is due to the release of charge carriers in the vicinity of structural change. It is also observed that, the hopping energy calculated by using equation (4.11), is almost identical with the activation energy calculated by using Arrhenius relation. The addition of Gd_2O_3 to the KNN can significantly change the Mott's VRH parameters, indicates that Gd^{3+} assisted the hopping of charge carriers in the vicinity of the Fermi level.

5.3.4.3 Voltage dependent dielectric properties

The voltage dependent dielectric properties of KNN + x wt.% Gd_2O_3 (x = 0 - 1.5) ceramics were measured in the DC voltage range from -8V to +8V at frequency 1 MHz . Both ε_r and *tanδ* showed a strong nonlinear behaviour which is shown in Figure 5.17 and depended on the sweep direction of the applied voltage. The x = 0 sample showed a large hysteresis width and asymmetry in the both ε_r and *tanδ* maxima are observed. As the Gd_2O_3 concentration increases in the KNN matrix, the width of the butterfly loop found to be decreased due to the decrease in grain size. Because, the domain wall motion can be influenced by the grain size of the ceramics.

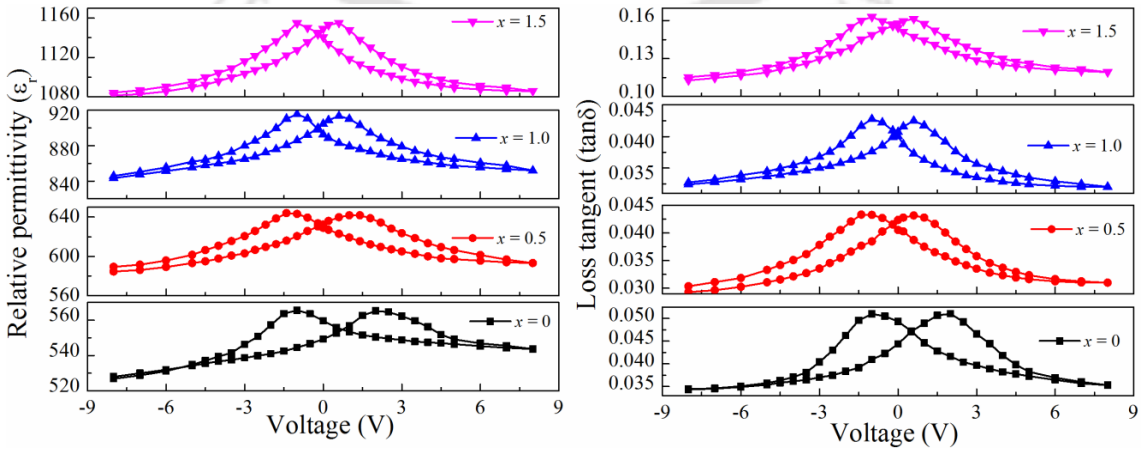

Figure 5.17: *DC voltage dependence of (a) ε_r and (b) tanδ for KNN + x wt.% Gd_2O_3 (x = 0 - 1.5) ceramics sintered at 1050 ^oC, measured at 1 MHz.*

The tunability of the ferroelectric material can be calculated by using the following equation [37],

$$Tunability\,(\%) = \left(\frac{\varepsilon(0V) - \varepsilon(8V)}{\varepsilon(0V)}\right) \times 100 \tag{5.7}$$

The tunability was found to be around 5.96% for x = 0 sample. The sample with x = 0.5 displayed higher tunability of 7.59% and its decreases for higher concentrations of Gd_2O_3.

5.3.4.4 Ferroelectric properties

The polarization-electric field (P-E) plots of the KNN + x wt.% Gd_2O_3 (x = 0 - 1.5) ceramics were measured at the room temperature and shown in Figure 5.18. All the ceramics exhibited the well saturated hysteresis loops, confirming the ferroelectric nature of KNN + x wt.% Gd_2O_3 ceramics. It has been observed that the values of remnant polarization ($2P_r$) found to be enhanced with increasing the Gd_2O_3 concentration, whereas the coercive field ($2E_c$) values decreased. The increase in $2P_r$ values and decrease in $2E_c$ are attributed to the more number of switchable domains available in Gd_2O_3 contained samples. The maximum value of $2P_r$ (31.46 μC/cm^2) is obtained for the composition x =1.0, which is due to the uniform grain size, high relative permittivity, and low dielectric loss (ε_r = 1112 and $tan\delta$ = 0.03 at 1MHz).

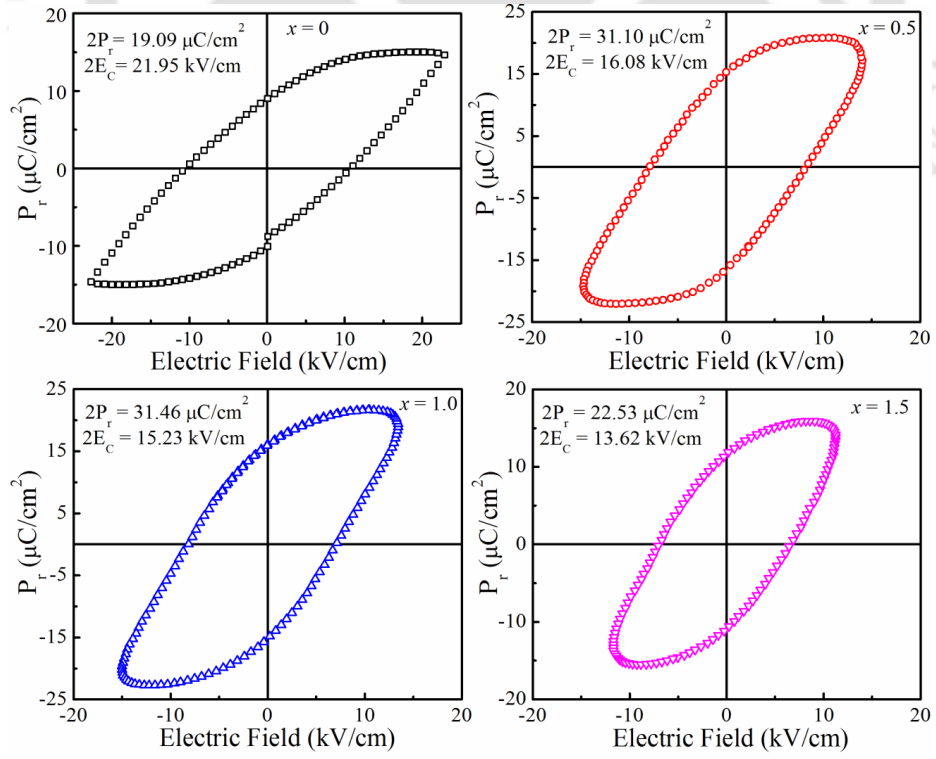

Figure 5.18: *The P-E loops of KNN + x wt.% Gd_2O_3 (x = 0 - 1.5) ceramics sintered at 1050^{o}C, measured at room temperature.*

The higher ε_r and $2P_r$ are the most important required parameters to get the high piezoelectric coefficient (d_{33}). Further with increasing the x (x = 1.5), both the $2P_r$ and $2E_c$ values decreases due to the increasing of leakage caused by the crystal distortion. The enhanced dielectric properties, improved tunability and ferroelectric properties were obtained for the Gd_2O_3 doped KNN ceramics can find applications in tunable RF circuits and high performance piezoelectric applications.

Therefore, KNN + 1wt.% Gd_2O_3 (KNN1G) is identified as the best composition for the deposition of thin films by using RF magnetron sputtering technique.

5.4 $(K_{0.5}Na_{0.5})NbO_3$+1.0 wt.% Gd_2O_3 thin films

5.4.1 Crystallinity of the thin films

The XRD patterns of the KNN1G thin films grown on the quartz substrate deposited under different OMPs. The Rietveld refinement of KNN1G films was carried out by considering the *P4mm* space group using FullProf program [69]. In case of 0% OMP, apart from (110) peak; other peaks are also present as shown in Figure 5.19. And even, increasing the OMP during the deposition, there is change (increasing) in (001)/(100) peak but no significant change in (110) peak is observed. The degree of orientation of KNN1G films for the (001) and (110) reflections was calculated by the Lotgering factor (F) using the equation (3.4 & 3.5) [70]. It is observed that the orientation factor for the (001) plane found to increase from -0.012 to 0.164 with a rise in the OMP. This is due to the lower Coulomb interaction energy (3.61 *eV*) between the adjacent planes of (001) plane and binding of atoms in this plane is strong as compared to other planes [71]. Furthermore, with increasing the OMP, the intensity of (001) diffraction peak improved, whereas the intensity of the (110) peak decreased. The peak positions of all the peaks are shifted to lower 2θ side and the FWHM of all the peaks found to be decreased with rising OMP. The Williamson-Hall expression was used to calculate the crystallite size and strain of the films [72]. The crystallite size of the films found to be increased from 30 nm to 42 nm with rise in OMP and the strain was in the range of 0.001-0.002. This is due to the fact that during the deposition, the sputtered atoms react with oxygen molecules and caused the heat generation as well as energy redistribution on the surface of the substrate, and this can promote the migration and crystallization upon annealing.

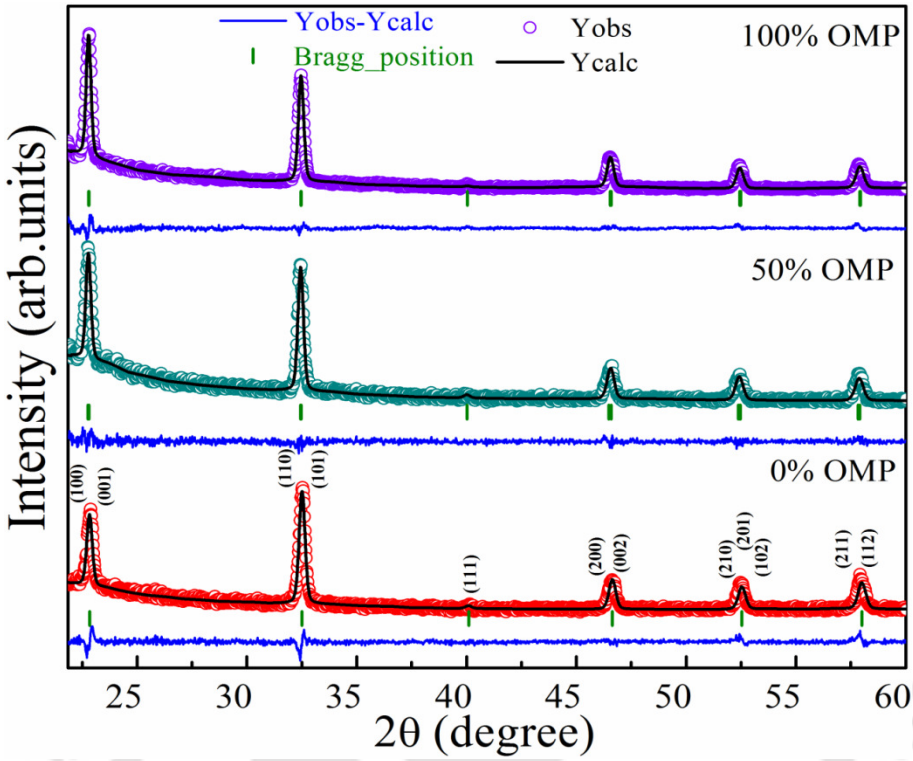

Figure 5.19: *The XRD patterns along with Retvield refinement of KNN1G thin films deposited at 400 °C under different OMPs and annealed at 700 °C for 1h.*

The lattice constants and the positions of all the atoms of KNN1G unit cell have been refined by using Fullprof software and listed in Table 5.6. For the film deposited under pure argon plasma, the obtained unit cell volume (*V*) and *c/a* ratio are found to be 58.9085 Å^3 and 0.9999 (χ^2 = 6.53), respectively. It is observed that both *V* and *c/a* ratio improved with increasing the OMP and reaches a maximum value of 59.2799 and 1.0023 (χ^2 = 3.88) for the film deposited under pure oxygen plasma, respectively. These lattice parameters are in good agreement with the earlier reports [69, 73-74]. The smaller values of lattice constants obtained for the films deposited in the pure argon plasma might be due to the higher oxygen vacancies as compared to that of deposited under different oxygen plasmas.

Table 5.6: *Lattice parameters extracted from the Rietveld refined XRD pattern of KNN1G thin films deposited at different OMPs.*

OMP (%)	*a* (Å)	*b*(Å)	*c*(Å)	*V*(Å^3)	*c/a*	$F_{(001)}$
0	3.8911	3.8911	3.8908	58.9085	0.9999	-0.012
50	3.8925	3.8925	3.8955	59.0232	1.0008	0.100
100	3.8961	3.8961	3.9052	59.2799	1.0023	0.164

5.4.2 Raman spectroscopy of thin films

The room temperature back-scattered Raman spectra of KNN1G thin films grown on quartz substrate and ceramic target employed to deposit the films is shown in Figure 5.20. The ceramic target exhibited the orthorhombic phase with a space group *Amm*2 and consistent with earlier reports [27-29]. In order to identify the modes and their FWHMs, the spectra were fitted with the sum of Gaussian peaks and listed in Table 5.7. As the OMP increases, the peak positions of v_1 and v_5 modes are shifted toward higher wavenumbers, whereas the FWHM of the v_1 and v_5 modes are found to be decreased. For the v_6 mode, both the peak position and FWHM found to be increased from 179.83 ± 0.21 to 185.22 ± 0.50 and 31.06 ± 06 to 37.75 ± 0.89 with rise in OMP, respectively.

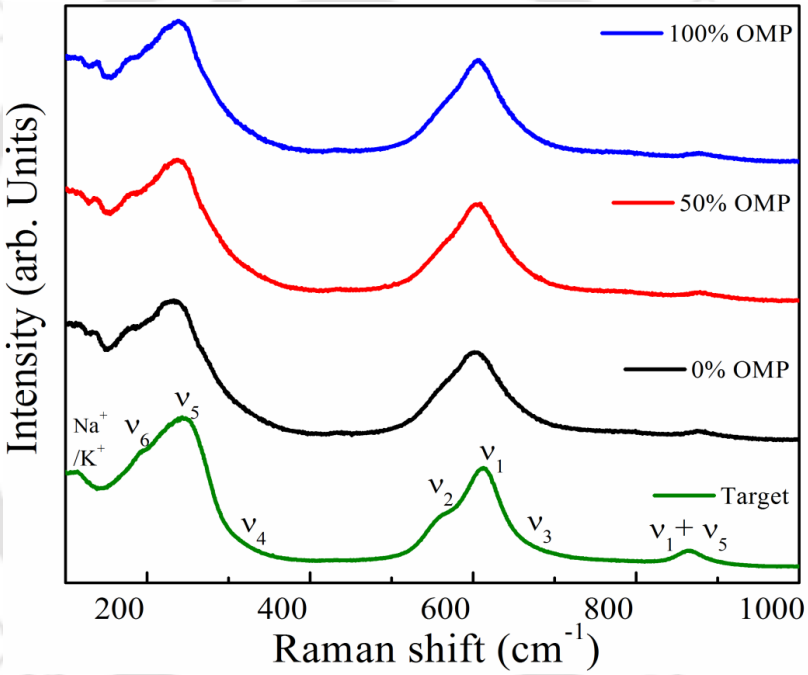

Figure 5.20: *Raman spectra of KNN1G ceramic target and annealed thin films deposited at various OMPs.*

Rubio-Marcos *et al.* [75] reported that the shift in the Raman modes toward higher wavenumber is related to the crystal stress, tetragonality and polarization. In the present study, the tetragonality (*c/a* ratio) calculated from XRD results shows the linear increase with OMP. Further, it is suggested that Raman shift of the modes v_1 and v_5 are very sensitive to the change in the preferred orientation and tetragonality. The relative intensities of the v_1 and v_5 vibrational modes with respect to the low frequency band at 110 cm^{-1} (equation (5.1)) were found to improve with the addition of OMP due to the increasing polarizability. In addition, the blue shift in the both modes v_1 and v_5 are due to

the enhanced binding strength caused by the shortening of the distance between Nb^{5+} and its coordinated oxygen atoms [27-29]. It is assumed that the reduction in the oxygen vacancies in the KNN1G films with increasing the OMP might enhance the binding strength as well as the force constant. Therefore, the obtained peak position and FWHM values of the film deposited under pure oxygen plasma are found to be comparable to the ceramic target.

Table 5.7: *The variation of spectral band position, FWHM of the of v_1 and v_5 modes and relative intensity ratios with respect to a low frequency band located at 110 cm^{-1}.*

OMP (%)	v_5 mode		v_1 mode		Iv_5/I_{110}	Iv_1/I_{110}
	Position(cm^{-1})	FWHM(cm^{-1})	Position(cm^{-1})	FWHM(cm^{-1})		
Target	250.30 ±0.26	59.18 ±0.41	612.88 ±0.14	44.58 ±0.14	1.56	1.03
0	232.34 ±0.35	66.81 ±0.94	602.85 ±0.62	60.30 ±2.29	1.18	0.77
50	235.94 ±0.51	65.12 ±0.99	606.22 ±0.55	55.47 ±1.77	1.26	0.89
100	236.64 ±0.48	61.98 ±1.25	607.27 ±0.53	53.74 ±1.72	1.30	0.96

5.4.3 Microstructural analysis

The FESEM surface micrographs of KNN1G thin films deposited with different OMPs at a substrate temperature of 400 ^oC and annealed at 700 ^oC are shown in Figure 5.21. The microstructure of films deposited under pure argon plasma exhibited a small and non-uniform grain size (28.09 ± 8.03 nm). This might be due to the high rate of deposition in the pure argon plasma; the sputtered atoms can nucleate in the form of islands rather than atomic layers. With a rise in OMP during the deposition, the rate of deposition decreased and the energy redistribution and diffusion of sputtered species increases; therefore, the grain size as well as crystallite size found to be enhanced. The film deposited under pure oxygen plasma shows a homogeneous and dense microstructure with the average grain size of 66.12 ± 14.92 nm. Figure 5.21(d) shows the chemical composition of 0% and 100% OMP films obtained from EDS analysis. It is observed that the composition of the film deposited under pure oxygen plasma found to be closer to target as compared to that of 0% OMP film.

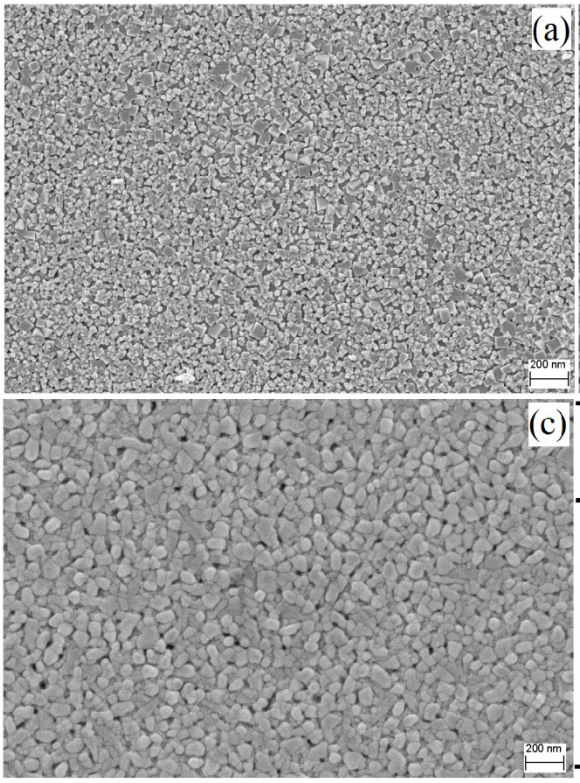

(d)

Element	Atomic percentages (%)	
	0% OMP	100% OMP
K	9.41	9.53
Na	9.30	9.24
Gd	0.35	0.75
Nb	22.19	20.53
O	58.74	59.94

Figure 5.21: *FESEM images for the KNN1G thin films annealed at 700 ^oC deposited at different OMPs (a) 0%, (b) 50%, and (c) 100% OMP and (d) chemical composition.*

5.4.4 Optical studies

5.4.4.1 Linear optical properties

The transmission spectra of KNN1G thin films deposited on quartz substrates and annealed at 700 ^oC in the wavelength range 200 - 900 nm is shown in Figure 5.22. All the films are highly transparent in the visible range, and the fringes in the spectra are due to the interference of the incident light between air-film and film-substrates. The oscillations in the transmittance indicate that KNN1G thin film has uniform thickness and plane surface. The transmittance of all the films drops sharply in the wavelength range of 270-280 nm and the absorption edge displayed a red shift with increasing the OMP. The equations (2.24 & 2.29) were used to estimate the refractive index (n) and thickness (d) of the films [76]. The optical packing density [77] of the films was calculated using the equation (3.3) by considering the refractive index of bulk KNN as 2.2 [78]. The refractive index (n_{700}) of the KNN1G films found to be increased from 2.07 to 2.19 with a rise in the OMP and is displayed in Figure 5.23(a). The observed n_{700} of the KNN1G thin films (2.19) is higher as compared to the KNN thin films (2.07) deposited under pure oxygen plasma [21]. The optical packing density of the KNN1G films improved from 93.1% to

98.5% with increasing the OMP. The enhancement in the refractive index is directly related to the optical packing density, crystallinity, electronic structure, oxygen vacancies, and A-site atoms [79]. The change in electronic structure, reduction in oxygen vacancies, and improvement in optical packing density was observed with increasing the OMP as compared to the pure KNN films. Therefore, the addition of Gd_2O_3 to KNN can significantly improve the optical properties.

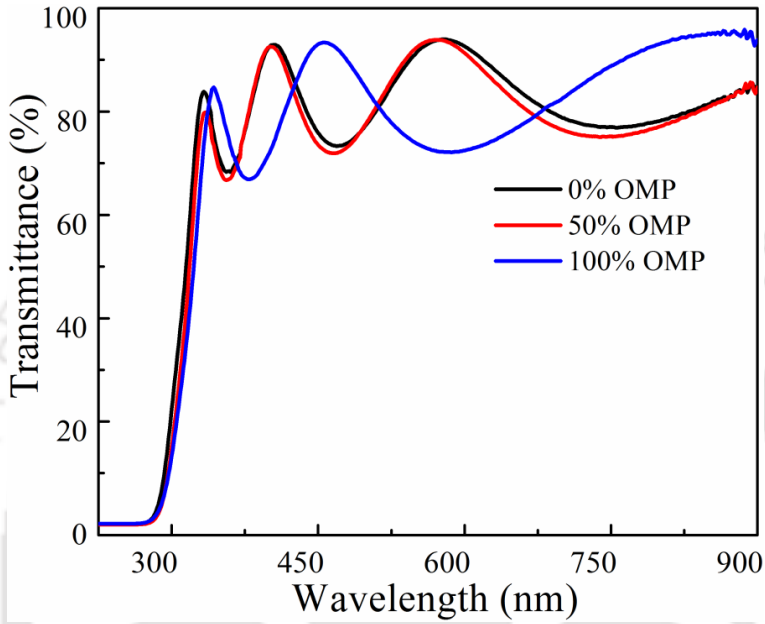

Figure 5.22: *Transmittance spectra of annealed KNN1G thin films deposited at different OMPs.*

The dispersion in the refractive index of KNN1G thin films were analyzed by using Wemple - DiDomenico single oscillator model [80-81]. The dispersion parameters are the key factors in optical communication and in fabricating the spectral dispersion devices. According to the single oscillator model, the material contains elastically bounded atoms, which vibrates with the same natural frequency (ν_o) by the incident light. The wavelength dependent refractive index is analyzed using the equation (3.6) and the parameters such as E_o, E_d and S_o are extracted from the slope and intercept of the $(n^2\text{-}1)^{-1}$ versus λ^{-2} plots, which are shown in Figure 5.23(b) and listed in Table 5.8. Further, the value of n_∞ calculated from the relation $S_o\lambda_o^2 = E_d/E_o = (n_\infty^2 - 1)$. It is observed that E_o, E_d, S_o, and n_∞ values found to be enhanced with increasing OMP, and the film deposited under 100% OMP exhibited these values comparable to six coordinated oxides [82]. The increment in these parameters with the variation in OMP might be due to the higher packing density at higher OMPs. The refractive-index dispersion parameter E_o/S_o of the

film deposited under 100% OMP is 6.64×10^{-14} *eV*. m^2, which is well agreement with reported constant value $6 \pm 0.5\times10^{-14}$ *eV*. m^2 [80].

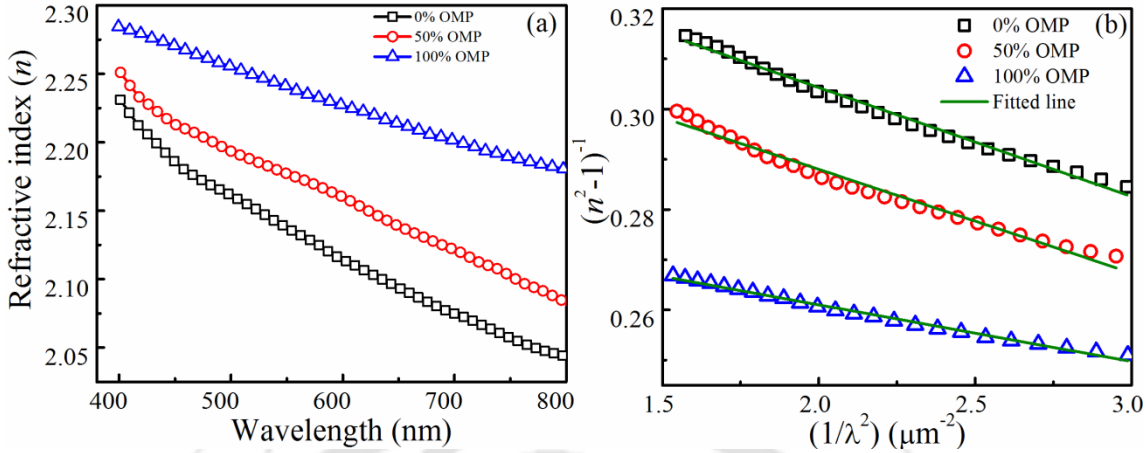

Figure 5.23: *(a) Refractive index as a function of wavelength, and (b) the single oscillator model fitting of annealed KNN1G thin films deposited at different OMPs.*

Table 5.8: *Optical parameters of annealed KNN1G thin films deposited at various OMPs.*

OMP (%)	E_{opt} (*eV*)	n_{700}	E_o (*eV*)	E_d (*eV*)	S_o (10^{14} m^{-2})	n_∞	E_o/S_o (10^{-14} *eV*. m^2)	E_u (*meV*)	Thickness (nm)
0	4.30	2.07	5.01	14.43	0.47	1.97	10.65	138	252
50	4.25	2.12	5.02	15.28	0.49	2.01	10.24	146	259
100	4.20	2.19	6.51	23.13	0.98	2.13	6.64	149	226

The optical bang gap energy (E_g) of the annealed KNN1G films measured using Tauc relation [83] and it is deduced from the extrapolated linear portion of $(\alpha hv)^2$ versus (hv) curve, which is shown in Figure 5.24(a). The E_g value found to be decreases with rise in OMP due to the lowering of the interatomic distance, enhancement in the grain size, and increase of crystallinity. The E_g values of the KNN1G films are in the range of 4.20 – 4.30 *eV* and were slightly less compare to the pure KNN (4.29 - 4.37 *eV*) thin films. It is understood that the addition of Gd_2O_3 to KNN lead to enhance the intermediate energy levels within the bandgap, therefore the E_g found to be lower compared to pure KNN thin films. The E_o/E_g ratio was calculated for all the KNN1G thin films and were in the range of 1.17 - 1.55, which is well agreement with most oxides ($E_o = 1.5\text{-}2E_g$) [81]. The Urbach energy [81] of the KNN1G thin films was estimated using the equation (3.7) from linear portion of $ln\alpha$ versus hv plot as shown in Figure 5.24(b). However, the obtained E_u of the KNN1G thin films is in the range of 138-149 *meV*, which is lower than the pure KNN

thin films (260 – 274 *meV*) indicating that the disorder in the films decreased with Gd_2O_3 doping. A small difference in the value of E_u (~10 *meV*) was observed with rise in the OMP may be due to the different deposition times.

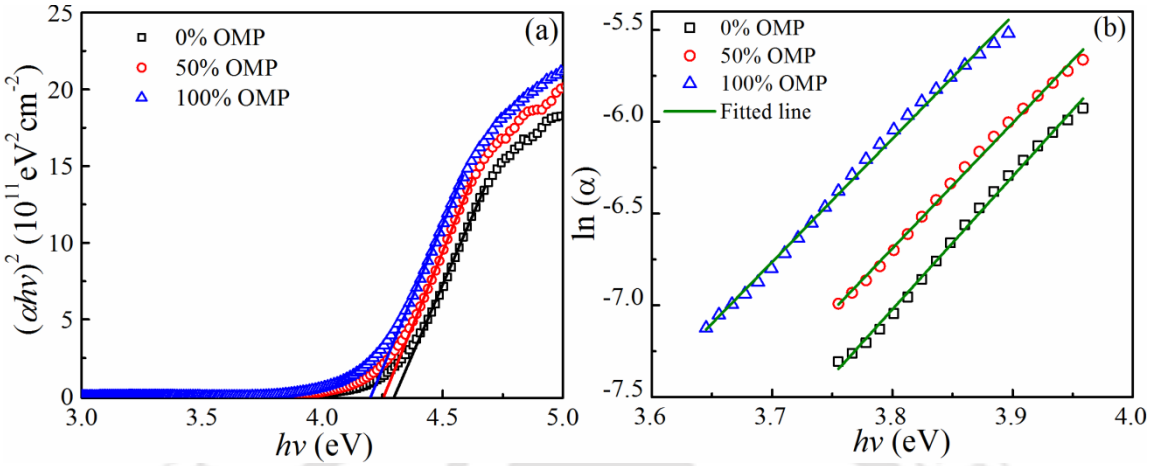

Figure 5.24: *(a) Absorption edges, (b) Urbach energy plots of annealed KNN1G thin films deposited at various OMPs.*

5.4.4.2 Nonlinear optical properties

The nonlinear optical properties of KNN1G thin films were studied using modified single beam z-scan technique [84]. The experimental procedure for the measurement using z-scan technique is explained in chapter 2 (section 2.3.10.2). The beam waist (ω_0) and Rayleigh length ($z_0 = \pi\omega_0^2\lambda$) of the used focused beam was estimated to be 22.58 μm and 2.53 mm, respectively. The peak intensity (I_0) at the focus estimated to be 7.47 kW/cm^2. The closed aperture (CA) and open aperture (OA) z-scan curves of the annealed KNN1G thin films are shown Figure 5.25. The estimated values of n_2, β_{eff}, $\chi_R^{(3)}$, $\chi_I^{(3)}$, and $|\chi^{(3)}|$ using the equations (2.36-2.39) [85, 86] are listed in the Table 5.9. The larger values of n_2, and β_{eff}, were obtained for the film deposited in pure oxygen atmosphere and are 2.46×10^{-5} cm^2/W and 5.02 cm/W, respectively. It can be correlated with the higher optical packing density and *c/a* ratio observed in this film. The high packing density in the medium causes the large absorption of laser energy and thermal agitation of particles leads to the change in the temperature of the medium and enhanced the nonlinearity. From the XRD results, the *c/a* ratio found to be increased with OMP indicates that the asymmetry in the unit cell enhanced. Therefore, the enhanced n_2 and β_{eff} are observed for the film deposited under pure oxygen plasma. Due to the large values of n_2 and β_{eff}, the higher real and imaginary part of nonlinear susceptibility was obtained for 100% OMP

film, were 3.07×10^{-3} esu and 3.16×10^{-3} esu, respectively. The estimated values of $|\chi^{(3)}|$ of the films are 1.04×10^{-3} esu and 4.41×10^{-3} esu for 0% and 100% OMPs, respectively.

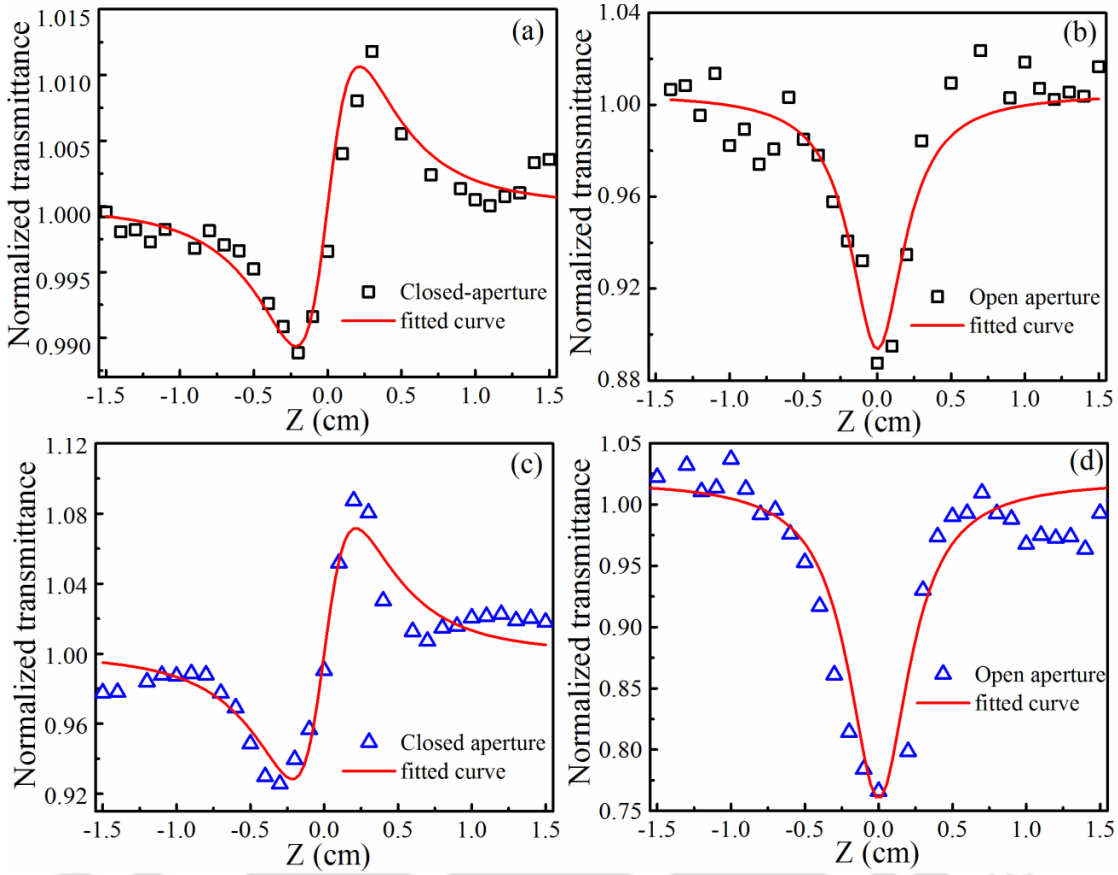

Figure 5.25: *Z-scan curves for annealed KNN1G thin films deposited under pure argon plasma ((a), (b)) and pure oxygen plasma ((c), (d)). The symbols are the experimental data, and the solid lines are theoretical fit curves.*

The figure of merit (FOM) of the KNN1G thin film was calculated by using the equation, $T = \beta_{eff}\lambda/n_2$, which is the essential parameter for optical switching devices [87]. The improved FOM (T = 12.98) was observed for 100% OMP film, compared to the 0% OMP film (T = 37.21). These large optical nonlinearities suggest that Gd_2O_3 doped KNN thin films have a great potential in nonlinear optical device applications.

Table 5.9: *Nonlinear optical properties of KNN1G thin films deposited under pure argon and oxygen plasmas.*

OMP (%)	n_2 (10^{-5} cm^2/W)	β_{eff} (cm/W)	$\chi_R^{(3)}$ (10^{-3} esu)	$\chi_I^{(3)}$ (10^{-3} esu)	$\|\chi^{(3)}\|$ (10^{-3} esu)
0	0.30	1.77	0.33	0.99	1.04
100	2.46	5.02	3.07	3.16	4.41

5.4.5 Dielectric properties

5.4.5.1 Low frequency dielectric properties

The frequency dependence (1 kHz – 1 MHz) of the relative permittivity (ε_r) and loss tangent (*tanδ*) of KNN1G thin films grown on Pt/Ti/SiO_2/Si substrates and annealed at 700 ^oC for 1h are displayed in Figure 5.26.

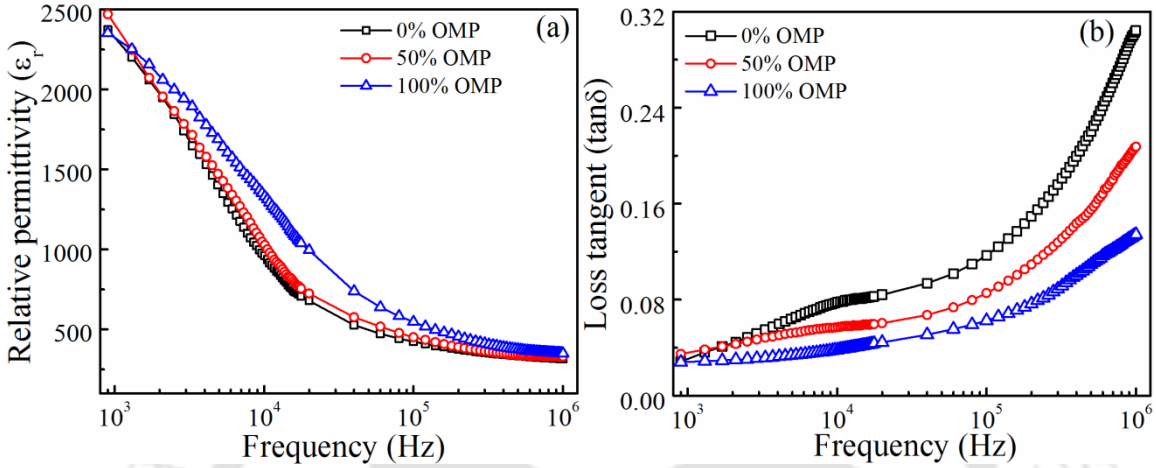

Figure 5.26: *Frequency dependence of dielectric properties of KNN1G thin films deposited various OMPs.*

The frequency dependence (1 kHz – 1 MHz) of the ε_r and *tanδ* of KNN1G thin films grown on Pt/Ti/SiO_2/Si substrates and annealed at 700 ^oC for 1h are shown in Figure 5.26. The frequency dependent ε_r and *tanδ* of KNN1G thin films were measured at room temperature. All the films exhibited the strong dispersion in ε_r over the frequency range of 1 kHz - 20 kHz due to the filter out of space charge polarization. The higher values of ε_r (349) and lower *tanδ* (0.13) at 1MHz was observed for the 100% OMP thin film compared to other films. The *tanδ* of the films were in the range of 2.8 -30.4% and 2.7 -13.4% for the films deposited under 0% and 100% OMPs, respectively. The film deposited under pure argon plasma shown the (110) preferred orientation and with increasing the OMP, the (001) orientation as well as the tetragonality ratio found to be enhanced. The obtained dielectric properties of KNN1G thin films are comparable to the highly (001) oriented KNN films (ε_r = 551 and *tanδ* = 0.03 at 100 kHz) [88]. Wang *et al.* [89] reported the dielectric properties (ε_r = 420 - 660 and *tanδ* = 0.026 - 0.042 at 100 kHz) of Co doped KNN thin films prepared using chemical solution deposition method. Tian *et al.* [90] reported the substrate temperature and crystallographic orientation dependent dielectric properties (ε_r = 350-930 and *tanδ* = 0.028 - 0.042 at 1 kHz) of KNN thin films

prepared using pulsed laser deposition method. They reported the high preferential (001) oriented and larger grain size KNN thin films exhibited the improved dielectric properties. In the present case, the improved dielectric properties are observed for 100% OMP deposited thin films and is attributed to the higher tetragonal ratio, packing density and better crystallinity.

5.4.5.2 Microwave dielectric properties

The microwave dielectric properties of KNN1G thin films on quartz substrates have been measured at 5, 10, and 15 GHz frequencies by using SPDR method [91]. Both ε_r and *tanδ* of the films were calculated based on the thickness and resonant frequencies in iterative method by using equations (2.40 & 2.41), and are listed in Table 5.10. The better ε_r and smaller *tanδ* was observed for the film deposited under 100% OMP at all the measured microwave frequencies. This might be due to the larger grain size, packing density and high tetragonal ratio displayed by this film. In general, the higher packing density can be obtained by lowering the distance between the atoms. It can be helpful to enhance the polarization by increase the electron charge transfer between cations and oxygen atoms [92]. The improved dielectric properties in the film deposited under 100% OMP can be explained in terms of (001) crystal orientation, and blue shift in the v_1 mode. In ABO_3 perovskite materials, a film with (001) crystallographic orientation will show higher relative permittivity than the film oriented in (110) direction due to high *c/a* ratio. Furthermore, the decrease in the FWHM and blue shift in the v_1 mode indicates the enhancement of polarization in the film with increasing the OMP.

Table 5.10: *Microwave dielectric properties of KNN1G thin films, measured by using SPDR technique.*

OMP (%)	at 5 GHz		at 10 GHz		at 15 GHz	
	ε_r	*tanδ*	ε_r	*tanδ*	ε_r	*tanδ*
0	295	0.018	279	0.025	248	0.042
50	306	0.016	288	0.020	251	0.041
100	328	0.010	296	0.012	274	0.017

The high relative permittivity and low loss tangent are the key factors to fabricate the high performance piezoelectric devices and tunable microwave devices. Therefore, the addition of Gd_2O_3 to the KNN matrix greatly enhances the microwave dielectric

properties of KNN thin films and is suitable for the above applications. With increasing the frequency from 5 GHz to 15 GHz, the low values of ε_r and higher *tanδ* were obtained and is attributed to the decrease in the polarization and high conductivity.

5.4.5.3 Temperature dependent dielectric properties

In order to know the Curie temperature (T_C), we have performed the temperature dependent dielectric properties of annealed KNN1G thin film deposited under pure argon plasma and shown in Figure 5.27. The ferroelectric to paraelectric transition temperature (T_C) of the film is determined on the basis of maxima of ε_r around 269 ^oC, which is lower than the ceramic target (T_C = 307^oC). The maximum value of ε_r at T_C is due to the softening in the frequency of transverse optical phonon, explained by Lyddane–Sachs–Teller (LST) relation [93]. Another clear transition was observed at temperature 191^oC, which corresponds to the ferroelectric orthorhombic to ferroelectric tetragonal structural change. Similar transitions were also observed in temperature dependent loss tangent.

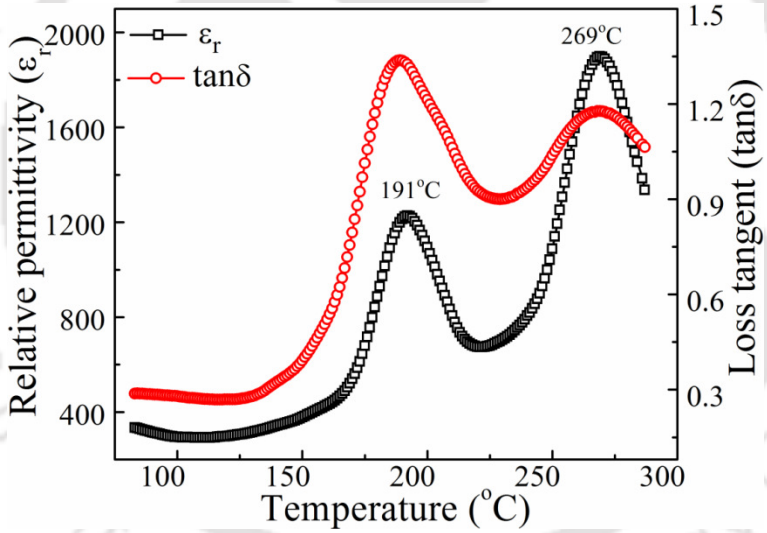

Figure 5.27: *Temperature dependence of dielectric properties of annealed KNN1G thin film deposited under pure argon plasma.*

5.4.5.4 AC-conductivity analysis

Figure 5.28 shows the frequency dependent ac-conductivity of the annealed KNN1G thin films deposited under different OMPs was analyzed by using Jonscher's double power law [54, 94]. The equation (3.9) was used to fit the frequency dependent ac-conductivity of the annealed KNN1G thin films over the frequency range of 1 kHz-1 MHz. The exponent s_1 ($0 \leq s_1 \leq 1$) evaluated from the low frequency region (1 kHz – 100 kHz), which characterizes the grain boundary conductivity. Whereas the exponent s_2 ($1 \leq$

$s_2 \leq 2$) evaluated from the high frequency region (100 kHz – 1 MHz), which characterizes grain conductivity indicating the existence of well localized or re-orientational hopping motion. The exponent s_1 was slightly decreased with increasing the OMP, but exponent s_2 found to be decreased drastically from 1.33 to 1.19 due to the reduction in the charge defects such as oxygen vacancies.

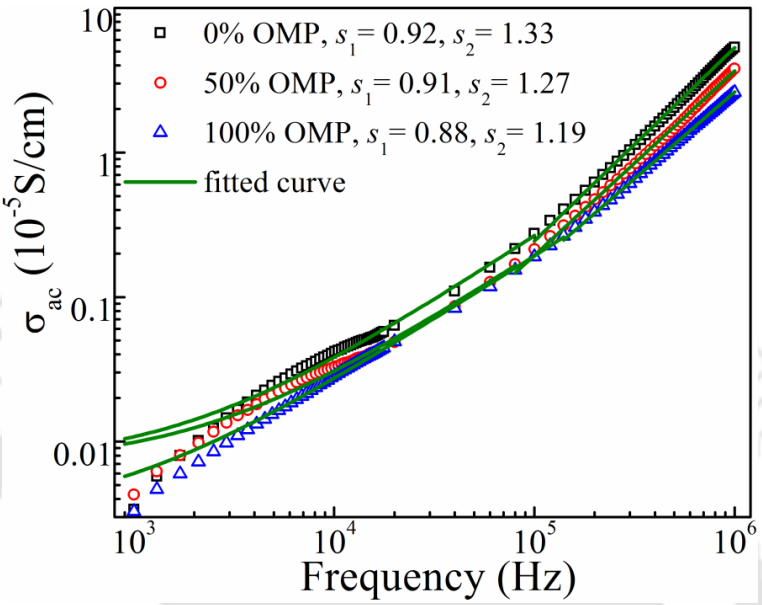

Figure 5.28: *Frequency dependence of ac-conductivity of annealed KNN1G thin films deposited under different OMPs.*

5.4.6 Leakage current characteristics

Materials with low leakage current are required for the fabrication of capacitors and energy harvester related devices. Therefore, it is essential to study the leakage current characteristics of the thin films. The leakage current densities of KNN1G thin films annealed at 700 ^oC, under oxygen atmosphere are shown in Figure 5.29. Relatively low and slow increase of leakage current density (1.47×10^{-8} A/cm^2 at 0 kV/cm, and 4.06×10^{-6} A/cm^2 at 153 kV/cm) is obtained for the film deposited under 100% OMP, which is due to the highly denser surface morphology and good crystallinity presented in the film. The obtained leakage current densities were comparable the highly (001) oriented KNN thin films (~10^{-6} A/cm^2 at 150 kV/cm) prepared by using rf magnetron sputtering technique [88] and found to be lower (~10^{-4} A/cm^2 at 150 kV/cm) as compared to the films reported by Wu *et al.* [95]. The sudden increase of leakage current density 3.32×10^{-5} A/cm^2, and 1.12×10^{-4} A/cm^2 at 153 kV/cm was observed in the 0% and 50% OMP films,

respectively. This is due to the fact that more grain boundary contribution and oxygen deficiencies, which can increase the leakage current density in the films.

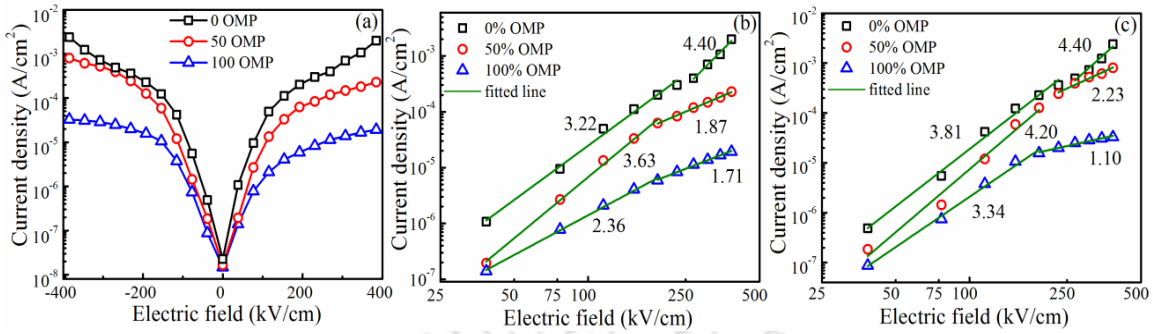

Figure 5.29: *(a) Leakage current densities, SCLC conduction fitting for (b) positive field side and (c) negative field side of log J- log E curves of the KNN1G thin films deposited at different OMPs.*

In order to confirm the conduction mechanism presented in the KNN1G thin films, we have plotted log$J$ – log$E$ curve and analyzed. For the low electric fields (≤ 38 kV/cm), the slopes found to be less than 1, indicating the Ohmic conduction ($J \propto E^{\gamma}$, γ ~1) presented in the system. Above 38 kV/cm, the leakage current density increases abruptly and the obtained slope values are found to be 3.81, 4.20, and 3.34 at 192 kV/cm for the films deposited under 0%, 50%, and 100% OMPs, respectively. Therefore, it can conclude that the space charge limited current (SCLC) is the dominant conduction mechanism in the KNN1G thin films [96]. With further increase in the electric field, γ found to be enhanced to 4.40 for 0% OMP thin film, and linearly decreases to 1.10 for the film deposited in pure oxygen plasma.

5.5 Conclusions

- KNN + x wt.% Gd_2O_3 (x = 0 - 1.5) ceramics have been prepared by solid state reaction method.
- Frequency and temperature dependent dielectric properties were revealed that the compositions with $x \geq 0.5$ exhibited the relaxor behaviour with enhanced dielectric properties.
- The relaxor behaviour of the KNN + x wt.% Gd_2O_3 (x = 0 - 1.5) ceramics is analyzed using modified Curie-Weiss law and Vogel-Fulcher law.
- The higher relative density (95.34%), uniform surface morphology, improved dielectric properties (ε_r = 1112 and $tan\delta$ = 0.03 at 1MHz), ferroelectric properties

($2P_r$ = 31.46 μC/cm^2 and $2E_c$ = 15.23 kV/cm) and tunability (6.74%) were observed for the composition KNN + 1 wt.% Gd_2O_3, and is suitable for high performance piezoelectric applications.

- KNN + 1 wt.% Gd_2O_3 thin films deposited by using RF magnetron sputtering technique.
- The film deposited under pure oxygen plasma exhibited the improved refractive index (n_{700} = 2.19), optical packing density (98.5%), lower optical bandgap (4.20 *eV*).
- The enhanced microwave dielectric properties were observed for the annealed film deposited under pure oxygen plasma, measured using SPDR technique.
- The Curie temperature of the film was found to be around 269 ^oC.
- The leakage current density of the films follows the SCLC conduction mechanism and low leakage current density 4.06×10^{-6} A/cm^2 at 153 kV/cm was observed for the 100% OMP film.
- The large values of optical nonlinear refractive index (2.46×10^{-5} cm^2/W), nonlinear absorption (5.07 cm/W), and third order nonlinear susceptibility (4.41×10^{-3} esu) showed that the Gd_2O_3 doped KNN thin films are promising candidates for nonlinear photonic devices and microwave tunable devices.

5.6 References

[1] J.-F. Li, K. Wang, B.-P. Zhang and L.-M. Zhang, *J. Am. Ceram. Soc.* **89** [2] (2006) 706.

[2] R. E. Jaeger and L. Egerton, *J. Am. Ceram. Soc.* **45** [5] (1962) 209.

[3] H. E. Mgbemere, R.-P. Herber and G. A. Schneider, *J. Eur. Ceram. Soc.* **29** [9] (2009) 1729.

[4] M. Masato, Y. Toshiaki, K. Koichi and H. Shin-ichi, *Jpn. J. Appl. Phys.* **44** [8R] (2005) 6136.

[5] J. Ryu, J.-J Choi, B.-D. Hahn, D.-S. Park, W.-H. Yoon and K.-Y. Kim, *IEEE Trans. Ultrason. Ferroelectr. Freq. Control* **54** [12] (2007) 2510.

[6] Y. Saito, H. Takao, T. Tani, T. Nonoyama, K. Takatori, T. Homma, T. Nagaya and M. Nakamura, *Nature* **432** [7013] (2004) 84.

[7] C.-W. Ahn, H.-C. Song, S. Nahm, S.-H. Park, K. Uchino, S. Priya, H.-G. Lee and N.-K. Kang, *Jpn. J. Appl. Phys.* **44** [44] (2005) L1361.

[8] L. Zhengfa, L. Yongxiang and Z. Jiwei, *Curr. Appl. Phys.* **11** [3] (2011) S2.

[9] Y. Guo, K.-i. Kakimoto and H. Ohsato, Appl. Phys. Lett. **85** [18] (2004) 4121.

[10] B.-Q. Ming, J.-F. Wang, P. Qi and G.-Z. Zang, *J. Appl. Phys.* **101** [5] (2007) 054103.

[11] A. Cheol-Woo, P. Chee-Sung, V. Dwight, N. Sahn, K. Dong-Heon, B. Kyoo-Sik and P. Shashank, *Jpn. J. Appl. Phys.* **47** [12R] (2008) 8880.

[12] Z. Wang, Y. Zhuo, D. Xiao, W. Wu, C. Zhang, X. Huang and J. Zhu, *Curr. Appl. Phys.* **11** [3] (2011) S143.

[13] D. Gao, K. W. Kwok, D. Lin and H. L. W. Chan, *J. Mater. Sci.* **44** [10] (2009) 2466.

[14] J. Yoo and B. Seo, *Ferroelectr.* **425** [1] (2011) 106.

[15] J. Hao, Z. Xu, R. Chu, W. Li and J. Du, *J. Appl. Phys.* **117** [9] (2015) 194104.

[16] Y. Wei, Z. Wu, Y. Jia, J. Wu, Y. Shen and H. Luo, *Appl. Phys. Lett.* **105** [4] (2014) 042902.

[17] I. Kanno, T. Ichida, K. Adachi, H. Kotera, K. Shibata and T. Mishima, *Sens. Actuators A: Phys.* **179** (2012) 132.

[18] B. Zhu, Z. Zhang, T. Ma, X. Yang, Y. Li, K. K. Shung and Q. Zhou, *Appl. Phys. Lett.* **106** [17] (2015) 173504.

[19] M. Blomqvist, S. Khartsev, A. Grishin and A. Petraru, *Integr. Ferroelectr.* **54** [1] (2003) 631.

[20] M. Blomqvist, S. Khartsev and A. Grishin, *Integr. Ferroelectr.* **80** [1] (2006) 97.

[21] M. Peddigari, B. Sindam, K. C. J. Raju, P. Dobbidi and J. Jones, *J Am. Ceram. Soc.* **98** [5] (2015) 1444.

[22] L. Wang, W. Ren, P. Shi, X. Chen, X. Wu and X. Yao, *Appl. Phys. Lett.* **97** [7] (2010) 072902.

[23] M. Abazari, T. Choi, S. W. Cheong and A. Safari, *J. Phys. D: Appl. Phys.* **43** [2] (2010) 025405.

[24] P. Mahesh and D. Pamu, *Thin Solid Films* **562** (2014) 471.

[25] Y. B. Yao, H. T. Chan, C. L. Mak and K. H. Wong, *Thin Solid Films* **537** (2013) 156.

[26] K. Wang and J.-F. Li, *Appl. Phys. Lett.* **91** [26] (2007) 262902.

[27] R. Singh, K. Kambale, A. R. Kulkarni and C. S. Harendranath, *Mater. Chem. Phys.* **138** [2-3] (2013) 905.

[28] Y. Wang, L. Hu, Q. Zhang and H. Yang, *Dalton Trans.* **44** [30] (2015) 13688.

[29] K.-i. Kakimoto, K. Akao, Y. Guo and H. Ohsato, *Jpn. J. Appl. Phys.* **44** [9B] (2005) 7064.

[30] C. W. Ahn, H.-I. Hwang, K. S. Lee, B. M. Jin, S. Park, G. Park, D. Yoon, H. Cheong, H. J. Lee and I. W. Kim, *Jpn. J. Appl. Phys.* **49** [9] (2010) 095801.

[31] W. L. Zhu, J. L. Zhu, Y. Meng, M. S. Wang, B. Zhu, X. H. Zhu, J. G. Zhu, D. Q. Xiao and G. Pezzotti, *J. Phys. D: Appl. Phys.* **44** [50] (2011) 505303.

[32] J. Chen, J. H. Walther and P. Koumoutsakos, *Nano lett.* **14** [2] (2014) 819.

[33] D. Lin, K. W. Kwok and H. L. W. Chan, *J. Phys. D: Appl. Phys.* **40** [21] (2007) 6778.

[34] M. Matsubara, K. Kikuta and S. Hirano, *J. Appl. Phys.* **97** [11] (2005) 114105.

[35] E. Buixaderas, V. Bovtun, M. Kempa, M. Savinov, D. Nuzhnyy, F. Kadlec, P. Vaněk, J. Petzelt, M. Eriksson and Z. Shen, *J. Appl. Phys.* **107** [1] (2010) 014111.

[36] Y. Chen, X.-L. Dong, R.-H. Liang, J.-T. Li and Y.-L. Wang, *J. Appl. Phys.* **98** [6] (2005) 064107.

[37] X. Chou, J. Zhai, H. Jiang and X. Yao, *J. Appl. Phys.* **102** [8] (2007) 084106.

[38] H. Cheng, W. Zhou, H. Du, F. Luo, D. Zhu, D. Jiang and B. Xu, *J. Alloy. Compd.* **579** (2013) 192.

[39] H. Du, W. Zhou, D. Zhu, L. Fa, S. Qu, Y. Li and Z. Pei, *J. Am. Ceram. Soc.* **91** [9] (2008) 2903.

[40] S. Xiao, S. Deng, J. Zhang, Y. Zhou, J. Tang, Y. Wang, L. Wang, H. Qi and J. Wang, *Ceram. Int.* **38** [7] (2012) 6071.

[41] L. E. Cross, *Ferroelectr.* **76** [1] (1987) 241.

[42] J. Ryu, S. Priya and K. Uchino, *Appl. Phys. Lett.* **82** [2] (2003) 251.

[43] V. V. Shvartsman, D. C. Lupascu and D. J. Green, *J. Am. Ceram. Soc.* **95** [1] (2012) 1.

[44] H. Yu and Z.-G. Ye, *J. Appl. Phys.* **103** [3] (2008) 034114.

[45] D. Viehland, S. J. Jang, L. E. Cross and M. Wuttig, *J. Appl. Phys.* **68** [6] (1990) 2916.

[46] G. H. Jonker, *Mater. Res. Bull.* **18** [3] (1983) 301.

[47] K. Uchino and S. Nomura, *Ferroelectr.* **44** [1] (1982) 55.

[48] H. Du, W. Zhou, F. Luo, D. Zhu, S. Qu and Z. Pei, *J. Appl. Phys.* **105** [12] (2009) 124104.

[49] X. Diez-Betriu, J. E. Garcia, C. Ostos, A. U. Boya, D. A. Ochoa, L. Mestres and R. Perez, *Mater. Chem. Phys.* **125** [3] (2011) 493.

[50] K. Funke, *Prog. Solid State Chem.* **22** [2] (1993) 111.

[51] F. A. Kröger and H. J. Vink, Solid State Physics, *Academic Press*, New York (1956).

[52] A. K. Jonscher, *Nature* **267** [5613] (1977) 673.

[53] N. Ortega, A. Kumar, P. Bhattacharya, S. B. Majumder and R. S. Katiyar, *Phys. Rev. B* **77** [1] (2008) 014111.

[54] S. Sumi, P. P. Rao, M. Deepa and P. Koshy, *J. Appl. Phys.* **108** [6] (2010) 063718.

[55] A. K. Jonscher, Dielectric Relaxation in Solids, *Chelsea Dielectrics Press Limited*, London (1983).

[56] D. Emin, *Phys. Rev. B* **48** [18] (1993) 13691.

[57] R. M. Hill, Phys. Status Solidi (a) **34** [2] (1976) 601.

[58] J. J. Hauser, *Physical Review B* **9** [6] (1974) 2623.

[59] S. Upadhyay, O. Parkash and D. Kumar, *J. Electroceram.* **18** [1-2] (2007) 45.

[60] S. Ke, P. Lin, H. Fan, H. Huang and X. Zeng, *J. Appl. Phys.* **114** [10] (2013) 104106.

[61] I. Rawal and A. Kaur, *J. Appl. Phys.* **115** [4] (2014) 043717.

[62] S. Upadhyay, O. Parkash and D. Kumar, *J. Phys. D: Appl. Phys.* **37** [10] (2004)1483.

[63] S. De, S. Niranajana, B. Satyanarayana and M. Rao, *J. Optoelectron. Adv. Mater. Rapid Commun.* **3** [12] (2009) 1365.

[64] V. Ambegaokar, B. I. Halperin and J. S. Langer, *Phys. Rev. B* **4** [8] (1971) 2612.

[65] H. Han, C. Davis and J. C. Nino, *J. Phys. Chem. C* **118** [17] (2014) 9137.

[66] S. Havriliak and S. Negami, *Polym.* **8**, (1967) 161.

[67] http://www.novocontrol.de/html/winfit.htm.

[68] A. Srivastava, P. Maiti, D. Kumar and O. Parkash, *Compos. Sci. Technol.* **93** (2014) 83.

[69] N. Ishizawa, J. Wang, T. Sakakura, Y. Inagaki and K.-i. Kakimoto, *J. Solid State Chem.* **183** [11] (2010) 2731.

[70] J. A. Horn, S. C. Zhang, U. Selvaraj, G. L. Messing and S. Trolier-McKinstry, *J. Am. Ceram. Soc.* **82** [4] (1999) 921.

[71] C.-R. Cho and A. Grishin, *J. Appl. Phys.* **87** [9] (2000) 4439.

[72] A. K. Zak, W. H. A. Majid, M. E. Abrishami and R. Yousefi, *Solid State Sci.* **13** (2011) 251.

[73] K. Tanaka, K.-i. Kakimoto and H. Ohsato, *J. Cryst. Growth* **294** [2] (2006) 209.

[74] S. Wiegand, S. Flege, O. Baake and W. Ensinger, *J. Mater.Sci. Technol.* **28** [6] (2012) 500.

[75] F. Rubio-Marcos, A. Del Campo, P. Marchet and J. F. Fernandez, *Nat. commun.* **6** (2015) 6594.

[76] R. Swanepoel, *J. Phys. E: Sci. Instrum.* **16** [12] (1983) 1214.

[77] Y.-F. Kuo and T.-Y. Tseng, *Mater. Chem. Phys.* **61** [3] (1999) 244.

[78] P. Yongsiri, S. Eitssayeam, G. Rujijanagul, S. Sirisoonthorn, T. Tunkasiri and K. Pengpat, *Nanoscale Res. lett.* **7** [1] (2012) 136.

[79] D. Bao, H. Yang, L. Zhang and X. Yao, *Phys. Status Solidi (a)* **169** [2] (1998) 227.

[80] M. DrDomenico and S. H. Wemple, *J. Appl. Phys.* **40** [2] (1969) 720.

[81] F. Yakuphanoglu, A. Cukurovali and İ. Yilmaz, *Phys. B: Condens. Matter* **353** [3-4] (2004) 210.

[82] S. H. Wemple and M. DiDomenico, *Phys. Rev. B* **3** [4] (1971) 1338.

[83] J. C. Tauc, Optical Properties of Solids, *North–Holland Publishing*, Amsterdam (1972).

[84] I. Kumar and A. Khare, *Opt. Laser Technol.* **77** (2016) 51.

[85] M. Sheik-bahae, A. A. Said, T.-H. Wei, D. J. Hagan, E. W. V. Stryland, *IEEE J. Quantum electron.* **26 [4]** (1990) 760.

[86] K. K. Nagaraja, S. Pramodini, A. Santhosh Kumar, H. S. Nagaraja, P. Poornesh and D. Kekuda, *Opt. Mater.* **35** [3] (2013) 431.

[87] A. Miller, K. R. Welford and B. Daino, Nonlinear Optical Materials and Devices for Applications in Information Technology, *Kluwer Academic Publishers*, Dordrecht (1995).

[88] T. Li, G. Wang, D. Remiens and X. Dong, *Ceram. Int.* **39** [2] (2013)1359.

[89] L. Wang , W. Ren, P. Shi and X. Wu, *J. Alloy. Compd.* **608** (2014) 202.

[90] A. Tian, W. Ren, L. Wang, P. Shi, X. Chen, X. Wu and X. Yao, *Appl. Surf. Sci.* **258** [7] (2012) 2674.

[91] J. Krupka, *Mater. Chem. Phys.* **79** [2–3] (2003) 195.

[92] P. Li, J. F. McDonald and T. M. Lu, *J. Appl. Phys.* **71** [11] (1992) 5596.

[93] R. H. Lyddane, R. G. Sachs and E. Teller, *Phys. Rev.* **59** [8] (1941) 673.

[94] A. K. Roy, A. Singh, K. Kumari, K. Amar Nath, A. Prasad and K. Prasad, *ISRN Ceram.* **2012** (2012) 1.

[95] J. Wu and J. Wang, *J. Appl. Phys.* **106** [6] (2009) 066101.

[96] A. Rose, *Phys. Rev.* **97** [6] (1955) 1538.

Chapter 6

Summary and future scope

6.1 Summary

The present chapter deals with the overall summary of the work carried out. Initially, the processing parameters such as calcination and sintering temperatures were optimized to obtain the single phase with maximum relative density, good dielectric and ferroelectric properties of KNN ceramics were prepared by solid state reaction method. The effect of distinctive additives and their concentrations on structural, microstructural, dielectric and ferroelectric properties are studied systematically. Successful efforts were made to enhance the dielectric and ferroelectric properties by reduction in the initial particle size and the addition of different additives.

In solid state reaction method, the KNN powders calcined at 700 ^{o}C for 5h exhibited the single phase without any secondary phase. Further, the sample sintered at 1050 ^{o}C for 5h exhibited the improved dielectric properties (ε_r = 614 and $tan\delta$ = 0.046) and ferroelectric properties ($2P_r$ = 19.09 μC/cm^2 and $2E_c$ = 21.95 kV/cm) as compared to the samples sintered at 950 ^{o}C and 1000 ^{o}C due to the maximum relative density (92.2%) and uniform grain size. The optimized composition was chosen to make the sputtering target to deposit the KNN thin films by using RF reactive magnetron sputtering technique. In order to know the crystallization temperature, the KNN thin films were deposited onto quartz and Pt/TiO_2/SiO_2/Si substrates at different substrate temperatures room temperature, 200 ^{o}C and 400 ^{o}C under various oxygen mixing percentage (OMP) atmospheres. The effects of substrate temperature and OMP on the structural, microstructural, optical and mechanical properties were studied systematically. The films deposited at 400 ^{o}C shown the crystallinity with a significant amount of secondary phase ($K_2Nb_6O_{16}$) with the good properties such as refractive index (2.02 - 2.17), packing density (89 - 97%), bandgap (4.03 – 4.32 *eV*), hardness (2.1 – 9.4 GPa), elastic modulus (38.1 - 100.2 GPa) and dielectric properties (ε_r = 229 and $tan\delta$ = 0.009 at 1 MHz). Therefore, to eliminate the secondary phase, the KNN thin films are deposited at 400 ^{o}C under different OMPs were annealed at 700 ^{o}C for 1h in oxygen atmosphere. The effect of OMP on the structural, microstructural, optical and dielectric properties was studied

systematically. For the first time, KNN thin films were deposited in pure oxygen plasma, and these films exhibited the pure perovskite KNN phase with improved optical (n_{700} = 2.07, P = 93.1%, E_g = 4.29 eV) and dielectric properties (ε_r = 310 and $tan\delta$ = 0.034 at 1MHz). Also, the dispersion in the refractive index of the KNN films was analyzed using Wemple - DiDomenico (W-D) single oscillator, and the microwave dielectric properties were measured using split post dielectric resonator method for the first time.

It is well known that the donor type dopants can enhance the electrical performance of the ferroelectric ceramics. Therefore, the rare earth oxides (REO) Dy_2O_3 and Gd_2O_3 of different concentrations of 0.5 - 1.5 wt.% were added to KNN ceramics and studied their effect on crystal structure, microstructure, density, dielectric and ferroelectric properties. In both the cases, it is observed that the crystal structure of the KNN ceramics changed from orthorhombic to psuedocubic structure with enhanced dielectric and ferroelectric properties as compared to pure KNN ceramics. The density of the REO doped KNN ceramics found to be improved, whereas the grain size decreased with increasing the concentration of REO in the KNN matrix. The relaxor behaviour is also observed for the higher concentrations of REO due to the compositional heterogeneity in the KNN matrix, which is analyzed using modified Curie-Weiss law and Vogel-Fulcher law. The ac-conductivity of the samples was analyzed using variable range hopping mechanism. In case of Dy_2O_3 contained KNN ceramics, KNN + 0.5 wt.% Dy_2O_3 (KNN05D) composition exhibited the improved dielectric properties (ε_r = 677 and $tan\delta$ = 0.04 at 1MHz) and ferroelectric ($2P_r$ = 27.36 μC/cm^2 and $2E_c$ = 15.46 kV/cm). However, for the Gd_2O_3 contained KNN ceramics, KNN + 1.0 wt.% Gd_2O_3 (KNN1G) displayed the maximum relative density (95.34%), uniform surface morphology, improved dielectric properties (ε_r = 1112 and $tan\delta$ = 0.03 at 1MHz), ferroelectric properties ($2P_r$ = 31.46 μC/cm^2 and $2E_c$ = 15.23 kV/cm) and tunability (6.74%).

Further, the thin films of KNN05D and KNN1G have been deposited by RF reactive magnetron sputtering from the ceramic target prepared using optimized conditions by solid state reaction method. The systematic investigation has been done on the effect of OMP on the crystal structure, surface morphology, linear and nonlinear optical properties, and low frequency and microwave dielectric properties. The as-deposited films are found to be partially crystalline. After annealing, all the films exhibited the crystalline phase without any secondary phase and crystallite size of the films increased with an increase in OMP. Both KNN05D and KNN1G thin films

exhibited the change in preferred orientation with OMP. The films deposited under pure oxygen plasma are highly oriented in (001) crystallographic direction and exhibited the higher tetragonality ratio and uniform grain size.

The optical properties of rare earth oxide contained thin films have been studied carefully. It was observed that the refractive index (n_{700}) of the films increased with an increase in OMP, whereas the bandgap decreased. The higher refractive index n_{700} = 2.21 obtained for KNN05D thin film as compared to KNN1G (2.19) and KNN (2.07) thin films, whereas the lower bandgap obtained for the KNN1G film (4.20 *eV*) as compared to KNN05D (4.28 *eV*) and KNN (4.29 *eV*) films deposited under pure oxygen plasma. For the first time, the nonlinear optical properties of the KNN based thin films measured using z-scan technique. Both the KNN05D and KNN1G thin films exhibited the strong optical nonlinearity and suitable for nonlinear photonic applications. The KNN05D thin films exhibited the larger values of nonlinear refractive index (n_2 = 7.04×10^{-6} cm^2/W), nonlinear absorption (β_{eff} = 1.70 cm/W), and third order nonlinear susceptibility ($|\chi^{(3)}|$ = 1.40×10^{-3} esu), whereas KNN1G films also displayed the larger values of n_2 = 2.46×10^{-5} cm^2/W, β_{eff} = 5.07 cm/W and $|\chi^{(3)}|$ = 4.41×10^{-3} esu for the films deposited under pure oxygen plasma.

The dielectric properties of pure KNN, KNN05D and KNN1G films were measured at low frequency as well as at microwave frequencies. In both the cases, the dielectric properties of the films showed the profound dependence on OMP and the properties were improved by an increase in OMP due to the reduction in the oxygen vacancies and conductivity. The KNN05D films exhibited the improved dielectric properties at low frequencies (ε_r = 343 and $tan\delta$ = 0.045 @ 1MHz) as well as at microwave frequencies (ε_r = 307 and $tan\delta$ = 0.014 @ 10 GHz) as compared to the KNN1G (ε_r = 296 and $tan\delta$ = 0.012 @ 10 GHz) and KNN (ε_r = 287 and $tan\delta$ = 0.010 @ 10 GHz) thin films, which is attributed to the higher tetragonality ratio. The obtained microwave dielectric properties of pure and REO doped KNN thin films make them suitable in microwave tunable applications.

Furthermore, the leakage current characteristics of pure and REO doped KNN thin films were measured, and the conduction mechanisms are responsible for the leakage current is identified. The leakage currents were also shown the enormous dependence on the crystallinity, microstructure, and OMP. It is noted that the low leakage current

densities were observed for the REO doped KNN thin films deposited under pure oxygen plasma, as compared to the pure KNN thin films.

From the present thesis, the obtained best linear and nonlinear optical properties, microwave dielectric properties, and low leakage current properties of the REO doped KNN thin films make this material suitable for optoelectronic, integrated electronic, antireflection nonlinear photonic and microwave tunable device applications.

6.2 Future scope

The results obtained in the present study come out from a systematic study and analysis of pure and REO doped KNN ceramics and thin films. However, further studies are required for the complete characterization of the REO doped KNN ceramics and thin films. Here, we proposed some future work as follows,

(a) Different sintering aids may be tried to reduce the sintering temperature and dwelling time. Also, pure and REO doped KNN ceramics would be sintered using microwave sintering method and compare the results with the conventional sintering methods.

(b) In the present study, we have investigated the third order nonlinear optical properties of REO doped thin films. It will be interesting to study the electro-optic properties such as second order nonlinear optical properties of pure and REO doped KNN thin films in detail.

(c) Earlier reports suggest that the doping of rare-earth ions can greatly enhance the photoluminescence performance of KNN ceramics. Therefore, the photoluminescence properties of Dy_2O_3 and Gd_2O_3 doped KNN ceramics and thin films will be studied and compared with the pure KNN.

(d) Till now, we have studied the dielectric and ferroelectric performance of pure and REO doped KNN ceramics and have not studied the fatigue and piezoelectric properties. Therefore, the complete ferroelectric and piezoelectric properties of pure and REO doped KNN ceramics, and thin films will be studied for the sensor application point of view.

(e) Further, the piezoelectric sensor can be fabricated using optimization conditions.

List of publications

1) **P. Mahesh**, Gyan Prakash Bharti, Alika Khare, Dobbidi Pamu, Optical and dielectric studies on radio frequency sputtered Gd_2O_3 doped $K_{0.5}Na_{0.5}NbO_3$ thin films for nonlinear photonic and microwave tunable device applications, *Journal of Alloys and Compounds*, **682** (2016) 634.
2) **P. Mahesh** and D. Pamu, Raman, Dielectric and AC-conductivity Behaviour of Dy_2O_3 Contained $K_{0.5}Na_{0.5}NbO_3$ Ceramics, *AIP Conference Proceedings*, **1731** (2016) 030010.
3) **P. Mahesh**, S. Thota, D. Pamu, Dielectric Response and AC-conductivity Studies of Gd_2O_3-Contained $K_{0.5}Na_{0.5}NbO_3$ Piezoelectric Ceramics, *IEEE Transactions on Dielectrics and Electrical Insulation*, **22** [6] (2015) 3668.
4) **P. Mahesh,** and Pamu Dobbidi, Raman, dielectric and variable range hopping nature of Gd_2O_3-doped $K_{0.5}N_{0.5}NbO_3$ piezoelectric ceramics, *AIP Advances*, **5** (2015) 107129.
5) **P. Mahesh**, Bashaiah Sindam, K.C. James Raju, and D. Pamu, Optical and Microwave Dielectric Properties of Phase Pure $(K_{0.5}Na_{0.5})NbO_3$ Thin Films Deposited by RF Magnetron Sputtering, *Journal of American Ceramic Society*, **98** [5] (2015) 1444.
6) **P. Mahesh**, D. Pamu, Raman and Dielectric Studies on Lead free $(K_{0.5}Na_{0.5})$ NbO_3 Piezoelectric Ceramics, *IOP Conf. Series: Materials Science and Engineering*, **73** (2015) 012141.
7) **P. Mahesh**, Subhash Thota, and Dobbidi Pamu, Dielectric and AC-conductivity studies of Dy_2O_3 doped $(K_{0.5}Na_{0.5})NbO_3$ ceramics, *AIP Advances*, **4** (2014) 087113.
8) **P. Mahesh** and D. Pamu, Effect of deposition temperature on structural, mechanical, optical and dielectric properties of RF sputtered nanocrystalline $(K_xNa_{1-x})NbO_3$ thin films, *Thin solid films*, **562** (2014) 471.
9) **P. Mahesh**, Ajeet Kumar, A. R. James, D. Pamu, Dielectric and Ferroelectric Studies on Lead Free Piezoelectric KNN Ceramics, *AIP conference proceedings*, **1512** (2013) 62.
10) **P. Mahesh**, Vivek Patel, Gyan Prakash Bharti, Alika Khare, Dobbidi Pamu, Microwave dielectric and nonlinear optical studies on radio frequency sputtered Dy_2O_3 doped KNN thin films (submitted).

Conferences and workshops

1) **P. Mahesh** and D. Pamu, Raman, Dielectric and AC-conductivity Behavior of Dy_2O_3 Contained $K_{0.5}Na_{0.5}NbO_3$ Ceramics, presented in *60th DAE Solid State Physics Symposium (DAE-SSPS-2015)*, 21-25 December 2015 at Amity University UP, Noida, Uttar Pradesh, India.
2) Participated in *Research Conclave*, during 23-26 March 2015 at IIT Guwahati, Guwahati, Assam, India.
3) Participated in *IUCr workshop on X-ray diffraction systems and related applications*, during 11-12 September 2014 at IIT Guwahati, Guwahati, Assam, India.
4) Participated in *Advanced Workshop on Dielectric Impedance Analyzer*, during 17 -18 January 2014 at University of Delhi, Delhi, India.
5) **P. Mahesh** and D. Pamu, Dielectric properties of Nanocrystalline Dy_2O_3 doped $K_{0.5}Na_{0.5}NbO_3$ lead free piezoelectric ceramics, presented in *3rd International Conference on Advanced Nanomaterials and Nanotechnology (ICANN 2013)*, 1-3 December 2013, IIT Guwahati, Guwahati, Assam, India.
6) **P. Mahesh** and D. Pamu, Dielectric Spectroscopy of Dy_2O_3 Doped $(K_{0.5}Na_{0.5})NbO_3$ Piezoelectric Ceramics, presented in *58th DAE Solid State Physics Symposium (DAESSPS-2013)*, 17-21 December 2013 at Thapar University, Patiala, Punjab, India.
7) **P. Mahesh**, T. Santhosh Kumar, D. Pamu, Effect of deposition temperature and O_2% on optical and mechanical properties of lead free piezoelectric $(K_{0.5}Na_{0.5})NbO_3$ thin films by RF sputtering, Presented in *17th National Seminar on Ferroelectrics and Dielectrics-XVI (NSFD-XVI)*, 17-19 December 2012, Odisha, Bhubaneswar, India.
8) **P. Mahesh**, Ajeet Kumar, A. R. James, D. Pamu, Dielectric and ferroelectric studies on lead free piezoelectric KNN ceramics, Presented in *57th DAE Solid State Physics Symposium (DAESSPS-2012)*, 3-7 December, 2012, IIT Mumbai, Maharastra, India.
9) **P. Mahesh**, B. Biswas, T. Santhosh Kumar, R. K. Bhuyan, D. Pamu, Raman and Dielectric studies on lead free $(K_{0.5}Na_{0.5})NbO_3$ piezoelectric ceramics, Presented in *International Conference on Materials science and Technology (ICMST)*, 10-14 June 2012, Kottayam, Kerala, India.

Outside thesis work

Journal publications

1) **P. Mahesh**, Srinivas Pattipaka, Gyan Prakash Bharti, Alika Khare, Dobbidi Pamu, Nonlinear optical and dielectric properties of Gd_2O_3 and Dy_2O_3 doped $K_{0.5}Na_{0.5}NbO_3$ thin films for nonlinear photonic applications, *Optical Materials* **58** (2016) 9.
2) Srinivas Pattipaka, **P. Mahesh**, and D. Pamu, Structural and dielectric properties of lead free $Bi_{0.5}Na_{0.5}TiO_3$ ceramics, *AIP Conference Proceedings* **1728** (2016) 020352.
3) Joshi D.C, Thota S, Nayak S, Harish D. D, **P. Mahesh**, Kumar. A, D. Pamu, Qureshi Md, Dielectric behavior of $Zn_{1-x}N_xO$/NiO two-phase composite, *Journal of Physics D: Applied Physics*, **47** (2014) 435305.
4) **P. Mahesh**, T. Subhash and D. Pamu, Dielectric Spectroscopy of Dy_2O_3 Doped $(K_{0.5}Na_{0.5})NbO_3$ Piezoelectric Ceramics, *AIP Conference Proceedings*, **1591** (2014) 90.
5) **P. Mahesh** and D. Pamu, Structural, mechanical and optical properties of nanocrystalline $(K_{0.34}Na_{0.65})NbO_{3.01}$ thin films deposited by RF sputtering, *Journal of Ceramic Science and Technology*, **5** [1] (2014) 23.

Conferences and workshops

1) Srinivas Pattipaka, **P. Mahesh**, and D. Pamu, Structural and Dielectric Properties of Lead Free $Bi_{0.5}Na_{0.5}TiO_3$ Ceramics, Presented in *International Conference on Condensed Matter and Applied Physics (ICC-2015)*, during 30-31 October 2015 at Bikaner, Rajasthan, India.
2) Participated in *Micromanufacturing for Biomedical Applications*, during 23-27 February 2015 at IIT Guwahati, Guwahati, Assam, India.
3) Participated in *Computational Techniques in Physics* during 1-6 August 2011, at IIT Guwahati, Guwahati, Assam, India.